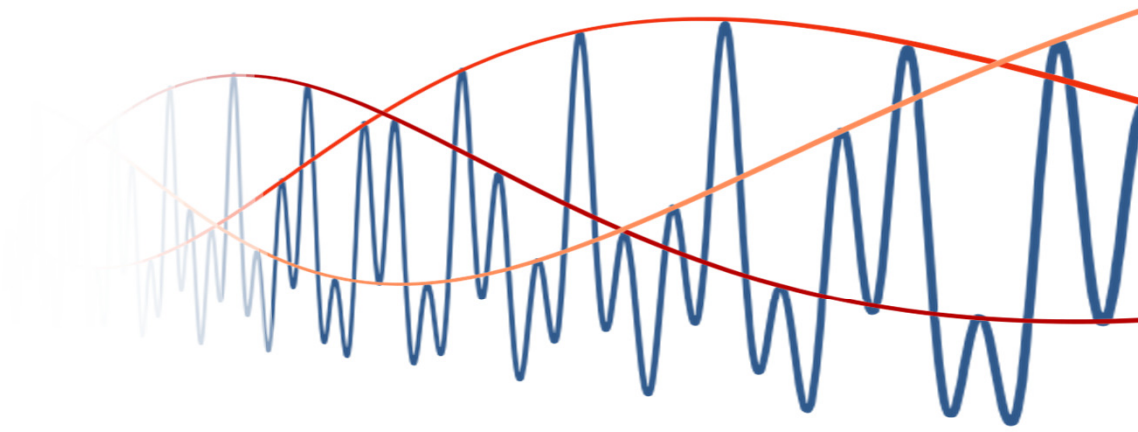

Advanced Fiber Sensing Technologies using Microstructures and Vernier Effect

André Rodrigues Delgado Coelho Gomes
Doctoral Program in Physics
Department of Physics and Astronomy
2021

Supervisor
Orlando José dos Reis Frazão, Invited Assistant Professor, FCUP

Co-supervisor
Hartmut Bartelt, Leibniz IPHT

Faculty of Sciences of the University of Porto

Advanced Fiber Sensing Technologies using Microstructures and Vernier Effect

André Rodrigues Delgado Coelho Gomes

Dissertation submitted to the Faculty of Sciences of the University of Porto for the degree of Ph.D in Physics

This dissertation was conducted under the supervision of

Prof. Dr. Orlando José dos Reis Frazão

Invited Assistant Professor at the Department of Physics and Astronomy, Faculty of Sciences, University of Porto, and Researcher at the Centre for Applied Photonics, INESC TEC, Portugal

and

Prof. Dr. Hartmut Bartelt

Full Professor (Emeritus) at the Faculty of Physics and Astronomy, Friedrich-Schiller University Jena, and Researcher at the Leibniz Institute of Photonic Technology, Germany

Declaration

I hereby declare that this submission is my own work and that, to the best of my knowledge and belief, it contains no material previously published or written by another person nor material which to a substantial extent has been accepted for the award of any other degree or diploma of the university or other institute of higher learning, except where due acknowledgment has been made in the text.

André Rodrigues Delgado Coelho Gomes

2021

Bolsa de investigação da Fundação para a Ciência e a Tecnologia com a referência SFRH/BD/129428/2017, financiada no âmbito do POCH - Programa Operacional Capital Humano, comparticipada pelo Fundo Social Europeu e por fundos nacionais do MCTES.

„Auch ist das Suchen und Irren gut, denn durch Suchen und Irren lernt man. Und zwar lernt man nicht blos die Sache, sondern den ganzen Umfang."

Johann Wolfgang von Goethe

"Searching and erring is also good, because through searching and erring one learns. And you don't just learn the 'thing', but the whole scope."

"Pesquisar e errar também é bom, porque através da pesquisa e do erro aprende-se. E não se aprende apenas a 'coisa', mas todo o âmbito."

Acknowledgments

First of all, I am deeply grateful to my supervisor, Professor Orlando Frazão, for all the advice, support, and friendship during these years. Since I first had the opportunity to work under his supervision, back in 2015, he always took special care of my personal development, as a researcher and has a human being. His knowledge, challenges, and willingness to pursue new ideas were key to the success of my work and career. Thanks to him, I had plenty of opportunities and adventures that made me grow, leave my mark, and be were I am today.

A very special gratitude also goes to my co-supervisor, Professor Hartmut Bartelt, who provided all the support during my time at the Leibniz IPHT, in Germany. Even though he was about to retire, he didn't refuse to embrace me as his student and was always ready to guide and advise me. He always took special care of my work and for many times he enlightened me during our fruitful conversations about my new results and new discoveries.

My journey was shared with colleagues and friends from the Centre of Applied Photonics, INESC TEC: Ricardo André, Rita Ribeiro, Luís Coelho, Nuno Silva, Diana Guimarães, Susana Silva, Duarte Viveiros, Prof. Paulo Marques, Prof. Ariel Guerreiro, Prof. Pedro Jorge, Prof. António Pereira Leite, Prof. Carla Rosa, Prof. Manuel Marques, Dr. Ireneu Dias, and our dear Luísa Mendonça, who provided me support, care, and interesting scientific and non-scientific dicussions. A special thanks to my university friends and colleagues: Catarina Monteiro, Miguel Ferreira, João Maia, and Vítor Amorim (with whom I shared this journey since the 12^{th} grade), for all the good times we had, for all the pranks, and for all the suffering we endure during these years.

I thank Prof. José Luís Santos for being our mentor and adviser at the SPIE Student Chapter. To SPIE for providing funding and support to our Student Chapter, of which I had the pleasure to belong to and to be officer. Thanks to all the colleagues that helped in organizing all the wonderful events during these last years.

I would also like to acknowledge Fundação para a Ciência e Tecnologia for my PhD scholarship (SFRH/BD/129428/2017), which allowed me to realize my work between INESC TEC, in Portugal, and the Leibniz Institute of Photonic Technology, in Germany.

From the Leibniz Institute of Photonic Technology (IPHT), a special thanks to Martin Becker, who was the first person I've met when I first arrived to the institute during my

Masters, and who was always my contact person, a guide, and a friend. I am especially grateful to Manfred Rothhardt and to the Passive Fiber Modules, for allowing me to do my research with them, providing all the facilities, equipment, support, and collaboration.

During my stay at IPHT, I was able to collaborate with many different groups. My thanks go to Jan Dellith, for all the time spent teaching me and providing me support on the use of the focused ion beam and scanning electron microscope systems. To Jörg Bierlich and Jens Kobelke, for providing new fibers, for all the interesting discussions, and for always being willing to cooperate and help. To Tina Eschrich, for all the time spent teaching me and providing me support on the use of the Vytran.

A special thanks also goes Professor Markus Schmidt, for receiving me in his group and allowing me to perform very interesting and challenging projects in parallel with my work for the PhD. It allowed me to experience and face new topics, and involved me in fruitful discussions. For that I am also thankful to the Fiber Photonics group: Jiangbo Zhao (Tim), Shiqi Jiang, Ramona Scheibinger, Kay Schaarschmidt, Bumjoon Jang, Jisoo Kim, Saher Junaid, Malte Plidschun, Xue Qi, Mona Nissen, Tilman Lühder, Ronny Förster, Torsten Wieduwilt, Henrik Schneidewind, Hartmut Lehman, and Matthias Zeisberger, for all the meetings, discussions, and experiences shared during this time.

Thanks to all my friends and colleagues from IPHT: Ivo Leite, Sergey Turtaev, Maria Chernysheva, Dirk Boonzajer Flaes, Yang Du, Professor Tomas Cizmar, Hana Cizmarova, Oguzhan Kara, Benjamin Rudolf, Ron Fatobene Ando, and especially Ravil Idrisov and Beatriz Silveira, for all the support, advise, discussions, and experiences shared inside and outside the institute. A very special gratitude goes to my friend Marta Ferreira, not only for all the guidance, inspiration, and collaboration at work (even very busy, she helped me and joined forces to develop interesting research work), but also for all the mutual complain moments about having to climb the “mountain”, for all the hikes, the cooking and baking, and the chocolate breaks (very important to feed the brain and to be very productive... except on fridays!).

At last, but not least, to all my Family, especially my parents, for supporting me through all these years and for always being there for me.

Abstract

The work presented in this PhD dissertation intends to explore and develop advanced sensing technologies in optical fiber. The sensing elements were designed to possess enhanced sensing capabilities, in particular the ability to achieve high sensitivity values. The developed structures were based on two main components: the creation of interferometric microstructures in optical microfibers and microfiber probes, and the application of the optical Vernier effect.

Taking advantage of the small dimensions of optical microfibers and their properties, different microstructured interferometers were combined with them to form sensing structures. One of the works combined a microfiber knot resonator with a Mach-Zehnder interferometer, both embedded in the same optical microfiber. The sensor was characterized in temperature and refractive index of liquids. The combined response of the two interferometric structures allowed to achieve simultaneous measurements of these two parameters, solving the common cross-sensitivity problem.

Competences in the use of focused ion beam technology were also acquired during the PhD programme. This technology was used to microfabricate interferometric structures in optical microfiber probes and to open access holes for liquids in specialty fibers. In this context, a Fabry-Perot interferometer was milled in a multimode optical microfiber probe for enhanced temperature sensing. The presence of multiple modes in the interferometric structure generated a beat signal at the output. The envelope modulation presented enhanced sensitivity in comparison with the normal sensing Fabry-Perot interferometer.

The application of the optical analog of the Vernier effect to optical fiber sensing interferometers has recently shown a huge potential to improve their performance. The use of two interferometers with slightly detuned interferometric frequencies introduces an envelope modulation to the output spectrum with increased sensitivity. A detailed analysis on the optical Vernier effect and its properties is included in this dissertation. The study and application of the optical Vernier effect during this PhD led to the discovery of an extension of the concept and new ways to surpass its limitations.

For the first time, the existence of optical harmonics of the Vernier effect was demonstrated, theoretically and experimentally. By increasing harmonically the optical path length of the reference interferometer by an integer multiple of the optical path length of the sensing interferometer, additional magnification proportional to the harmonic order

could be obtained. The configurations of the effect in parallel and in series have been experimentally demonstrated. The parallel configuration consisted of two Fabry-Perot interferometers made of a hollow capillary tube and was characterized for applied strain. The series configuration explored a complex case of optical Vernier effect, where both interferometers act as sensors and, therefore, no reference is used. The structure also consisted of two Fabry-Perot interferometers, in this case a hollow microsphere and a section of a multimode fiber. Simultaneous measurement of applied strain and temperature with high sensitivity was achieved.

Lastly, two sensing configurations were specially designed and characterized to measure properties of liquids, in this case the refractive index and viscosity. The first sensor combined different techniques and concepts developed during the PhD. The structure combined an extreme case of optical Vernier effect in a few-mode Fabry-Perot interferometer made from a hollow capillary tube, together with focused ion beam milling to open access holes for the liquid. The extreme optical Vernier effect allowed to achieve giant magnification factors, an order of magnitude beyond the expected limit of the conventional optical Vernier effect, whilst preserving a measurable size of the envelope modulation. When applied to liquid sensing, the result is a giant refractometric sensitivity for a refractive index around water. The second sensing structure explored a different way to post-process the hollow capillary tube to form a small-size probe with an access hole for liquids. Through interferometric measurements of the liquid displacement inside the probe, the viscosity of the liquid could be determined.

Most of the works reported in this dissertation can still be further improved. Moreover, the studies here presented related with the optical Vernier effect and its variants provide a launching pad for the development of a new generation of highly sensitive sensors.

Resumo

O trabalho apresentado nesta dissertação de doutoramento pretende explorar e desenvolver tecnologias sensoras avançadas em fibra óptica. Os elementos sensores foram desenhados para possuírem capacidades sensoras aprimoradas, em particular a capacidade de atingir altos valores de sensibilidade. As estruturas desenvolvidas foram baseadas em duas componentes principais: a criação de microestruturas interferométricas em microfibras ópticas e sondas em microfibra, e a aplicação do efeito óptico de Vernier.

Aproveitando as pequenas dimensões das microfibras ópticas e as suas propriedades, diferentes interferómetros microestruturados foram combinados com elas para formar estruturas sensoras. Um dos trabalhos combinou um nó ressonador em microfibra com um interferómetro de Mach-Zehnder, ambos incorporados na mesma microfibra óptica. O sensor foi caracterizado em temperature e índice de refração de líquidos. A resposta combinada das duas estruturas interferométricas permitiu atingir medições simultâneas destes dois parâmetros, resolvendo o problema comum da sensibilidade cruzada.

Competências no uso da tecnologia de feixe de iões focado também foram adquiridas durante o programa de doutoramento. Esta tecnologia foi usada para microfabricar estruturas interferométricas em sondas de microfibra óptica e para abrir orifícios de acesso para líquidos em fibras especiais. Neste contexto, um interferómetro de Fabry-Perot foi fresado numa sonda de microfibra óptica para deteção aprimorada de temperatura. A presença de multiplos modos na estrutura interferométrica gerou um sinal de batimento na saída. A modulação envolvente apresentou uma sensibilidade melhorada em comparação com o interferómetro sensor de Fabry-Perot normal.

A aplicação do analógico óptico do efeito de Vernier a interferometros sensores em fibra óptica demonstrou recentemente um enorme potencial para melhorar o seu desempenho. O uso de dois interferómetros com frequências interferométricas ligeiramente desafinadas introduz uma modulação envolvente no espectro de saída com sensibilidade aumentada. Uma análise detalhada do efeito óptico de Vernier e das suas propriedades está incluída nesta dissertação. O estudo e aplicação do efeito óptico de Vernier durante este doutoramento levaram à descoberta de uma extensão do conceito e de novas formas de superar as suas limitações.

Pela primeira vez foi demonstrada, teoricamente e experimentalmente, a existência de harmónicos ópticos do efeito de Vernier. Ao aumentar harmonicamente o caminho óptico

do interferómetro de referência por um um múltiplo inteiro do caminho óptico do interferómetro sensor, uma magnificação adicional proporcional à ordem do harmónico pode ser obtida. As configurações do efeito em paralelo e em série foram demonstradas experimentalmente. A configuração em paralelo consistiu em dois interferómetros de Fabry-Perot feitos de um tubo capilar oco e foi caracterizada em deformação. A configuração em série explorou um caso complexo do efeito óptico de Vernier, onde ambos os interferómetros atuam como sensores e, portanto, nenhuma referência é usada. A estrutura também consistiu em dois interferómetros de Fabry-Perot, neste caso uma microesfera oca e uma secção de fibra multimodo. Medição simultânea de deformação aplicada e temperatura com alta sensibilidade foi alcançada.

Por fim, duas configurações sensoras foram especialmente desenhadas e caracterizadas para medir propriedades de líquidos, neste caso o índice de refração e a viscosidade. O primeiro sensor combinou diferentes técnicas e conceitos desenvolvidos durante o doutoramento. A estrutura combinou um caso extremo do efeito óptico de Vernier num interferómetro de Fabry-Perot de poucos modos feito a partir de um tubo capilar oco, juntamente com maquinação por feixe de iões focado para abrir orifícios de acesso para o líquido. O efeito óptico de Vernier extremo permitiu alcançar fatores de magnificação gigantes, uma ordem de magnitude além do limite esperado para o efeito óptico de Vernier convencional, preservando ao mesmo tempo um tamanho mensurável da modulação envolvente. Quando aplicado à deteção de líquidos, o resultado é uma sensibilidade refractométrica gigante para um índice de refração em torno da água. A segunda estrutura sensora explorou uma forma diferente de pós-processar o tubo capilar oco para formar uma sonda de tamanho pequeno com um orifício de acesso para líquidos. Através de medidas interferométricas da deslocação do líquido dentro da sonda, a viscosidade do líquido pôde ser determinada.

A maioria dos trabalhos reportados nesta dissertação ainda pode ser melhorada. Além disso, os estudos aqui apresentados relacionados com o efeito óptico de Vernier e as suas variantes fornecem uma plataforma de lançamento para o desenvolvimento de uma nova geração de sensores altamente sensíveis.

Contents

List of Figures

List of Tables

Nomenclature

DCF	Double-Core Fiber
DSHF	Dual Side-Hole Fiber
DSO	Dimethyl Silicone Oil
FBG	Fiber Bragg Grating
FFT	Fast Fourier Transform
FIB	Focused Ion Beam
FMF	Few-Mode Fiber
FSR	Free Spectral Range
GIF	Graded-Index Fiber
HCF	Hollow-Core Fiber
HC-PCF	Hollow-Core Photonic Crystal Fiber
Hi-Bi	High-Birefringent
IFFT	Inverse Fast Fourier Transform
LC	Liquid Crystal
LMAF	Large Mode Area Fiber
MKR	Microfiber Knot Resonator
MZI	Mach-Zehnder Interferometer
OSA	Optical Spectrum Analyzer
PCF	Photonic Crystal Fiber
PM-PCF	Polarization Maintaining Photonic Crystal Fiber
RIU	Refractive Index Units

SEM	Scanning Electron Microscope
SHF	Side-Hole Fiber
SHTECF	Single Hole Twin Eccentric Cores Fiber
SI	Sagnac Interferometer
SMF	Single Mode Fiber
SNOM	Scanning Near-Field Optical Microscopy
TCF	Triple-Core Fiber

Chapter 1.

Introduction

The beginning of optical fibers life history take us back to the 20's, where the first optical fibers were produced. Initially, they were used to guide light at short distances for illumination purposes. The concept of clad fiber (a core protected by a cladding with a lower refractive index) only appeared in the 50's [13]. At that time, the idea of transferring information through optical fibers was growing. However, losses were limiting the transmission of information over long distances through optical fibers. In 1966, Prof. Charles Kao, together with George Hockham, proposed glass fibers as a possible low-loss optical waveguide for a new form of communication medium [14]. The idea of optical fiber communications was then born, reason why Kao received the Nobel Prize in 2009. Henceforth, optical fibers became a topic of extensive research, opening with it new research fields. One of them is the use of optical fibers, not as a communication medium, but as a sensing device.

For telecommunications, a basic fiber structure such as a clad fiber (core, cladding) is sufficient. For sensing applications, a similar fiber structure by itself can also act as a sensor, yet more complex and special optical fiber structures are attractive and desirable, providing many different and additional features. Over the years, several different types of optical fiber sensing structures were created and tested for measuring physical, chemical, and biochemical parameters. Some traditional examples are fiber Bragg gratings, Mach-Zehnder interferometers, Fabry-Perot interferometers, multimode fiber devices, fiber loop mirrors, among others.

Nowadays, the fast development in different fields of research that make use of optical sensing is creating new challenges also in the field of optical fiber sensing. There is an increasing demand for miniaturized sensing structures, especially with the capability of achieving higher sensitivities and resolutions than what current conventional fiber sensors can provide. Hence, it is necessary to explore alternative options for advanced fiber sensing structures that meet the state-of-the-art demands.

Optical microfibers opened new doors to the study and development of new and enhanced sensors. Due to their properties and small size, optical microfibers are a good

platform for the creation of miniaturized sensing structures. Additionally, optical microfibers can also be microstructured by means of different post-processing techniques, in order to create special and complex sensing devices, designed to have improved sensitivity to certain parameters. The creation of microstructures in optical microfibers and microfiber probes are explored in this dissertation.

The optical Vernier effect has recently shown its huge potential to greatly enhance the sensitivity and resolution of optical fiber sensors. Although it can be challenging to understand and apply, the optical Vernier effect is a tool that provides impressive improvements in sensing performance. This effect is also a case of study of this dissertation.

This chapter provides an overview on the motivation and objectives of this work, followed by a description of the dissertation structure. Finally, the main contributions to the field are presented, as well as the list of publications that resulted from this PhD.

1.1. Motivation and Objectives

The motivation for the research activities developed in the context of the PhD program consisted of performing an original study on new advanced optical fiber sensing technologies relying on microstructures and optical Vernier effect. This includes the combination of different techniques and concepts learned over these last years to achieve new and innovative sensing structures in optical fibers with enhanced sensing performances. Naturally, the desire of learning new concepts and acquire new skills and competences in this field was also a driving force towards the success of the research activities that culminated in this dissertation. Another major motivation was the opportunity to test and try out my own ideas, as well as to solve different challenges and find new solutions for problems and difficulties that constantly emerged as the research activities progressed. Finally, a personal motivation was to give my contribution and make relevant developments in the field of optical fiber sensing, in particular on the application of the optical Vernier effect to fiber sensing interferometers.

The main objectives of the research activities developed during the PhD program consisted in:

- Modeling, fabrication, and characterization of advanced interferometric optical fiber sensors based on microstructures;
- Acquiring competences in using the focused ion beam technology to create sensing microstructures in optical microfiber probes, as well as to open access holes in specialty fibers for liquid sensing inside the fiber;
- Studying and further developing the concept of optical Vernier effect as a tool to enhance the performance of optical fiber sensing interferometers;

- Creating a new generation of optical fiber microsensors of high sensitivity for different applications, including sensing in liquid media.

1.2. Dissertation Overview

This dissertation is organized in 8 chapters that take the the reader on a journey through advanced interferometric sensing configurations based on microstructures in optical microfibers and on the optical Vernier effect.

Chapter 1 provides a brief introduction to the research subject and clarifies the motivation, the goals, and the structure of this dissertation. It also includes the main contributions to the research area and publications that resulted from it.

Chapter 2 presents an introductory overview on optical microfibers and sensing interferometers that will be used along the dissertation. This chapter also explores the application of focused ion beam milling to optical microfiber probes, together with the necessary sample preparation.

Chapter 3 proposes two interferometric microstructured sensing devices with optical microfibers and microfiber probes for enhanced sensing capabilities. The first combines a microfiber knot resonator with a Mach-Zehnder interferometer embedded in the same microfiber for simultaneous measurement of refractive index and temperature. The second device consists of a Fabry-Perot interferometer microfabricated with a focused ion beam in a multimode microfiber probe for enhanced temperature sensing.

Chapter 4 is dedicated to the optical Vernier effect for optical fiber interferometers. The fundamentals of the effect are introduced and explored, using a parallel configuration as the starting point. This chapter presents important discussions regarding the different properties of the effect from a fiber sensing perspective, and an extensive state-of-the-art review on the different configurations and applications of the optical Vernier effect.

Chapter 5 describes the new concept of optical harmonic Vernier effect for optical fiber interferometers. The mathematical description and the new properties that arise from introducing harmonics to the optical Vernier effect, especially the increase in sensing sensitivity, are here addressed. Simulations that demonstrate the mechanics and properties of the effect are also presented. This chapter also includes important discussions related with the difference between the two main configurations: parallel and series, and with the limitations of this concept.

Chapter 6 is dedicated to the experimental demonstration of the optical harmonic Vernier effect for both, the parallel and the series configuration. In a first approach, the parallel configuration is addressed using Fabry-Perot interferometers based on hollow capillary tubes. This work has a strong focus on validating the properties of the effect deduced theoretically in the previous chapter. In the second part, a more specific and complex case of the effect based on a series configuration using a hollow microsphere and

a section of multimode fiber is explored. In this case, both interferometers are physically connected without a separation while, simultaneously, there is no reference interferometer. Additionally, simultaneous measurement of two parameters using this last configuration is also demonstrated.

Chapter 7 presents two advanced sensing configurations based on microstructures for measuring liquid media. It combines different concepts and techniques to achieve novel optical fiber sensing devices with enhanced performances. The first configuration explores an extreme case of optical Vernier effect based on a few-mode Fabry-Perot interferometer, made from a hollow capillary tube. At the same time, focused ion beam milling is used to open access holes on the Fabry-Perot interferometer, enabling it to be filled with liquids. A giant refractometric sensitivity and huge magnification factors, that are impossible to be achieved with the conventional optical Vernier effect, are demonstrated here to be possible through the extreme optical Vernier effect. As for the second configuration, a section of hollow capillary tube is post-processed using electric arc to create a microprobe with a small access hole for viscosity measurement of liquids. The viscosity is obtained through the analysis of a two-wave interferometric signal that changes in time proportionally to the liquid displacement inside the optical fiber probe.

Chapter 8 summarizes the main results obtained during the PhD and reanalyzes the initial objectives. At last, the opportunities for future work emerging from the research presented in this dissertation are also discussed.

1.3. Main Contributions

From the works presented in this dissertation, it is the author's opinion that the following main contributions to the field stand out. First, a more compact and novel hybrid sensing structure combining a microfiber knot resonator with a Mach-Zehnder interferometer using microfibers is presented. The novelty here is the structure, where the Mach-Zehnder interferometer is created using a single microfiber, the same as used to create the microfiber knot resonator, containing two propagating modes, instead of relying on two separated microfibers to create the two arms of the Mach-Zehnder interferometer. Second, the use of focused ion beam to mill Fabry-Perot cavities in microfiber probes is not new, however using a multimode fiber to make the milled Fabry-Perot multimode and introduce the Vernier effect is. Third, the post-processing of a capillary tube led to the development of a small size viscometer probe that only requires tiny volumes (picoliters) to perform the measurement. At last, the works related with the optical Vernier effect represent a large contribution to the field, providing a deeper understanding and control of the effect. The existence of optical harmonics of the Vernier effect was demonstrated for the first time, to the best of the author's knowledge, theoretically and experimentally. The work represents a paradigm shift that required the development of a new mathematical description

to correctly describe the novel properties and behaviors of this extended concept of the optical Vernier effect. The optical harmonics of the Vernier effect are a new tool that other researchers can use from now on, not just applied to Fabry-Perot interferometers, as demonstrated in this dissertation, but also to other different types of interferometers and for other applications. The combination of a hollow microsphere and a multimode fiber section, together with harmonics of the Vernier effect allowed simultaneous measurement of two parameters with high sensitivity. A novel extreme optical Vernier effect is also demonstrated, leading to giant refractometric sensitivity values and huge magnification factors, which are otherwise impossible to achieve with state-of-the-art optical Vernier effect.

1.4. List of Publications

From the activities developed within this PhD resulted a total of 7 publications as a first author in scientific journals (1 of them under revision and 1 review paper to be submitted) 7 communications in national/international conferences, and 1 book chapter. Besides, four additional papers as first authors, including two invited paper, and three as co-author were also published as a result of work and collaborations outside the scope of this dissertation, as well as one communication in international conferences. The list of publications as first author is presented next.

Scientific Journal Publications

1. **A. D. Gomes**, H. Bartelt, and O. Frazão, "Optical Vernier effect: recent advances and developments," Laser and Photonics Reviews, 2021. *doi: 10.1002/lpor.202000588*

2. **A. D. Gomes**, J. Zhao, A. Tuniz, and M. A. Schmidt, Direct observation of modal hybridization in nanofluidic fiber [Invited]," Optical Materials Express 11(2), 559, 2020. *doi: 10.1364/OME.413199* [15]

3. **A. D. Gome**s, J. Kobelke, J. Bierlich, J. Dellith, M. Rothhardt, H. Bartelt, and O. Frazão, "Giant refractometric sensitivity by combining extreme optical Vernier effect and modal interference," Scientific Reports 10(1), 19313, 2020. *doi: 10.1038/s41598-020-76324-7* [16]

4. P. Robalinho, **A. D. Gomes**, and O. Frazão, "Colossal enhancement of strain sensitivity using the push-pull deformation method in interferometry," IEEE Sensors Journal 21(4), 4623-4627, 2020. *doi: 10.1109/JSEN.2020.3033581* [17]

5. P. Robalinho, **A. D. Gomes**, and O. Frazão, "High enhancement strain sensor based on Vernier effect using 2-fiber loop mirrors," IEEE Photonics Technology Letters 32(18), 1139-1142, 2020. *doi: 10.1109/LPT.2020.3014695* [18]

6. **A. D. Gomes**, M. S. Ferreira, J. Bierlich, J. Kobelke, M. Rothhardt, H. Bartelt, and O. Frazão, "Hollow microsphere combined with optical harmonic Vernier effect for strain and temperature discrimination," Journal of Optics and Laser Technology (127), 106198, 2020. *doi: 10.1016/j.optlastec.2020.106198* [19]

7. **A. D. Gomes**, M. S. Ferreira, J. Bierlich, J. Kobelke, M. Rothhardt, H. Bartelt, and O. Frazão, "Optical harmonic Vernier effect: a new tool for high performance interferometric fibre sensors," MDPI Sensors 19(24), 5431, 2019. *doi: 10.3390/s19245431* [20]

8. **A. D. Gomes**, M. Becker, J. Dellith, M. I. Zibaii, H. Latifi, M. Rothhardt, H. Bartelt, and O. Frazão, "Multimode Fabry–Perot interferometer probe based on Vernier effect for enhanced temperature sensing," MDPI Sensors 19(3), 453, 2019. *doi: 10.3390/s19030453* [21]

9. **A. D. Gomes**, J. Kobelke, J. Bierlich, K. Schuster, H. Bartelt, and O. Frazão, "Optical fiber probe viscometer based on hollow capillary tube," Journal of Lightwave Technology 37(18), 4456-4461, 2019. *doi: 10.1109/JLT.2019.2890953* [22]

10. B. Silveira, **A. D. Gomes**, M. Becker, H. Schneidewind, and O. Frazão, "Bunimovich stadium-like resonator for randomized fiber laser operation," MDPI Photonics 5(3), 17, 2018. *doi: 10.3390/photonics5030017* [23]

11. **A. D. Gomes**, C. S. Monteiro, B. Silveira, and O. Frazão, "A brief review of new fiber microsphere geometries," MDPI Fibers 6(3), 48, 2018. (invited) *doi: 10.3390/fib6030048* [24]

12. **A. D. Gomes**, F. Karami, M. I. Zibaii, H. Latifi, and O. Frazão, "Multipath interferometer polished microsphere for enhanced temperature sensing," IEEE Sensors Letters 2(2), 1-4, 2018. *doi: 10.1109/LSENS.2018.2819365* [25]

13. **A. D. Gomes**, B. Silveira, J. Dellith, M. Becker, M. Rothhardt, H. Bartelt, and O. Frazão, "Cleaved silica microsphere for temperature sensing," IEEE Photonics Technology Letters 30(9), 797-800, 2018. *doi: 10.1109/LPT.2018.2817566* [26]

14. **A. D. Gomes** and O. Frazão, "Microfiber knot with taper interferometer for temperature and refractive index discrimination," IEEE Photonics Technology Letters 29(8), 1517-1520, 2017. *doi: 10.1109/LPT.2017.2735185* [27]

Communications in National/International Conferences

1. **A. D. Gomes**, M. S. Ferreira, J. Bierlich, J. Kobelke, M. Rothhardt, H. Bartelt, and O. Frazão, "Challenging the limits of interferometric fiber sensor sensitivity with

the optical harmonic Vernier effect," 27th International Conference on Optical Fiber Sensors (OFS-27), Alexandria, Virginia, USA, 2020. [Accepted but postponed to 2022]

2. **A. D. Gomes**, M. Becker, J. Dellith, M. I. Zibaii, H. Latifi, M. Rothhardt, H. Bartelt, and O. Frazão, "Enhanced temperature sensing with Vernier effect on fiber probe based on multimode Fabry-Perot interferometer," IV International Conference on Applications of Optics and Photonics (AOP2019), Lisbon, Portugal, 2019. *(3rd place best student paper, awarded by SPIE) doi:10.1117/12.2527399* [28]

3. **A. D. Gomes**, J. Kobelke, J. Bierlich, K. Schuster, and O. Frazão, "Optical fiber probe for viscosity measurements," 26th International Conference on Optical Fiber Sensors (OFS-26), Lausanne, Switzerland, 2018. *doi: 10.1364/OFS.2018.TuE8* [29]

4. **A. D. Gomes**, C. S. Monteiro, J. Kobelke, J. Bierlich, K. Schuster, H. Bartelt, and O. Frazão, "Interferómetro de duas ondas em sonda de fibra óptica para medição de viscosidade", 21ª Conferência Nacional de Física, Universidade da Beira Interior, Portugal, 2018.

5. **A. D. Gomes,** B. Silveira, F. Karami, M. I. Zibaii, H. Latifi, J. Dellith, M. Becker, M. Rothhardt, H. Bartelt, and O. Frazão, "Multi-path interferometer structures with microspheres," SPIE Optics & Photonics 2018, Interferometry XIX, San Diego, California, United States, 2018. *doi: 10.1117/12.2319082* [30]

6. **A. D. Gomes** and O.Frazão, "Simultaneous measurement of temperature and refractive index based on microfiber knot resonator integrated in an abrupt taper Mach-Zehnder interferometer," III International Conference on Applications of Optics and Photonics (AOP2017), Faro, Portugal, 2017. *doi: 10.1117/12.2275813* [31]

7. **A. D. Gomes** and O. Frazão, "Microfiber knot resonator as sensors: a review," 5th International Conference on Photonics, Optics and Laser Technology (Photoptics 2017), Porto, Portugal, 2017. *doi: 10.5220/0006264803560364* [32]

Book Chapters

1. **A. D. Gomes** and O. Frazão, "Microfiber knot resonators for sensing applications", Optics, Photonics and Laser Technology 2017, Springer Series in Optical Sciences vol. 222, 145-163, Springer Nature Switzerland AG, 2019. *doi: 10.1007/978-3-030-12692-6_7 / ISBN: 978-3-030-12691-9* [33]

Chapter 2.

Overview on Optical Microfibers and Sensing Microstructures

2.1. Introduction

Optical fiber tapers were initially developed in the late 20$^{\text{th}}$ century, in the context of optical fiber communication. Their main purpose was to fabricate single mode fiber couplers [34–36]. Since then, optical fiber tapers were continuously studied and applied, not just in the fields of optical communication, but also for optical fiber sensing.

Optical microfibers by themselves can already be a sensing structure [37]. Their small size and guidance properties provide a great interaction between the propagating light and the external environment. Nevertheless, different sensing microstructures can additionally be fabricated in optical microfibers, increasing their versatility and range of applications [3, 38, 39]. These sensing microstructures can be interferometers created either by manipulating the optical microfiber [38], or through microfabrication techniques like femtosecond laser inscription [40] and ablation [41] or focused ion beam milling [4, 42].

This chapter intends to provide an insight on optical microfibers, sensing interferometers, and microfabrication techniques used across the dissertation. First, the properties and the structure of optical microfibers are explored, as well as some fabrication techniques used to produce them. Then, a small overview on different interferometric sensing structures is presented. Here, it is intended to provide some background knowledge on the different interferometric structures that will later appear in the dissertation. A small state-of-the-art description of the application of such structures, especially to optical microfibers and microfiber probes, is also included. The last section of the chapter explores the focused ion beam technology as a microfabrication technique to create microstructures in optical microfiber probes. This section also contains an important discussion regarding the sample preparation necessary to apply the technique to optical fibers.

2.2. Optical Microfibers and Microfiber Probes

Optical microfibers are optical fibers tapered down from typical fiber diameters of e.g. 125 μm to diameters of few micrometers (around 1 µm - in the order of the wavelength of light propagating along the fiber), or even to diameters of hundreds of nanometers, the so called nanofibers. The fabrication of optical microfibers consists of heating the fiber to its softening point while stretching it to decrease its diameter, obtaining a narrow stretched filament linked to the rest of the non-stretched fiber through a transition region. By finding a balance between parameters such as the heating source and the stretching, optical microfibers with different taper transition regions can be fabricated: linear, parabolic, sinusoidal, polynomial, or others [43].

Microfibers with dimensions close to 1 μm present new properties: low optical loss [44], outstanding mechanical flexibility [45, 46], tight optical confinement [47], large waveguide dispersion [48], and large interaction with the external environment through their large evanescent field [49]. This last property is of great value for sensing applications, since the larger the interaction with the external medium, the more sensitive the structure tends to be.

Due to the huge scale down (e.g. from 125 μm to around 1 μm), and also to the high temperatures subjected during the production, the doping of the optical fiber core is diffused to the cladding and disappears. Hence, optical microfibers and nanofibers present a high index contrast: the microfiber itself acts as a core for light guidance while the external medium acts as a cladding (usually $n_{fiber} \gg n_{surrounding\,medium}$, where n is the refractive index).

Microfibers with larger diameters can support multimode propagation, being the fundamental mode predominantly confined within the microfiber. However, when talking about optical microfibers with diameters close to 1 µm or nanofibers, where the diameter is much smaller than the propagated radiation wavelength ($d \ll \lambda$), only the fundamental mode is propagated along the structure. This mode then propagates mostly outside of the micro/nanofiber due to the large evanescent field [50]. The single mode condition for optical fibers is defined by the generalized frequency (V), also known as the V-number, in this case given by [48]:

$$V = 2\pi \frac{a}{\lambda_0} \sqrt{(n_{fiber}^2 - n_{external}^2)} \approx 2.405, \tag{2.1}$$

where a is the radius of the micro/nanofiber, λ_0 is the propagation wavelength (in vacuum), n_{fiber} is the refractive index of the micro/nanofiber, and $n_{external}$ is refractive index of the external medium. For a microfiber in air with a propagation wavelength of 1550 nm, considering the refractive index of the microfiber equal to the refractive index of silica (1.444 at 1550 nm [51]), the single mode condition occurs for a diameter of around 1.14 µm.

At such dimensions, under these conditions, the cut-off of the higher-order modes occurs. Hence, below this diameter the microfiber is single mode.

2.2.1. Structure

A schematic of an optical microfiber structure is shown in figure 2.1. The structure can be divided into three main sections:

1. The down-taper consists of a transition region, where the diameter of the optical fiber decreases from its original size to the final size of the optical microfiber. As mentioned before, this transition can have a specific profile, depending on the fabrication parameters;

2. The taper waist is the narrowest region of the optical microfiber and presents a uniform diameter (from a few microns to hundreds of nanometers). The taper waist region can be very small, long, or in some cases it may not even exist;

3. The up-taper, similarly to the down-taper, is a transition region where the optical microfiber increases its diameter from the taper waist size until it matches the original size of the optical fiber.

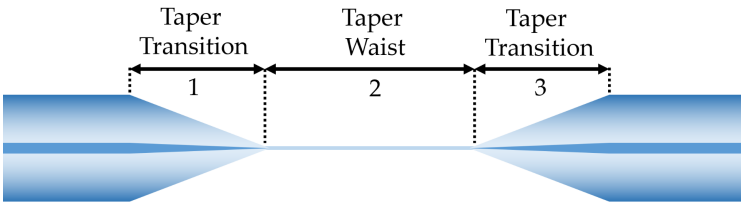

Figure 2.1. – Structure of an optical microfiber. 1: Transition region (down-taper); 2: Taper waist; 3: Transition region (up-taper).

A microfiber probe consists of about half of an optical microfiber, either just a single taper transition region, or also including part of the taper waist region. The objective of such structure is to have a probe with small dimensions at the edge, but where light is still guided. Sensing microstructures can then be fabricated in this region via post-processing, as will be discussed later.

In general, low-loss optical microfibers are obtained if the transition regions satisfy the adiabaticity criteria. In short, the reduction rate of the optical fiber diameter should be small enough to provide a smooth transition of the fundamental mode of the initial fiber into the fundamental mode propagating in the taper waist of the microfiber. If such condition is not verified, the fundamental mode of the initial fiber will transfer energy to few higher order modes. Most of these modes contribute to losses, since they are not well-guided by the microfiber structure. In some cases, where the taper waist is large

enough to support multimode propagation, some of these higher order modes might still propagate along the microfiber, which can be useful for sensing as it will be discussed in the next chapter.

The adiabaticity criteria corresponds to an approximate boundary between an optimal adiabatic taper and a lossy taper. In a more concrete way, the adiabaticity criteria is verified when the beat length between the fundamental mode (LP_{01}) and the next higher order local mode is smaller than the local variation of the taper diameter in relation to the propagation direction [43, 52]:

$$\left|\frac{dr}{dz}\right| < \frac{r\left(\beta_1 - \beta_2\right)}{2\pi}, \tag{2.2}$$

where $r = r\left(z\right)$ is the local cladding radius, z is the propagation direction, $\beta_1 = \beta_1\left(z\right)$ and $\beta_2 = \beta_2\left(z\right)$ are the local propagation constants of the fundamental mode (LP_{01}) and the next higher order mode. The smaller the final diameter targeted for the taper waist, the longer the transition regions should be to obtain a low-loss microfiber. However, it might happen that the final length of the microfiber is larger than what the fabrication equipment might be able to produce, due to the need for longer transition regions. Therefore, each fabrication setup imposes a limitation on the fabrication parameters of very small microfiber, being necessary to adapt the fabrication conditions (diameter, length, adiabaticity).

Next, the fabrication techniques to produce optical microfibers will be addressed, as well as some advantages and disadvantages of each method.

2.2.2. Fabrication Techniques

The typical techniques used to fabricate optical microfibers are similar to each other and the main difference between them relies on the heating source. There are different heating sources which are normally associated with the name of a specific tapering technique. The heating source can be a gas flame [49, 53], an electric arc created by electrodes as in a splicing machine [54, 55] or in a 3SAE Ring of Fire [56], a focused CO_2 laser [57, 58], a microheater [59, 60], or even a heating filament as used in commercial machines such as the VYTRAN - Glass Processing Workstation [61, 62]. However, not all of these techniques can achieve optical microfibers with diameters of around 1 µm or even below.

Traditional electric arc discharge methods, as in a fusion splicer, are not able to produce microfibers with diameters of around 1 µm. The electric arc from a fusion splicer does not provide the necessary temperature uniformity to reach such small dimensions, and the heat transfer rate to the fiber is slow [57]. Some of these issues are overcomed in equipment such as the 3SAE Ring of Fire, where a plasma is created using three electrodes, providing a controllable thermal profile in three dimensions [56].

A common fabrication method is the flame-brush technique, using a hydrogen flame

[63–65]. Figure 2.2 shows a typical schematic of the fabrication setup. The system is composed of a flame torch and two translation stages, where the initial optical fiber is fixed. The translation stages move in opposite directions to stretch the optical fiber as the flame heats and scans through the fiber section. The flame should be of pure hydrogen to avoid contamination of the produced optical microfibers with additional impurities, apart from the combustion by-products. Furthermore, other problems may arise from the flame-brush technique, such as non-uniformities in the taper waist diameter, difficulty in controlling the taper shape, among others [60]. Nevertheless, despite all these mentioned problems, the flame-brush technique is reported as the one providing the best results (micro and nanofibers with transmissions up to 99.7% [65]).

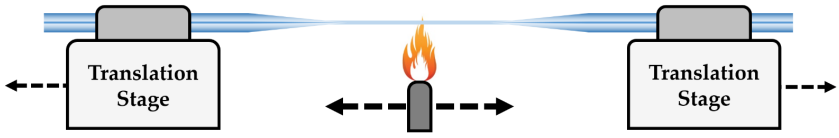

Figure 2.2. – Schematic of an optical microfiber fabrication setup using a gas flame.

The optical microfibers and microfiber probes used in the context of this dissertation were all fabricated using a CO_2 direct heating technique. Instead of a flame, the heating source is a CO_2 laser (wavelength: $\lambda = 10.6\,\mu m$), whose radiation is absorbed by the optical fiber. A schematic of the tapering setup using a CO_2 laser from the Center for Applied Photonics, INESC TEC, is represented in figure 2.3. The CO_2 laser source (SYNRAD 48-1, operation wavelength: $10.6\,\mu m$) is focused on the optical fiber with a 25.4 mm-diameter ZnSe-coated plano-convex lens with a focal length of 100 mm. On the opposite side of the optical fiber, the rest of the remaining laser light is refocused onto the optical fiber with a 50.8 mm silver-protected concave mirror with a focal length of 150 mm. Therefore, the concave mirror helps to increase the symmetry of the produced microfibers. Similarly to the flame-brush technique, two translation stages (AEROTECH motorized stages) hold and stretch the fiber during the tapering process. However, in this case both translation stages move in the same direction, but the leading translation stage moves at a faster velocity. A LabView program controls the setup, allowing to produce microfibers with the desired parameters. Other variants of the CO_2 laser tapering technique can also be found in the literature, namely the use of a scanning mirror to scan the focus of the beam across the fiber section, or even the use of a bi-directional beam together with two scanning mirrors to scan both sides of the optical fiber simultaneously [66].

The microfibers fabricated with the CO_2 laser tapering technique have a limitation in terms of the minimum diameter achievable for the taper waist (around $6\,\mu m$). The power transfered from the laser beam to the optical fiber drops with the fiber radius squared and the power dissipated by the fiber drops linearly with the fiber radius. There is a certain radius for which the rate of power dissipation equals the rate of power acquired, and

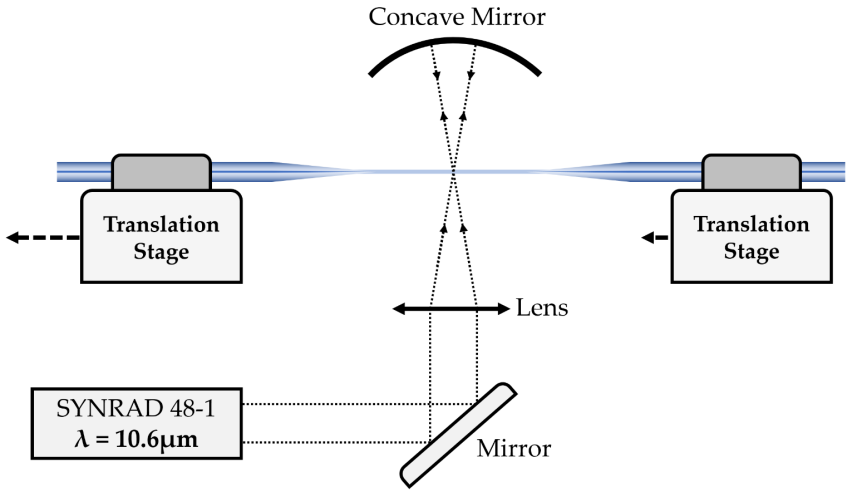

Figure 2.3. – Schematic of an optical microfiber fabrication setup using a CO_2 laser.

therefore the melting of the fiber is no longer possible, resulting in a broken fiber [57, 67]. To overcome these issues, an indirect CO_2 heating technique can be employed. The method involves the use of a ceramic microfurnace comprising a corundum tube (multi-crystalline Al_2O_3) indirectly heated with a bi-directional CO_2 laser beam [66, 68]. In this process, the optical fiber is placed inside the tube, which makes it difficult to be removed after the fabrication. Nevertheless, the use of a microfurnace allows to fabricate sub-micron-diameter optical fibers with excellent surface smoothness and diameter uniformity [68].

Another variant of heating source is the thermoelectric microheater. The principle is similar to the use of an indirectly heated ceramic microfurnace and has the advantage of providing a more stable and uniform heat source [60, 69]. However, as opposed to the CO_2 indirect heating method, the microheater presents an aperture to facilitate the insertion and removal of the optical fiber. Nanofibers with a taper waist diameter of 800 nm and transmissions of over 99% can be routinely produced using a microheater, as reported in [60].

2.3. Interferometric Sensing Structures

Sensing with light involves making the light interact with the measurand and its variations. In other words, the measurand shapes the propagation properties of light: intensity, wavelength, phase, polarization, and/or time of travel [70]. When changes in the light properties occur inside the fiber, i.e. when the measurand alters the properties of the fiber, which in return change the properties of the propagating light, the sensor is designated as intrinsic. In contrast to this, when changes in the light properties occur outside of the fiber, i.e. when the light leaves the fiber to interact with the measurand, and then recouples back into the fiber, the sensor is defined as extrinsic [71].

From the different types of optical fiber sensors, the focus of this dissertation is towards interferometric optical fiber sensors, which more easily provide higher sensitivities than other types of sensors. In these kind of structures, an interference signal in the spectral domain (intensity as a function of wavelength) is typically monitored and analyzed. From the interference spectrum, the measurements are usually performed in terms of wavelength shift: the measurand variations induce a wavelength shift of the interference spectrum. Upon characterization of the wavelength shift as a function of the measurand variation, the optical fiber sensor is then calibrated and ready to be used.

The works developed in the context of this dissertation rely on interferometric structures such as Mach-Zehnder interferometers, Fabry-Perot interferometers, and even resonant structures like microfiber knot resonators (a type of ring resonators), mainly produced in optical microfibers and microfiber probes. This section intends to briefly introduce and discuss these interferometric structures for further understanding of the following chapters.

2.3.1. Microfiber Knot Resonator

The microfiber knot resonator (MKR) is a resonant-type microfiber sensor fabricated by tying a knot in the taper waist region of a microfiber. Initially, the diameter of the MKR is large (typically a few millimeters). At that point, the diameter of the MKR is progressively reduced by pulling one end of the microfiber until the desired dimensions are obtained. Figure 2.4 presents a schematic of an MKR structure. The overlap of the fiber with itself, at the knot coupling region, does not require a precise alignment, revealing to be a great advantage compared with other resonator-type structures like the microfiber loop resonator [46].

Light that propagates in the microfiber is divided, in the knot region, between the ring and the output. New light that reaches the knot region will be partially combined with

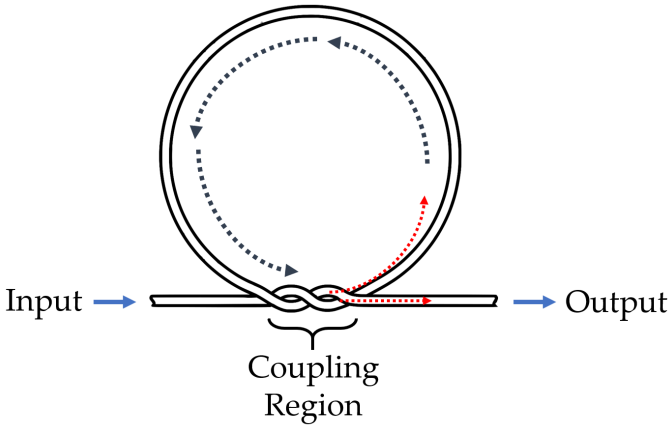

Figure 2.4. – Schematic of a microfiber knot resonator. In the coupling region, light is split between the ring and the output.

the light that previously traveled in the ring towards the output, while feeding at the same time the ring. For specific wavelengths, called the resonant wavelengths (λ^{res}), light that enters the ring is in phase with the one already traveling in it, resulting in accumulation of light in the ring. As a consequence, light at those resonant wavelengths gets trapped inside the ring, producing a dip in the transmission spectrum [33].

The distance between two adjacent resonant wavelengths (λ_1^{res} and λ_2^{res}) in the MKR transmission spectrum, known as the free spectral range (FSR), is defined as:

$$FSR_{MKR} = \lambda_1^{res} - \lambda_2^{res} = \frac{\lambda_1^{res}\lambda_2^{res}}{n_{eff}L} = \frac{\lambda_1^{res}\lambda_2^{res}}{2\pi r n_{eff}}, \tag{2.3}$$

where n_{eff} is the effective refractive index of the microfiber and L is the cavity length, which for an MKR is given by the perimeter of the ring ($L = 2\pi r$, where r is the radius of the ring). The dependence of the FSR in the radius of the ring can be very useful, since one can tune the FSR by adjusting the diameter of the MKR.

The FSR is an important quantity for sensing applications, along with the sensitivity of the structure to a certain measurand. In general, the FSR imposes a limitation in the measurement range. The wavelength shift of a resonance dip due to a certain physical or chemical measurand must be smaller than the FSR. Otherwise, the new position of the resonance dip will overlap the position of a different resonance dip at a previous value of the measured parameter. In other words, if the spectrum shifts by a FSR, the positions of the resonance dips overlap and are indistinguishable from the previous state.

The transmission spectrum of a microfiber knot resonator can be, from a different point of view, similar to that of a Fabry-Perot cavity. The cavity in the MKR structure is the ring and the mirrors can be seen as the knot coupling region. In a Fabry-Perot cavity with high reflectance mirrors, light travels longer in the cavity before leaving it. In an MKR, the high reflectance mirrors correspond to a greater coupling of light between adjacent fibers in the knot structure, increasing the amount of light accumulated in the ring. A larger coupling efficiency in the knot region is achieved by using microfibers with small diameters in the taper waist region (ideally around 1 to 2 μm), which present a larger evanescent field.

The MKR has been widely studied as a sensing element, due to its large evanescent field that interacts with the external medium and also to the resonant property. The use of MKRs to measure different parameters, by means of the wavelength shift of a resonance dip, was demonstrated in the literature. The measured parameters include temperature [38, 72, 73], concentration of sodium chloride [74], refractive index (RI) [6, 75], and others. For refractive index sensing, a simple MKR embedded in a Sagnac loop reflector was proposed by Lim *et al.* [75], achieving a sensitivity of 30.49 nm/refractive index units (RIU) in a refractive index range from 1.334-1.348. In 2014, a Teflon-coated MKR was demonstrated to have a sensitivity of 30.5 nm/RIU between 1.3322 and 1.3412

[74]. Coating the MKR with low refractive index polymers, in this case with Teflon, makes the structure more stable and protects it against degradation over time. High sensitivity can be achieved by combining multiple MKRs in a cascaded configuration, as presented by Xu et al. [6]. The sensor achieved a refractive index sensitivity of 6523 nm/RIU in a refractive index range from 1.3320 to 1.3350.

2.3.2. Mach-Zehnder Interferometer

The Mach-Zehnder interferometer (MZI), in its basic configuration, consists of the interference between light propagating in two independent arms (a sensing arm and a reference arm) [1]. As shown in figure 2.5, the two arms correspond to the two paths between two fiber couplers, where light is split and recombined. The resultant interference signal is an oscillatory response, typical of a two-wave interferometer. Ideally, the reference arm is kept stable and isolated from the sensing environment, while the sensing arm is exposed to the measurand. Hence, the measurand only affects the optical path length (OPL) of the sensing arm, whose change is detected as a wavelength shift in the output interference signal.

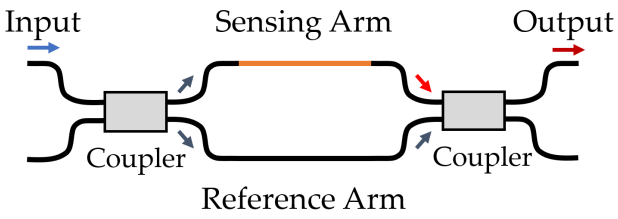

Figure 2.5. – Schematic of a fiber Mach-Zehnder interferometer. Light is split between the two arms and recoupled via two fiber couplers.

The FSR for an MZI is described as [76]:

$$FSR_{MZI} = \frac{\lambda_1 \lambda_2}{OPL_{sensing} - OPL_{reference}}, \tag{2.4}$$

where λ_1 and λ_2 are the wavelengths of two consecutive interference maxima (or minima), $OPL_{sensing}$ is the optical path length of the sensing arm and $OPL_{reference}$ is the optical path length of the reference arm, which are given by $OPL = nL$, being n the effective refractive index and L the length of the arm.

Initially, the MZI technique was mainly used to measure the refractive index of a medium [77]. However, over the years new configurations were developed, also for other applications such as strain [78] or acoustic sensing [79], increasing therefore the scope of this sensing technique. For instance, the two physical arms of the interferometer can be condensed into a single physical arm. By means of two propagating modes with different effective refractive indices, the MZI response can still be generated, as it will be presented in the

next chapter.

Different optical fiber MZI configurations have been reported using optical microfibers. For instance, a simple biconical fiber taper reported by Kieu *et al.* [37] can achieve refractive index sensitivities of around 705 nm/RIU in a range of 1.333 to 1.350, and temperature sensitivities up to 10 pm/°C from around 30 °C to 120 °C. Higher sensitivities were reported when using a taper-based MZI embedded in a thinned optical fiber [39]. Such sensor obtained a maximum refractive index sensitivity of 2210.84 nm/RIU between 1.3997 and 1.4096. In water, the same structure achieved a temperature sensitivity of -6.66 pm/°C between 30 °C and 70 °C. Different configurations, such as an MZI based on a large knot fiber resonator can also be used for refractive index sensing [80], presenting a sensitivity of 642 nm/RIU in a wide range of refractive indices (1.3735 to 1.428). As for temperature sensing in water, this sensor reached a sensitivity of -42 pm/°C from around 22 °C to 41 °C.

Some configurations using MZIs and optical microfibers have also been demonstrated for simultaneous measurement of refractive index and temperature [81–83]. A microfiber MZI combined with an MKR was also reported for the same purpose [84, 85].

2.3.3. Fabry-Perot Interferometer

A Fabry-Perot interferometer (FPI) is made of two parallel mirror interfaces separated from each other by a certain length (L), forming a cavity [86]. The input light is partially reflected and transmitted at the first reflective interface. Then, the light transmitted to the cavity suffers successively multiple reflections and transmissions at the cavity interfaces. The final interference signal measured in reflection at the output (i.e. through the same input fiber) is given by the superposition of the multiple transmitted and reflected light paths that are guided towards the output.

In terms of optical fibers, FPIs can be created in various ways. As an example, a simple structure can consist of two cleaved optical fibers, where the end faces are parallel to each other and with an air gap [1], as shown in figure 2.6. The two fiber sections can be fixed by means of a capillary tube.

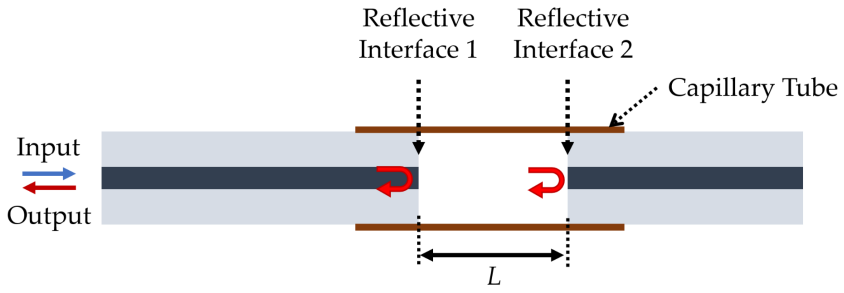

Figure 2.6. – Schematic of a fiber Fabry-Perot interferometer using two cleaved fiber end faces. Adapted from [1].

In general, optical fiber FPIs are composed of low reflectivity interfaces, which depend on the Fresnel reflection between the fiber (silica) and the material or substance that fills the cavity (gas, liquid, or others). Subsequently, only a single reflection at each interface can be considered, since the intensity of the following reflections is too small to have a major impact in the interference signal. Therefore, under these conditions the FPI interference signal can be approximated to the response of a two-wave interferometer. The FSR of an FPI is defined as [87]:

$$FSR_{FPI} = \frac{\lambda_1 \lambda_2}{2 n_{eff} L}, \tag{2.5}$$

where λ_1 and λ_2 are the wavelengths of two consecutive interference minima (or maxima) in the FPI spectrum, n_{eff} and L are the effective refractive index and the physical length of the FPI cavity, respectively. Light that enters the cavity and is back-reflected at the second interface towards the output travels twice the length of the cavity. Therefore, the OPL of an FPI is given by:

$$OPL = 2 n_{eff} L. \tag{2.6}$$

Apart from FPIs made from conventional single mode optical fibers, other FPI configurations were also demonstrated using different types of fibers. Examples of this are the use of hollow-core silica fibers (or hollow capillary tubes) [88–91], silicon-core fibers [92], photonic crystal fiber [93–97], or even hollow microspheres [24, 98–101].

Small size FPIs can be produced using microfabrication with a femtosecond laser or with a focused ion beam (FIB). On one hand, a femtosecond laser can be used to quickly mill optical fibers, creating a hollow cavity that behaves as an FPI [102–104]. On the other hand, FIB milling achieves a more precise milling with lower interface roughness, but it is more expensive and time-consuming. Moreover, FIB is suitable to create FPIs in microfiber probes, with the advantage of creating micro-cavities that can be as smaller as a single cell [4]. This technique allows to fabricate air and silica FPIs, as demonstrated by André et *al.* in 2016 [3]. Ultra-short FPI cavities milled in microfiber probes were also proposed as miniaturized sensing devices [4].

Along this dissertation, focused ion beam milling will be used to create microstructures in optical microfiber probes, as well as to create access holes for liquids in hollow capillary tubes. The next section presents an overview on microstructuring optical microfiber probes using focused ion beam milling.

2.4. Microstructuring Fiber Probes with a Focused Ion Beam

The focused ion beam (FIB) is an instrument very similar to a scanning electron microscope that uses accelerated ions rather than accelerated electrons [105]. Apart from imaging, the ion beam is capable of milling structures with feature sizes of 1 µm or below, or even to deposit ions in a sample (ion implantation) [106]. The FIB technology is of high importance in the semiconductor industry for structural modifications, repairing, or even for failure analysis or debugging of integrated circuits [106, 107]. Additionally, the FIB is also employed for preparation of samples for transmission electron microscopy [105].

This powerful technology found its way towards optical fibers, not only to create apertures or patterning fiber end-faces, but also to microstructure fiber probes, creating cavities and other sensing structures. Next, an overview on the FIB technology with focus on optical fibers will be presented. The preparation method used along this dissertation for optical fibers to be milled with the FIB will also be discussed.

2.4.1. Overview on the Focused Ion Beam

The principle of FIB milling consists in transferring energy from accelerated ions into the sample by collision. Ions are much heavier than electrons, which makes it easier to remove atoms from the sample surface [108]. Therefore, the interaction process between the ions and the sample is destructive, resulting in sputtered and backscattered sample material, along with secondary electrons, as shown in the schematic of figure 2.7(a). The FIB system uses a liquid-metal ion source, which can be of different metals. The most common metal used in commercial FIB systems is gallium. This metal has a low melting point (around 30 °C) and it is more stable than other liquid-metal sources [105].

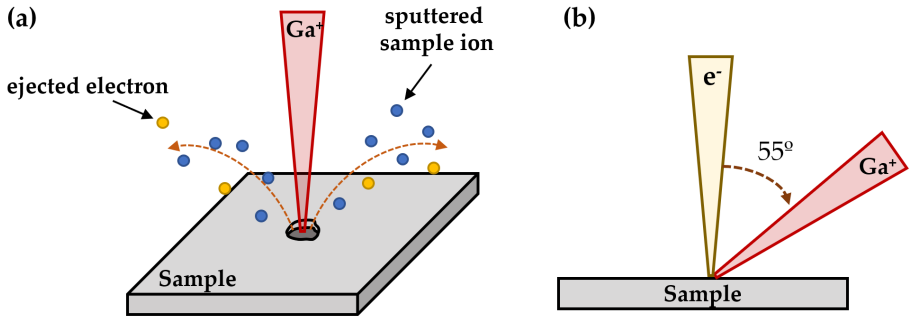

Figure 2.7. – (a) Schematic of the FIB milling. The accelerated gallium ions remove material from the substrate, resulting in sputtered ions and secondary electrons. (b) Positioning of the SEM in relation to the FIB at the Tescan Lyra XMU system. The ion beam is tilted by 55º in relation to the electron beam.

Along this dissertation, the works involving FIB milling were performed at Leibniz-IPHT, with a Tescan (Lyra XMU) FIB-SEM (focused ion beam – scanning electron mi-

croscope) dual-beam system. The FIB runs with gallium ions and the ion beam is tilted by 55º in relation to the vertical axis, where the electron beam from the SEM is located, as seen in figure 2.7(b). Hence, the sample surface, initially perpendicular to the electron beam, needs to be tilted by 55º to be parallel to the ion beam.

Gallium ions (Ga^+) have a size of around 0.2 nm [108] and typically produce a FIB spot size in the order of nanometers (usually not below 10 nm) [105]. It is worth mentioning that higher resolutions and sub-nanometer beam sizes can nowadays be achieved using helium ions, in a focused helium ion beam system [109]. Gallium ions have a positive charge, which is only partially compensated by the ejected electrons from the sample. Therefore, if the sample is non-conductive (such as optical fibers), an excess of charge is built on the surface of the sample. Charge accumulation in the sample induces drifting effects in the ion beam, resulting in unwanted milled regions and inaccurate milling geometries [110]. One way to solve this problem is to cover the sample with a conductive material to suppress charging effects, as it will be discussed later in this section.

Redeposition of a fraction of the milled sample material on the open milled regions and on the side walls of the milled structure occurs along the milling process. Such effect makes the amount of removed material hard to control [110]. Thus, the milling rate might not be the same as initially expected. For a given material, the milling rate depends on the energy and ion species, as well as on the surrounding atmosphere and on the angle of incidence of the ion beam [111]. Redeposition of material on the side walls of the milled structure increases the roughness and decreases the quality of the surface, which can be critical for some application in optical microfiber probes, as it will be presented in the next chapter. Fortunately, the FIB system allows to perform a fine polishing of these surfaces by using a low ion current and a small beam spot size.

At last, before any milling procedures it is crucial to make sure that the system is well-aligned and adjusted, as it reveals to have a high impact on the milling performance. Centering the objectives and correcting the beam astigmatism ensures a correct beam shape, increasing the sharpness of the image generated, as well as the quality of the milling.

2.4.2. Focused Ion Beam Milling of Optical Fibers

The use of FIB milling to structure optical fibers started at the end of the 90's, with the purpose of structuring optical fiber probes for scanning near-field optical microscopy (SNOM) [2,112,113]. Etched optical fibers with an apex end-shape, typically covered with a gold layer, were then post-processed with a FIB. As shown in figure 2.8, FIB milling was applied to drill the apex along the axis of the optical fiber, controlling this way the size of the aperture. The same technique was also used to slice the apex horizontally to the fiber axis.

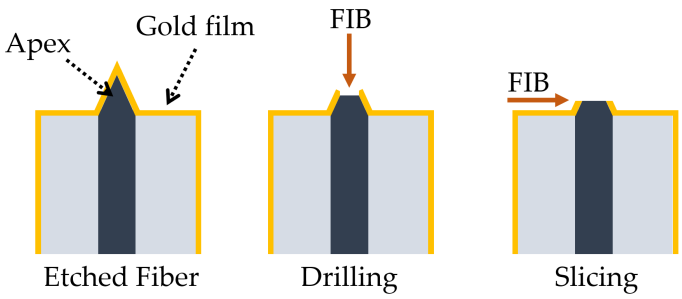

Figure 2.8. – Example of FIB milling applied to optical fiber probes for scanning near-field optical microscopy. Schematic adapted from [2].

Until today, FIB milling has been used not only for structuring and templating fiber probes, but also to create sensing structures in microfiber probes and access holes for gas or fluids in microstructured fibers.

Optical fiber facets with a specific coating were microstructured to create sub-wavelength resonant structures for plasmonic applications [114]. Templating of fiber facets with FIB milling was also explored for optical fiber tweezers. Different lenses in the optical fiber facet were FIB-milled with the purpose of trapping particles and cells [115, 116].

For sensing applications, different structures microfabricated with FIB milling in optical fibers, and especially in microfibers and microfiber probes, were demonstrated. At first, long period gratings (LPGs) were proposed in 2001 [117]. 10 years later, fiber Bragg gratings (FBGs) in microfibers, also called microFBGs, were fabricated and demonstrated. Kou *et al.* developed a first-order Bragg grating in a microfiber probe for temperature sensing [118]. Feng et al. proposed a different FBG structure, also in a microfiber probe for temperature sensing [42]. High-index contrast microFBGs were reported by Liu *et al.*, where the grating was fabricated with FIB milling in a complete microfiber, instead of in a probe [119]. The fabrication of FBGs in nanofibers with FIB milling was also achieved in 2011 by Nayak *et al.* [120]. In their work, FBGs were milled in nanofibers with taper waist diameters between 400 nm and 600 nm.

FIB milling is also a powerful technique to create, with high precision, miniaturized Fabry-Perot cavities in microfiber probes. An air Fabry-Perot cavity was fabricated in a microfiber probe by Kou et *al.* [121]. The cavity is only 3.5 μm long and allows for refractive index sensing of liquid solutions. Wieduwilt *et al.* demonstrated a different Fabry-Perot cavity for refractive index sensing, also milled in a microfiber, but with a length of around 25 μm [122]. André *et al.* developed a chemically etched specialty fiber containing a microwire, where FIB milling was used to fabricated a Fabry-Perot cavity [123]. The Fabry-Perot structure was able to act as a cantilever for vibration sensing. Later on, the same group proposed a microfiber probe with both an air FPI and a silica FPI within the same probe, as depicted in figure 2.9(a). The structured probe achieved simultaneous

measurement of refractive index of liquid solutions and temperature [3]. Refractive index sensing with ultra-short Fabry-Perot cavities milled with a FIB, as presented in figure 2.9(b), were demonstrated by Warren-Smith *et al.* [4].

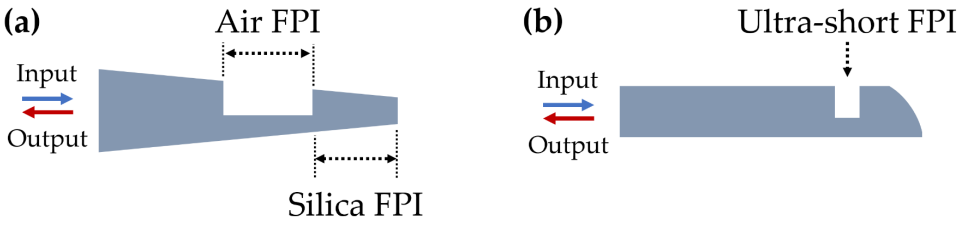

Figure 2.9. – Example of FIB-milled FPIs in optical microfibers. (a) Two FPIs (an air cavity and a silica cavity) in a single microfiber probe. Adapted from [3]. (b) Ultra-short FPI in a microfiber probe. Adapted from [4].

More complex fiber sensing devices combining FIB milling were also reported. A microfiber knot resonator combined with a Mach-Zehnder interferometer, milled with a FIB in the same microfiber, was shown by Gomes *et al.* [124]. Warren-Smith *et al.* reported a direct core structuring of exposed core fibers with FIB milling [125]. The application of FIB milling to fabricate asymmetric microspheres was demonstrated in 2018 by Gomes *et al.* [24,26]. These microspheres generate a random signal that can be analyzed to retrieve information regarding temperature variations.

At last, FIB milling was used to open access holes for gas and fluids in specialty fibers, such as in photonic crystal fibers or in multi-hole step-index fibers [110]. Gomes *et al.* also demonstrated an acetone evaporation and water vapor detection sensor using a caterpillar-like microstructured fiber [126]. FIB milling was applied to open access holes for the gas vapor to circulate inside the microstructured fiber.

2.4.3. Sample Preparation

Using FIB and/or SEM in optical fibers requires a prior sample preparation to eliminate charging effects. In this dissertation the optical fibers were initially mounted and fixed in an aluminium holder with a droplet of carbon glue (DOTITE XC-12, Fujikura Kasei Co., LtD Tokyo, Japan). The sample holder is conductive and the carbon glue ensures a good electrical contact between the holder and the fiber, which will then be coated with a conductive film to suppress surface charges. The optical fiber can be coated with different materials, such as gold, platinum, tantalum, carbon, and others. It is useful to deposit a conductive film of a material with a low milling rate, avoiding its fast removal during the milling process and the need to redeposit a new film. All the FIB-milled optical fibers along this dissertation were coated with a carbon film. In general, carbon is more stable and presents a lower milling rate compared with other conductive films, such as platinum or gold. With this, only a few nanometers of carbon coating are necessary, instead of a

few tens of nanometers, having a lesser impact in the final performance of the structure (ex. inducing losses through light absorption).

The optical fiber samples were carbon-coated by means of a LEICA EM ACE600. This system allows to tilt the stage for a better positioning of the sample in relation to the carbon source. Moreover, the stage can also rotate during the deposition process to provide a good coating distribution, not just on the top of the sample, but also on the sides.

At last, the milled optical fiber samples can be removed from the holder using acetone to dissolve the carbon glue. Additional cleaning can also be performed using an ultrasonic bath with acetone, removing parts of the dissolved carbon glue that attached to the milled region.

2.5. Conclusion

Optical microfibers and microfiber probes are a useful platform to achieve miniaturized sensors. Their properties, combined with different post-processing techniques, allows to create distinct sensing interferometers with potential to attain high sensitivities.

An introductory overview of three distinct fiber interferometric configurations was here presented, providing a basic background for a more comprehensive understanding of the following chapters. The microfiber knot resonator has improved light-environment interaction due to the its resonant property. The Mach-Zehnder interferometer relies on the phase shift induced by the measurand in one of the arms. This effect can be very sensitive to small variations in parameters such as the refractive index or concentration of certain compounds in solutions, which is indirectly related with the refractive index. The response of a Fabry-Perot interferometer is measured in reflection (the input and the output fiber is the same), which is extremely useful to incorporate in microfiber probes. As here discussed, this kind of structures can be fabricated by means of femtosecond laser ablation or focused ion beam milling.

Much of the work in this dissertation makes use of focused ion beam milling to create sensing structures in microfiber probes and to open access holes in hollow capillary tubes. Therefore, this chapter also provided a brief introduction to the principle of focused ion beam milling, with strong focus on optical fiber applications.

The next chapter explores the development of microstructured sensing devices in optical microfibers and microfiber probes. Different techniques and sensing interferometers here introduced are combined together, creating novel sensing structures with enhanced sensing capabilities.

Chapter 3.

Microstructured Sensing Devices with Optical Microfibers

3.1. Introduction

This chapter explores the study and development of microstructured sensors based on optical microfibers. The objective is to create small sensing devices with enhanced sensing capabilities, such as simultaneous measurement of physical quantities or enhanced sensitivity to a certain measurand. In the first section, a complete optical microfiber is structured to combine two different sensing configurations into a single and compact optical sensing device. This approach intents to create a versatile sensor that allows simultaneous measurement of refractive index and temperature, solving this way the problem of cross-sensitivity. On the other hand, the second section explores the use of a multimode microfiber probe to achieve enhanced sensitivity to temperature. At the same time, the work trends towards the miniaturization of fiber sensing devices for point measurements. Here, only half of a microfiber is used to create a small size sensing probe with a small footprint. Additionally, this work also explores microfabrication with a focused ion beam to post-process the microfiber probe.

3.2. Microfiber Knot Resonator combined with Mach-Zehnder Interferometer

Cross-sensitivity is a common problem in the domain of optical fiber sensors that needs to be solved, especially when using the fiber sensing element outside of a stable and controlled environment. In most cases, apart from the measurand, the measurement signal is also influenced by different outside parameters. In fiber sensing interferometers, variations of these external physical quantities induce similar wavelength shifts as the measurand, making it rather complicated, or nearly impossible, to determine exactly the response of the target measurand. When measuring a certain quantity, undesired variations of other

additional parameters introduce an error in the measurement, leading to inaccurate results.

Fluctuations of temperature turned out to be one of the most problematic cases of cross-sensitivity. Physical parameters are temperature dependent, and the sensing structure itself may also change due to temperature effects (either by thermal expansion or thermo-optic effect). Consequently, different fiber sensing configurations and techniques had to be developed to compensate for possible temperature fluctuations [81, 127–131]. On a basic level, a simple thermometer could be used to monitor in real time the temperature fluctuations, using these values to compensate and correct the final response of the fiber sensor. However, in real applications the use of an external thermometer is inconvenient.

As an alternative approach, it is possible to incorporate a temperature sensor inside the optical fiber together with a different sensing structure, for instance, by multiplexing a fiber sensing interferometer with a fiber Bragg grating (FBG) [132]. The FBG was, and still is, extensively studied and applied to monitor temperature variations in different environments [133, 134]. A different way to compensate for temperature fluctuations involves the combination of two fiber interferometers with distinct responses to temperature and to the target measurand. As a drawback, the optical signal of the sensing structure becomes more complex, requiring additional signal processing. Nevertheless, simultaneous measurement of both measurands is then enabled by means of a matrix method [135].

Enlightened by this last concept, this section explores the combination of two distinct interferometric structures within a single optical microfiber: a microfiber knot resonator (MKR) and a Mach-Zehnder interferometer (MZI). The aim of such sensing device is to enable simultaneous measurement of refractive index variations of liquid solutions and temperature variations. A key aspect of the following configuration, as will be further explained later on this section, is a slight structural modification of the microfiber during the fabrication process. This allows the Mach-Zehnder interferometer to be embedded in the microfiber, forming a compact structure.

3.2.1. Principle and Fabrication

The base of the structure consists of a microfiber knot resonator made from an optical microfiber. As discussed in the previous chapter 2, the MKR produces resonance dips in the transmission spectrum due light being trapped in the MKR ring. Now, the trick consists of fabricating the microfiber with a slightly abrupt transition region. In such case, a few other modes are excited in the microfiber. These modes co-propagate with an effective refractive index different than the fundamental mode one, hence accumulating a phase difference. Then, in the knot region, the modes interfere due to the inherent curvature of the microfiber, creating a Mach-Zehnder interferometer whose response is susceptible to refractive index variations of the surrounding environment. A schematic of the two main structures are depicted in figure 3.1.

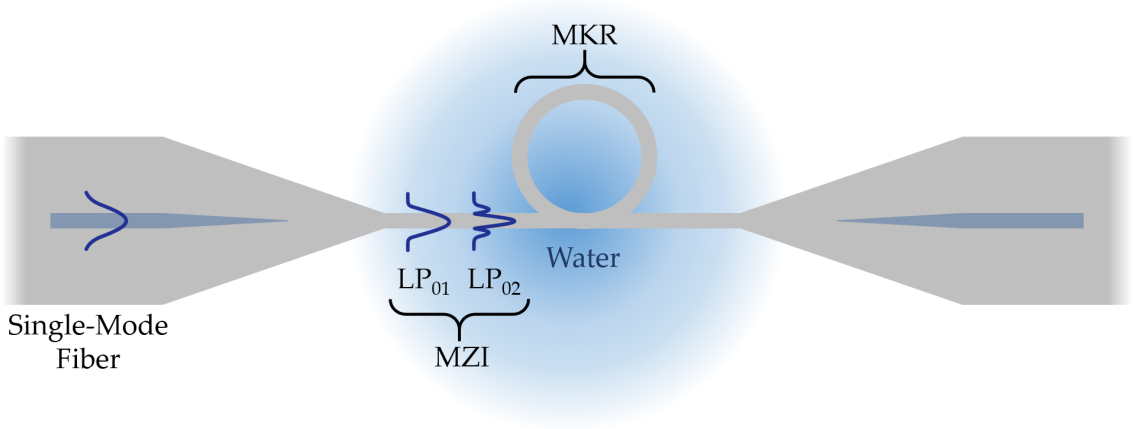

Figure 3.1. – Schematic of the two main structures: a microfiber knot resonator (MKR) and a Mach-Zehnder interferometer (MZI). Illustration of the main modes in the microfiber with a slightly abrupt transition region, when immersed in water. The fundamental mode of the single-mode fiber is coupled preferentially to the fundamental mode, LP_{01}, and to the higher order mode, LP_{02}, of the microfiber. The co-propagation and interference between these two modes forms the MZI. (Not drawn to scale.)

It is important to mention that, the fundamental mode of the initial fiber is, in the slightly-abrupt taper transition region, preferentially coupled into the fundamental mode, LP_{01}, of the microfiber and also to the higher order mode, LP_{02} (see figure 3.1). These two modes are preferentially excited since they present similar azimuthal symmetry and smaller phase mismatch than other higher order modes [136, 137]. The rest of the higher modes carries much less intensity, which leads to interference signals with very low visibility. Therefore, they can be negligible. For this reason, the MZI response is mainly composed of the modal interference between the fundamental mode, LP_{01}, and the higher order mode, LP_{02}, of the microfiber. The final response of the sensing device is expected to be the superposition between the MKR and the MZI responses.

The sensor was fabricated with a CO_2 laser tapering facility. The tapering setup has

Table 3.1. – Parameters used in the CO_2 laser system to fabricate the microfiber. The CO_2 laser setup can be found in chapter 2 in figure 2.3.

Initial Velocity (Stage A)	$40\ \mu m/s$
Initial Velocity (Stage B)	$20\ \mu m/s$
Final Velocity (Stage A)	$5000\ \mu m/s$
Initial Acceleration (Stage A)	$200\ \mu m/s^2$
Variation in Time of Acceleration (Stage A)	$200\ \mu m/s^3$
CO_2 Laser Output Power	$10\ W$
CO_2 Laser Pulse Width Modulation	27%
Lens-Fiber Distance	$32.5\ mm$

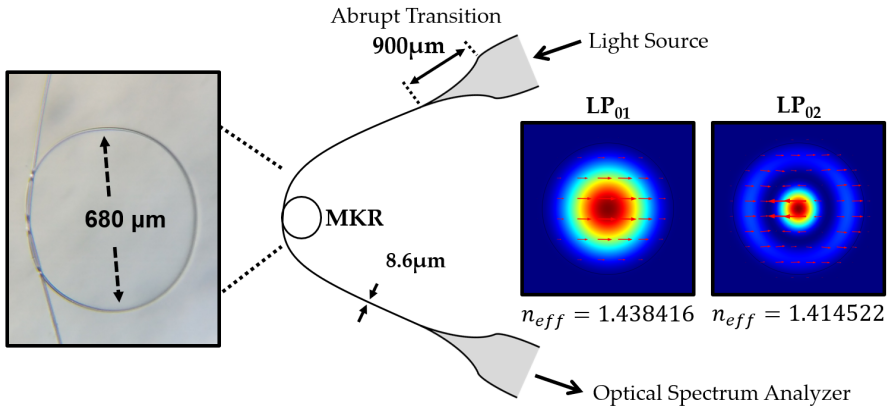

Figure 3.2. – Schematic of the sensing structure. The sensing structure consists of an MKR made from an 8.6 μm-diameter microfiber with slightly abrupt transition regions. On the right: profile of the two main modes with higher intensity excited in the microfiber waist region (LP_{01} and LP_{02}), when surrounded by water at 44 °C, at a wavelength of 1550 nm.

been previously explored in chapter 2. Details on the parameters used to fabricate the microfiber with slightly abrupt transition regions are presented in table 3.1.

The fabricated microfiber has a length of 50 mm and 900 μm-long slightly abrupt transition regions. In the taper waist region the microfiber has a diameter of 8.6 μm. An MKR with a final diameter of around 680 μm was manually tied using the fabricated microfiber. A schematic of the sensing structure is depicted in figure 3.2, together with a micrograph of the MKR region.

The structure is intended to be immersed in water, in order to sense refractive index and temperature variations simultaneously. The effective refractive indices of the two main modes of the microfiber (LP_{01} and LP_{02}) were calculated using COMSOL Multiphysics. The microfiber refractive index was considered as 1.4440 (refractive index of silica at a wavelength of 1550 nm). An intermediate situation of refractive index and temperature was considered for the simulations. As a first rough approximation, the external medium refractive index was assumed as 1.3292, corresponding to the refractive index of water (at a wavelength of 632.8 nm) adjusted to the temperature of 44 °C (see appendix A). In this situation, the simulated effective refractive indices were 1.4385 and 1.4149, respectively for the LP_{01} and the LP_{02}. To be more correct, the refractive index value of water should be adjusted to the correct operating wavelength. So, by means of the Sellmeier equation (see appendix A), the simulations were repeated using an external refractive index of 1.31278, corresponding to water at 44 °C at 1550 nm. The simulated effective refractive indices were 1.43842 and 1.41452, respectively for the LP_{01} and the LP_{02}. Their mode profiles are also displayed in figure 3.2.

3.2.2. Experimental Setup and Characterization

The spectral response of the sensor was obtained using a simple transmission setup, described by figure 3.3. The sensor was connected between a broadband optical source, with a central wavelength of 1550 nm and a bandwidth of 100 nm, and an optical spectrum analyzer (OSA) with 0.04 nm of resolution. The whole characterization was performed with the sensor immersed in a water reservoir. The water temperature could be increased via a hot plate and monitored with an external thermometer placed close to the sensor. Before immersing in water, the structure was fixed onto a glass substrate with cyanoacrylate adhesive in the single-mode fiber (SMF) regions. The microfiber knot resonator was attached to the glass substrate only by Van-der-Waals forces, owing to the small dimensions of the microfiber. For temperature measurements, the water temperature was progressively decreased from 50 °C to 38 °C.

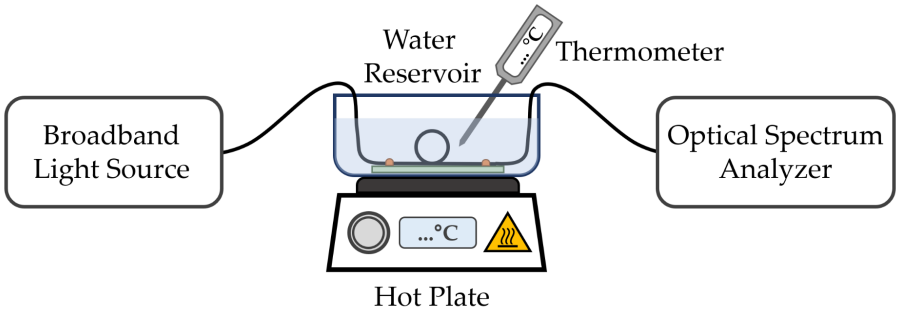

Figure 3.3. – Diagram of the experimental setup. The sensor was fixed onto a glass substrate and immersed in a water reservoir. The water temperature is regulated with a hot plate and simultaneously monitored by an external thermometer.

Figure 3.4(a) shows the transmission spectrum of the sensor in an intermediate situation, corresponding to a water temperature of 44 °C. The optical signal was previously normalized to the broadband light source signal. The transmission spectrum is given by the superposition of two components: a fast oscillatory signal originated by the MKR, and a slow oscillatory envelope due to the MZI, which modulates the MKR response.

In terms of spectral properties, the MKR component has a free spectral range (FSR) of around 0.78 nm. On the other hand, the MZI component corresponds to a low frequency signal with a free spectral range of around 9.62 nm. Since both interferometers have optical responses with distinct frequencies, the MZI component can easily be isolated using a low-pass fast Fourier transform (FFT) filter to track and characterize its response without the influence of the MKR. The low-pass FFT filter had a cutoff frequency of 0.5 nm^{-1}. The filtered MZI component is represented in figure 3.4(a) with a red line. The cutoff frequency of the lowpass FFT filter is directly related with the signal FSR through:

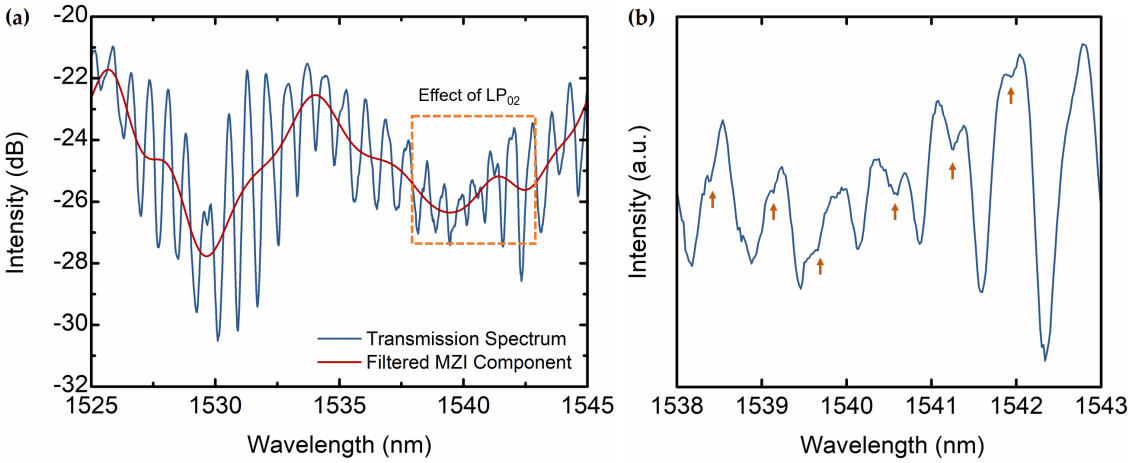

Figure 3.4. – (a) Transmission spectrum of the sensing structure in water at 44 °C. The red line corresponds to the Mach-Zehnder interferometer component, filtered by means of a low-pass filter (cutoff frequency: 0.5 nm^{-1}). The spectral region inside the dashed box is magnified in (b). The minima marked with an arrow are originated from the mode LP_{02}.

$f_{cutoff}\,[nm^{-1}] = 1/FSR\,[nm]$. Therefore, applying a lowpass FFT filter with a cutoff frequency of 0.5 nm^{-1} is equivalent to blocking all signal components with an FSR smaller than 2 nm, filtering out this way the MKR response ($FSR_{MKR} = 0.78$ nm).

As discussed before, the MZI is caused by the modal interference between the LP_{01} and the LP_{02} modes. The interferometer physical length, L, can be estimated through equation 2.4 as [76]:

$$L = \frac{\lambda_1 \lambda_2}{\Delta n \times FSR}, \tag{3.1}$$

where λ_1 and λ_2 are the wavelengths of two consecutive interference maxima (or minima), Δn is the effective refractive index difference between the two modes, and FSR is the free spectral range of the MZI signal. From the experimental spectrum presented in figure 3.4(a), two consecutive minima of the filtered MZI component are located at 1529.66 nm and 1539.45 nm. Hence, together with the calculated FSR and the simulated effective refractive indices at 1550 nm, an MZI length of 10.07 mm is estimated through equation 3.1. The value matches with the distance between the beginning of the microfiber and the knot region (note that the knot is located closer to the input of the microfiber rather than in the center due to the fabrication constrains). Please observe that the rough approximation of using the refractive index of water for the sodium D line would give an estimated MZI length of 10.19 mm which is, for this specific case, not so different as using a more correct values for the refractive index of water.

Similarly, one can estimate the diameter, d, of the MKR based on equation 2.3 as [33]:

$$d = \frac{L}{\pi} = \frac{\lambda_1 \lambda_2}{\pi \times n_{eff} \times FSR}. \tag{3.2}$$

where L is the cavity length, which for an MKR is given by the perimeter of the ring ($L = \pi d$), and n_{eff} is the effective refractive index of the propagating mode. Two consecutive resonant wavelengths of the MKR response are located at 1530.12 nm and 1530.90 nm. Adopting the simulated effective refractive index for the fundamental mode (LP_{01}), the calculated knot diameter is 665 µm. Keep in mind that the MKR response occurs for both modes, but they present similar FSRs and peak positions. However, the fundamental mode LP_{01} is dominant over higher order mode LP_{02} [138]. The resonances originated from the mode LP_{02} have much lower visibility, yet they can still be visible in figure 3.4(b) when magnifying the spectrum near 1540 nm.

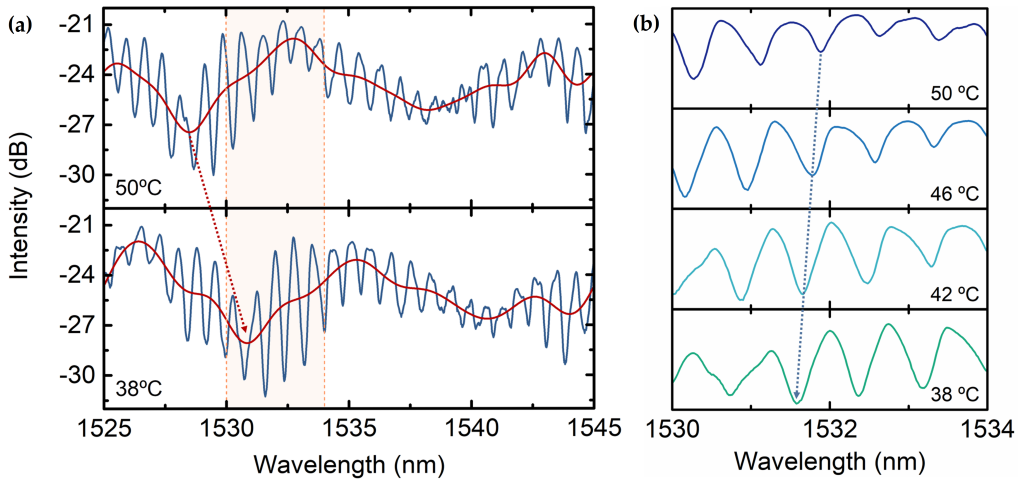

Figure 3.5. – (a) Transmission spectra of the sensing structure, in water, at different temperatures: 50 °C and 38 °C. The shaded region is magnified in (b). The red line corresponds to the Mach-Zehnder interferometer component, filtered by means of a low-pass filter (cutoff frequency: 0.5 nm^{-1}). (b) Zoom-in of the transmission spectra, in water, at four different temperatures.

Figure 3.5(a) displays the transmission spectra at two distinct water temperatures: 38 °C and 50 °C. The MZI component, given by the red line in figure 3.5(a), shifts towards longer wavelength as the water temperature decreases. On the other hand, the MKR component shifts towards shorter wavelengths as the water temperature decreases, as visible in figure 3.5(b). To characterize the sensing structure, the wavelength shifts of the MZI interference dip around 1530 nm and the MKR resonance dip around 1531.7 nm were monitored. The wavelength shift as a function of the temperature variation in water for both components, the MZI and the MKR, is depicted in the inner plot of figure 3.6. In water, temperature sensitivities of -196 ± 2 pm/°C and 25.1 ± 0.9 pm/°C were obtained for the MZI and the MKR, respectively. Such values correspond to the effect of temperature variations but

also to water refractive index variations due to thermo-optic effects. In order to obtain a correct response of the sensor only to water temperature variations (due only to thermo-optic effect), the temperature behavior of the structure in air (thermal expansion) needs to be removed [3]. The temperature sensitivity of the structure, in air, is 10.2 pm/°C [37] and 20.6 pm/°C [75], respectively for the MZI and MKR. After removing these components, the sensor response due to water temperature variations is shown in figure 3.6. The new temperature sensitivities, in water and due only to its thermo-optic effect, are now -206 ± 2 pm/°C and 4.5 ± 0.9 pm/°C, respectively for the MZI and the MKR.

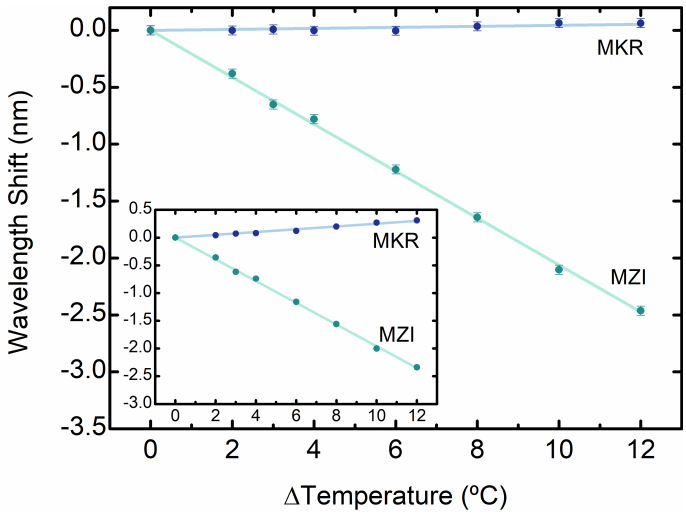

Figure 3.6. – Wavelength shift as a function of water temperature variation (only due to thermo-optic effect) for both components, the microfiber knot resonator (MKR) and the Mach-Zehnder interferometer (MZI), after removing the temperature sensitivity in air (thermal expansion). The inner plot shows the measured values before extracting the temperature behavior in air.

To characterize the sensor as a function of refractive index variations, a simple technique is to convert the temperature measurements, in water, into the equivalent refractive index variations through the thermo-optic coefficient. The thermo-optic coefficient of water, $\frac{dn}{dT}$, at a wavelength of 1550 nm, is given by [139]:

$$\frac{dn}{dT} = -1.044 \times 10^{-4} - 1.543 \times 10^{-7} T, \tag{3.3}$$

where T is the water temperature, given in degrees Celsius, and n is the refractive index of water, given in refractive index units (RIU). To obtain the refractive index values of water at different temperatures, equation 3.3 needs to be integrated. Taking into consideration that the water refractive index at 20 °C is 1.3154, at a wavelength of 1550 nm [140], one

obtains that[1]:

$$n(T) = 1.3154 + 2.11886 \times 10^{-3} - 1.044 \times 10^{-4}T - 7.715 \times 10^{-8}T^2, \tag{3.4}$$

with T given in degrees Celsius and n given in RIU. By making use of this conversion, the wavelength response of the sensor to refractive index variations is now depicted in figure 3.7. In this case, the MZI dip shifts to longer wavelengths with increasing external refractive index, while the MKR dip shifts to shorter wavelengths. The obtained refractive index sensitivity was 1848 ± 13 nm/RIU for the MZI and -59 ± 6 nm/RIU for the MKR. The refractive index ranged from 1.31211 to 1.31344, at a wavelength of 1550 nm, performing a total variation of 1.33×10^{-3} RIU.

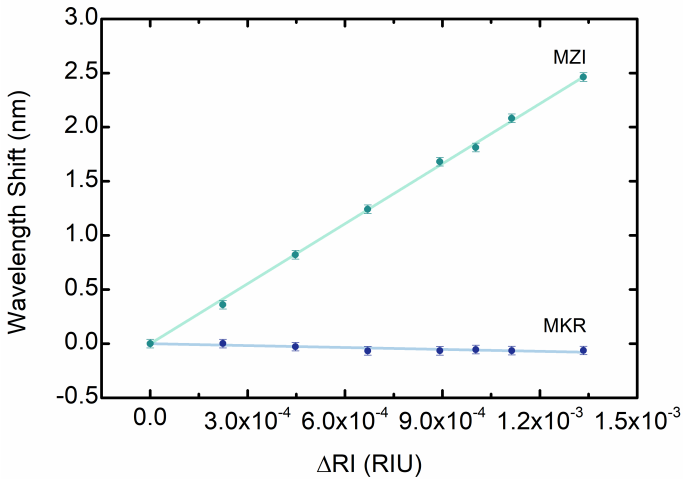

Figure 3.7. – Wavelength shift as a function of water refractive index variations for both components, the microfiber knot resonator (MKR) and the Mach-Zehnder interferometer (MZI).

The two components have distinct sensitivity values, allowing for simultaneous measurement of refractive index and temperature variations using a matrix method. The matrix of relation between refractive index (Δn) and temperature variations (ΔT), and the corresponding wavelength shifts ($\Delta\lambda_{MZI}$ and $\Delta\lambda_{MKR}$) can be obtained using the sensitivities of each component to the measured parameters [135]. For the developed sensor, the matrix is expressed as:

$$\begin{bmatrix} \Delta n \\ \Delta T \end{bmatrix} = \frac{1}{D} \begin{bmatrix} k_{2T} & -k_{1T} \\ -k_{2n} & k_{1n} \end{bmatrix} \begin{bmatrix} \Delta\lambda_{MZI} \\ \Delta\lambda_{MKR} \end{bmatrix}, \tag{3.5}$$

where $D = k_{1n}k_{2T} - k_{2n}k_{1T}$ is the determinant of the relationship matrix, being k_{in} and k_{iT} the sensitivities to refractive index and temperature, with $i = 1, 2$. The matrix

[1]Further details in appendix A.

method works well when the components have distinct sensitivity values, as long as the matrix determinant, D, is large. A small value of D introduces significant errors and low accuracy. Replacing the sensitivity values of the MZI and the MKR in equation 3.5, the matrix can be expressed as:

$$\begin{bmatrix} \Delta n \\ \Delta T \end{bmatrix} = 0.0267 \begin{bmatrix} 0.0206 & -0.0102 \\ 59 & 1848 \end{bmatrix} \begin{bmatrix} \Delta\lambda_{MZI} \\ \Delta\lambda_{MKR} \end{bmatrix}, \tag{3.6}$$

where $\Delta\lambda_{MZI}$ and $\Delta\lambda_{MKR}$ are given in nanometers. The obtained refractive index and temperature variations are given in RIU and in degrees Celsius, respectively. The matrix method presents a standard deviation (σ) of 3×10^{-5} RIU and 0.1 °C in the determination of the resulting refractive index and temperature variations, respectively.

3.2.3. Discussion

In this section, a new compact sensing structure was presented, combining two distinct optical interferometers into a single device: a microfiber knot resonator and a slightly abrupt taper-based Mach-Zehnder interferometer. The structure was fabricated only via post-processing with a CO_2 laser. The sensor presents two distinct spectral components, characteristic from the MZI and the MKR, that respond differently to temperature and refractive index variations. Both components could be separated by applying FFT filters, making it easier to monitor each response separately. The MZI component has higher sensitivity to refractive index than the MKR component, mainly because it relies on the difference between the effective refractive indices of the two main modes (the LP_{01} and the LP_{02}).

The device can be used to simultaneously measure temperature and refractive index variations. Hence, the influence of temperature in the refractive index measurement can be compensated, as initially targeted. Moreover, the proposed sensor is more compact and stable than similar reported structures [84,85], since the MZI relies on a single taper structure and not on a second microfiber connected through Van-der-Waals forces. Structures like [84,85], which use coupling between two microfibers, can be very fragile and unstable. On the other hand, the proposed structure might have some issues while immersing in water (or removing). During this process, the surface tension of water can change the diameter of the MKR, or even break the microfiber. Hence in the future, it is important to explore the possibility of coating the structure with a thin protective layer of a low refractive index polymer. Such coatings increase the stability of the structure and avoid modifications in its dimensions. Moreover, this type of coatings might have low impact on the performance of the sensor, as its refractive index is lower than silica. Therefore, the modes of the structure are preserved. However, one should not forget that the coating is a small barrier between the propagating modes and the external environment, which might

result in a slightly lower refractive index sensitivity.

3.3. FIB-Structured Multimode Fiber Probe

The use of a microfiber sensing device in a transmission configuration, as the one demonstrated before, is less practical or inconvenient for applications that require local measurements (point measurements). For instance, some biological and medical applications require point measurements combined with minimally invasive sensors, especially for in-vivo operation. Therefore, the current tendency is towards developing miniaturized sensors capable of measuring physical, chemical, and biochemical parameters. A microfiber probe (half of a microfiber) could be used for such applications instead of a complete microfiber. Then, a sensing structure can be added to the microfiber probe via post-processing. A useful sensing structure suitable to be adapted to a microfiber probe and interrogated in a reflection configuration is the Fabry-Perot interferometer (FPI).

Microfabrication with a focused ion beam is an interesting approach to form FPIs in microfiber probes. This technique has the advantage of creating small sensing structures in thin microfiber probes, which can be smaller than a single cell. Examples of air and silica FPIs in microfiber probes were demonstrated in 2016 [3]. One year later, ultra-short FPI cavities milled in microfiber probes were also proved to be feasible and applicable as miniaturized sensing devices [4]. For temperature sensing, conventional silica FPIs are limited by the thermo-optic coefficient of silica, and to a lesser degree by the thermal expansion coefficient. Typically, the temperature sensitivity values for those structures range from 10 pm/°C to around 20 pm/°C [3, 90, 141, 142]. Polymers started to be implemented to partially solve this issue of limited sensitivity. Polymer FPIs can attain one order of magnitude higher temperature sensitivities due to their high thermal expansion coefficient [143, 144]. Yet, their use is also limited to temperatures below the melting point of the polymer. Apart from the use of polymeric structures, other possibilities to surpass the sensitivity limitations were studied, including the application of other effects beyond the normal FPI. Multimode interference [145] or non-linear responses [143, 145] are examples of that.

In this section, the improvement of a focused ion beam-milled FPI in a microfiber probe is explored for temperature sensing. For this purpose, the usual SMF used to fabricate the microfiber was replaced by a multimode fiber (MMF). Thus, multiple propagating modes are present in the structure, generating different FPI responses. The interference between the FPI responses gives raise to a low-frequency envelope modulation, which mainly depends on the refractive index differences between the propagating modes. Consequently, one should expect such component to achieve higher sensitivity as it depends on an optical path difference, similarly to the MZI demonstrated in the last section.

3.3.1. Fabrication

The microfiber probe used in this work was fabricated using a step-index multimode optical fiber (FG050LGA, Thorlabs GmbH). The MMF has a core diameter of 50 μm and a standard cladding diameter (125 μm). The microfiber probe was provided by the Center for Laser and Plasma Research (Shahid Beheshti University, Iran). There, the MMF was tapered down using a CO_2 laser tapering facility and then broken in half, creating a sharp tip suitable to be post-processed. Subsequently, a Fabry-Perot interferometer (FPI) was microstructured at the microfiber probe by focused ion beam milling.

A previous sample preparation, already described in section 2.4.3, is necessary to use such microstructuring technique in optical fibers. In the carbon coating step, the sample was placed at a working distance of 50 mm, with a 5^{o} stage tilt towards the carbon source. Nine pulses were applied at a chamber pressure of 6×10^{-5} mbar, depositing a carbon film of nearly 6 nm.

The fabrication of the FPI in the microfiber probe was realized at Leibniz IPHT with a Tescan (Lyra XMU) focused ion beam—scanning electron microscope (FIB-SEM). The fabrication process is illustrated in figures 3.8(a-c). Initially, the fiber end was cleaved, not only to remove damaged regions from breaking the microfiber after the tapering process, but also to slightly reduce the size of the microfiber probe. A longer microfiber probe is more susceptible of bending and breaking. The cleave was executed with an ion current of nearly 1 nA. Then, a 2 μm-wide air gap with a depth of 7 μm was milled 60 μm away from the cleaved edge using the same ion current. At the position of the air gap, the microfiber has a diameter of 11.6 μm. A silica cavity is now formed between the cleaved edge and the

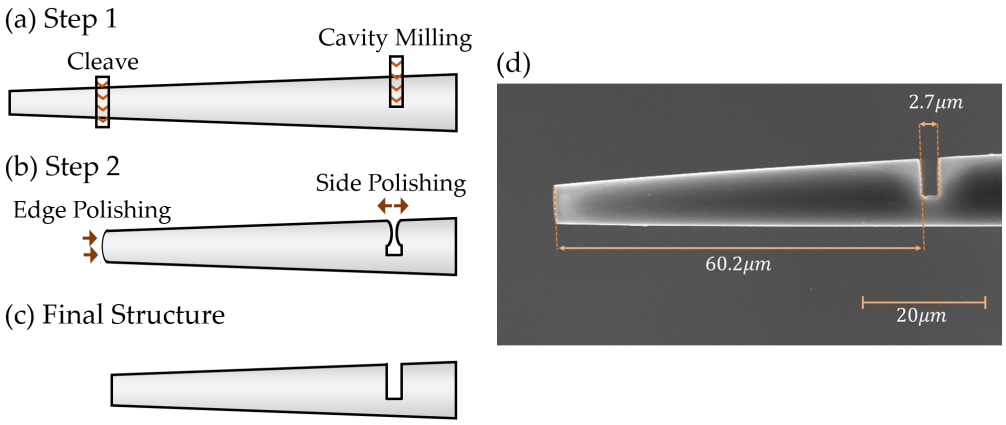

Figure 3.8. – Schematic of the fabrication process by focused ion beam milling. (a) Step 1: fiber tip cleavage and milling of a small air cavity. (b) Step 2: edge and cavity side polishing. (c) Appearance of the final structure. (d) Scanning electron microscope image of the final fabricated structure. The structure is composed of a 60.2 μm-long silica cavity with a 2.7 μm-long air gap.

air gap, which will act as mirrors of the silica FPI through Fresnel reflections. However, at this point the mirrors are very lossy due to high surface roughness. Some of the removed material during the milling process is redeposition on the side walls, creating an irregular surface. Hence, it is crucial to polish the cleaved edge, as well as the sides of the air gap, creating smooth surfaces and reducing the amount of light scattered to the outside. The fiber edge was polished using the same current as before. The side polishing of the air gap was performed at a slightly lower current (800 pA) to avoid fiber movements during the milling process. A scanning electron microscope image of the final microstructured probe is shown in figure 3.8(d). The microfiber probe is comprised of a 2.7 μm-wide air gap and a 60.2 μm-wide silica cavity located between the air gap and the polished fiber edge. The final height of the air gap is 6.1 μm instead of the predicted 7 μm due to material redeposition during the milling process. At last, the sensor was disassembled from the aluminum holder using acetone to remove the carbon glue. The whole structure was then placed in an ultrasonic bath with acetone for 10 minutes to clean the sensing microfiber probe and remove carbon glue residues.

The structure was interrogated in a reflection configuration by means of an optical

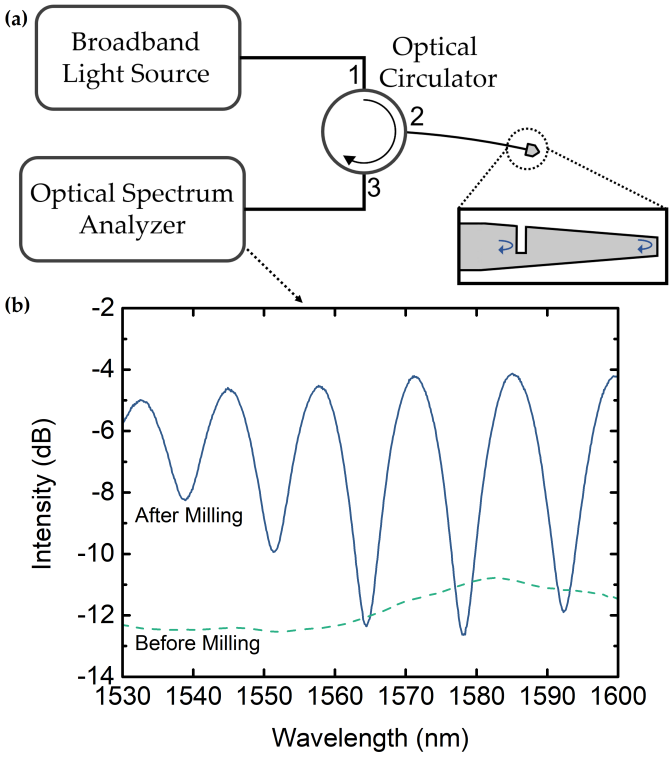

Figure 3.9. – (a) Schematic of the interrogation system. The microfiber probe is monitored in reflection by means of an optical circulator. (b) Reflection spectrum of the microfiber tip, before and after milling.

circulator, as schematized in figure 3.9(a). A broadband optical source, with a central wavelength of 1550 nm and a bandwidth of 100 nm, was used to illuminate the sensor and the reflected signal was recorded using an OSA with 200 pm of resolution. The reflection spectrum of the structure, before and after milling, is shown in figure 3.9(b). The signal was previously normalized to the reflected signal from a cleaved SMF in air (around 3.3% Fresnel reflection). Before milling, the microfiber had a damaged end due to the fabrication process, resulting in a lossy reflection spectrum with no interferometric behavior. After milling, the silica cavity and the air gap work as FPIs, and so the reflection spectrum presents an interferometric behavior.

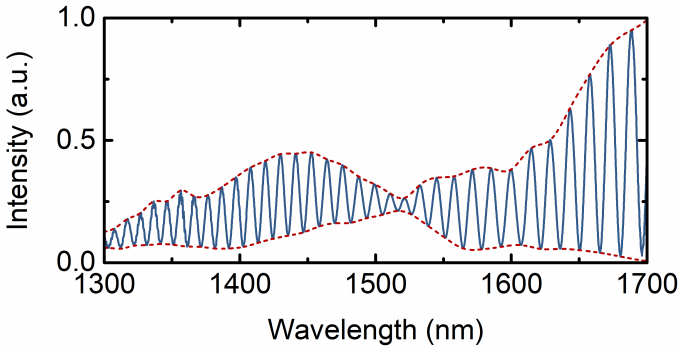

Figure 3.10. – Reflection spectrum of the microfiber tip in a broader wavelength range. The upper and lower envelope modulations are traced with a dashed line. Intensity represented in a linear scale.

To observe more spectral features, the spectrum of the microstructured fiber probe was recorded in a broader wavelength range by means of a supercontinuum source (Fianium WL-SC-400-2, wavelength range: 410nm to 2400nm). The measured spectrum is depicted, in a linear scale, in figure 3.10. The oscillatory interferometric signal presents a complex modulation with a node at around 1518 nm. The upper and lower envelope modulations are represented with dashed lines. Next, the principle of operation of the sensing structure will be analyzed.

3.3.2. Principle

Both the silica cavity and the air gap act as FPIs, where light is partially reflected at each air-silica interface through Fresnel reflections. However, the reflections at each interface are very small, with an intensity reflection coefficient of around 3.3% (considering the refractive index of silica equal to 1.4440 at 1550 nm, and the refractive index of air equal to 1.0003, at 1550 nm at a temperature of 15 °C [146]). Under these circumstances, the FPI response can be approximated as a two-wave interferometer, considering only one reflection at each interface, as discussed in the previous chapter. The distance between

two consecutive interference minima (or maxima), commonly known as the free spectral range (FSR), can be expressed as a function of the cavity length (L) based on equation 2.5 as [87]:

$$FSR = \frac{\lambda_1 \lambda_2}{2n_{eff}L} = \frac{\lambda_1 \lambda_2}{OPD}, \tag{3.7}$$

where λ_1 and λ_2 are the wavelengths of the two consecutive interference minima (or maxima), n_{eff} is the effective refractive index of the propagating mode, L is the physical length of the FPI cavity, and $OPD = 2n_{eff}L$ is known as the optical path difference. In reality, the structure presents multiple propagating modes which generate several FPI responses, one for each mode. The generated FPIs have slightly different frequencies, since the propagating modes have different effective refractive indices. Hence, the output is the superposition between the multiple FPI responses, resulting in different beating modulations that form a complex envelope. The upper and lower envelope modulations are represented in figure 3.10 with dashed lines. Considering that the physical length of the silica cavity (L) is the same for every FPI, the complex envelope modulation only depends on the effective refractive index differences between the various propagating modes, similar to the MZI proposed in section 3.2.

To understand more about the principle of operation, let us deconstruct the spectrum by applying a fast Fourier transform (FFT). The range of wavelengths used in the measurements is very broad, which makes the FSR change slightly across the spectrum due to the wavelength dependency. To perform a fast Fourier transform, one needs to make sure that the spacing between the interference fringes (FSR) is approximately the same in all regions of the spectrum, eliminating therefore its wavelength dependence. An easy solution is to convert the wavelength data into optical frequency domain ($\nu = c/\lambda$, where c is the speed of light in vacuum). Between two interference minima (or maxima), the phase change is equal to 2π, which in terms of optical frequencies can be translated as:

$$\Delta\varphi = 2\pi = \frac{2\pi}{\lambda_1} n_{eff} 2L - \frac{2\pi}{\lambda_2} n_{eff} 2L = \frac{2\pi\nu_1}{c} n_{eff} 2L - \frac{2\pi\nu_2}{c} n_{eff} 2L, \tag{3.8}$$

where n_{eff} is assumed the same for both wavelengths. The FSR in wavelength, given by equation 3.7, can now be converted into FSR in frequency ($FSR_\nu = \nu_1 - \nu_2$) expressed as [4]:

$$FSR_\nu = \frac{c}{2n_{eff}L} \longleftrightarrow OPD = 2n_{eff}L = \frac{c}{FSR_\nu}, \tag{3.9}$$

where OPD is the optical path difference. The FFT of the reflection spectrum in optical frequencies can be represented in terms of OPD through equation 3.9, since the FFT X-axis corresponds to an inverse unit of frequency ($1/FSR_\nu$). The FFT of the reflection spectrum from figure 3.10 is shown in figure 3.11(a).

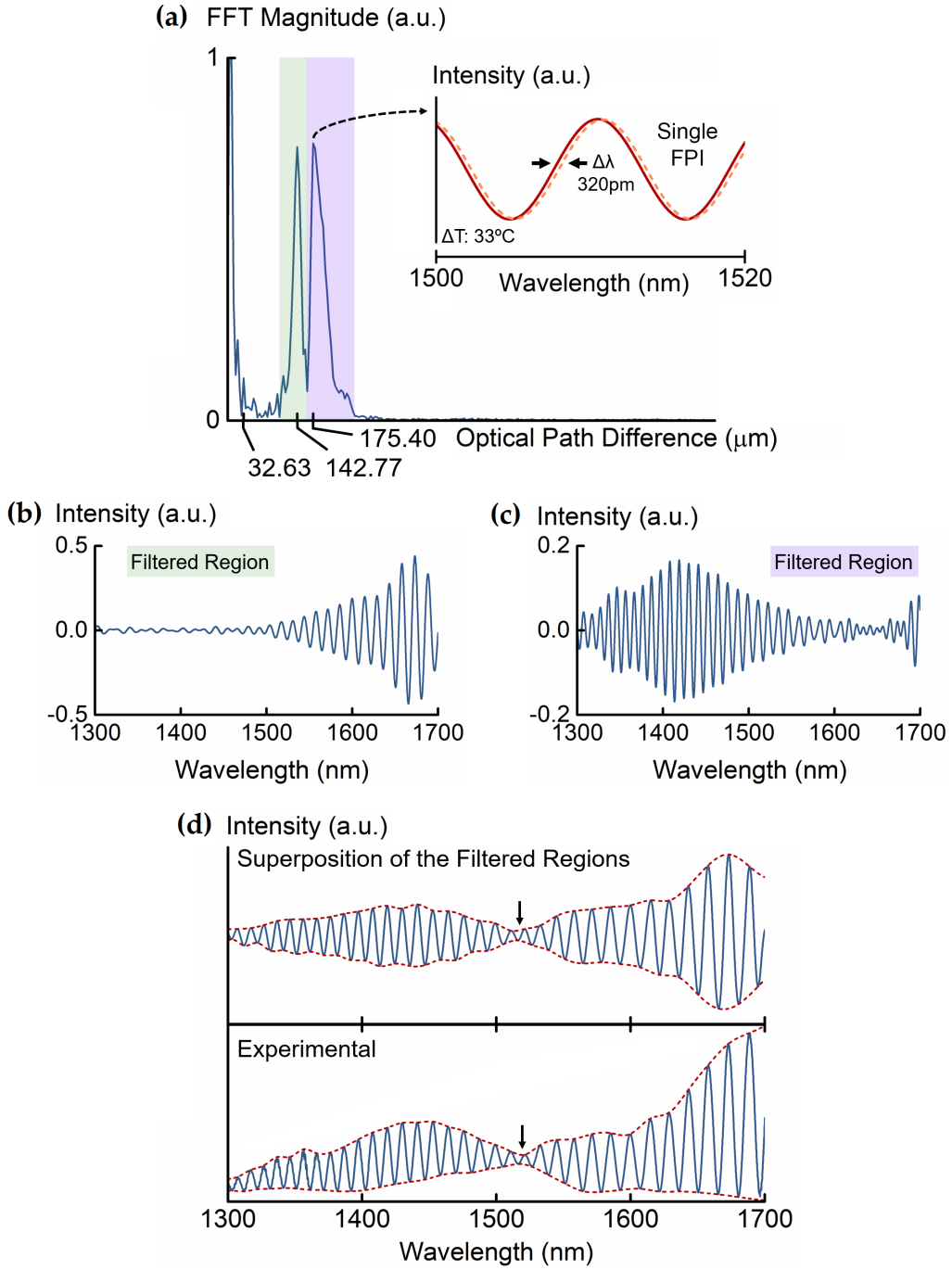

Figure 3.11. – (a) Fast Fourier transform of the reflection spectrum from figure 3.10. Inset: filtered spectrum correspondent to a single FPI. Filtered reflection spectrum from the (b) lower frequency region and (c) higher frequency region. (d) Superposition of the reflection spectrum for the two filtered regions and experimental measured reflection spectrum.

The fundamental mode (mode with higher n_{eff}) propagating in the silica cavity should correspond to the FFT peak of higher intensity. In this case, the FFT peak has an OPD equal to 175.4 μm. The FPI response generated by such mode was filtered out using a narrow FFT bandpass filter. The result is depicted in the inset of figure 3.11(a). The response is similar to a single-mode low-finesse FPI, where the signal is a two-wave interferometer. The temperature sensitivity can be estimated by filtering with the same procedure the spectrum of the sensor at a different temperature. For a temperature change of 33 °C, the FPI response shifted 320 pm, resulting in an estimated sensitivity of 9.7 pm/°C. This value of sensitivity is typical of other sensing structures that rely on silica, such as fiber Bragg gratings (FBGs) [133].

Two regions are also clearly visible and marked in the FFT, each of them composed of a broad peak. These broad peaks are actually the overlap of several individual peaks, due to the multiple FPIs with slightly different frequencies (slightly different OPDs). However, the FFT does not have the necessary resolution to differenciate between them. The two marked regions can be separated by means of an FFT bandpass filter. The filtered response from the lower frequency region is depicted in figure 3.11(b), while the filtered response from the higher frequency region is shown in figure 3.11(c). Both filtered responses are already modulated by complex envelopes resulting from the beating between different FPI responses with frequencies within the filtered regions. The combined response of these two regions, represented in figure 3.11(d), contains a node at around 1518 nm, marked with an arrow. Compared with the experimental response(fig. 3.10), the position of the node is the same for both cases.

It is important to note that the combined filtered responses do not contain the effect of the single FPI given by the air gap. Assuming an effective refractive index of 1.0003 (refractive index of air at 1550 nm at a temperature of 15 °C [146]), the OPD of the air gap can be calculated using the measured length (2.7 μm), obtaining 5.4 μm. In fact, the air gap represents a low-frequency component, whose FFT peak is masked by the zero OPD region (DC component), and it does not have a main contribution to the position of the envelope node. During the analysis performed along the rest of this section, the effect of the air cavity was neglected.

Apart from the air gap, two distinct physical cavities are also presented in the structure: the silica cavity with an $OPD = 2 \times 1.444 \times 60.2 = 173.9\,\mu m$, and the air gap together with the silica cavity, with an $OPD = 2 \times 2.7 + 2 \times 1.444 \times 60.2 = 179.3\,\mu m$. In both cases, only one propagating mode was considered to estimate the OPDs, assuming its effective refractive index to be the refractive index of pure silica (1.444 at 1550 nm), as an approximation. Moreover, the OPD of the silica cavity is slightly different than the one presented in the FFT, due to the small approximation made to the effective refractive index and also due to some uncertainty in the measurement of the cavity length.

3.3.3. Temperature Characterization

To evaluate the improvement of sensitivity provided by the modulating envelope, the sensing probe was characterized in terms of temperature. The probe was submitted to different temperatures in air, ranging from 30 °C to 120 °C, using a tubular oven (Ströhlein Instruments). Then, the envelope shift was determined by tracking the position of the node, located at 1518 nm, as a function of temperature. To obtain a more accurate value for the position of the node, the average between the local minimum of the upper envelope and the local maximum of the lower envelope was taken.

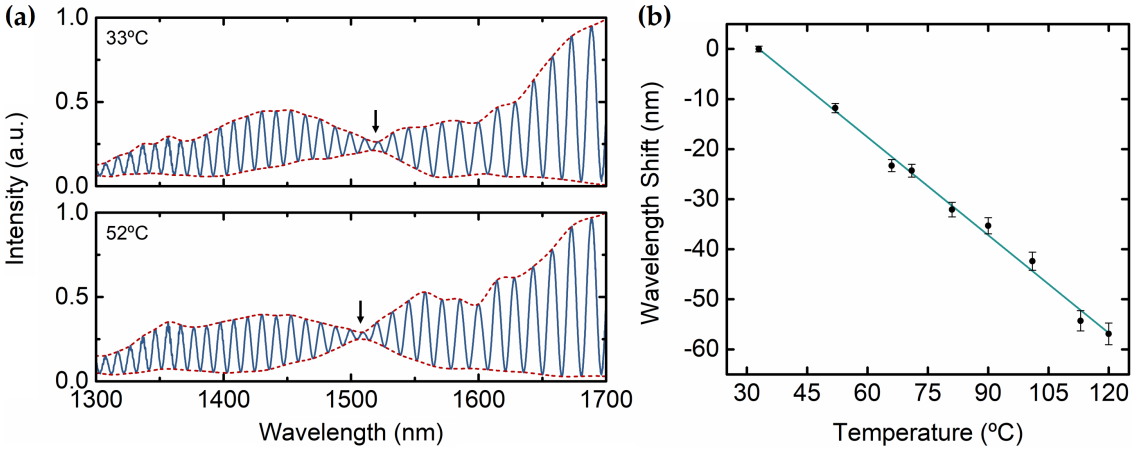

Figure 3.12. – (a) Reflection spectrum at two distinct temperatures. The position of the envelope node, marked with an arrow, was monitored during the experiment. (b) Wavelength shift of the envelope node as a function of temperature. The slope corresponds to a temperature sensitivity of (-654 ± 19) pm/°C.

Figure 3.12(a) shows the reflection spectrum of the sensing probe at two distinct temperatures: 33 °C and 52 °C. The position of the node is marked with an arrow. The position of the envelope node shifts towards shorter wavelengths with increasing temperature. The full temperature characterization curve is depicted in figure 3.12(b). The temperature sensitivity of the envelope is determined through a linear fit applied to the wavelength shift of the node as a function of temperature. By means of this, a temperature sensitivity of (-654 ± 19) pm/°C was achieved for the envelope modulation.

The stability of the sensing structure was also evaluated. Ten consecutive measurements were performed at two different temperatures, 89.54 °C and 94.51 °C, in order to determine the sensor resolution. To perform such kind of measurements, it is crucial to ensure a good thermal stability, maintaining the same temperature along the measurements. Therefore, the sensing probe was placed inside an aluminum box, and the whole set was installed inside a Carbolite oven with high volumetric capacity. The aluminum box partially attenuates the

thermal fluctuations of the oven caused by its PID controller[2]. A PT100 thermometer was also set inside the aluminum box, together with the sensing probe, to help in monitoring thermal stability. To promote a good thermal equilibrium, the oven was allowed to stabilize for 4 h at each temperature, prior to any measurement.

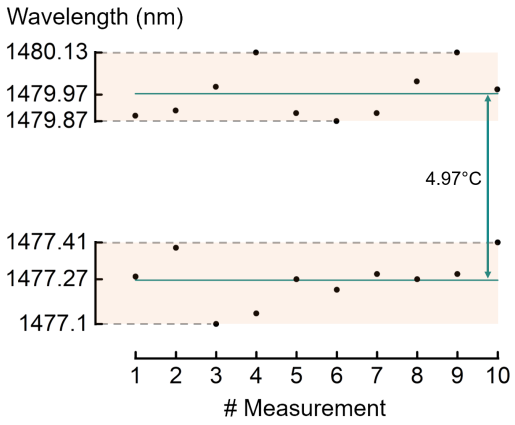

Figure 3.13. – Stability measurements: 10 measurements at two distinct temperatures, 89.54 °C and 94.51 °C.

Figure 3.13 shows the results of the stability measurements. A maximum standard deviation achieved was 96.98 pm, by analyzing the wavelength fluctuations. A resolution of 0.14 °C is obtained by performing the ratio between the maximum standard deviation and the temperature sensitivity previously determined. This value corresponds to half of the OSA resolution used for the measurements (200 pm). Therefore, the sensor resolution is limited by the resolution of the interrogation system. The theoretical resolution for the demonstrated sensing probe, while considering an interrogation system with a resolution of 10 pm, would be 0.015 °C. Such wavelength resolution can already be accomplished by modern high resolution OSA systems.

3.3.4. Discussion

A small size microfiber probe structured with a focused ion beam was successfully demonstrated and designed to have enhanced temperature sensitivity, as shown below. The core of the improved performance relies on the use of a multimode fiber. The complex envelope modulation presented in the reflection spectrum arises from effective refractive index differences between the propagating modes. This effect is comparable to the Mach-Zehnder interferometer demonstrated in the previous section.

The FPI response correspondent to the fundamental propagating mode could be extracted and analyzed. Its temperature sensitivity, around 9.7 pm/°C, is in agreement with

[2]PID controller: proportional-integral-derivative controller.

Table 3.2. – Table of comparison between different configurations. NL stands for non-linear response.

Configuration	Sensitivity (pm/°C)	Range (°C)	Resolution (°C)
FIB-milled FP modal interferometer (2010) [142]	20	19-520	-
Polyvinyl alcohol FPI (2012) [143]	173.5 (NL)	>80	-
SMF + etched P-doped fiber FPI (2014) [123]	11.5-15.5	100-550	-
Silicon FPI (2015) [92]	82	10-100	0.3
Silicon FPI (2015) [147]	84.6	20-100	6×10^{-4}
Hollow-core FPI + Vernier effect (2015) [148]	816.65	20-90	-
Hollow-core FPI + Vernier effect (2015) [148]	1019	250-300	-
FIB-milled silica FPI in fiber taper (2016) [3]	15.8	40-140	-
Double polymer-capped FPI (2017) [144]	689.68	20-75	-
MMF tip FPI + UV adhesive (2017) [145]	213 (NL)	55-85	-
Cascaded FPI with Vernier effect (2018) [149]	-97	30-60	-
Cascaded FPI with polymer + Vernier effect (2018) [150]	67350	20-25	-
This work [21]	**-654**	**30-120**	**0.14**

other conventional silica FPIs [3]. On the other hand, the envelope modulation exhibits a magnified response, with a temperature sensitivity of −654 pm/°C achieved between 30 °C and 120 °C. This value is over 60-fold higher than the single silica FPI originated by the fundamental propagating mode. Moreover, the temperature of operation of the structure includes typical temperature ranges that are used in biological applications (30 °C +). Table 3.2 compares the sensitivity values and resolution for different Fabry–Perot configurations, up to the date of publication of this work. The proposed fiber probe presents higher temperature sensitivity than many reported Fabry–Perot configurations, especially when considering that it is a silica sensor.

Stability measurements were also performed, demonstrating a maximum standard deviation of 96.98 pm, corresponding to a resolution of 0.14 °C. However, it is limited by the resolution of the interrogation system used. This limitation should be further checked by using an interrogation system with higher wavelength resolution (10 pm or lower).

In the future, extensive studies still need to be performed to assess the response of the sensing probe to specific target applications. The aim of applying such small sensing structures for medical or chemical applications require further analysis on the response of the sensor when immersed in liquid solutions. Under those circumstances, the effective refractive indices of the propagating modes will be completely different, requiring a new characterization. Upon characterization, the sensing structure might need possible adaptations, either on the microfiber size and fabrication, or on the microstructuring process, to optimize its final response and performance.

3.4. Conclusion

The aim of this chapter was to develop microstructured devices based on optical microfibers with enhanced sensing capabilities. The first work tackled the problem of cross-sensitivity in optical fiber sensing, especially targeting the influence of temperature variations. Here, the microfiber was fabricated with abrupt transitions regions, generating a Mach-Zehnder interferometer, and then tied up forming a microfiber knot resonator. Merging both sensing configurations, the Mach-Zehnder interferometer and the microfiber knot resonator, enabled simultaneous measurement of refractive index and temperature. Additionally, the Mach-Zehnder interferometer achieved higher sensitivities than the microfiber knot resonator. This effect is mainly due to its dependence on the difference between the effective refractive indices of the two main propagating modes in the microfiber.

The objective of the second work was to make use of focused ion beam milling to structure the microfiber into a small sensing probe. In this context, a Fabry-Perot interferometer was milled with this technique in a microfiber probe, showing improved temperature sensing. The enhancement, similarly to the Mach-Zehnder interferometer of the first work, is based on differences between effective refractive indices of the propagating modes.

Until now, the presented sensing structures are high quality micro-interferometers in fiber, providing mostly the expected typical sensitivity. However, the cases here explored also indicate the possibility of using different modes to increase the sensitivity, through an envelope modulation. From a different perspective, this enhancement of the envelope wavelength shift can be interpreted as the Vernier effect. In the optical domain, the Vernier effect consists of the superposition of two interferometric signals with slightly shifted frequencies, originating a beating envelope with interesting properties. One of them is the magnification of the spectral shift of the envelope, when compared with the normal shift of the single interferometer. As seen before, the frequency of the different Fabry-Perot interferometers in the microfiber probe is directly related with the effective refractive index of each propagating mode, through equation 3.9. Note that the structure does not have only two interferometers with slightly different interferometric frequencies, but as many as the number of propagating modes. Hence, the generated Vernier beating envelope is rather complex. Moreover, in this current form the Vernier effect is uncontrollable, since one does not have control over the modes propagating in the structure. The next chapter explores the optical Vernier effect from an optical fiber sensing perspective, and especially how to apply it to maximize its enhancement effects in a controllable way.

Chapter 4.

Optical Vernier Effect in Fiber Interferometers

4.1. Introduction

The use of a secondary scale in measuring equipment and instruments, such as calipers and ancient astronomical quadrants, allows to increase the resolution and reduce the uncertainty of measurements. The caliper was invented in 1631 by Pierre Vernier [151]. Some people name such instrument after his inventor as the "Vernier caliper", where the two scales overlapping each other are referred as the Vernier scale. Eventually, Pierre Vernier may have been inspired by a portuguese measuring tool of the 16^{th} century called - the Nonius. The Nonius, created in 1542 by the mathematician and cosmographer Pedro Nunes, was a tool used to perform finer measurements on circular instruments, improving the angular measurements of devices like the astrolabe [152].

In the field of optical fibers, the Vernier effect (or the Vernier principle) also left his mark. In 1988, Paul Urquhart was studying and designing compound resonators in optical fibers for application in fiber lasers and optical communications systems [153]. In his work, Urquhart used the Vernier principle by combining optical fiber rings with unequal lengths in parallel. In his configuration, the Vernier effect acted as a mechanism to suppress spectral modes (suppression of resonance peaks in the spectrum) and to narrow the linewidth of fiber lasers. Moreover, adaptations of the Vernier effect in the fields of optics also led to the development of the optical frequency comb technique, which gave the Nobel Prize in Physics to John Hall and Theodor Hänsch [154, 155]. Such technique is widely used in Vernier spectroscopy [156].

The fast development in many research fields that make use of optical fibers, together with the specific technical challenges in their use, places strong pressure and new challenges in the fields of optical fiber sensing research. The demand for sensing structures able to achieve higher sensitivities and resolutions than what conventional fiber sensors can offer is increasing. With this, researchers are driven to find new options for improved optical

fiber sensors, able to achieve higher sensitivities and resolutions. The optical version of the Vernier effect applied to optical fiber sensing has demonstrated a huge potential to solve these needs. In fact, it quickly became a hot topic in this field over the last two years and gained a lot of interest among the researchers, as seen by the bar chart in figure 4.1. The first report that mentions the use of the optical Vernier effect in optical fiber sensors was published by the end of 2012 by Xu *et al.* [157]. However, it took about 2 years until some of the optical Vernier effect properties, as we know them today, were reported for optical fiber sensing [158]. This chapter describes the optical Vernier effect with optical fiber interferometers, from a sensing perspective. The different properties of the effect are also here discussed. At the end, an extensive review on the state-of-the-art of the multiple optical Vernier effect configurations for fiber sensing is presented.

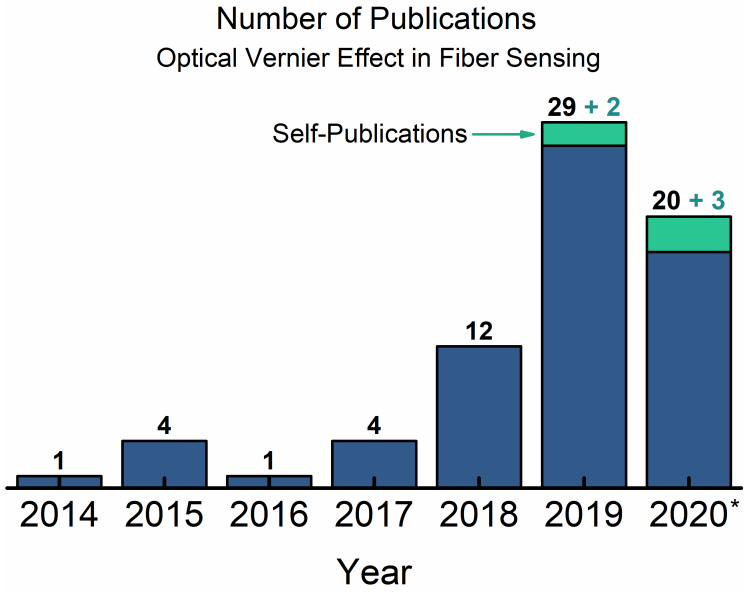

Figure 4.1. – Bar chart of the number of publications on the optical Vernier effect for fiber sensing along the years. It shows an increase of publications in the last year, especially in 2019. *The publications were only counted until October 2020.

4.2. Mathematical Description

Just like a caliper uses two distinct scales to achieve higher resolution measurements, the optical Vernier effect is based on the overlap between the responses of two interferometers with slightly detuned interference signals. This effect will be mentioned along the dissertation as the fundamental optical Vernier effect, which requires two interferometers with slightly shifted interferometric frequencies. In fact, the concept of optical Vernier effect can be extended, as will be shown later in chapter 5, by introducing harmonics with new properties and high impact in the performance of the effect.

The fundamental optical Vernier effect in interferometric fiber sensing has two possible configurations: either one can place the two interferometers in series, or in a parallel configuration. From the two interferometers used to generate the fundamental optical Vernier effect, one is used as the sensor and the other acts as a stable reference. The interferometric frequency of optical fiber interferometers can be adjusted by modifying their optical path length. This is achieved by changing the refractive index and/or the physical length of the interferometer. Therefore, given the properties of an initial interferometer, the second interferometer can be adjusted to maximize the enhancement provided by the optical Vernier effect. To fully understand how this can be made possible, let us go in detail through the mathematical description of the effect, from an optical fiber sensing perspective.

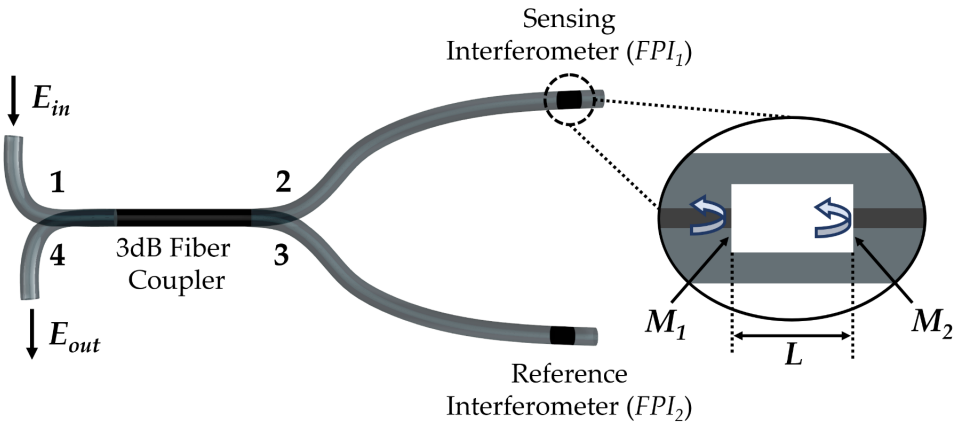

Figure 4.2. – Schematic illustration of the experimental setup. The sensing interferometer (FPI_1) and the reference interferometer (FPI_2) are separated by means of a 50/50 fiber coupler. Light is reflected at both interfaces of the capillary tube, M_1 and M_2. The length of the interferometer (L) is given by the length of the capillary tube.

The following analysis will consider a parallel configuration by means of a 3dB fiber coupler, as schematized in figure 4.2, where each arm contains a single interferometer. This configuration allows both interferometers to be physically separated, where one of them can easily be maintained as a stable reference. It is worth mentioning now that a series configuration (without a physical separation provided by an optical fiber coupler) would show equivalent results. However, additional factors would have to be considered in order to describe the effect under such conditions, as will be further discussed at the end of this section. Both interferometers will be considered as Fabry-Perot interferometers (FPIs) formed by a silica capillary tube between two sections of single-mode fiber. Although the following theoretical considerations are valid for any FPI structure, they can easily be extended to other types of interferometers, such as the Mach–Zehnder interferometer or the Michelson interferometer, expanding the range of configurations and applications of this powerful technique.

For simplification, the two FPIs are assumed to have identical interfaces, with an intensity reflection coefficient R_1 for the first mirror interface (M_1) and R_2 for the second mirror interface (M_2). In this case, all interfaces provide a silica/air Fresnel reflection. Note that the reflection coefficient due to a silica/air Fresnel reflection is small (around 3.3% at 1550 nm), and hence, only one reflection at each interface was considered, corresponding to a two-wave approximation. In this configuration, a coherent light source is injected at port 1 and split between the two arms (port 2 and 3) with equal intensity. The light reflected by the system is collected and measured at port 4. The electric field of the input light, E_{in}, propagating in the structure will be reflected at different points. In both interferometers, the electric field of light reflected at the interface M_1 is given by:

$$E_{R1}(\lambda) = \sqrt{R_1}\frac{E_{in}(\lambda)}{\sqrt{2}}, \tag{4.1}$$

while the electric field of light transmitted at the same interface is expressed as:

$$E_{T1}(\lambda) = \sqrt{(1-A_1)}\sqrt{(1-R_1)}\frac{E_{in}(\lambda)}{\sqrt{2}}, \tag{4.2}$$

where A_1 represents the transmission losses through interface M_1, related to mode mismatch and surface imperfections.

Light transmitted at interface M_1, expressed by equation 4.2, will then travel through the FPI, being partially reflected and transmitted at interface M_2. The electric field of light reflected at interface M_2 of the sensing interferometer (FPI_1) is expressed as:

$$E_{R2}^{1}(\lambda) = \sqrt{(1-A_1)}\sqrt{(1-R_1)}\exp(-\alpha L_1)\sqrt{R_2}\frac{E_{in}(\lambda)}{\sqrt{2}}\exp\left[-j\left(\frac{2\pi n_1 L_1}{\lambda}-\pi\right)\right], \tag{4.3}$$

where $\exp(-\alpha L_1)$ represents the propagation losses up to interface M_2 of the sensing interferometer (FPI_1), λ is the vacuum wavelength of the input light, n_1 and L_1 are the effective refractive index and the length of the sensing interferometer (FPI_1). The factor $2\pi n_1 L_1/\lambda - \pi$ corresponds to the phase accumulated in the propagation from the interface M_1 to the interface M_2, with a reflection phase of π. This reflection phase arises from the Fresnel reflection coefficient, which turns negative for incident light reflected at the interface with a material of higher refractive index than the propagation medium. Therefore, there is a phase difference of π between the incident and the reflected waves.

The reflected light, $E_{R2}^{1}(\lambda)$, will propagate back in the structure and get partially transmitted at interface M_1 towards the output, interfering with the light initially reflected at that interface, described by equation 4.1. Hence, the electric field of the light coming from the sensing interferometer, $E_{FPI1}(\lambda)$, is given by:

$$E_{FPI1}(\lambda) = \frac{E_{in}(\lambda)}{\sqrt{2}} \left\{ A + B \exp\left[-j \left(\frac{4\pi n_1 L_1}{\lambda} - \pi \right) \right] \right\}, \tag{4.4}$$

with A and B given by:

$$A = \sqrt{R_1}, \tag{4.5}$$

$$B = (1 - A_1)(1 - R_1) \exp(-2\alpha L_1) \sqrt{R_2}. \tag{4.6}$$

At the interface M_2, the transmitted light leaves the interferometer and no longer contributes to the system.

The same analysis can be performed for the reference interferometer (FPI_2), where the electric field of the light coming from the reference interferometer, $E_{FPI2}(\lambda)$, can be expressed in a similar form as in equation 4.4 as:

$$E_{FPI2}(\lambda) = \frac{E_{in}(\lambda)}{\sqrt{2}} \left\{ A + C \exp\left[-j \left(\frac{4\pi n_2 L_2}{\lambda} - \pi \right) \right] \right\}, \tag{4.7}$$

where n_2 and L_2 are the effective refractive index and length of the reference interferometer (FPI_2), and C corresponds to:

$$C = (1 - A_1)(1 - R_1) \exp(-2\alpha L_2) \sqrt{R_2}. \tag{4.8}$$

If no propagation losses are considered as a simplification ($\alpha = 0$), the coefficients described by equations 4.6 and 4.8 are the same ($B = C$). With this, one can express the total electric field leaving the output at port 4 as the combination of the electric field from both interferometers ($E_{FPI1} + E_{FPI2}$):

$$\begin{aligned} E_{out}(\lambda) = {} & \sqrt{2} A E_{in}(\lambda) \\ & + B \frac{E_{in}(\lambda)}{\sqrt{2}} \left\{ \exp\left[-j \left(\frac{4\pi n_1 L_1}{\lambda} - \pi \right) \right] + \exp\left[-j \left(\frac{4\pi n_2 L_2}{\lambda} - \pi \right) \right] \right\}, \end{aligned} \tag{4.9}$$

where B is now defined as:

$$B = (1 - A_1)(1 - R_1) \sqrt{R_2}. \tag{4.10}$$

The output light intensity, $I_{out}(\lambda)$, normalized to the incident light, can now be calculated by:

$$I_{out}(\lambda) = \left| \frac{E_{out}(\lambda)}{E_{in}(\lambda)} \right|^2 = \frac{E_{out}(\lambda) E_{out}^*(\lambda)}{E_{in}^2(\lambda)}, \tag{4.11}$$

where $E^{*}_{out}(\lambda)$ is the complex conjugated of $E_{out}(\lambda)$. By substituting equation 4.9 in equation 4.11, after some algebraic manipulation the expression for the reflected light intensity measured at the output is [20]:

$$I_{out}(\lambda) = I_0 - 2AB\left[\cos\left(\frac{4\pi n_1 L_1}{\lambda}\right) + \cos\left(\frac{4\pi n_2 L_2}{\lambda}\right)\right] + B^2 \cos\left[\frac{4\pi\left(n_1 L_1 - n_2 L_2\right)}{\lambda}\right], \tag{4.12}$$

where $I_0 = 2A^2 + B^2$. The reflected light intensity is the combination of the oscillatory responses of both FPIs, plus a lower frequency component given by the difference between the optical path lengths of the two interferometers.

To simulate the reflected light intensity given by equation 4.12, the case of no transmission losses was considered ($A_1 = 0$). For simplification, both FPIs are considered to have the same refractive index ($n_1 = n_2$) and to be equal to 1.0003. The length of the sensing interferometer (FPI_1) was considered 100 μm. As explained before, to introduce the fundamental optical Vernier effect the two interferometers should have slightly shifted interferometric frequencies, which is equivalent to slightly shifted optical path lengths. Hence, a length of 90 μm was chosen for the reference interferometer (FPI_2). All the intensity reflection coefficients, assumed as air/silica interfaces, are given by:

$$R = \left(\frac{n_{silica} - n_{air}}{n_{silica} + n_{air}}\right)^2 = \left(\frac{1.4440 - 1.0003}{1.4440 + 1.0003}\right)^2 = 0.033, \tag{4.13}$$

where 1.4440 is the refractive index of silica [51] and 1.0003 is the refractive index of air at 15 °C [146], both at a wavelength of 1550 nm.

Considering all these parameters, the simulated reflected light intensity is shown in figure 4.3. The simulated spectrum of the fundamental Vernier effect, for the considered parameters, resembles a two-wave interferometer response modulated by a low frequency envelope, called the Vernier envelope.

Let us deconstruct the simulated response by performing a fast Fourier transform (FFT). Due to the broad wavelength range used (1300 nm to 1600 nm), it is important to eliminate the wavelength dependency of the free spectral range to ensure a constant spacing along the measured spectrum. Hence, one can convert the wavelength data into the optical frequency domain, as previously demonstrated in section 3.3.2. The FFT can be represented as a function of the optical path length through equation 3.9. In this case, to make a straightforward comparison with the lengths of the FPIs, the FFT x-axis displays half of the optical path length. The result is depicted in figure 4.4.

The FFT shows three main peaks: two of them match with the lengths assumed for the sensing interferometer (FPI_1) and the reference interferometer (FPI_2), while the

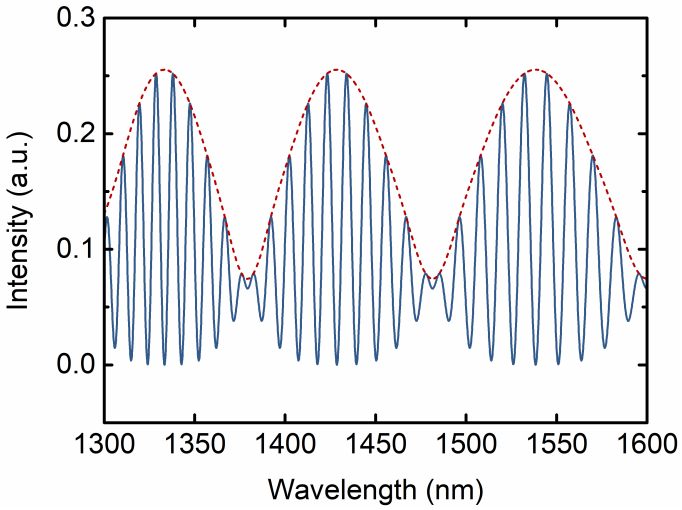

Figure 4.3. – Simulated reflected spectrum with the fundamental Vernier effect. The upper Vernier envelope is traced with a dashed line.

peak of lower frequency corresponds to the difference between the optical path lengths of the two FPIs ($FPI_1 - FPI_2$). This last component is the Vernier envelope modulation, represented in figure 4.3 with a dashed line. All three components are also clearly described by the three cosine functions in equation 4.12.

4.2.1. Free Spectral Range

The phase of the Vernier envelope ($\varphi_{envelope}$) is described by the argument of the low frequency cosine in equation 4.12:

$$\varphi_{envelope} = \frac{4\pi\left(n_1 L_1 - n_2 L_2\right)}{\lambda} = \frac{2\pi\left(OPL_1 - OPL_2\right)}{\lambda}. \tag{4.14}$$

Between two consecutive maxima (or minima) of the Vernier envelope, λ_1 and λ_2, the phase of the Vernier envelope changes by 2π. Therefore, using the previous equation one obtains:

$$2\pi = 4\pi\left(n_1 L_1 - n_2 L_2\right)\left(\frac{1}{\lambda_1} - \frac{1}{\lambda_2}\right) = 4\pi\left(n_1 L_1 - n_2 L_2\right)\left(\frac{\lambda_2 - \lambda_1}{\lambda_2 \lambda_1}\right). \tag{4.15}$$

As seen in previous sections, the free spectral range (FSR) is the distance between two consecutive interference maxima (or minima). The FSR of the Vernier envelope ($FSR_{envelope} = \lambda_2 - \lambda_1$) can be expressed with the help of equation 4.15 as:

$$FSR_{envelope} = \left|\frac{\lambda_2 \lambda_1}{2\left(n_1 L_1 - n_2 L_2\right)}\right|. \tag{4.16}$$

Note that the 2π phase change of the Vernier envelope can be either positive or negative, depending also on the difference between the optical path lengths of the two FPIs

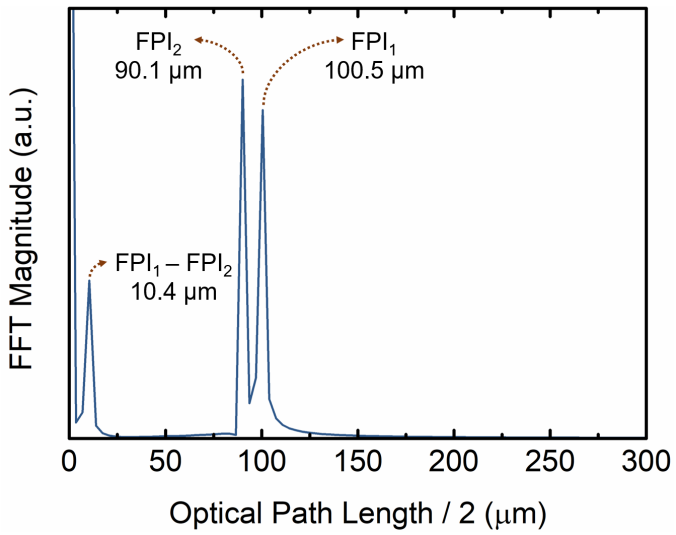

Figure 4.4. – FFT of the simulated reflected spectrum from figure 4.3, expressed as a function of half of the optical path length.

$(n_1L_1 - n_2L_2)$. Regardless of the situation, the FSR should be always a positive value, reason why the modulus was applied to equation 4.16.

The initial situation here presented, with two simple FPIs with similar characteristics, led to a reflected light intensity (equation 4.12) where the phase of the envelope is clearly visible in the equation. However, in more complex cases where both interferometers are distinct, it is not always possible to deduce a simple equation for the measured intensity that can be easily interpreted. Hence, the previous deduction of the Vernier envelope FSR might not be trivial. Yet, there is a different way to obtain an expression for it.

The FSR of the Vernier envelope can also be described more generally by the relationship between the FSRs of each individual interferometer. Let us consider the hypothetical overlap between the responses of two FPIs with slightly shifted interferometric frequencies. The individual spectral responses are shown in figure 4.5. The red curve corresponds to the first interferometer, whose maxima are represented as λ_k^1, and the blue curve corresponds to the second interferometer, with interference maxima described as λ_k^2, where k is the number of the peak.

From observing figure 4.5, both interferometers are in phase at an initial wavelength λ_0^m. The wavelength position of a maximum "k" can be expressed using the FSR of the interferometer as:

$$\lambda_k^1 = \lambda_0^1 + kFSR_1, \tag{4.17}$$

for the first interferometer, and similarly as:

$$\lambda_k^2 = \lambda_0^2 + kFSR_2, \tag{4.18}$$

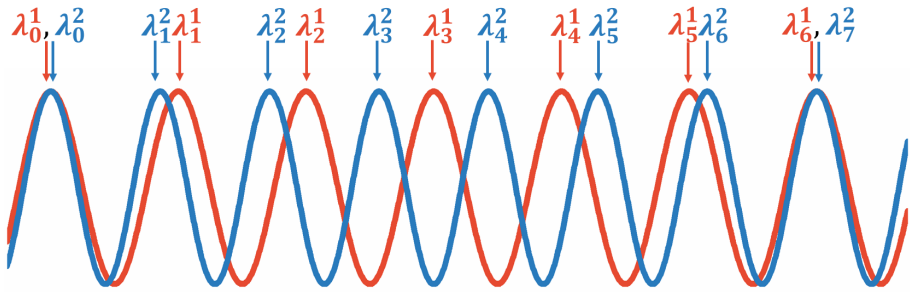

Figure 4.5. – Schematic of the spectral response of two FPIs (1 and 2). The wavelengths of the different peaks are labeled as λ_k^m, where $m = 1, 2$ is the number of the interferometer and k is the number of the peak.

for the second interferometer. At a certain wavelength, both interferometers will be once again in phase. In figure 4.5, both interferometers are again in phase when:

$$\lambda_k^1 = \lambda_{k+1}^2. \tag{4.19}$$

Replacing equations 4.17 and 4.18 in equation 4.19, and considering that $\lambda_0^1 = \lambda_0^2$, the following relationship is obtained:

$$kFSR_1 = (k+1)\, FSR_2. \tag{4.20}$$

One can express "k" as a function of the FSR of both interferometers in the form of:

$$k = \frac{FSR_2}{FSR_1 - FSR_2}. \tag{4.21}$$

In the fundamental optical Vernier effect, the FSR of the Vernier envelope is the wavelength distance between two consecutive situations where both interferometers are in phase. Therefore, the FSR of the Vernier envelope can be expressed as:

$$FSR_{envelope} = \lambda_k^1 - \lambda_0, \tag{4.22}$$

which by equation 4.17 is the same as:

$$FSR_{envelope} = kFSR_1. \tag{4.23}$$

Substituting now equation 4.21 in equation 4.23, the final expression for the FSR of the Vernier envelope as a function of the FSR of each individual interferometer is:

$$FSR_{envelope} = \left| \frac{FSR_2 FSR_1}{FSR_1 - FSR_2} \right|, \tag{4.24}$$

where once more the modulus was considered, since the FSR is a positive value. The FSR of a Fabry-Perot interferometer is usually defined by equation 2.5 as [87]:

$$FSR = \frac{\lambda_1 \lambda_2}{2 n_{eff} L}, \tag{4.25}$$

where λ_1 and λ_2 are the wavelengths of two consecutive maxima (or minima) of the FPI spectrum, n_{eff} is the effective refractive index of the FPI, and L is the length of the interferometer. The expression deduced initially for the FSR of the Vernier envelope, given by equation 4.16, can be retrieved by replacing equation 4.25 in equation 4.24, but with a rough approximation of considering λ_1 and λ_2 the same for both interferometers, and equal to the consecutive Vernier envelope maxima (or minima), λ_0^1 and λ_k^1:

$$FSR_{envelope} \approx \left| \frac{\lambda_0^1 \lambda_k^1}{2\left(n_1 L_1 - n_2 L_2\right)} \right|. \tag{4.26}$$

Nevertheless, whenever possible, equation 4.24 should be used, as it provides a more rigorous value.

4.2.2. Magnification Factor (M-Factor)

The magnification factor (M-factor) is an important characteristic of the optical Vernier effect. Currently there are two definitions for this parameter [20]. In the first definition, the M-factor expresses how large the FSR of the Vernier envelope is when compared with the individual sensing FPI. In other words, the M-factor is defined as the ratio between the FSR of the Vernier envelope and the FSR of the individual sensing interferometer. Since the FPI_1 was initially considered as the sensing interferometer, the M-factor is expressed as:

$$M = \frac{FSR_{envelope}}{FSR_1} = \frac{FSR_2}{FSR_1 - FSR_2}, \tag{4.27}$$

which is the same as the index "k" defined in equation 4.21. In practical situations, it is sometimes useful to have an estimate of the order of the M-factor value. Instead of having to determine the FSR of the sensing and reference interferometers, one can substitute equations 4.25 and 4.26 in equation 4.27, with the rough approximation of $\lambda_0^1 \lambda_k^1 \approx \lambda_1 \lambda_2$. This way, the M-factor can be roughly estimated as a function of the refractive index and physical length of the interferometers as:

$$M \approx \frac{n_1 L_1}{n_1 L_1 - n_2 L_2} = \frac{OPL_1}{OPL_1 - OPL_2}. \tag{4.28}$$

It is important to notice that, similarly to the FSR of the Vernier envelope described by equation 4.24, the M-factor also depends on the OPLs of the interferometers that form the structure. This property is extremely helpful when dimensioning the sensing and reference interferometers for real applications, as it will be demonstrated later in chapter 5.

The second definition for the M-factor is related to sensing applications and describes

how much the wavelength shift of the Vernier envelope is magnified in comparison to the wavelength shift of the individual sensing interferometer, under the effect of a certain measurand. In this definition, the M-factor is given by:

$$M = \frac{S_{envelope}}{S_{FPI1}}, \tag{4.29}$$

where $S_{envelope}$ is the sensitivity of the Vernier envelope to a certain measurand and S_{FPI1} is the sensitivity of the individual sensing interferometer (FPI_1 for this case), if the second interferometer acts as a stable reference. It is crucial to emphasize these last words: if the second interferometer does not act as a stable reference, equation 4.29 in its current form is no longer valid. In the eventual case of having no reference interferometer, where both interferometers are affected by the measurand, equation 4.29 becomes more complex involving the sensitivities of both interferometers plus the sensitivity of the Vernier envelope. Such complex case will be later explored in chapter 6.

The M-factor increases when the difference between the OPLs of the sensing and the reference interferometers gets smaller. Taking into consideration the definition of the optical Vernier effect, the OPL of the reference interferometer can be seen as a slightly detuned value from the OPL of the sensing interferometer. This way, the OPL of the reference interferometer (FPI_2) can be defined as:

$$OPL_2 = OPL_1 - 2\Delta, \tag{4.30}$$

where Δ is the detuning, which can be positive or negative. Contrary to the FSR of the Vernier envelope, the M-factor can assume positive or negative values. A negative M-factor simply means a wavelength shift of the Vernier envelope in the opposite direction to that of the single sensing interferometer, as allowed by equation 4.29.

For the same values of the sensing interferometer used to simulate figure 4.3, the M-factor as a function of the detuning (Δ) of the reference interferometer is displayed in figure 4.6. Negative detunings were not plotted, however they present a similar M-factor behavior but with negative values (negative Vernier envelope wavelength shift). The right y-axis shows the correspondent FSR of the Vernier envelope, which also depends on the detuning. From a different perspective, according to equation 4.27: $FSR_{envelope} = MFSR_1$, where the FSR of the Vernier envelope can be seen as a rescaling of the M-factor. The M-factor and the FSR of the Vernier envelope plotted in figure 4.6 are based on equations 4.28 and 4.26, with the approximation of assuming λ_0^1 and λ_k^1 as the Vernier envelope peaks from figure 4.3 (1379.32 nm and 1481.52 nm, respectively).

The M-factor trends towards infinity as the detuning reduces, which is to say that the interferometric frequency of both interferometers approach each other. Simultaneously, the FSR of the Vernier envelope increases with the same trend, imposing a limitation regarding

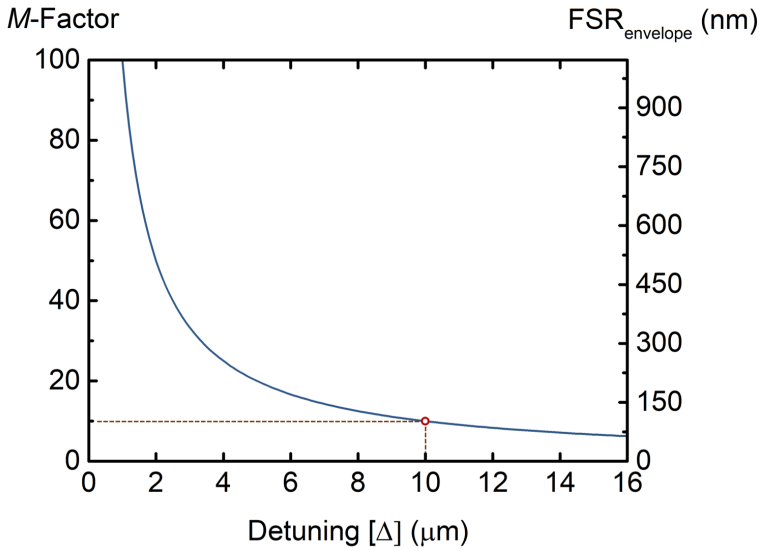

Figure 4.6. – M-factor and FSR of the Vernier envelope as a function of the detuning (Δ) of the reference interferometer (FPI_2) from the sensing interferometer (FPI_1). Based on equations 4.28 and 4.26, where λ_0^1 and λ_k^1 were assumed as the Vernier envelope peaks from figure 4.3 (1379.32 nm and 1481.52 nm, respectively).

the maximum magnification achievable. In practical applications, the maximum M-factor is limited by the FSR of the Vernier envelope, where one period should stay within the wavelength range available from the detection system. The M-factor is infinite when no detuning is considered, translating in a Vernier envelope with an infinite FSR. Hence, it corresponds to an impractical situation where the Vernier envelope cannot be tracked and measured. Both interferometers would have the same interferometric frequency and the spectral responses would add up. With this in mind, one has to deliberately apply, in a controlled way, a detuning to the reference interferometer OPL. To maximize the enhancement provided by the optical Vernier effect, one should target high M-factor values which are below the maximum size of the Vernier envelope measurable.

The simulated reflected spectrum for the fundamental Vernier effect, presented previously in figure 4.3, corresponds to a detuning of 10 μm, as marked in figure 4.6. For this situation, the expected M-factor is 10. To estimate the wavelength shift of the Vernier envelope, the OPL of the sensing interferometer (FPI_1) was increased from 100 μm to 100.2 μm, simulating the effect of a measurand (ex. applied strain). Figure 4.7 shows the simulated reflected spectra before and after the sensing interferometer hypothetically suffers from the effect of a measurand. The minimum of the Vernier envelope, marked with an arrow, was measured to estimate the envelope wavelength shift. The Vernier envelope shifted by 27.62 nm. Considering the shift in the sensing interferometer OPL (0.2 μm), the simulated sensitivity of the Vernier envelope ($S_{envelope}$) is 138.1 nm/μm.

To verify the expected M-factor value through equation 4.29, the wavelength shift of the

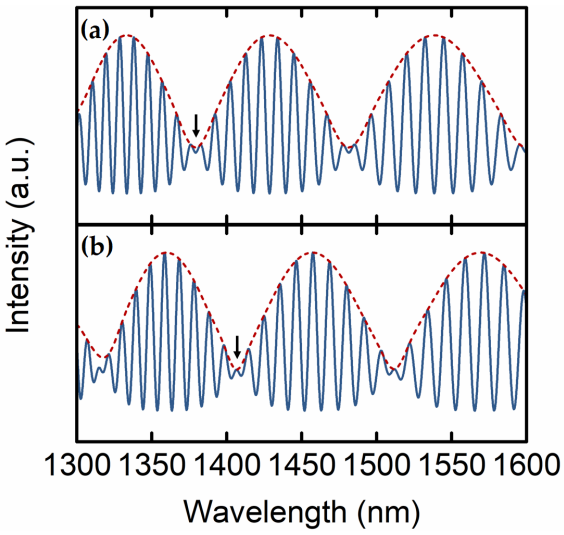

Figure 4.7. – Simulated reflected spectrum with the fundamental Vernier effect. (a) Initial situation: $OPL_1 = 100\,\mu m$ (figure 4.3). (b) Final situation: $OPL_1 = 100.2\,\mu m$. The Vernier envelope shifted by 27.62 nm.

individual sensing FPI, for the same situation, needs to be determined. The output electric field of the sensing FPI alone is expressed by equation 4.4. The output light intensity is obtained by replacing the previous expression in equation 4.11. With this, the intensity spectrum of the sensing FPI is given by:

$$I_{FPI1}(\lambda) = A^2 + B^2 - 2AB\cos\left(\frac{4\pi n_1 L_1}{\lambda}\right), \tag{4.31}$$

which is the traditional two-wave interferometric response. The simulated individual sensing FPI spectrum, described by equation 4.31, is shown in figure 4.8(a). The same parameters as in the simulated Vernier spectrum were used. After applying the same OPL change (0.2 μm) due to a measurand (dashed line), the individual sensing FPI shifted by 2.89 nm. This corresponds to a simulated sensitivity of 14.45 nm/μm for the individual sensing FPI (S_{FPI1}). Hence, through equation 4.29, the M-factor obtained is 9.56, which is close to the expected value of 10. The small deviation might come from equation 4.28 used to calculate the M-factor, which is an approximation of the equation 4.27. Another deviation factor is the wavelength dependency of the wavelength shift: regions of the spectrum at longer wavelengths shift more than at shorter wavelengths.

It is vital to understand that the sensitivity S_{FPI1} in equation 4.29, used to determine the M-factor, is the sensitivity of the individual sensing interferometer, as given in figure 4.8(a). It is incorrect to use the sensitivity of the two-wave interferometric response within the Vernier spectrum, as shown in figure 4.3, to calculate the M-factor. Although they might seem similar, their response is distinct. To prove this difference, figure 4.8(b) shows a zoom of the simulated reflected spectra with the optical Vernier effect from figure 4.7.

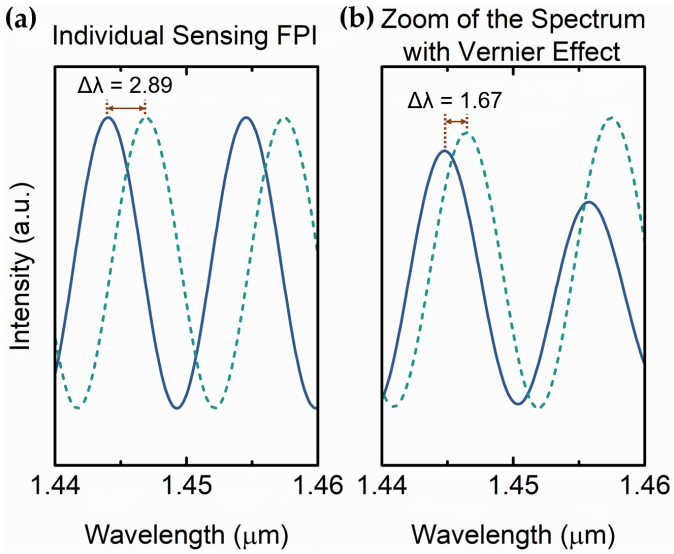

Figure 4.8. – (a) Simulated shift of the individual sensing FPI. (b) Zoom of the Vernier spectrum from figure 4.7.

The two-wave interferometric response with the Vernier effect shifted by 1.67 nm under the same conditions, which is very different from the sensing FPI response alone (2.89 nm). If this value is used to calculate the M-factor, one obtains 16.54, which is much larger than its real value determined before. In fact, one should not forget that the response of the stable reference FPI is also part of the Vernier spectrum, and so it is responsible for the reduction of sensitivity of the interferometric peaks.

The M-factor can also be calculated through equation 4.27. The FSR of the envelope, from figure 4.3, is 102.2 nm, while the FSR of the individual sensing FPI, from figure 4.8(a), is 10.5 nm. Therefore, the M-factor calculated through the FSRs is estimated to be around 9.73, which is of the same order as the one estimated through the sensitivity values (9.56). The estimated value might also present some deviations from the real M-factor value since the FSR is wavelength dependent. The distance between consecutive interferometric maxima (or minima) increases for longer wavelengths.

4.2.3. Series vs Parallel Configuration

The mathematical description of the fundamental optical Vernier effect presented before was based on the parallel configuration. This configuration allows both interferometers to be physically separated, making it easier to have one as a stable reference. A similar mathematical description can also be deduced for a configuration in series, where both interferometers are place one after the other in the same fiber. Since in this configuration the placement of the interferometers is different (see figure 4.9 for a better understanding), the output reflected spectrum would also be slightly different, as it will be demonstrated

in chapter 5. However, the magnification properties of the fundamental optical Vernier effect are the same.

The configuration in series implies, most of the times, that both interferometer are physically connected in the sense of having one interferometer placed after the other, sharing the same interface. In exceptional situations it is possible to place both interferometers away from each other along the same fiber. However, it compromises the visibility of the interference, since the amount of light reaching the interferometer that is further away from the light source is much smaller. If both interferometers are physically connected, it is extremely difficult to keep one as a stable reference. In general, both interferometers are affected by the measurands at the same time, and so they must be considered as a combined sensing structure. In this combined structure, there is no specific interferometer as a reference, unlike in a parallel configuration. Although equation 4.29 describes correctly the M-factor for the situations described until now, it is no longer valid when both interferometers act as sensors. One expects then that the sensitivity of the Vernier envelope will depend on both interferometers. Such complex case of optical Vernier effect will be analyzed later in chapter 6.

A way to avoid the inexistence of a reference interferometer in a series configuration is to use distinct interferometric structures, where one of the interferometers is insensitive to the measurand. For example, if one interferometer is sensitive to pressure but the second interferometer is designed to be insensitive to the same parameter, it can act as a reference interferometer.

Nevertheless, the fundamental optical Vernier effect in a series configuration was the first to be employed in optical fiber sensing [157–159]. Only later, in 2019, the parallel configuration by means of an optical fiber coupler was demonstrated [160, 161].

4.3. State-of-the-Art Applications and Configurations

In the last 2 to 3 years, the fundamental optical Vernier effect became a hot topic in the field of optical fiber sensing. Many distinct optical fiber interferometers were combined with this technique to create sensing devices with enhanced sensitivity capabilities. This section presents an overview on the state-of-the-art configurations and applications using the fundamental optical Vernier effect. The configurations used to generate the optical Vernier effect are divided in two main groups. The first group consists of configurations containing a single-type of interferometer. The second group is made of hybrid configurations, where two different types of interferometers are combined together. The configurations are presented here without a chronological order.

4.3.1. Single-Type Fiber Configurations

Fabry-Perot Interferometers

The use of Fabry-Perot interferometers (FPIs) to generate the optical Vernier effect is quite popular. In fact, almost half of the publications in this topic only make use of this type of interferometers. Figure 4.9 shows the typical configurations used to generate the optical Vernier effect with FPIs. One possibility is to assemble two FPIs in a parallel configuration, schematized in figure 4.9(a), by means of a 50/50 fiber coupler. Another is to place both FPIs in series, as exemplified in figure 4.9(b), either physically connected or physically separated.

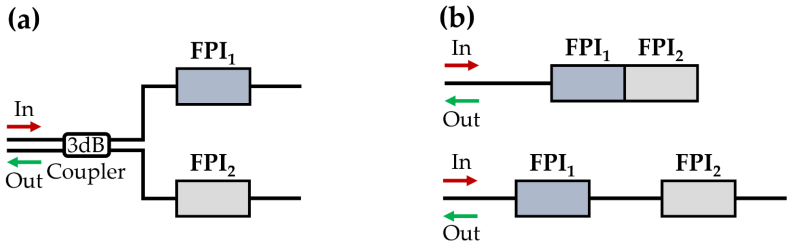

Figure 4.9. – Fabry-Perot interferometer configuration: (a) in parallel; (b) in series (physically connected or separated).

One of the first works employing the optical Vernier effect for optical fiber sensing was reported by Hu *et al.* [159]. In 2012, they proposed a sensing structure composed of two FPIs physically connected in a series configuration, as represented in figure 4.9(b). The first FPI was given by a section of simplified hollow-core fiber (HCF), while the second FPI was a hollow silica microsphere, forming also the tip of the sensing structure. The authors observed a low frequency envelope modulation in the measured reflected spectrum. Interestingly, at that time the authors were not aware of, or familiarized with, the optical Vernier effect. Hence, they did not identify the obtained low frequency envelope as being the Vernier envelope. The proposed sensor was characterized in temperature between 100 °C and 1000 °C. The work reported a temperature sensitivity of 17.064 pm/°C for the low frequency envelope. Such value is much higher than the one obtained for an individual interferometric peak in the reflection spectrum, which achieved only 1.349 pm/°C. Today, we know that the cause of the higher sensitivity reached by the low frequency component is the optical Vernier effect.

Two years later, Zhang *et al.* demonstrated the optical Vernier effect with FPIs in series, but physically separated [158]. In this case, both interferometers are made of hollow-core photonic crystal fiber (HC-PCF), separated by a section of single-mode fiber. In this configuration, represented in figure 4.9(b), one FPI is employed for sensing while the other is taken as a stable reference. The sensing structure was proposed for axial strain and magnetic field sensing. The Vernier envelope achieved a strain sensitivity of 47.14 pm/$\mu\varepsilon$

from 0 to 200 $\mu\varepsilon$, corresponding to an M-factor of 29.5. For magnetic field sensing, the Vernier envelope achieved 71.57 pm/Oe from 20 to 35 Oe, corresponding to an M-factor of 28.6. For many researchers this work is seen as the first report of optical Vernier effect in the field of optical fiber sensing.

An extended concept of the optical Vernier effect using physically connected FPIs in a series configuration, without a reference interferometer, to be presented later in chapter 6, was reported in 2020 [19]. The structure consists of a hollow microsphere followed by a section of a multimode fiber and was applied for strain and temperature sensing. The Vernier envelope achieved a strain sensitivity of 146.3 pm/$\mu\varepsilon$ from 0 to around 500 $\mu\varepsilon$, and a temperature sensitivity of 650 pm/°C from room temperature up to 100 °C. Simultaneous measurement of strain and temperature was also demonstrated with this structure.

The series configuration with physically separated FPIs seemed very promising, however it has only been used again since 2018 [149, 150, 162–165]. Until then, few works were published using the series configuration with the interferometers physically connected to each other [148, 166, 167]. Nevertheless, from the optical Vernier effect configurations using only FPIs, the case of two FPIs physically connected in series was the most studied, corresponding to almost half of the publications within this group [148, 166–176].

The parallel configuration using FPIs was only proposed in 2019, initially by Yao *et al.* [160]. In their publication, a sensing FPI and a reference FPI are physically separated by means of a 50/50 fiber coupler, just as schematized in figure 4.9(a). The sensing interferometer is open, enabling it to be filled by liquids for refractive index sensing. In such case, the Vernier envelope achieved a sensitivity of 30801.53 nm/RIU between 1.33347 and 1.33733 RIU. The authors reported an M-factor of 33. Followed by this publication, a few more works were published using the parallel configuration [161, 177–180]. The main advantage of such configuration is the possibility of having a reference interferometer without compromising the visibility. The case of two FPIs physically separated in a series configuration, shown in figure 4.9(b), may lead to visibility issues due to the presence of an additional interface. In other words, the amount of light reaching the second FPI is much lower than in the case of two FPI physically connected, or for a parallel configuration as in figure 4.9(a).

The focused ion beam-structured multimode fiber tip presented in the previous chapter was published in 2019 [21] and corresponds to a special case of FPIs in parallel. It consists of a single cavity, where multiple FPI responses are generated due to the different modes co-propagating the cavity at the same time. The structure was reported for temperature sensing, achieving a sensitivity of -654 pm/°C between 30 °C and 120 °C. An extended concept of the optical Vernier effect in a parallel configuration using FPIs, to be presented later in chapter 6, was also reported in 2019 [20] for strain sensing. A maximum strain sensitivity of 93.4 pm/$\mu\varepsilon$, from 0 to 600 $\mu\varepsilon$, was obtained for the Vernier envelope, corresponding to an M-factor of 27.7. Such sensing structure only relies on FPIs made from

hollow capillary tubes.

In terms of applications, the configurations using FPIs were mainly used for temperature [148, 150, 159, 168, 170, 174, 176, 177, 179, 181] and strain sensing [158, 161, 163–165]. Apart from these two applications, others such as magnetic field sensing [158], gas refractive index [166, 171] and pressure sensing [162, 169], airflow sensing [167], hydrogen sensing [149], humidity sensing [175], volatile organic compounds sensing [173], and refractive index sensing of liquids [160] were also reported. Simultaneous measurement of parameters is also possible, combining the response of the Vernier envelope with the individual interferometric peaks from the reflection spectrum. Examples of this are simultaneous measurement of refractive index of liquids and temperature [172], or simultaneous measurement of salinity and temperature [178].

Mach-Zehnder Interferometers

The different configurations involving only Mach-Zehnder interferometers (MZIs) and the optical Vernier effect are depicted in figure 4.10. To the best of my knowledge, the first demonstration of optical Vernier effect with MZIs was done by Liao *et al.* in 2017 [182]. In their work, the principle of operation was deduced based on two MZIs connected in series, as described by figure 4.10(a). Each MZI is a traditional two-path interferometer, where light is split between two arms with different optical path lengths, recombining and interfering at the end due to the accumulated phase difference. Liao *et al.* proposed a modified version of the optical Vernier effect, where the envelope is extracted in the frequency domain, rather than performing the typical curve fitting methods in the wavelength domain to extract the envelope. Their method involves extracting the frequency component correspondent to the Vernier envelope and then applying an inverse fast Fourier transform

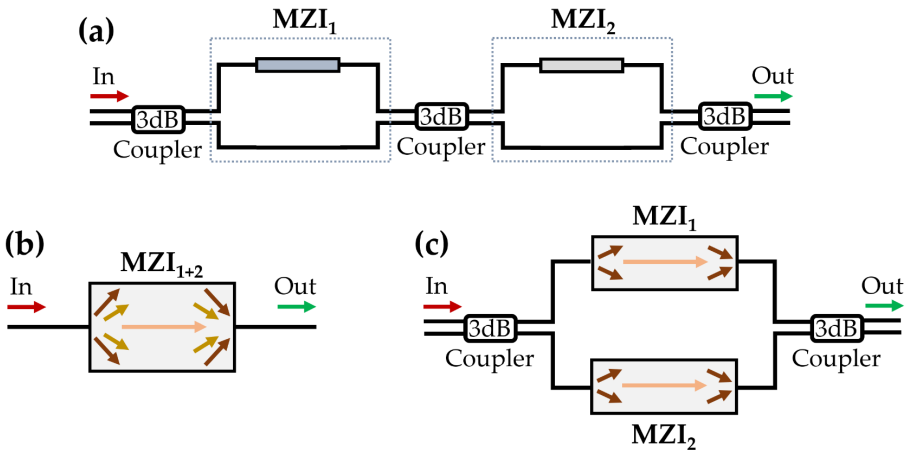

Figure 4.10. – (a) Mach-Zehnder interferometers in series. Mach-Zehnder interferometers in parallel: (b) within the same fiber, or (c) physically separated.

(IFFT). Experimentally, the authors used an offset spliced single-mode fiber to create each MZI. Keeping one interferometer as a reference, the structure was demonstrated for temperature and curvature sensing. For temperature sensing, the Vernier envelope achieved a sensitivity of 397.36 pm/°C, with an M-factor of 8.8. With regard to curvature sensing, the sensitivity of the Vernier envelope was -36.26 nm/m^{-1}, with an M-factor of 8.0.

Instead of offset spliced fibers, the MZIs can also be fabricated by other means [183,184]. For example, Lin *et al.* used a multimode fiber (MMF), with a femtosecond laser machined air cavity, between single-mode fibers [185], and Zhao *et al.* spliced hollow core fibers between MMFs [186].

In 2018, a new type of configuration was introduced. Such configuration, represented in figure 4.10(b), is composed of two integrated MZIs in a parallel configuration. Lin *et al.* used a dual side-hole fiber (DSHF) spliced between two pieces of MMF to form the structure [187]. Light travels through the core of the dual side-hole fiber and simultaneously through the two side holes. In their work, the authors opened an access to one of the air holes, allowing to measure gas pressure with a sensitivity of -60 nm/MPa, between 0 and 0.8 MPa. The structure achieved an M-factor of 7. The same type of configuration was demonstrated in a different way by Ni *et al.*, by means of a single hole twin eccentric cores fiber (SHTECF) spliced between two single-mode fibers [188]. In each splice position the fiber was collapsed. In this case, the authors used the structure for temperature sensing, obtaining a sensitivity of 2.057 nm/°C for the Vernier envelope, corresponding to an M-factor of 48.8. In 2019, this configuration was also demonstrated by Hu *et al.*, where the integrated MZI structure consisted of an offset spliced side-hole fiber (SHF) between two coreless fibers [189]. The authors applied the proposed sensor for refractive index sensing, reporting a Vernier envelope sensitivity of 44084 nm/RIU from 1.33288 to 1.33311. In this work, the M-factor achieved was only 3.1.

At last, the parallel configuration using separated MZIs, as represented in figure 4.10(c) was proposed by Wang *et al.*, in 2019 [190]. In their work, each MZI consists of a simple hollow core fiber spliced between two MMFs. The parallel configuration is achieved by connecting two MZIs using two 50/50 fiber couplers. The authors used the structure for temperature sensing, achieving a sensitivity of 528.5 pm/°C, between 0 °C and 100 °C. An M-factor of 17.5 was also reported.

Sagnac Interferometers

An optical fiber Sagnac interferometer (SI) consists of an optical fiber ring, assembled using a 50/50 fiber coupler, in which two beams are propagating in counter directions with different polarization states [1]. In fiber sensing, a section of polarization maintaining fiber (PMF) is typically placed inside the optical fiber ring, providing different propagating constants along the slow and fast axis. The output signal is given by the interference

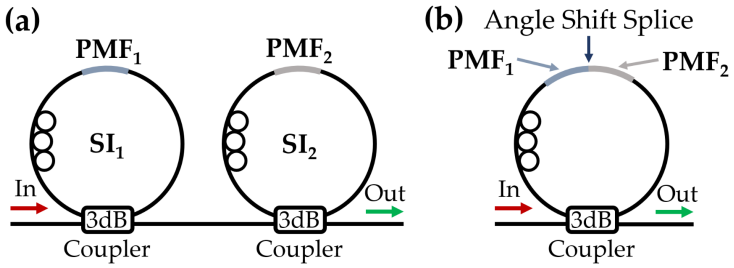

Figure 4.11. – (a) Sagnac interferometers in series. (b) Single Sagnac interferometer with two polarization maintaining fibers (PMFs) spliced with an angle shift between their fast axes.

between the light beams polarized along the slow axis and the fast axis. Since the polarization state of the input light is unknown, a polarization controller (PC) is also placed in the beginning of the optical fiber ring to adjust the light polarization until the output interference pattern has maximum visibility.

Until 2018, Sagnac interferometers were only considered with the optical Vernier effect in a series configuration. The structure consists of two fiber rings with a section of PMF in each of them, as shown in figure 4.11(a). The two PMFs act in a similar way as the two interferometers needed to form the optical Vernier effect. Hence, given the birefringence of the PMFs, the optical Vernier effect can be optimized by adjusting the lengths of the PMFs.

Shao *et al.* used a section of a PANDA fiber in both Sagnac interferometers [191]. In their work, the structure was studied for temperature sensing, while keeping one of the Sagnac interferometers as a stable reference. The authors reported a Vernier envelope sensitivity of -13.36 nm/°C, achieving an M-factor of around 9.2. Three years later, Wang *et al.* reported a similar configuration [192]. However, one of the Sagnac interferometers incorporates a graphene oxide-coated microfiber, while the second contains a PANDA fiber. The presence of the coating makes the microfiber highly birefingent. The authors used the sensor for refractive index sensing of liquids, achieving a sensitivity of 2429 nm/RIU, corresponding to an M-factor of 5.4. The same structure was also demonstrated as a biosensor of bovine serum albumin.

These last configurations combine the high sensitivity achieved by high-birefringent (Hi-Bi) fibers together with the optical Vernier effect. Nevertheless, similar configurations using only optical fiber rings without any PMF were also demonstrated for temperature [193] and strain sensing [194].

In 2018, an alternative compact version to generate the optical Vernier effect with Sagnac interferometers was demonstrated. This new configuration, reported by Wu *et al.* [195], only requires a single Sagnac interferometer ring, as shown in figure 4.11(b), which contains two PMFs spliced with an angle shift between their fast axes. In their work, the authors spliced the two PMFs with a 40^{o} angle shift. One of the PMFs was coated with Pt-

load WO_3/SiO_2 powder, which heats up under the presence of hydrogen. The authors reported a temperature sensitivity of -2.44 nm/°C for the Vernier envelope. The structure was also applied for hydrogen sensing, achieving a sensitivity of -14.61 nm/% between 0 and 0.8% of hydrogen. Liu *et al.* used the same configuration with two sections of PANDA fiber, spliced with an angle of 45º between their fast axes [196]. The authors used the structure for strain and temperature sensing. The Vernier envelope attained a strain sensitivity of 58 pm/$\mu\varepsilon$ from 0 to 1440 $\mu\varepsilon$, achieving an M-factor of 9.8. As for temperature sensing, the Vernier envelope had a sensitivity of -1.05 nm/°C between 20 °C and 80 °C. The authors also reported simultaneous measurement of strain and temperature using a matrix method. For a completely different application, Wu *et al.* employed the same configuration for isopropanol measurement [197]. One of the PMFs was coated with polypyrrole polymer, which swells in the presence of isopropanol, inducing strain in the fiber. The authors reported a sensitivity of 239 pm/ppm of isopropanol for the Vernier envelope, between 0 and 42 ppm, corresponding to an M-factor of 4.2.

Michelson Interferometers

Similarly to Mach-Zehnder interferometers, the Michelson interferometer consists of the interference between light propagating in two arms. However, in the Michelson interferometer the propagating light is reflected at the end of each arm [1]. In 2019, Zhang *et al.* demonstrated the generation of the optical Vernier effect using two juxtaposed fiber Michelson interferometers [5]. In their configuration, the structure is made of a triple-core fiber (TCF) spliced to a dual-side-hole fiber, as shown in the schematic of figure 4.12. The triple-core fiber was tapered down, allowing the input light to split between the other cores. The output signal is given by the interference between the light propagating in the central core and the light propagating in the side cores, where both present slightly different refractive indices. The authors proposed such structure for curvature sensing, achieving a sensitivity of -57 nm/m^{-1} between 0 and 1.14 m^{-1} for the Vernier envelope. The same sensor was also characterized in temperature, where the Vernier envelope obtained a sensitivity of 143 pm/°C between 30 °C and 100 °C.

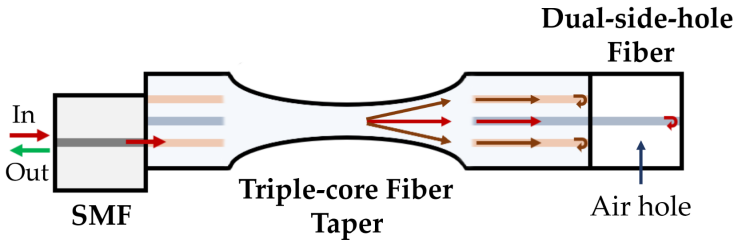

Figure 4.12. – Michelson interferometers in parallel. The structure consists of a tapered triple-core fiber spliced to a dual-side-hole fiber. Adapted from [5].

Later in that year, the same group proposed a similar device for bending sensing [198]. Instead of a triple-core fiber, now the authors used a double-core fiber (DCF) spliced to the dual-side-hole fiber with a slight offset. This offset allows the light traveling in the central core of the double-core fiber to split between the core and the cladding of the dual-side-hole fiber. With that structure, the authors achieved a bending sensitivity of $38.53\,\mathrm{nm/m^{-1}}$ from 0 to $1.24\,\mathrm{m^{-1}}$ for the Vernier envelope. Regarding temperature, the Vernier envelope reached a sensitivity of $67.2\,\mathrm{pm/°C}$ between 50 °C and 130 °C.

Fiber Coupler Interferometers

A novel way to generate the optical Vernier effect was proposed in 2018 by Li *et al.* [199]. They have shown the possibility of accomplishing the optical Vernier effect using an optical microfiber coupler, as depicted in figure 4.13(a). The trick is to make the optical microfiber coupler highly birefringent, causing mode interference between the x and y-polarizations. The authors applied the sensor to measure refractive index variations, obtaining a sensitivity of 35823.3 nm/RIU for the Vernier envelope, at a refractive index around 1.333 RIU. The proof-of-concept of label-free biosensing of human cardiac troponin was also demonstrated with the same proposed structure. This was achieved through functionalization of the optical microfiber coupler with the specific antibody. The sensor achieved a limit of detection of 1 ng/ml of human cardiac troponin.

Similarly, Chen *et al.* developed a double helix microfiber coupler, which is highly birefringent, producing the optical Vernier effect [200]. The authors also used the device to sense variations of refractive index. They reported a Vernier envelope sensitivity of 27326.59 nm/RIU between 1.3333 and 1.3394, achieving an M-factor of around 5.3.

Recently in 2020, Jiang *et al.* have discussed the possibility of generating the optical

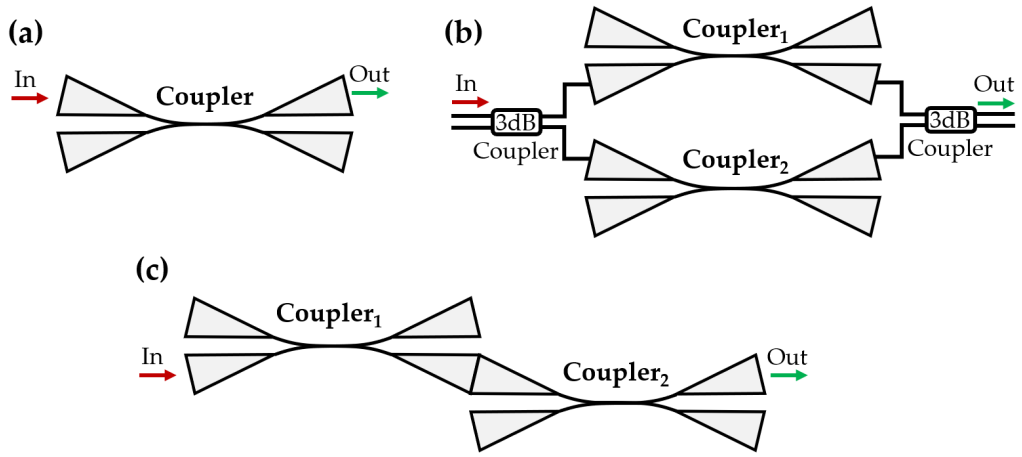

Figure 4.13. – (a) Microfiber coupler with birefringence. (b) Microfiber couplers in parallel. (c) Microfiber couplers in series.

Vernier effect with two optical microfiber couplers in a parallel configuration, as shown in the schematic of figure 4.13(b), or in a series configuration, as in figure 4.13(c). The authors demonstrated ultra-high sensitivity to refractive index with the parallel configuration. The Vernier envelope reached a sensitivity of 114620 nm/RIU between 1.3350 and 1.3355, corresponding to an M-factor of 19.7. Moreover, the Vernier envelope also achieved a sensitivity of 126540 nm/RIU in a refractive range between 1.3450 and 1.3455, corresponding to an M-factor of 21.7.

Microfiber Knot Resonators

The combination of microfiber knot resonators (MKRs) and the optical Vernier effect was proposed by Xu *et al.* in 2015 [6]. In their work, two microfiber knot resonators were fabricated and assembled in series, as depicted in the schematic of figure 4.14. The radius of both microfiber knot resonators is slightly different, achieving therefore slightly different resonant frequencies. One of the microfiber knot resonators was taken as a stable reference, while the other was used for refractive index sensing of liquids. The authors demonstrated a Vernier envelope sensitivity of 6523 nm/RIU between 1.3315 and 1.3349. A refractive resolution of 1.533×10^{-7} RIU was also reported.

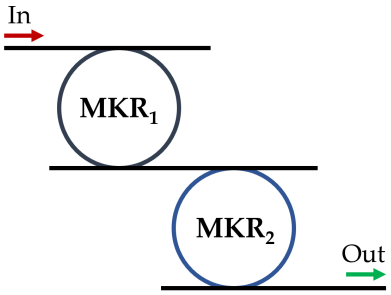

Figure 4.14. – Microfiber knot resonators in series. Adapted from [6].

4.3.2. Hybrid Fiber Configurations

Fabry-Perot Interferometer with Mach-Zehnder Interferometer

The combination between a Fabry-Perot interferometer and a Mach-Zehnder interferometer was introduced by Ying *et al.* in 2019 [201]. In their publication, the authors make use of the Mach-Zehnder interferometer as a tool to demodulate the Fabry-Perot interferometric response, through the optical Vernier effect. Figure 4.15 presents a schematic of the proposed configuration, where a Mach-Zehnder interferometer is incorporated in the structure, right before the signal reaches the output. The Fabry-Perot interferometer consisted of a hollow-core fiber spliced between two single-mode fibers, while the Mach-Zehnder interferometer is a traditional configuration of two 50/50 fiber couplers and different arm

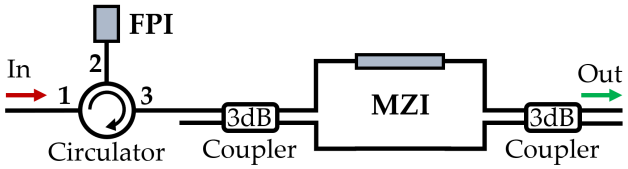

Figure 4.15. – Combination of a Fabry-Perot interferometer in series with a Mach-Zehnder interferometer.

lengths. The optical path difference between the two arms of the Mach-Zehnder interferometer needs to be adjusted to match closely the optical path length of the Fabry-Perot interferometer. The authors proposed the structure for temperature sensing, being the Fabry-Perot interferometer the sensor and the Mach-Zehnder interferometer the reference. A temperature sensitivity of -107.2 pm/°C between 30 °C and 80 °C was reported for the Vernier envelope. According to the authors, the sensor achieved a high M-factor of 89.3.

One year later, Li *et al.* proposed a similar configuration, where the Fabry-Perot and the Mach-Zehnder interferometers are composed of a single-mode fiber spliced between two other similar fibers, but with a core-offset [202]. The core offset of the central fiber is large (80 μm) for the Fabry-Perot interferometer, creating an open air cavity. As for the Mach-Zehnder interferometer, the central fiber core offset is slightly smaller (62.5 μm) so that light travels through air and also through the cladding of the central fiber, forming the two arms of the interferometer. In their work, the authors presented and demonstrated an optimized version of the complex case of optical Vernier effect, where both interferometers act as sensors. They have shown that the Vernier envelope sensitivity can be further improved by using two interferometers with opposite wavelength shift responses, which the authors called enhanced Vernier effect. Such effect will be further discussed in chapter 6. The authors reported a refractive index sensitivity of -87261.06 nm/RIU for the Vernier envelope between 1.332 and 1.334. The temperature response was also evaluated, obtaining a sensitivity of 204.7 pm/°C for the Vernier envelope between 30 °C and 130 °C.

Sagnac Interferometer with Fabry-Perot Interferometer

Fabry-Perot interferometers were also combined with fiber Sagnac interferometers in a hybrid configuration to generate the optical Vernier effect. In 2019, Zhou *et al.* explored a configuration similar to the one represented in figure 4.16(a), where a Fabry-Perot interferometer is introduced before a Sagnac interferometer, without an optical circulator [203]. However, the Fabry-Perot interferometer is not made out of an optical fiber structure, but rather by two collimators and a quartz wave plate coated with reflective coating on both ends, acting as the reference interferometer. The Sagnac interferometer is made of optical fiber and contains a section of a PANDA fiber. Temperature sensing was performed by changing the temperature from 23 °C to 25 °C around the Sagnac interferometer. The

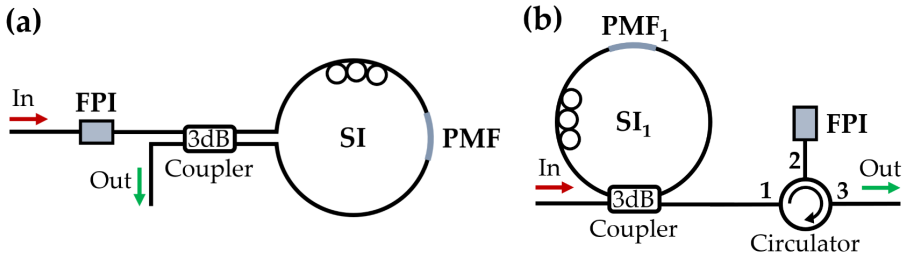

Figure 4.16. – Combination of a Fabry-Perot interferometer in series with a Sagnac interferometer. (a) Fabry-Perot interferometer used in transmission. (b) Fabry-Perot interferometer applied in reflection.

authors reported a sensitivity of 10.28 nm/°C for the Vernier envelope, corresponding to an M-factor of 6.0.

A similar hybrid configuration can also be realized using an optical circulator to embed the response of the Fabry-Perot interferometer in reflection, as shown in figure 4.16(b). Such configuration was initially reported by Yang *et al.* in 2017 [204]. The Sagnac interferometer contains a section of a PANDA fiber and the Fabry-Perot interferometer consists of a silica capillary tube between two single-mode fibers. The structure was demonstrated for temperature sensing. The authors placed both sensors inside a furnace, changing the temperature of both simultaneously. As discussed before, this is a complex case of the optical Vernier effect, where no reference interferometer is used. However in the authors approach, the Fabry-Perot interferometer has much lower temperature sensitivity compared with the Sagnac interferometer. Hence, within the short temperature range used (between 42 °C and 44 °C), the temperature effect on the Fabry-Perot interferometer can be negligible. The authors reported a temperature sensitivity of -29.0 nm/°C for the Vernier envelope, achieving an M-factor of around 20.7.

Two years later, Wang *et al.* demonstrated an equivalent configuration for acoustic sensing [205]. The Sagnac interferometer contains a section of a dual-core photonic crystal fiber and acts as the reference interferometer. The Fabry-Perot interferometer is tunable and contains a polymer film that slightly deforms when vibrations occur. The authors reported a maximum sound pressure sensitivity of 37.1 nm/Pa between 62.2 dB and 92.4 dB, for the Vernier envelope.

Microfiber Knot Resonator with Fabry-Perot Interferometer

Xu *et al.* developed in 2017 a θ-shaped microfiber knot resonator combined with a Fabry-Perot interferometer to generate the optical Vernier effect with tunable properties [7]. The structure is monitored in a reflection configuration, where the microfiber knot resonator is connected to the Fabry-Perot interferometer with a 50/50 fiber coupler, as seen in figure 4.17. The Fabry-Perot interferometer is a commercially available device and the θ-shaped

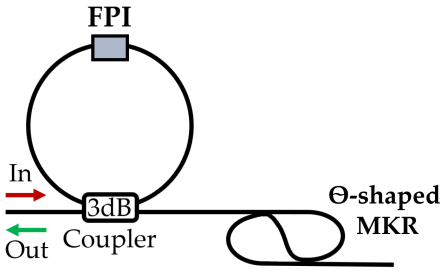

Figure 4.17. – Combination of a Fabry-Perot interferometer in series with a θ-shaped microfiber knot resonator. Adapted from [7].

microfiber knot resonator was fabricated with optical microfibers.

The authors demonstrated the possibility of tuning the magnification factor obtained through the optical Vernier effect by simply changing the diameter of the microfiber knot resonator. This way, the final sensitivity of the Vernier envelope can be adjusted depending on the applications. In their work, the structure was used to sense refractive index variations around the θ-shaped microfiber knot resonator, obtaining a sensitivity that can be tuned from 311.77 nm/RIU to around 2460.07 nm/RIU, corresponding to an M-factor changing from 12 to around 73.

Sagnac Interferometer with Mach-Zehnder Interferometer

In 2019, Liu *et al.* demonstrated the optical Vernier effect generated through the combination of a Sagnac interferometer with a Mach-Zehnder interferometer [8] in a series configuration, described by figure 4.18. The Sagnac interferometer contained a section of a PANDA fiber and acted as the reference interferometer. The Mach-Zehnder interferometer is made of a section of a few-mode fiber (FMF) spliced between two single-mode fibers, with a slight core-offset at the input to excite more than just the fundamental mode. Therefore, the Mach-Zehnder interferometer can be seen as a modal interferometer. The response of the sensor to strain was studied by the authors, obtaining a sensitivity of

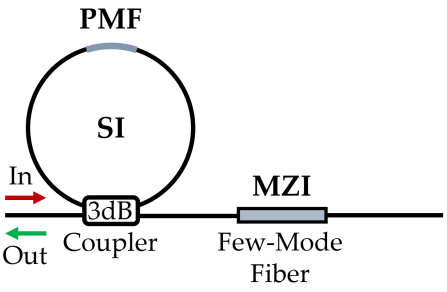

Figure 4.18. – Combination of a Sagnac interferometer with a Mach-Zehnder interferometer. Adapted from [8].

65.71 pm/$\mu\varepsilon$ between 0 and 300 $\mu\varepsilon$ for the Vernier envelope. The authors reported an M-factor of 20.8.

4.4. Conclusion

This chapter presented the concept of the fundamental optical Vernier effect with optical fiber interferometers, especially dedicated to optical fiber sensing. The ability to magnify the wavelength shift of the Vernier envelope brings new opportunities to fabricate highly sensitive sensors, ultimately with higher resolution than the ones available with more conventional interferometers.

The optical Vernier effect can be generated with different types of interferometers. The configurations can involve just one type of interferometer or combine different types in a hybrid structure, together with additional advantages. A summary of the sensitivities and M-factors for the different configurations reported in literature can be found in tables B.1 and B.2 for single-type configurations involving Fabry-Perot interferometers, and in table B.3 for the rest of the single-type configurations and hybrid configurations, in appendix B. The M-factors reported range from values as low as 1.9 (coated Sagnac interferometer for hydrogen sensing [195]) to values of 89.3 (hybrid structure combining an FPI with an MZI for temperature sensing [201]). Single-type configurations using FPIs have typically M-factors between 10 and 30. Curiously, MZI configurations have, in general, lower M-factors, as well as configurations with Sagnac interferometer, with values normally below 10. Some publications do not provide the M-factor or enough data to estimate it. Nevertheless, one can see that the sensitivities obtained are higher than those normally obtained for such type of sensors, for instance, the ability of reaching a new order of magnitude in refractive index sensing (126540 nm/RIU [206]).

By tailoring the characteristics of the interferometers, the fundamental optical Vernier effect can be maximized to achieve high magnification factors. However, one needs to be careful and analyze, in each case, if such high magnification factors can be experimentally feasible, given the restrictions of the setup available. The higher the magnification factor achieved, the larger is the Vernier envelope. Therefore, there is a maximum size of the Vernier envelope for which the detection system is able to track and measure. This imposes a limit in the maximum magnification factor achievable with this effect.

However, the next chapter explores the introduction of harmonics to the optical Vernier effect, as an extension of the concept, bringing with it new properties and breaking the limits of the fundamental optical Vernier effect.

Chapter 5.

Optical Harmonic Vernier Effect

5.1. Introduction

The fundamental optical Vernier effect, as seen in the previous chapter, relies on the fabrication of two interferometers with a small detuning between their optical path lengths (OPLs) (i.e. slightly shifted interferometric frequencies). The interference signal produced by these two interferometers is employed like the two Vernier scales in a caliper. In this configuration, high magnification factors (M-factors) are only achieved if the OPLs of the two interferometers are really close. From a practical point of view, considering the current fabrication processes of fiber sensing structures, which is usually at sub-millimeter scale, this requirement can be challenging, and in certain situations unfeasible. Additionally, the Vernier envelope trends towards infinity, limiting the maximum M-factor achievable.

This chapter introduces the concept of optical harmonic Vernier effect, as an extension of

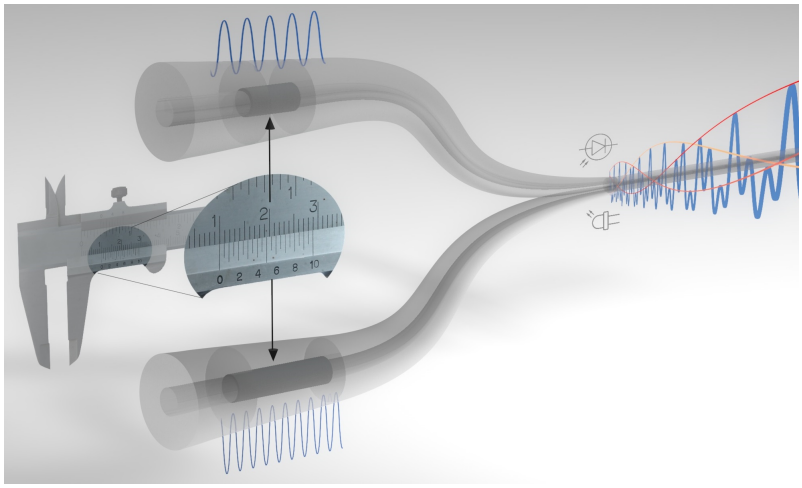

Figure 5.1. – Illustration of the optical harmonic Vernier effect. The novel concept of harmonics of the Vernier effect shows that it is, in fact, possible to use two interferometers with very different frequencies as the Vernier scale. The result is a complex harmonic response with enhanced magnification properties.

the fundamental case described before. The novel concept, illustrated in figure 5.1, reveals that it is possible to use two interferometers with very different OPLs. With this, a complex harmonic response is generated with enhanced sensing resolution and sensing magnification capabilities when compared to the fundamental case. This approach increases significantly the design possibilities of the sensors, with new ways of dimensioning and tailoring the interferometers to enhance the overall performance of the structure.

5.2. Mathematical Description

The following description still relies on the parallel configuration using two Fabry-Perot interferometers, as in the previous chapter. In a Fabry-Perot interferometer, the optical path length (OPL) is defined as:

$$OPL = 2nL, \tag{5.1}$$

where n and L are the effective refractive index and the length of the FPI, respectively. In a round-trip, light travels twice the length of the cavity, hence the presence of the factor 2 in the equation. The introduction of harmonics to the optical Vernier effect happens when the OPL of the reference interferometer (FPI_2) is increased by a multiple (i-times) of the OPL of the sensing interferometer (FPI_1). Mathematically, this relationship is described as [20]:

$$OPL_2 = 2n_2L_2 + 2in_1L_1, \tag{5.2}$$

where i indicates the harmonic order. The indices 1 and 2 refer to the sensing and reference interferometer, respectively. In the case of $i = 0$, the effect is reduced to the fundamental case presented in the previous chapter, indirectly seen by equation 4.14. The same relationship can also be expressed as a function of the detuning (Δ), defined previously in equation 4.30. The OPL of the reference interferometer can be seen as:

$$OPL_2 = 2\,(i+1)\,n_1L_1 - 2\Delta, \tag{5.3}$$

where twice the detuning corresponds to the optical path difference between the actual reference interferometer and the closer situation of a perfect harmonic case (where $OPL_2 = (i+1)\,OPL_1$). In other words, the detuning is defined as:

$$\Delta = n_1L_1 - n_2L_2 \tag{5.4}$$

An illustration of the relationship between the dimensions of the sensing and reference FPIs, for different optical harmonics of the Vernier effect, is presented in figure 5.2. For simplification, the refractive index of both interferometers was considered as 1 (air).

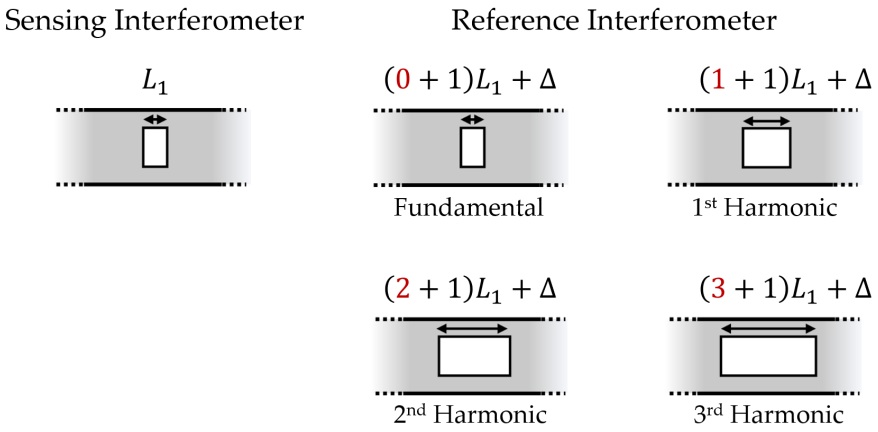

Figure 5.2. – Illustration of the reference FPI dimensioning for the fundamental optical Vernier effect and for the first three harmonic orders. The detuning (Δ) is the same in every situation.

The free spectral range (FSR) of the reference interferometer, depending on the harmonic order, is now redefined as:

$$FSR_2^i = \frac{\lambda_1\lambda_2}{2\left(n_2L_2 + in_1L_1\right)}, i = 0, 1, 2... \tag{5.5}$$

At this point, before introducing the properties of the optical harmonic Vernier effect, it is useful to visualize the appearance of the reflected spectrum for different harmonic orders. To do so, equation 5.2 must be replaced in equation 4.12. The obtained general equation for the output reflected light intensity as a function of the harmonic order (i) is defined as:

$$\begin{aligned} I_{out}\left(\lambda\right) = I_0 - 2AB\left\{\cos\left(\frac{4\pi n_1L_1}{\lambda}\right) + \cos\left[\frac{4\pi\left(n_2L_2 + in_1L_1\right)}{\lambda}\right]\right\} \\ + B^2\cos\left[\frac{4\pi\left(n_1L_1 - n_2L_2 - in_1L_1\right)}{\lambda}\right], \end{aligned} \tag{5.6}$$

where $I_0 = 2A^2 + B^2$.

Once more, the ideal case of no transmission losses related to mode mismatch and surface imperfections, and no propagation losses was considered. Using the intensity reflection coefficient for a silica/air interface calculated in equation 4.13, the coefficients A and B were assumed as 0.182 and 0.176, respectively. The refractive indices of the sensing and reference interferometers, n_1 and n_2, were considered as equal to 1 (air). A length of 41 μm was taken for the sensing interferometer, which is the same as in the experimental demonstration later shown in chapter 6. As for the reference interferometer, its length was considered as 32 μm plus multiples of the sensing interferometer length ($32\,\mu m + i \times 41\,\mu m$), depend-

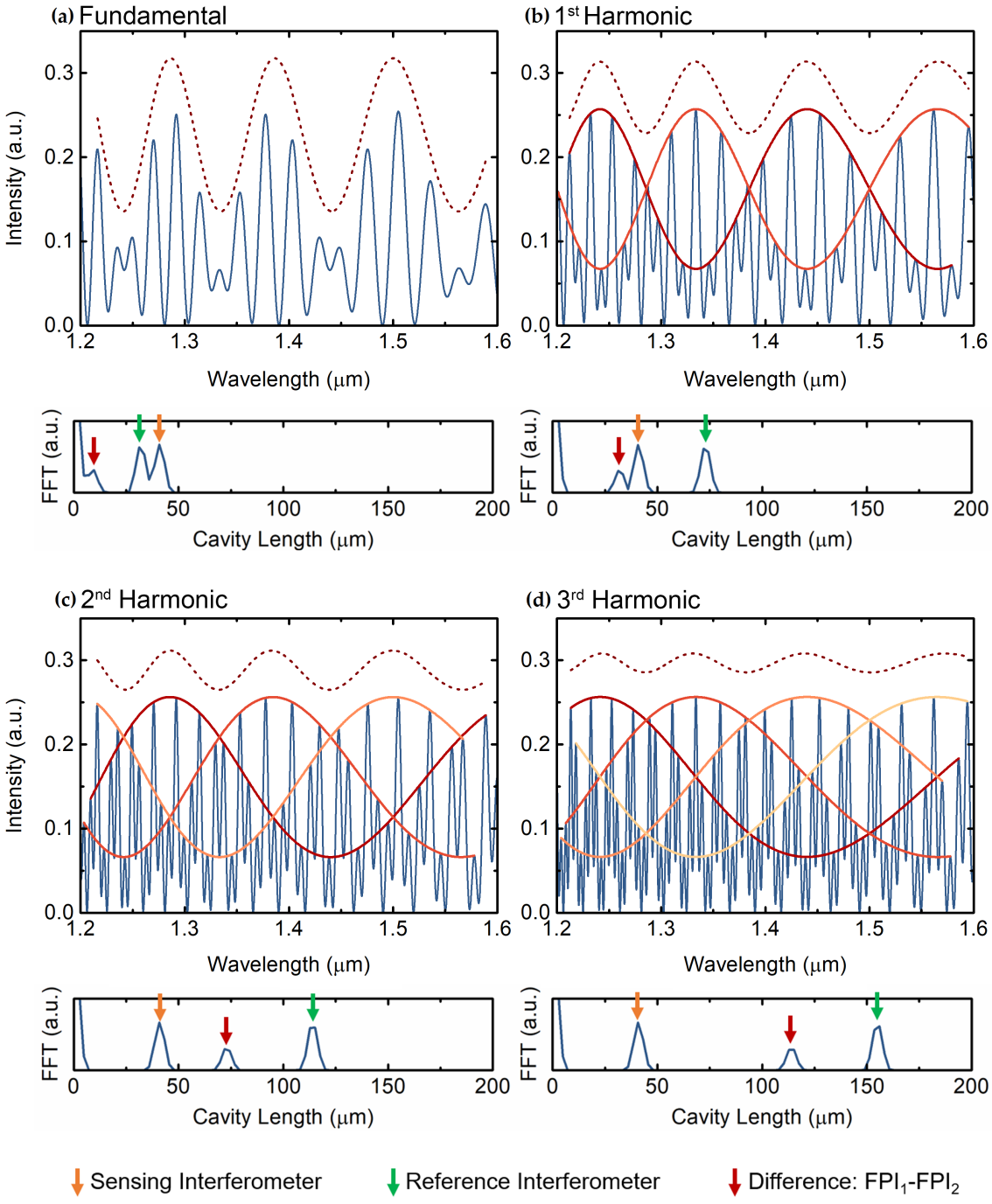

Figure 5.3. – Simulated output spectra described by equation 5.6 in four different situations and the corresponding fast Fourier transform (FFT): (a) fundamental optical Vernier effect; (b-d) first three harmonic orders. Dashed line: upper envelope (shifted upwards to be distinguishable). Red-orange lines: internal envelopes.

ing on the order of the harmonic. In other words, the reference interferometer is detuned by $9\,\mu$m from the perfect case of $(i+1) \times 41\,\mu m$. The simulated results are depicted in

figure 5.3(a) for the fundamental case corresponding to $i = 0$, and in figures 5.3(b-d) for the first three harmonic orders corresponding to $i = 1, 2, 3$, together with the fast Fourier transform (FFT) of the respective spectrum.

At first sight, the simulated spectra become more complex as the harmonic order increases. Naturally, as the reference interferometer OPL scales up, the reflected spectrum contains higher frequencies. The FFT was obtained from the reflected spectrum converted into the optical frequency domain, using the same method as in section 3.3.2. The FFTs in figure 5.3 are expressed as a function of the cavity length (L) of the interferometers, which is easier to interpret as one knows the values used in the simulations. The peak at 41 μm is constant along the different cases and corresponds to the sensing interferometer. As for the reference interferometer, the FFT shows the up scaling of its optical path length, which is directly proportional to the cavity length and also to the frequency of the interferometer.

5.2.1. Traditional Vernier Envelope (Upper Envelope)

The traditional Vernier envelope, marked in figure 5.3 with a dashed line, was shifted upwards to be distinguishable from the internal envelopes, marked with red-orange lines. The optical harmonics of the Vernier effect regenerate the upper Vernier envelope with the same frequency, and FSR, as in the fundamental case. Interestingly, one also observes a π-shift of the upper envelope for odd harmonic orders ($i = 1, 3, 5...$).

To obtain a more general expression for the FSR of the upper envelope, previously described by equation 4.24, let us first consider the hypothetical overlap between the responses of two FPIs. However, now the OPL of the second interferometer (FPI_2) is increased by one-time the OPL of the first interferometer (FPI_1). Hence, $OPL_2 = n_2L_2 + in_1L_1$, with $i = 1$. The individual responses of the two FPIs are overlapped in figure 5.4. The red curve corresponds to the first interferometer, whose maxima are represented as λ_k^1, and the blue curve corresponds to the second interferometer, with interference maxima described as λ_k^2, where k is the number of the peak.

Since the OPL of the second interferometer was increased, its FSR is now redefined through equation 5.5 as:

$$FSR_2^{i=1} = \frac{\lambda_1\lambda_2}{2\left(n_2L_2 + 1n_1L_1\right)}. \tag{5.7}$$

In figure 5.4, both interferometers are in phase at an initial position λ_0^m. The wavelength position of a maximum "k" can be expressed using the FSR of the interferometer as:

$$\lambda_k^1 = \lambda_0^1 + kFSR_1, \tag{5.8}$$

for the first interferometer, and in the same way as:

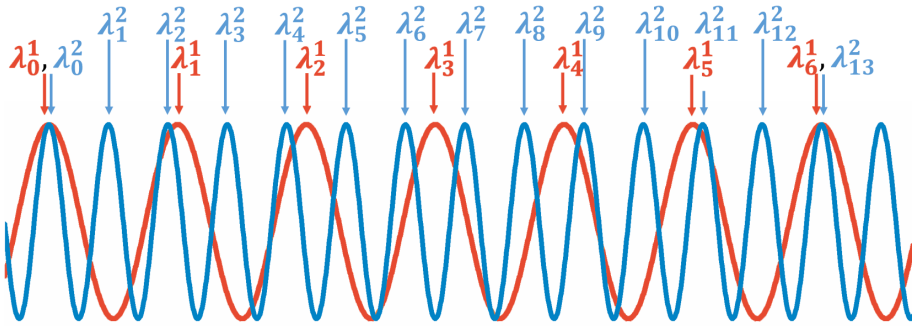

Figure 5.4. – Schematic of the spectral response of two FPIs (1 and 2), where the OPL_2 was increased by one-time the OPL_1. The wavelengths of the different peaks are labeled as λ_k^m, where $m = 1, 2$ is the number of the interferometer and k is the number of the peak.

$$\lambda_k^2 = \lambda_0^2 + kFSR_2^{i=1}, \tag{5.9}$$

for the second interferometer. In figure 5.4, both interferometers will be once again in phase when:

$$\lambda_k^1 = \lambda_{2k+1}^2. \tag{5.10}$$

Combining equations 5.8 and 5.9 in equation 5.10, and considering that $\lambda_0^1 = \lambda_0^2$, the following relationship is attained:

$$kFSR_1 = (2k+1)\, FSR_2^{i=1}. \tag{5.11}$$

Expressing "k" as a function of the FSR of both interferometers, one obtains:

$$k = \frac{FSR_2^{i=1}}{FSR_1 - 2FSR_2^{i=1}}. \tag{5.12}$$

The traditional Vernier envelope (upper envelope) in the optical Vernier effect is the wavelength distance between two consecutive situations where both interferometers are in phase. Hence the FSR of the Vernier upper envelope can be described as:

$$FSR_{envelope} = \lambda_k^1 - \lambda_0, \tag{5.13}$$

which through equation 5.8 is the same as:

$$FSR_{envelope} = kFSR_1. \tag{5.14}$$

Replacing equation 5.12 in equation 5.14, the FSR of the the upper envelope for the first harmonic of the Vernier effect as a function of the FSR of the two interferometers is:

$$FSR_{envelope} = \left| \frac{FSR_2^{i=1} FSR_1}{FSR_1 - 2FSR_2^{i=1}} \right|, \tag{5.15}$$

where the modulus was taken, since the FSR is a positive value.

This analysis can be generalized for any harmonic order (i) by considering that $OPL_2 = n_2 L_2 + i n_1 L_1$. Therefore, equation 5.7 can be expressed more generally through equation 5.5. Starting from an initial in-phase situation, both interferometer will be once again in phase when:

$$\lambda_k^1 = \lambda_{(i+1)k+1}^2, \tag{5.16}$$

being i the order of the harmonic. With this, equation 5.11 is generalized to:

$$kFSR_1 = [(i+1)\,k + 1]\, FSR_2^i, \tag{5.17}$$

where "k" is now defined as:

$$k = \frac{FSR_2^i}{FSR_1 - (i+1)\, FSR_2^i}. \tag{5.18}$$

At last, the general expression for the FSR of the upper envelope as a function of the FSR of the two interferometers, for any harmonic order, is obtained when equation 5.18 is replaced in equation 5.14. The result is:

$$FSR_{envelope}^i = \left| \frac{FSR_2^i FSR_1}{FSR_1 - (i+1)\, FSR_2^i} \right|, \tag{5.19}$$

where again the modulus was taken, since the FSR is always a positive quantity.

This general expression represents the regeneration property of the upper envelope, as it turns out to be independent of the order of the harmonic. If one replaces the general expression for the FSR of the reference FPI (equation 5.5) and the FSR of the sensing FPI (equation 4.25) both in equation 5.19, assuming that the wavelengths λ_1 and λ_2 are the same for both interferometers, the FSR of the upper envelope is independent of the harmonic order i.

When using optical harmonics of the Vernier effect for sensing applications, tracing the upper envelope and measuring the wavelength shift seems to have a drawback. The visibility of the upper envelope decreases with the order of the harmonics, as seen in figure 5.3. In 2016, Zhao *et al.* had already discovered that increasing the ratio between the OPLs by a multiple integer, keeping the same detuning, would reduce the visibility of the upper envelope, while maintaining its FSR constant [167]. However, at that time they did not figure out the concept of optical harmonic Vernier effect, together with its benefits. Despite the reduction in visibility might seem to be a disadvantage, in practical

applications the problem is easily solved by using alternatively the internal envelopes, represented in figure 5.3 by the red-orange lines.

5.2.2. Internal Envelopes

The internal envelopes are obtained by fitting, in a special way, the maxima in the harmonic spectrum. The maxima are classified into groups of $i + 1$ peaks, the same as the number of internal envelopes generated for the case of a parallel configuration. Then each group is fitted independently from the others.

Figure 5.5 shows the 2^{nd} harmonic of the optical Vernier effect, containing therefore 3 distinct internal envelope. Since it is the 2^{nd} harmonic order, the maxima are grouped into groups of 3 peaks, as represented by the dark blue line. Each of these three peaks is part of a distinct internal envelope. Hence, in this case, the first peak of every group of 3 is fitted to form the first internal envelope, and similarly for the other internal envelopes.

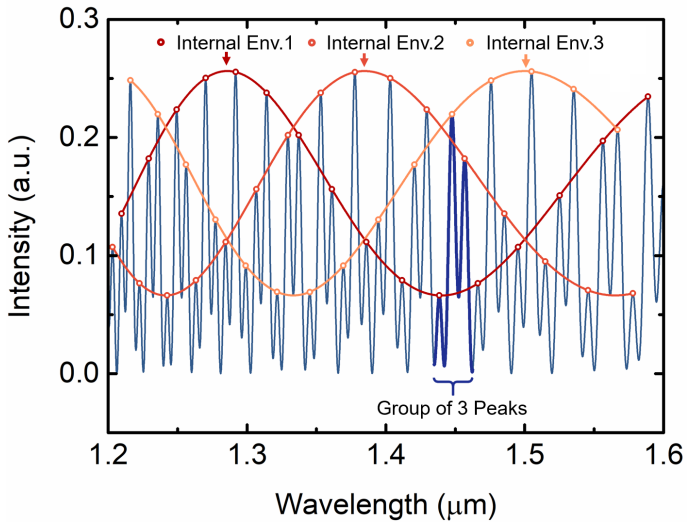

Figure 5.5. – Simulated output spectrum for the 2^{nd} harmonic of the optical Vernier effect, from figure 5.3(c). The maxima are grouped into groups of $(2 + 1)$ peaks. Each of these peaks belongs to a distinct internal envelope.

The intersection points between internal envelopes provide multiple points useful to monitor the wavelength shift, instead of using the upper envelope. Moreover, this kind of fitting technique, described in detail in appendix C, reduces the impact of intensity fluctuations in the spectrum. Intensity fluctuations might contribute to an error in the determination of the position of the envelope, and consequently to an error in the determination of the wavelength shift.

Contrary to the upper envelope, the FSR of the internal envelopes scales with the order of the harmonics, as also visible in figure 5.3. As the frequency of the reference interferometer (inverse of the FSR) increases harmonically with the order of the harmonic, the frequency

of the internal envelopes reduces, also harmonically. In other words, the internal envelopes get larger as the order of the harmonic increases. It is important to mention that the detuning is considered the same for all the presented cases. The FSR of the internal envelopes can be expressed as:

$$FSR^{i}_{internal\,envelope} = \left| \frac{(i+1)\,FSR^{i}_{2} FSR_{1}}{FSR_{1} - (i+1)\,FSR^{i}_{2}} \right| = (i+1)\,FSR^{i}_{envelope}, \tag{5.20}$$

where the internal envelopes are $(i+1)$ larger than the upper envelope (equation 5.19), which is also evident in figure 5.3. Note that, if high finesse Fabry-Perot interferometers were used, the spectral dips would become narrower, which can be helpful in some cases to track their position and trace envelopes. Overall, the position of the maxima and minima would still be the same and the properties of the effect, including the envelopes, would still be maintained.

5.2.3. M-Factor

Regarding the magnification factor (M-factor), in the fundamental optical Vernier effect the M-factor was obtained by dividing the FSR of the upper envelope by the FSR of the sensing interferometer (equation 4.27). Although this approach is true for the fundamental case, it turns out to be not correct for the harmonics. Since the FSR of the upper envelope is the same for every harmonic, as discussed before in equation 5.19, the result would be an M-factor independent of the order of the harmonics. However, in fact the M-factor does not depend on the upper envelope, but rather on the internal envelopes, as will be demonstrated later in this chapter by simulations, and experimentally in the next chapter. Hence, the general expression for the M-factor as a function of the order of the harmonic (i) is defined as:

$$M^{i} = \frac{FSR^{i}_{internal\,envelope}}{FSR_{1}} = \left| \frac{(i+1)\,FSR^{i}_{2}}{FSR_{1} - (i+1)\,FSR^{i}_{2}} \right| = (i+1)\,M, \tag{5.21}$$

where the first interferometer (FPI_1) is taken as the sensor, while the second interferometer (FPI_2) is the reference. M is the magnification factor for the fundamental optical Vernier effect, described by equation 4.27. In the case of $i = 0$, the M-factor for the fundamental optical Vernier effect is recovered.

Considering the same detuning (Δ), the M-factor scales up linearly with the order of the harmonic. For a harmonic of order i, the M-factor increases by $i+1$ times the value of M-factor for the fundamental optical Vernier effect. In other words, this means that the wavelength shift of the envelope also increases linearly with the order of the harmonic. Therefore, the use of optical harmonics of the Vernier effect allows for the realization of sensors with a sensitivity enhanced by $i+1$ times.

In a situation where no detuning is considered ($OPL_2 = (i+1)\,OPL_1$), the FSR of

the sensing interferometer is an integer multiple $(i+1)$ of the FSR of the reference interferometer, corresponding to a perfect harmonic situation where $FSR_1 = (i+1)\,FSR_2^i$. Therefore, the M-factor would trend towards infinity, translated by a Vernier envelope with an infinite FSR. In practical applications, such case is useless since the Vernier envelope cannot be traced and measured. Just like in the fundamental optical Vernier effect, a detuning must be deliberately applied to the OPL of the reference interferometer to slightly move away from the perfect harmonic case, making the sensing structure useful.

The maximum M-factor achievable by the fundamental optical Vernier effect, as discussed in the previous chapter, is limited in practical application by the FSR of the upper envelope, where one period should stay within the wavelength range available by the measuring system. However, when introducing harmonics, the maximum M-factor is not directly limited by the FSR of the upper envelope or the FSR of the internal envelopes, even though it scales up with the order of the harmonic. In a situation where the period of the upper envelope stays out of the wavelength range available, one can still rely on the internal envelope intersections to monitor the wavelength shift.

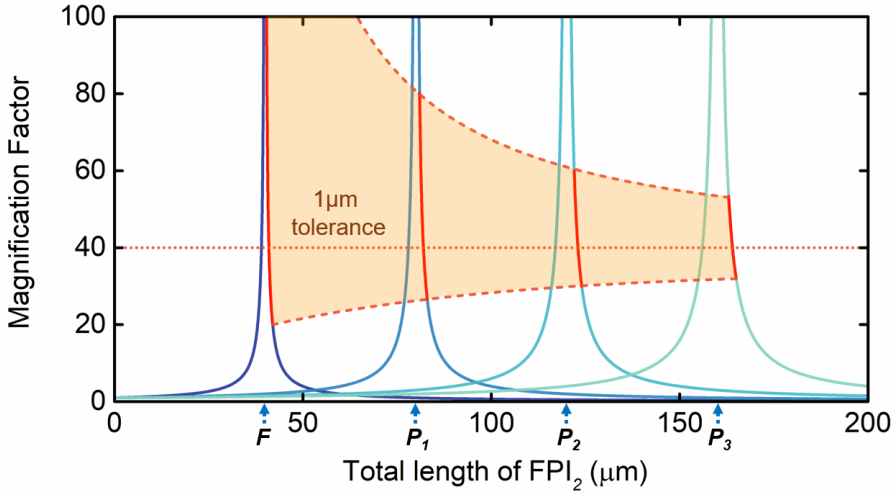

Figure 5.6. – Modulus of the magnification factor as a function of the total length $(L_2 + iL_1)$ of the reference interferometer (FPI_2), for a fixed length (L_1) of the sensing interferometer (FPI_1), where i corresponds to the order of the harmonic. The perfectly harmonic cases, where the M-factor is infinite, are marked with F, P_1, P_2, and P_3, respectively for the fundamental and the first three harmonic orders. A deviation of 1 μm in the length of FPI_2 produces smaller variations in the M-factor for higher harmonic orders, as exhibited by the red line.

Figure 5.6 shows the modulus of the M-factor curve, defined through equation 5.21, as a function of the total length of the reference interferometer, for a fixed length of the sensing interferometer. The length of the sensing interferometer was considered the same as before $(41\,\mu m)$, as well as the refractive index of both interferometers $(n = 1)$. The M-factor trends toward infinity as the OPLs of the two interferometers become attuned, approaching a perfect harmonic situation $(OPL_2 = (i+1)\,OPL_1)$. The points marked

as F, P_1, P_2, and P_3 correspond to these perfect harmonic cases, respectively for the fundamental and the first three harmonic orders of the Vernier effect.

An interesting property is noticeable in the diagram of figure 5.6: the M-factor curve broadens for higher harmonic orders. The M-factor curve broadening allows higher M-factors to be achieved more easily. Moreover, it also reduces the impact of small detuning errors. The red line in figure 5.6 targets a specific M-factor ($M = 40$). When changing the length of the reference FPI by ± 1 μm, simulating a detuning error, the variation caused in the M-factor value is smaller for higher harmonic orders. Therefore, higher harmonic orders allow larger tolerances in sensor fabrication without compromising its performance.

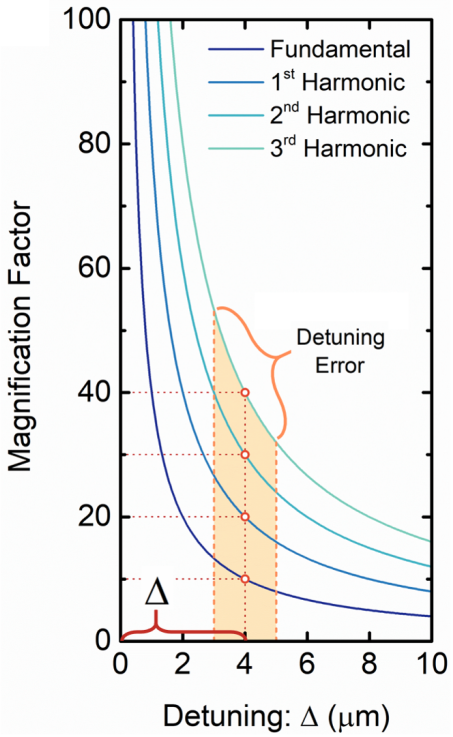

Figure 5.7. – Magnification factor as a function of the detuning (Δ) from a perfectly harmonic situation applied to the reference interferometer (FPI_2). For the same detuning, the magnification factor scales up linearly with the order of the harmonics as can be seen e.g. by the values at the red circles. Small detuning errors from multiple sources, such as fabrication tolerances, can modify the obtained magnification factor.

There are different sources of detuning errors. Environmental effects, such as temperature changes or deformation/strain, typically result in a percentage change in the interferometer length and would become more relevant for longer reference interferometers. Aside from these environmental effects, errors and tolerances in the fabrication process also contribute as detuning errors. Strain or deformation effects are negligible in this case, since the reference interferometer is considered stable, where no strain is applied to it. The thermal expansion coefficient of silica is around $0.55 \times 10^{-6}\, K^{-1}$ [104], which for a

5 °C temperature variation corresponds to a length variation of 2.75×10^{-4} %. In practical terms, the length variation caused by such temperature change in a 100 μm-long FPI cavity is of about 0.275 nm. For a 1 mm-long FPI cavity that corresponds to a length variation of 0.275 μm. Note that these variable parameters produce a detuning error which is, in general, below the error imposed by the accuracy of the fabrication procedures (normally between 1 μm to a few micrometers). In sum, the limiting factor here is the detuning error caused by the fabrication process, which is a fixed value dependent on the available fabrication technology.

Figure 5.7 represents a different way to approach these concepts. Here, the M-factor is shown as a function of the detuning (Δ) from the perfectly harmonic case, for the fundamental case and for the first three harmonic orders of the optical Vernier effect. One can observe that, for the same detuning, the M-factor scales up linearly with the order of the harmonics, as seen by the value at the red circles. It is worth mentioning that, even though the red circles do not represent a perfect harmonic case, for a fixed detuning the scaling properties of the effect (magnification factor, number of internal envelopes, frequency of the internal envelope) can still be seen as harmonic. Recalling what has been discussed previously, the detuning is introduced on purpose to make the envelope measurable. Figure 5.7 also presents a detuning error of 1 μm, showing how it can affect the final M-factor.

The next section presents simulated results of the optical harmonic Vernier effect for sensing applications. The improvement of sensitivity, due to the enhancement of the M-factor, will especially be demonstrated.

5.3. Simulation

To simulate the enhanced response obtained through the optical harmonic Vernier effect, let us first start from the initial situation described in figure 5.3. The sensing FPI has an OPL of 41 μm and the OPL of the reference FPI is adjusted to introduce the fundamental optical Vernier effect (32 μm), as well as the first three harmonic orders (32 $\mu m + i \times 41\ \mu m$, with $i = 1, 2, 3$, respectively), while keeping the same detuning of 9 μm.

The effect of a measurand is perceived by the sensing interferometer as a variation of its OPL (refractive index and/or physical length). Hence, in all cases, the sensing interferometer OPL was increased by steps of 0.02 μm, to a maximum of 0.08 μm, simulating the effect of a measurand. Figure 5.8(a) shows the response of the sensing FPI for the variations of OPL applied. The sensing FPI presents a wavelength shift towards longer wavelengths, as indicated by the arrow. The resulting upper envelope for the fundamental optical Vernier effect, as well as the internal envelopes for the first three harmonic orders, are also depicted in figures 5.8(b-e). For the sake of clarity only the upper envelope and internal envelopes were plotted, instead of the whole spectra. In all cases, a wavelength

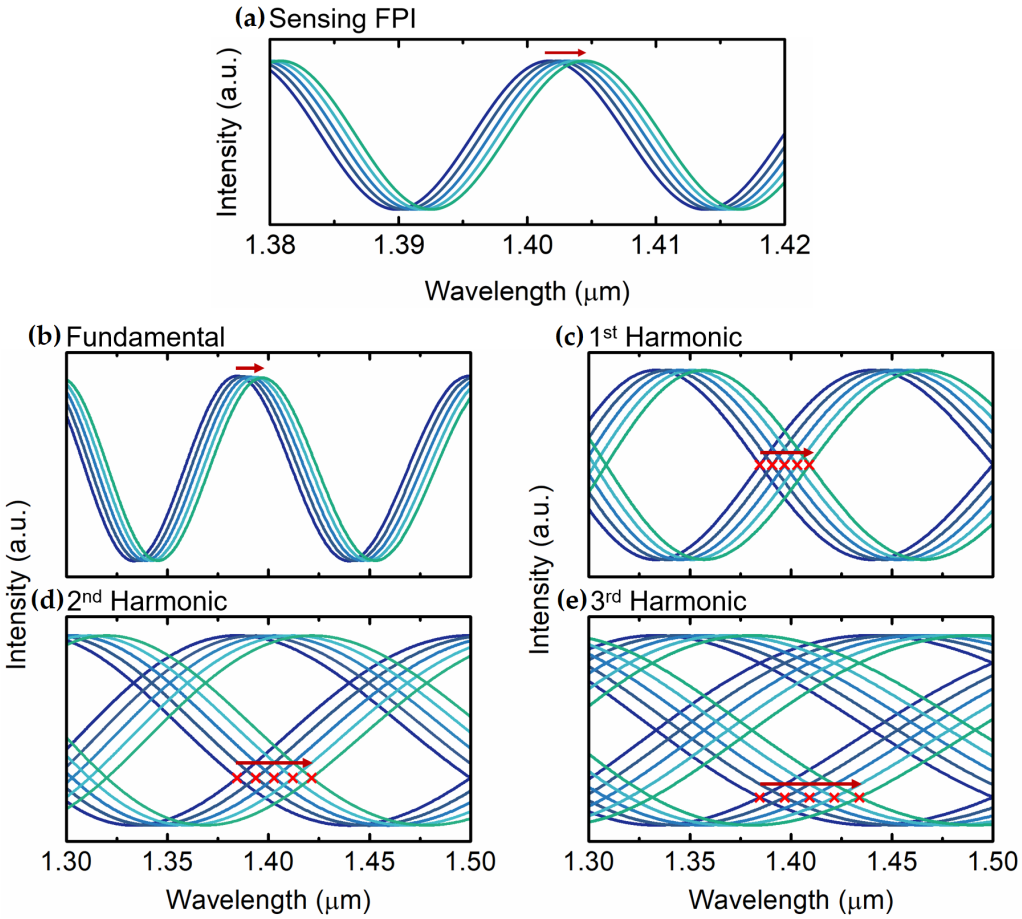

Figure 5.8. – Spectral shift when the OPL of the sensing FPI increases by steps of 0.02 μm. (a) Sensing FPI. (b) Upper envelope of the fundamental optical Vernier effect. (c-e) Internal envelopes of the first three harmonic orders, respectively. The monitored intersections are marked with a cross.

shift towards longer wavelength is also observed. The detuning is positive, which results in a positive M-factor, producing a wavelength shift of the Vernier envelope in the same direction as the wavelength shift of the sensing FPI[1].

For the fundamental optical Vernier effect, the wavelength shift of the upper envelope can be monitored, for example, at the maximum around 1.40 μm. As for the optical harmonic Vernier effect, is it useful to monitor the wavelength shift at the intersection between two internal envelopes, marked in figures 5.8(c-e) with a cross. As the harmonic order increases, the internal envelope intersections present a longer wavelength shift, which is in accordance with the definition of the M-factor for the optical harmonic Vernier effect (equation 5.21). The M-factor increases with the harmonic order, which is directly related with the sensitivity.

The wavelength shifts of the simulated results from figure 5.8 are represented in figure

[1]See section 4.2.2.

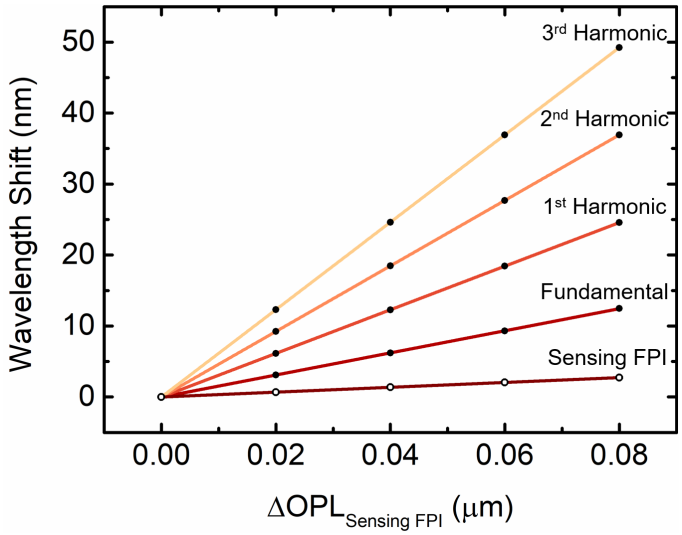

Figure 5.9. – Wavelength shift as a function of the change in the OPL of the sensing FPI. Results presented for the sensing FPI and for the Vernier envelope of the fundamental optical Vernier effect, as well as the first three harmonic orders.

5.9 as a function of the variation applied to the OPL of the sensing FPI. It is clearly visible an increase of the sensitivity (given by the slope of the linear fit) with the increase of the harmonic order.

Table 5.1 summarizes the results obtained in this simulation. The ratio between the M-factor of each harmonic case and the M-factor for the fundamental optical Vernier effect (M_0) increases linearly, following a relationship of $(i+1)$ predicted by equation 5.21.

Table 5.1. – Overview of the simulated results.

	Sensitivity (S) (nm/μm)	***M*-factor** (S_i/S_{FPI})	M_i/M_0	**Relationship** $M_i = (i+1)M_0$
Sensing FPI	34.18	-	-	-
Fundamental	**155.75**	$M_0 = 4.56$	1.00	1
1st Harmonic	**307.20**	$M_1 = 8.99$	1.97	2
2nd Harmonic	**461.61**	$M_2 = 13.51$	2.96	3
3rd Harmonic	**615.50**	$M_3 = 18.01$	3.95	4

Until now, all the descriptions considered the same sensing FPI, while the OPL of the reference FPI was increased to introduce optical harmonics of the Vernier effect. What happens if the OPL of the sensing FPI was increased to introduce harmonics of the Vernier effect, instead of the reference FPI?

To simulate this case, the OPL of the reference FPI was kept constant and equal to

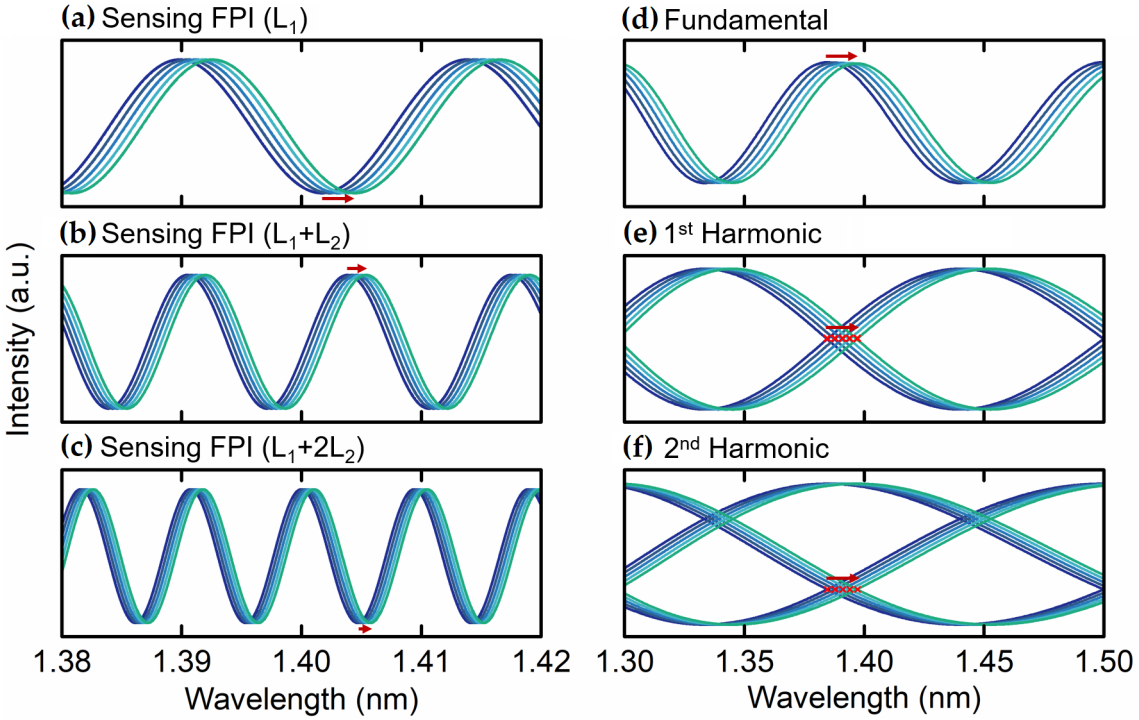

Figure 5.10. – Spectral shift when the OPL of the sensing FPI increases by steps of 0.02 µm. Sensing FPI used in the (a) fundamental effect; (b) 1st harmonic; and (c) 2nd harmonic. (d) Upper envelope of the fundamental effect. Internal envelopes of the (e) 1st harmonic; and (f) 2nd harmonic. The monitored intersections are marked with a cross.

32 μm. The OPL of the sensing FPI was adjusted to introduce the fundamental optical Vernier effect (42 μm), as well as the first two harmonic orders of the optical Vernier effect (42 $\mu m + i \times 32\,\mu m$, with $i = 1, 2$,respectively), while keeping the same detuning of 9 μm. Similarly to the previous simulation, the OPL of the sensing FPI was increased by steps of 0.02 μm, to a maximum of 0.08 μm.

In this approach, a new characterization of the individual sensing FPI needs to be performed for each harmonic case. Contrary to the other cases, now the OPL of the sensing FPI is increasing with the increase of the harmonic order, which might results in a different sensitivity depending on the actual length of the sensing FPI. Figure 5.10 presents the individual sensing FPI responses for each case, together with the corresponding upper Vernier envelope and internal envelopes for the fundamental and the first two harmonic orders of the Vernier effect, respectively.

The wavelength shift of the individual sensing FPI decreases for longer cavity lengths, as visible in figures 5.10 (a-c). In the other cases, the sensitivity of the individual sensing FPI was the same, independently of the harmonic order used. Now, to calculate the M-factor (equation 5.21) one needs to consider the correspondent sensitivity of the sensing FPI in each situation, since it is different depending on the harmonic order.

The wavelength shifts of the upper envelope of the fundamental optical Vernier effect, represented in figure 5.10 (d), and the internal envelopes for the first and second harmonic orders, shown in figure 5.10(e) and (f), are approximately the same. The wavelength shift of the Vernier envelope does not improve with the increase of the harmonic order. In fact, it remains constant and independent of the harmonic order. Nevertheless, one should not forget that the sensitivity of the individual sensing FPI is decreasing, which technically results in an M-factor that is still increasing with the harmonic order. However, it does not follow the relationship $(i+1)$ presented before. To have a clear picture of these results, a summary is shown in table 5.2.

Table 5.2. – Overview of the simulated results.

	Sensitivity (S) (nm/μm)	***M*-factor** (S_i/S_{FPI})	$\boldsymbol{M_i/M_0}$	**FSR** (nm)	**FSR$_{\text{Int.}}$** (nm)	***M*-Factor** eq. 5.21
Sensing FPI	33.8	-	-	23.96	-	
Fundamental	**155.24**	$M_0 = 4.59$	1.00	106.39	106.39	$M_0 = 4.44$
Sensing FPI	19.05			13.37	-	
1$^{\text{st}}$ Harmonic	**154.26**	$M_1 = 8.10$	1.76	106.85	213.70	$M_1 = 15.98$
Sensing FPI	13.33			9.40	-	
2$^{\text{nd}}$ Harmonic	**153.95**	$M_2 = 11.55$	2.52	106.66	319.97	$M_2 = 34.05$

From the results depicted in the table, one observes that the M-factor increases with the harmonic order, even though the sensitivity of the envelope is constant. As explained before, this is caused by the reduction of the sensitivity of the individual sensing FPI. Nevertheless, the ratio M_i/M_0 does not follow the relationship $(i+1)$ deduced previously. Moreover, the M-factor calculated using the FSR of the internal envelopes, through equation 5.21, does not match with the one obtained by the sensitivities. In fact, the M-factor calculated with the sensitivity values is approximately the same as if one calculates it through the FSR of the upper envelope (instead of the internal envelope), which does not change with the harmonic order.

The M-factors achieved in this case, shown in table 5.2, are slightly smaller than the ones obtained in the results of table 5.1. However in practical applications, the sensitivity of the Vernier envelope increases substantially in the first simulated situation, where the OPL of the reference FPI is increasing. On the contrary, the second simulated case, where the OPL of the sensing FPI is increasing, leads to a constant sensitivity, independent of the harmonic order.

From a different point of view, increasing the OPL of the sensing FPI leads to a decrease in its FSR, which is to say that the frequency of the interference signal increases. This

would correspond to a finer scale in a caliper. When adding the Vernier effect with the reference FPI, the frequency of the reference FPI is much lower (larger FSR) than the frequency of the sensing FPI, corresponding to a coarser scale. Hence, one is trying to improve the measurement performed with a fine scale (sensing FPI) by technically adding a coarser scale (reference FPI), which results in no improvement at all. However, in the first situation, where the OPL of the reference FPI is increasing with the harmonic order, its frequency is also increasing, corresponding to a finer scale. Hence, in this case one is trying to improve the measurement performed with a coarse scale (sensing FPI) by adding a finer scale (reference FPI), resulting in a considerable improvement of the sensitivity. The higher the harmonic order, the finer is the scale provided by the reference FPI, and consequently the larger is the enhancement obtained.

5.4. Parallel vs Series Configuration

Until now, only examples using the parallel configuration were demonstrated. Although the magnification properties are the same for a configuration in series, there are some additional factors that need to be considered. In a series configuration, where two FPIs are connected to each other, the equation that describes the output spectrum is slightly different.

As an example, let us consider a structure consisting of a hollow capillary tube as the first FPI (FPI_1) and a section of SMF as the second FPI (FPI_2), as depicted in figure 5.11. The structure presents three interfaces: the first corresponds to the initial interface of the hollow capillary tube, the second corresponds to the middle interface that connects both FPIs, and the third corresponds to the interface between the end of the SMF and air.

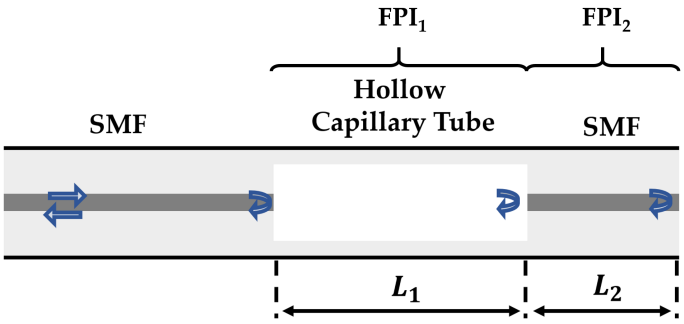

Figure 5.11. – Schematic of a series configuration, where the first interferometer (FPI_1) is a hollow capillary tube of length L_1 and the second interferometer (FPI_2) is a section of SMF of length L_2.

The output electric field is the sum of the electric fields of the propagating light that is backreflected at those three interfaces. These three reflected components can be expressed

as:

$$E_{R1}(\lambda) = AE_{in}(\lambda), \tag{5.22}$$

$$E_{R2}(\lambda) = BE_{in}(\lambda)\exp\left[-j\left(\frac{4\pi n_1 L_1}{\lambda} - \pi\right)\right], \tag{5.23}$$

$$E_{R3}(\lambda) = CE_{in}(\lambda)\exp\left[-j\frac{4\pi\left(n_1 L_1 + n_2 L_2\right)}{\lambda}\right]. \tag{5.24}$$

The coefficients A, B, and C are given by:

$$A = \sqrt{R_1}, \tag{5.25}$$

$$B = (1 - A_1)(1 - R_1)\exp(-2\alpha_1 L_1)\sqrt{R_2}, \tag{5.26}$$

$$C = (1 - A_1)(1 - A_2)\exp(-2\alpha_1 L_1)\exp(-2\alpha_2 L_2)(1 - R_1)(1 - R_2)\sqrt{R_3}, \tag{5.27}$$

where R_i is the intensity reflection coefficient at the interface i (with $i = 1, 2, 3$), A_1 and A_2 represent the transmission losses through the first and second interfaces, respectively, α_1 and α_2 are related with the propagation losses.

Through equation 4.11, the reflected light intensity measured at the output can then be expressed as:

$$\begin{aligned} I_{out}(\lambda) = I_0 &- 2AB\cos\left(\frac{4\pi n_1 L_1}{\lambda}\right) - 2BC\cos\left(\frac{4\pi n_2 L_2}{\lambda}\right) \\ &+ 2AC\cos\left[\frac{4\pi\left(n_1 L_1 + n_2 L_2\right)}{\lambda}\right], \end{aligned} \tag{5.28}$$

where $I_0 = A^2 + B^2 + C^2$.

Once again, if the OPL of the second interferometer (FPI_2) is increased by a multiple (i-times) of the OPL of the first interferometer (FPI_1), then optical harmonics of the Vernier effect are introduced. With this, the expression for the reflected light intensity measured at the output can be rewritten as:

$$I_{out}^{i}(\lambda) = I_0 - 2AB\cos\left(\frac{4\pi n_1 L_1}{\lambda}\right) - 2BC\cos\left[\frac{4\pi\left(n_2 L_2 + i n_1 L_1\right)}{\lambda}\right] + 2AC\cos\left\{\frac{4\pi\left[(i+1)\, n_1 L_1 + n_2 L_2\right]}{\lambda}\right\}. \tag{5.29}$$

Comparing the output spectrum for a parallel configuration, given by equation 5.6, with the output spectrum for a series configuration, expressed by equation 5.29, the main difference relies on the last cosine function, apart from the prefactors A, B, and C. In a series configuration, the last cosine expresses the sum between the OPLs of both interferometers, while in a parallel configuration it is actually the difference. This leads to the presence of an additional higher frequency component in the output spectrum for the series configuration.

Interestingly, the output spectrum for a series configuration is visually one harmonic order ahead of the output spectrum for a parallel configuration. For example, the output spectrum for a series configuration corresponding to the first harmonic ($i = 1$), is given by:

$$I_{out}^{i=1}(\lambda) = I_0 - 2AB\cos\left(\frac{4\pi n_1 L_1}{\lambda}\right) - 2BC\cos\left[\frac{4\pi\left(n_2 L_2 + n_1 L_1\right)}{\lambda}\right] + 2AC\cos\left[\frac{4\pi\left(2n_1 L_1 + n_2 L_2\right)}{\lambda}\right], \tag{5.30}$$

and the output spectrum for a parallel configuration corresponding to the second harmonic ($i = 2$), is given by (equation 5.6, with $i = 2$):

$$I_{out}^{I=2}(\lambda) = I_0 - 2AB\left\{\cos\left(\frac{4\pi n_1 L_1}{\lambda}\right) + \cos\left[\frac{4\pi\left(2n_1 L_1 + n_2 L_2\right)}{\lambda}\right]\right\} + B^2\cos\left[\frac{-4\pi\left(n_2 L_2 + n_1 L_1\right)}{\lambda}\right]. \tag{5.31}$$

Apart from the prefactors and the negative signs, the three frequencies presented in both cases are the same. As a result, the output spectrum for a series configuration of harmonic order i looks similar to the output spectrum for a parallel configuration of harmonic order $i+1$. To verify this property, the output spectra for both configurations, given by equation 5.6 and equation 5.29, are represented in figure 5.12 for the fundamental and the first two harmonic orders of the optical Vernier effect, respectively.

The output spectrum for a series configuration looks one harmonic order ahead of the parallel configuration, which is also visible by the number of internal envelopes in figure 5.12. The number of internal envelopes for a series configuration increases with $i + 2$, and

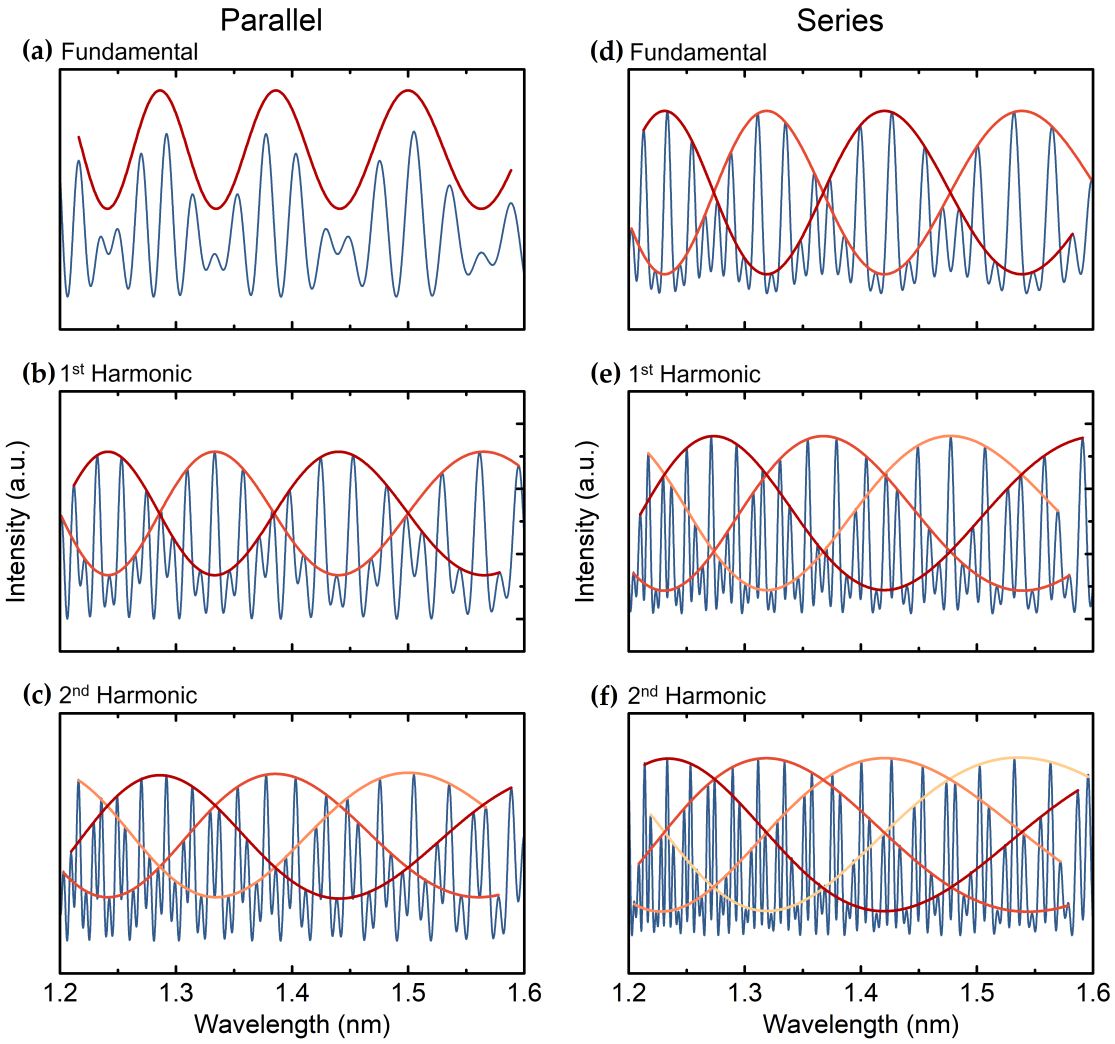

Figure 5.12. – Simulated output spectra: (a-c) parallel configuration; (d-f) series configuration. The fundamental optical Vernier effect, as well as the first two harmonic orders are represented in both cases.

the FSR of the internal envelopes is defined as:

$$FSR^{i}_{internal\,envelope} = (i+2)\,FSR^{i}_{envelope}. \tag{5.32}$$

Despite this additional factor regarding the number and FSR of the internal envelopes, the magnification properties of both configurations (M-factor) are the same. This is only valid if the second interferometer in the series configuration is also used as a stable reference, and if both interferometers (FPI_1 and FPI_2) have, respectively, the same OPL in both configurations. However, the definition of M-factor for a series configuration needs to be slightly adjusted to:

$$M^i = \frac{(i+1)\, FSR^i_{envelope}}{FSR_1} = (i+1)\, M, \tag{5.33}$$

by using $(i+1)$-times the FSR of the upper envelope, instead of using directly the FSR of the internal envelopes, which scales differently for this configuration, as discussed before. This expression for the M-factor is valid for both, the parallel and series configurations.

Moreover, the internal envelopes for a series configuration seem to have slightly higher visibility. However, the increased visibility of the internal envelopes is actually caused by the small maxima in the output spectrum. These maxima are smaller in the series configuration due to the presence of a third interface in the sensing structure, whose backreflected light has much lower intensity (prefactor C) compared with the backreflected light at the other two interfaces (prefactors A and B). In practical applications, if the sensor is a bit lossy, the small maxima become even smaller, indistinguishable, and therefore problematic if one needs to fit the internal envelopes.

5.5. Limitations

The application of the optical harmonic Vernier effect to optical fiber sensors brings a range of advantages, but it also has some drawbacks. Hence, it is relevant to discuss about the limitations of this effect.

In general, the effect requires monitoring a wide wavelength range. The more tuned the effect is, the larger is the Vernier envelope and the more sensitive the sensing structure is. Therefore, the larger is the wavelength shift. With this, one needs to ensure that the wavelength shift of the tracked point does not make it fall outside the available wavelength range.

Another limiting factor is the complexity of the output spectrum. The higher the harmonic order, the more components the spectrum contains, which makes it more complex and harder to analyze. Therefore, the higher the harmonic order, the more signal processing is required.

Losses, such as propagation losses or imperfect interfaces that cause mode mismatch, are enemies of signal processing. They reduce the visibility of the interference peaks, which might lead to problems when tracking and fitting internal envelopes. Higher harmonic orders require longer OPLs, usually obtained by increasing the length of the reference interferometer, and therefore making propagation losses even more relevant.

At last, the sampling or resolution of the detection system imposes a major limitation in terms of the maximum harmonic order achievable. The higher the harmonic order, the finer and narrower the interference peaks are, due to the presence of higher frequency components that also scale up with the harmonic order. In many detection systems, to measure such a broad wavelength range requires, in return, to reduce the resolution of the

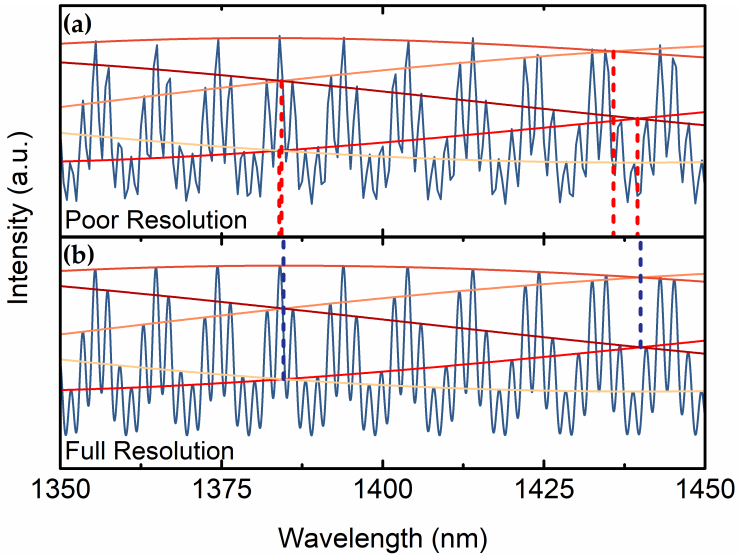

Figure 5.13. – Simulated output spectrum for the 4$^{\text{th}}$ harmonic of the optical Vernier effect. (a) Poor resolution spectrum: resolution of 500 pm. (b) Full resolution spectrum: resolution of 1 pm. The position of the intersections between internal envelopes are marked with dashed lines.

measurement. If the detection system has poor resolution, the position of the interference peaks are misleading and not well defined. Ultimately, tracing the upper envelope or internal envelopes under these conditions can introduce large errors, producing an incorrect result. Moreover, in worst scenarios where the resolution of the detection system (or sampling rate) is not enough to detect the higher frequencies presented in higher harmonic orders, then spectral aliasing is introduced. As a result, the output spectrum is malformed and some interference peaks might be missing.

Figure 5.13 shows the simulated output spectrum for the 4$^{\text{th}}$ harmonic of the optical Vernier effect for two different cases. The OPL of the sensing interferometer is 100 μm and the reference interferometer has a detuning of 9 μm, with an OPL of (91 $\mu m + 4 \times 100\,\mu m$). In figure 5.13(a), the resolution is poor (500 pm) and the position of the interference peaks are not well defined. On contrary, figure 5.13(b) presents the same spectrum but with a resolution of 1 pm, where all the interference peaks are well defined. In both cases, the interference peaks were tracked and the internal envelopes were traced. It is clearly visible that for a poor resolution spectrum the positions of the intersections between internal envelopes are misplaced, when compared with the real positions showed in the full resolution spectrum.

Note that the poor resolution spectrum is in the limit of the Nyquist criterion[2]. In such case, performing a correct interpolation of the spectrum might still allow to achieve

[2]Nyquist criterion: the sampling rate should be higher than twice the highest frequency component of the spectrum

a corrected position of the interference peaks. Nevertheless, if one wants to use the next harmonic order, the highest frequency of the spectrum would be even higher, falling out of the Nyquist criterion. Moreover, the larger the initial sensing FPI, the smaller is its FSR. Therefore, higher harmonic orders require an even longer reference FPIs, with even smaller FSRs, and hence even higher frequencies.

5.6. Conclusion

As a way of closing this chapter, it is relevant to leave a few comments on the optical harmonic Vernier effect as a summary of the different points discussed here.

In the previous chapter, the size of the upper Vernier envelope was a limiting factor to the maximum M-factor achievable using the fundamental optical Vernier effect. With the introduction of optical harmonics of the Vernier effect, the upper Vernier envelope is regenerated with the same size as for the fundamental case. However, for the same size of the upper Vernier envelope, the M-factors obtained are higher when using optical harmonics of the Vernier effect. Hence, the proposed concept is a way to break the limits of the fundamental effect, allowing for the realization of sensors with a sensitivity enhanced by $i+1$ times. For example, achieving M-factors beyond 30 for single-type configurations using FPIs becomes realistic. Moreover, the impact of detuning errors decreases with the increase of the harmonic order.

Harmonics of the optical Vernier effect present internal envelopes that provide additional intersection points to better measure the wavelength shift. Measuring an intersection points is, in general, more accurate than measuring the position of a minimum (or maximum) of the upper Vernier envelope.

When scaling up harmonically the sensing interferometer, instead of the reference interferometer, no improvement in sensitivity of the Vernier envelope is obtained when increasing the harmonic order. In such case, the sensitivity for any harmonic order is the same as the sensitivity of the fundamental case. Furthermore, the M-factor will not follow a relationship of $i+1$.

In a series configuration, the magnification properties of the optical harmonic Vernier effect are the same as for a parallel configuration. However, the output spectrum for a series configuration looks visually one harmonic order ahead of the parallel configuration. This means the series spectrum contains the higher frequencies of the next harmonic order of the parallel spectrum, including also an extra internal envelope.

At last, some limitations of the effect were discussed, especially the impact of having a detection system with a poor resolution or sampling rate.

The experimental demonstration of optical harmonics of the Vernier effect, in parallel and in series, will be presented in the next chapter for real specific applications. Additionally, the special case of having no reference interferometer will also be explored.

Chapter 6.

Demonstration and Applications of Optical Harmonic Vernier Effect

6.1. Introduction

The optical harmonic Vernier effect was until now explored theoretically, together with simulations that demonstrate the diverse properties of the effect. This chapter seeks to demonstrate experimentally the introduction and application of optical harmonics of the Vernier effect. Several experimental details are here discussed from a practical perspective, especially regarding the fabrication of the structures.

The chapter is divided in two sections. The first one addresses the parallel configuration, with a strong focus on validating the properties of the effect deduced theoretically, comparing experimental results with the theoretical ones. The second section is dedicated to the series configuration, in particular to the special case of two interferometers physically connected without a separation. This particular case can have three possible outputs, of which one of them is the proposed structure and the other two are briefly discussed, but not here demonstrated. The section also presents a way to use the structure for simultaneous measurement of two parameters.

6.2. Parallel Configuration

6.2.1. Introduction

This section intends to demonstrate experimentally the optical harmonic Vernier effect in a parallel configuration using Fabry-Perot interferometers (FPIs). Strain sensing is used as possible application and as a mechanism to characterize and demonstrate the effect. Important properties deduced in the previous chapter are here verified, as well as the validation of the two definitions for the M-factor. At last, a compensated wavelength shift method is presented as a way to compare the performance of the different structures

without the influence of the detuning (Δ), which is different in every case.

6.2.2. Fabrication and Experimental Setup

In this experiment, the Fabry-Perot interferometers used were based on sections of a hollow capillary tube spliced between two single mode fibers (SMF28), as also considered in the previous two chapters. The capillary tube was fabricated at Leibniz-IPHT by the optical fiber technology group. Its internal diameter is 60 μm and outer diameter is 125 μm. The fabrication process of the sensing and reference FPIs is as follows.

First, the cleaved ends of a single mode fiber and a hollow capillary tube were spliced together using a splicing machine (Fitel S177). This step was performed in manual mode of the fusion splicer, ensuring that the center of the electric arc was mainly applied to the single mode fiber, thus avoiding the collapse of the hollow capillary tube. The splice consisted of two electric arc discharges with an arc duration of 400 ms and arc power of 30 arbitrary units (absolute arc power was not possible to attain, only relative values provided by the splicer).

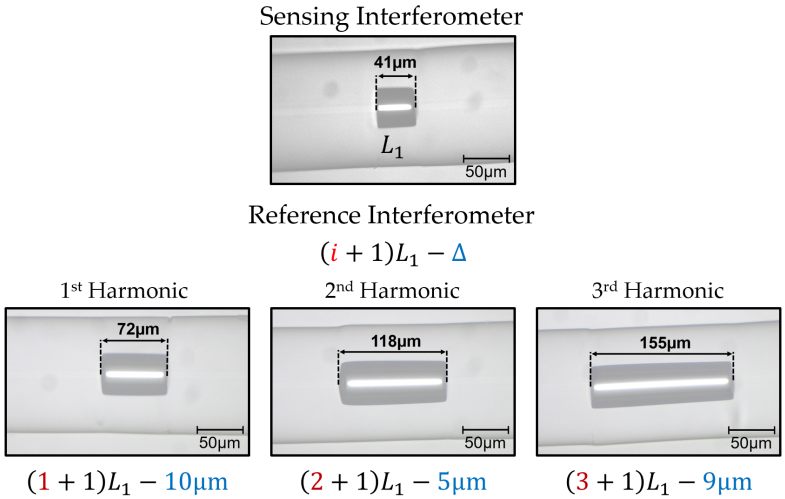

Figure 6.1. – Micrograph of the experimental fiber sensing interferometer (FPI_1) and the three different reference interferometers (FPI_2) used to excite the first three harmonic orders of the optical Vernier effect. The length of the reference interferometers scale with the harmonic order, i, and depend on the length of the sensing interferometer (L_1). All reference interferometers also present a detuning (Δ).

Afterwards, the other end of the hollow capillary tube was cleaved with the desired length using a fiber cleaver, together with the help of a magnification lens. This step should be performed with the maximum precision possible, especially when fabricating the reference FPI, since it has huge impact on the final detuning (Δ).

At last, the cleaved end of the hollow capillary tube was spliced to a different section of single mode fiber, adopting the same procedures as in the previous splice.

The sensing interferometer (FPI_1) was initially fabricated with a length of 41 μm (L_1). Then, three reference interferometers (FPI_2) were fabricated to introduce the first three harmonic orders of the optical Vernier effect, respectively. Considering that the FPIs are hollow, as an approximation their refractive index can be assumed as 1. With this, the length of the reference interferometers depends mainly on the length of the sensing interferometer, L_1, and on the detuning (Δ).

A micrograph of the different FPIs fabricated is shown in figure 6.1. The first harmonic was introduced using an FPI_2 with a length of 72 μm, corresponding to $2L_1$ minus a detuning of 10 μm. In the second harmonic, the reference FPI_2 had a length of 118 μm, resembling $3L_1$ minus a detuning of 5 μm. Lastly, an FPI_2 with a length of 155 μm, equal to $4L_1$ minus a detuning of 9 μm, was used to introduce the third harmonic.

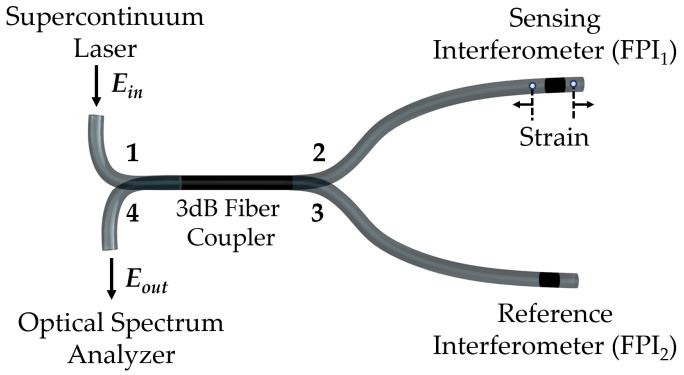

Figure 6.2. – Schematic illustration of the experimental setup. The sensing interferometer (FPI_1) and the reference interferometer (FPI_2) are separated by means of a 3db fiber coupler. A supercontinuum laser source is connected to the input and the reflected signal from the device is measured at the output with an optical spectrum analyzer. Strain is only applied to FPI_1, keeping FPI_2 as a stable reference.

The schematic of the experimental setup is illustrated in figure 6.2. The sensing and reference interferometers (FPI_1 and FPI_2) were physically separated in a parallel configuration by means of a 3db fiber coupler. The sensing interferometer was connected to port 2 of the fiber coupler. For each harmonic case ($i = 1, 2, 3$), the respective reference interferometer was connected to port 3. A supercontinuum laser source (Fianium WL-SC-400-2) was connected to the input port 1. The reflected signals from the FPIs at ports 2 and 3 are combined and measured at port 4 by means of an optical spectrum analyzer (OSA ANDO AQ-6315A, resolution of 0.1 nm).

The structure was tested for strain sensing, applying strain only to the sensing interferometer (FPI_1), for all three cases of different reference FPIs. Therefore, the reference interferometer (FPI_2) was kept stable during the whole experiment. To perform the strain measurements, the two single mode fibers connected on both sides of the sensing FPI were glued with cyanoacrylate adhesive to a fixed platform and to a translation stage with a

displacement resolution of 0.01 mm. A small pre-tension was added to the system, ensuring that the fiber was not bent. The total length over which strain was applied is 344 mm, and corresponds to the length between the fixed points. All the strain experiments were carried out at room temperature (23 °C). The strain measurements were realized by applying strain up to 600 $\mu\varepsilon$, with steps of 87.2 $\mu\varepsilon$ (translation stage displacement of 0.03 mm). Only static measurements were performed.

6.2.3. Characterization

The experimental output spectrum of the sensing FPI alone is represented in figure 6.3(a), together with its fast Fourier transform (FFT) expressed as a function of the cavity length. The FFT was performed, once again, from the reflected spectrum converted into the optical frequency domain, using the same method as in section 3.3.2. The peak in the FFT at around 41 μm matches with the physical length of the sensing FPI measured in figure 6.1.

To confirm experimentally the enhancement provided by the optical harmonics of the Vernier effect, it is crucial at first to characterize the sensing FPI without the optical Vernier effect. The sensing FPI presents a free spectral range (FSR) of 23.52 nm. Regarding the strain sensitivity, the sensing FPI achieved a value of (3.37 ± 0.02) pm/$\mu\varepsilon$.

Then, the three reference FPIs were successively applied as the reference interferometer, in order to respectively introduce the first three harmonic orders of the optical Vernier effect. The experimental spectra for the first three harmonic orders are depicted in figures 6.3 (b-d), respectively, together with their FFT. Visually, the appearance of the output spectra for the optical harmonics of the Vernier effect is similar to the theoretical results predicted by equation 5.6 and presented in figure 5.3. Please note that the different experimental harmonic orders have reference interferometers with different detunings (Δ), while the simulated results considered the same detuning value for every case. The detuning, as explained in the previous chapter, influences the FSR of the upper envelope and internal envelopes, as well as the M-factor. For example, the detuning of the 2$^{\text{nd}}$ harmonic (5 μm) is smaller than the detuning of the 3$^{\text{rd}}$ harmonic (9 μm), and therefore the FSR of the upper envelope and internal envelopes is larger.

The number of internal envelopes scales up linearly with the order of the harmonics, as also demonstrated theoretically, providing multiple intersection points suitable for monitoring the wavelength shift in sensing applications. The FSR of the upper envelope for the first three harmonic orders is 98.56 nm, 222.80 nm, and 107.77 nm, respectively. The FSR of the internal envelopes is given approximately by $i + 1$ times the FSR of the upper envelope, as described by equation 5.20.

Figure 6.4 shows the results of the experimental output spectra for the three harmonic orders depicted in figures 6.3(b-d), under three distinct situations of applied strain. In each case, the internal envelope intersection, marked with a red circle, can be traced and

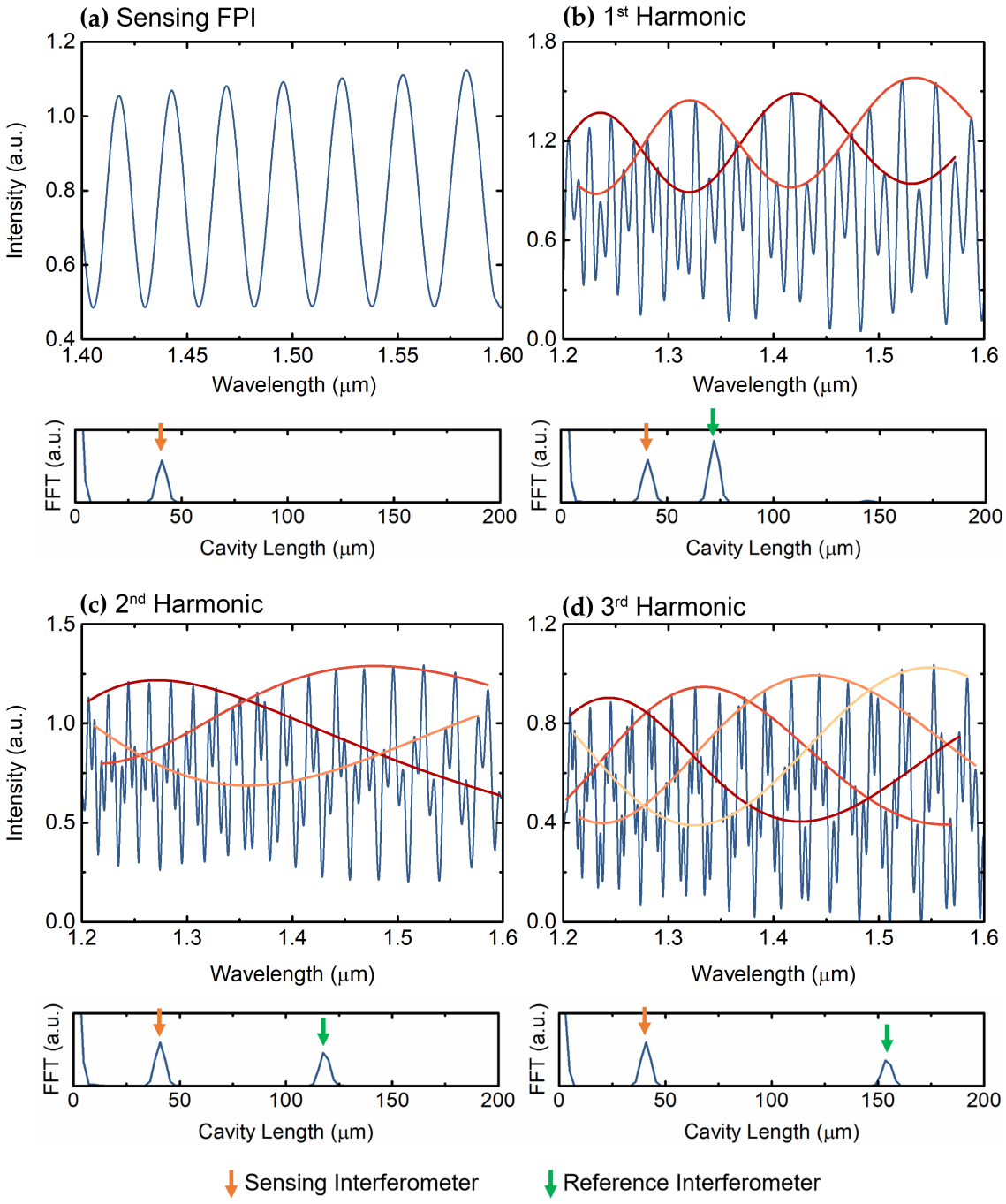

Figure 6.3. – Experimental output spectrum and corresponding fast Fourier transform (FFT). (a) Individual sensing interferometer (FPI_1). (b-d) First three harmonic orders. Red-orange lines: internal envelopes.

monitored as a function of the applied strain. As expected, since the second harmonic has a small detuning, the M-factor is large, and consequently the wavelength shift is also larger.

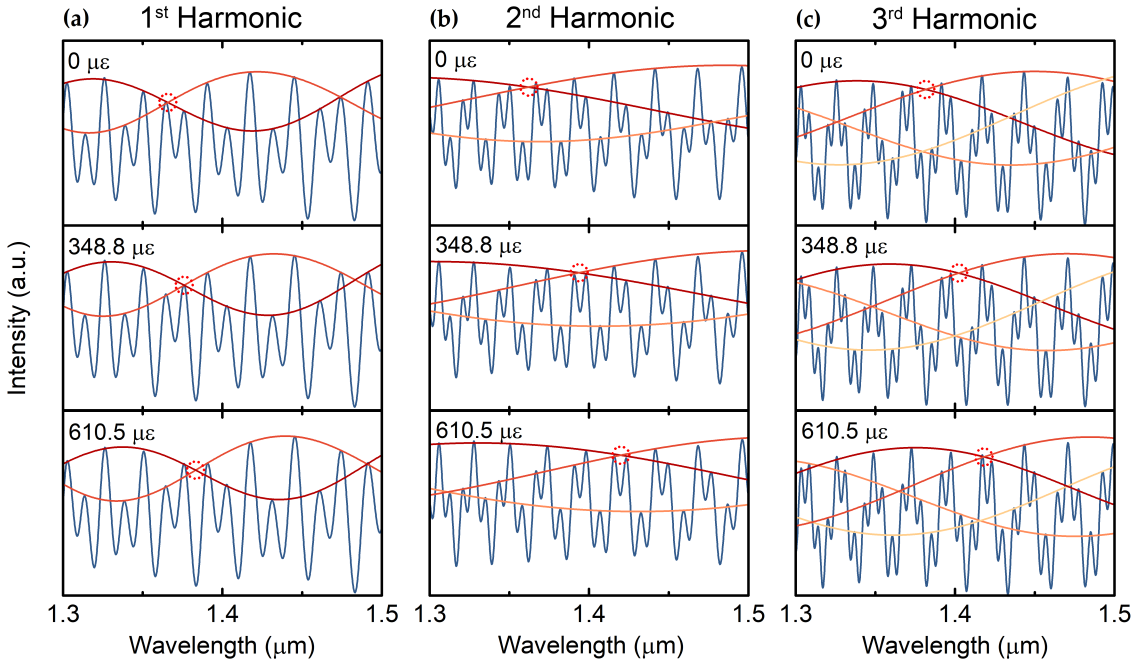

Figure 6.4. – Experimental output spectra at three different strain values: 0 με, 348.8 με, and 610.5 με. (a) 1st Harmonic. (b) 2nd Harmonic. (c) 3rd Harmonic. One of the multiple intersections between internal envelopes is marked with a red circle. There is a wavelength shift of the envelopes towards longer wavelengths when strain is applied to the sensing interferometer.

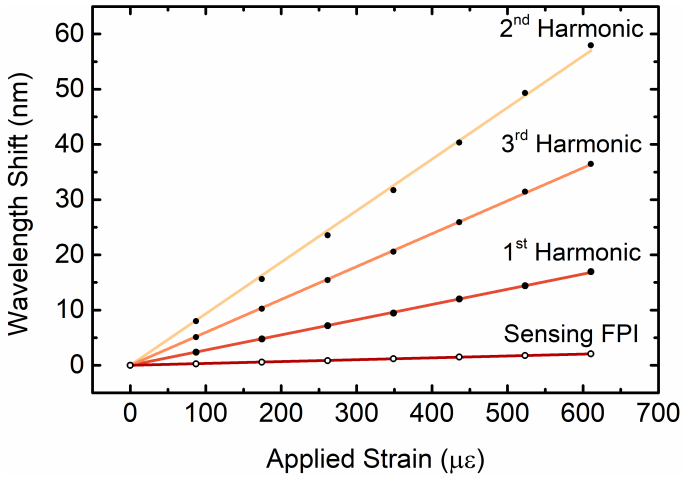

Figure 6.5. – Experimental wavelength shift of the Vernier envelope as a function of the applied strain for the first three harmonic orders, together with the wavelength shift of the individual sensing FPI alone.

The wavelength shift of the Vernier envelope, given by the internal envelope intersections, is presented in figure 6.5 as a function of the applied strain. The wavelength shift of the individual sensing FPI is also shown in the same figure. The sensitivity values (S) for the first three harmonic orders are $(27.6 \pm 0.1)\,\mathrm{pm}/\mu\varepsilon$, $(93.4 \pm 0.6)\,\mathrm{pm}/\mu\varepsilon$, and

$(59.6 \pm 0.1)\,\mathrm{pm}/\mu\varepsilon$, respectively.

Note that all the three cases have distinct detunings (Δ). Therefore, it is not fair to compare the sensitivity values under these conditions. For example, even though the third harmonic should have a wavelength shift enhanced by 4-times ($i+1$, with $i=3$), it ended up having smaller sensitivity than the second harmonic because of the larger detuning. Hence, the correct way to analyze the response of the structures, in order to make a fair comparison between them, is going to be presented next.

6.2.4. Demonstration of the Optical Harmonic Vernier Effect Enhancement

The sensitivity values obtained before for each harmonic order, together with the sensitivity value for the individual sensing FPI, allows to calculate the M-factor through equation 4.29. The M-factors for the first three harmonic orders, calculated through the sensitivity values, are 8.18, 27.7, and 17.7, respectively. On the other hand, the M-factor can also be obtained via a second definition, using equation 5.21. Hence, performing the ratio between the FSR of the internal envelope and the FSR of the individual sensing FPI, the M-factors achieved are 8.38, 28.42, and 18.33, respectively for the first three harmonic orders. Both M-factors, defined using the FSR (equation 5.21) or using the sensitivities (equation 4.29), are approximately the same, with a maximum deviation of 3.5 %. In other words, the two definitions for the M-factor are equivalent.

Yet, these values still depend on the detuning (Δ) between the sensing and the reference interferometers, and therefore it is not possible to make a fair comparison between them. One way to eliminate this dependency and observe the improvement introduced by the optical harmonic Vernier effect is to compare the M-factor of each harmonic order with the M-factor obtained if it was the fundamental case. In other words, by performing the ratio between the M-factor for a harmonic order i and the M-factor for $i=0$, the result should be $i+1$, according to equation 5.21. Due to the regeneration property of the upper envelope, its FSR for any harmonic order is the same as for the fundamental case. Hence, for each harmonic order, the FSR of the upper envelope can be used to calculated the M-factor of the respective fundamental case, with the same detuning, using equation 4.27. With this, the M-factors of the fundamental case (M_0) for the each situation are 4.19, 9.47, and 4.58, respectively. The ratios between the M-factor obtained via the sensitivities and the corresponding M_0 are 1.95, 2.93, and 3.86, respectively for the first three harmonic orders. As seen by these ratios, the M-factor for each harmonic order is increasing approximately by a factor of $i+1$, as theoretically predicted through equation 5.21.

In fact, both the M-factor for each harmonic and the respective M_0 depend on the detuning, since the FSR of the upper envelope and the internal envelopes also depend on the detuning. Therefore, the ratio between these two is independent of the detuning (Δ).

A different way to demonstrate more directly the linear enhancement of the M-factor with the order of the harmonics is to use a compensated wavelength shift. The compensated wavelength shift takes into consideration the FSR of the upper envelope which, as discussed before, is an indicator of the detuning (Δ). Therefore, the compensated wavelength shift can be expressed as:

$$\Delta\lambda_{compensated} = \frac{\Delta\lambda}{FSR_{envelope}}, \tag{6.1}$$

which is independent of the detuning between the sensing and the reference interferometers. This quantity can be transformed into a more meaningful value as:

$$\Delta\varphi_{envelope} = \frac{2\pi\Delta\lambda}{FSR_{envelope}}, \tag{6.2}$$

corresponding to the phase shift of the Vernier envelope, which is also independent of the detuning. Figure 6.6 shows the Vernier envelope phase shift as a function of the applied strain.

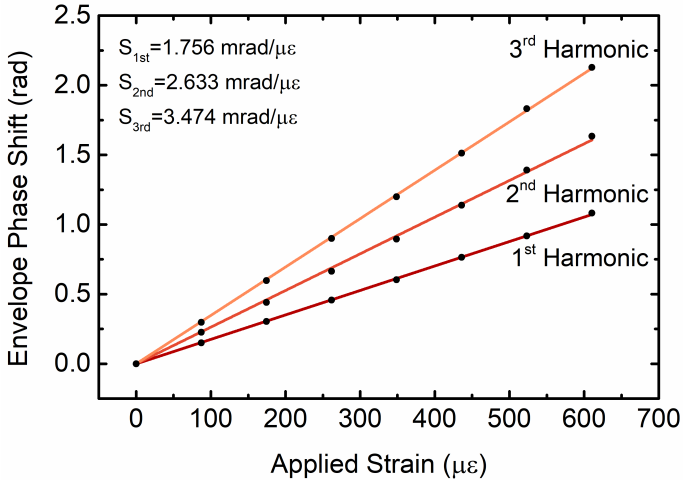

Figure 6.6. – Phase shift of the Vernier envelope as a function of the applied strain for the first three harmonic orders. The sensitivity values are given by the slope of the linear fit.

The envelope phase sensitivity ($S_{\varphi env}$) to the applied strain ($\Delta\varepsilon$) is given by the slope of the linear fit, defined as:

$$S_{\varphi env} = \frac{2\pi}{FSR_{envelope}}\frac{\Delta\lambda}{\Delta\varepsilon}. \tag{6.3}$$

The envelope phase sensitivities to strain for the first three harmonic orders of the optical Vernier effect are, respectively, $(1.756 \pm 0.005)\,\mathrm{mrad}/\mu\varepsilon$, $(2.633 \pm 0.002)\,\mathrm{mrad}/\mu\varepsilon$, and $(3.474 \pm 0.009)\,\mathrm{mrad}/\mu\varepsilon$. These values are independent of the detuning (Δ), allowing to compare each experimental harmonic order. As observed, the envelope phase sensitivity

Table 6.1. – Overview of the experimental results for the first three harmonic orders. First group: Experimental results. Second group: M-factor via two definitions (equations 5.21 and 4.29) are approximately the same. Third group: M-factor for each harmonic order compared with the M-factor for the fundamental optical Vernier effect (M_0). It shows the $i+1$ improvement factor with the order of the harmonic.

	S ($pm/\mu\varepsilon$)	$S_{\varphi env}$ ($mrad/\mu\varepsilon$)	**M-factor** (via FSR_{env}) equation 5.21	**M-factor** (via S) equation 4.29	**M (via S)/ M_0**	$(i+1)$
1^{st} H.	27.6	1.765	8.38	8.18	1.95	2
2^{nd} H.	93.4	2.633	28.41	27.70	2.93	3
3^{rd} H.	59.6	3.474	18.32	17.70	3.86	4

increases with the order of the harmonics, which is also in accordance with equation 5.21.

Table 6.1 summarizes the main values of the experimental results. The results are organized in three groups. The first resumes the experimental results for strain sensitivity of the Vernier envelope (S) and the envelope phase strain sensitivity ($S_{\varphi env}$). The envelope phase sensitivity to strain is a way to observe only the enhancement provided by the optical harmonics, since it is independent of the detuning between the sensing and the reference interferometers. The second group presents the M-factors achieved using the two definitions: via the FSR of the internal envelopes, through equation 5.21, and via the sensitivity of the Vernier envelope, through equation 4.29. The values obtained are very similar, validating the use of both definitions. At last, the third group consists of the ratio between the M-factor for each harmonic order, determined using the Vernier envelope sensitivity, and the M-factor for the equivalent fundamental optical Vernier effect (M_0). It shows the $i+1$ factor improvement in the M-factor with the order of the harmonic, as predicted by equation 5.21.

6.3. Series Configuration

6.3.1. Introduction

The use of optical harmonics of the Vernier effect in a series configuration without a physical separation between the interferometers is experimentally explored in this section. This case corresponds to a complex optical Vernier effect, where none of the interferometers in the configurations is used as a reference. The proposed structure was characterized for strain and temperature sensing. This section also explores simultaneous measurement of these two parameters by making use of the Vernier envelope response, together with the response of the higher frequency of the Vernier spectrum.

6.3.2. Fabrication

A schematic of the developed sensing structure is presented in figure 6.7. The sensing structure consists of two Fabry-Perot interferometers (FPIs) in a series configuration. The first interferometer (FPI_1) is a hollow microsphere fabricated from a special splice between two sections of a multimode graded-index fiber (GIF). Hollow microspheres exhibit a strain sensitivity that increases with the dimensions of the microsphere [207]. Such effect is the opposite of what is observed for most of the fiber FPIs reported, whose strain sensitivity increases for smaller cavity lengths. In fact, the increasing strain sensitivity of a hollow microsphere with its dimensions results from mechanical effects, due to the intrinsic shape of the hollow microsphere. The second interferometer (FPI_2) is given by a section of the multimode GIF used to fabricate the hollow microsphere. At the end, a hollow capillary tube is spliced after the second interferometer, only for the purpose of providing a fiber extension to enable the application of strain, as will be discussed later.

The first interferometer (FPI_1) is then formed by an air cavity between the mirror interfaces M_1 and M_2, with reflection coefficients R_1 and R_2, while the second interferometer (FPI_2) consist of a silica cavity between the mirror interfaces M_2 and M_3, with reflection coefficients R_2 and R_3, as illustrated in figure 6.7. In this case, all the interfaces provide a silica/air Fresnel reflection, resulting in a reflection coefficient equal for all interfaces. The proposed structure is similar to the one described theoretically in section 5.4. Therefore, the output spectrum as a function of the harmonic order is given by equation 5.29.

Figure 6.8 presents the fabrication steps to produce the sensing structure. Initially, a multimode GIF (core diameter of 62.5 μm and a cladding diameter of 125 μm, from Fibercore) was spliced to a single-mode fiber (SMF28), and then cleaved with a length of around 1 cm. Subsequently, a hollow microsphere was created between the cleaved multimode fiber (MMF) and another section of the same fiber employing a post-processing technique reported by Novais *et al.* [208]. This technique consists of three different steps:

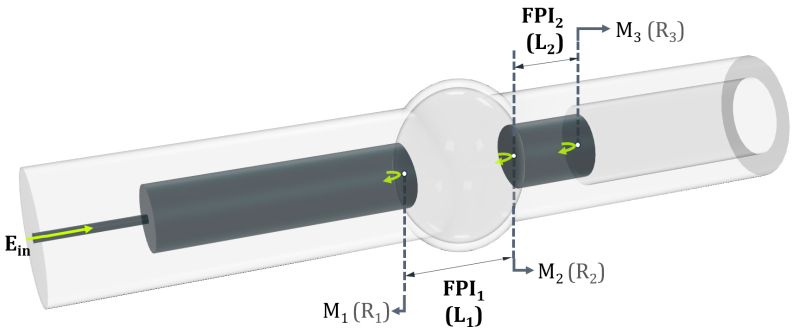

Figure 6.7. – Schematic of the sensing structure consisting of two Fabry-Perot interferometers (FPIs) in series. FPI_1 is a hollow microsphere with length L_1. FPI_2 is a section of multimode fiber with length L_2, followed by a hollow capillary tube. The three interfaces are marked as M_1, M_2, and M_3, respectively with reflection coefficients R_1, R_2, and R_3.

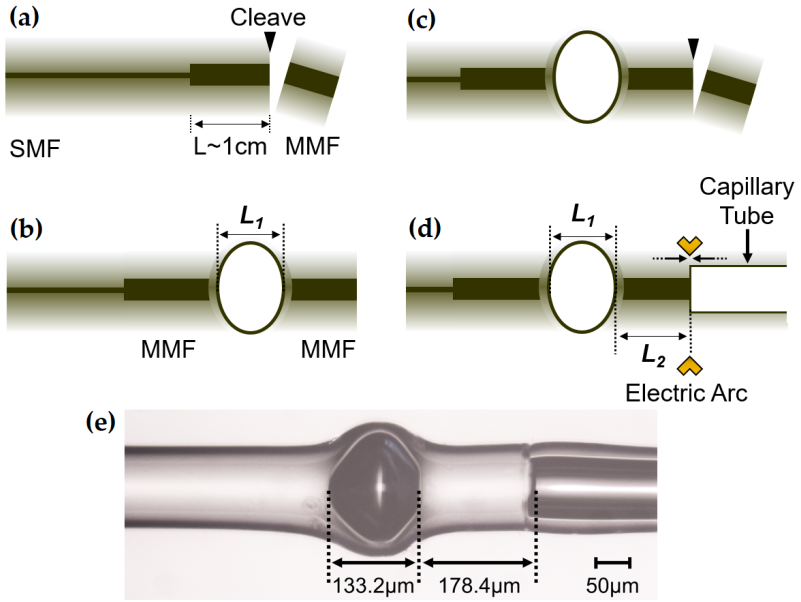

Figure 6.8. – Fabrication steps: (a) cleaving an MMF spliced to an SMF; (b) air bubble formation; (c) cleaving of the second MMF; (d) splice with a hollow capillary tube; (e) micrograph of the final structure.

rounding the multimode GIF, forming and growing the hollow microsphere. These three stages of the process were executed using a Fitel S177 splicing machine, together with the parameters described in table 6.2. The size of the hollow microsphere is controlled by the number of electric arcs applied. Simultaneously, the reflected spectrum was monitored to ensure that the hollow microsphere was not multimode, hence producing approximately a two-wave interferometer (FPI with low finesse).

An example of a reflected spectrum from a single hollow microsphere is depicted in figure 6.9(a). All the reflected spectra in this work were measured using a traditional reflection configuration, previously described in figure 3.9(a). The M-factor provided by the optical Vernier effect depends largely on the detuning between the two FPIs. Therefore, it is crucial to cleave the second MMF with the exact length needed to generate an optical Vernier effect with a large M-factor, considering the dimensions of the hollow microsphere

Table 6.2. – Post-Processing – Splicer Parameters.

	Rounding	**μ-sphere Formation**	**μ-sphere Growing**
Power [arb. units]	20	40	40
Duration [ms]	700	300	300
Z-push distance [µm]	0	0	0
Gap [µm]	0	5	5

fabricated before. To do so, one needs to estimate the cavity length (L_1) of the hollow microsphere through the interferometric signal obtained in figure 6.9(a), according to equation 4.25. The retrieved length is then used to estimate the length of the MMF (FPI_2) that would produce an optical Vernier effect with a large M-factor, but still with an envelope FSR within the wavelength range available by the measuring equipment. As a result of this constrain, an envelope FSR of 300 nm was considered for the estimations. To cleave the MMF (FPI_2), as illustrated in figure 6.8(c), a magnification lens above the cleaver can help to increase the precision of the cleaving, since the target dimensions are in the order of hundreds of microns. After cleaving the MMF the main structure is finished and the optical Vernier effect can already be observed in the reflected spectrum, as depicted in figure 6.9(b). The structure was fabricated to generate the fundamental optical Vernier effect.

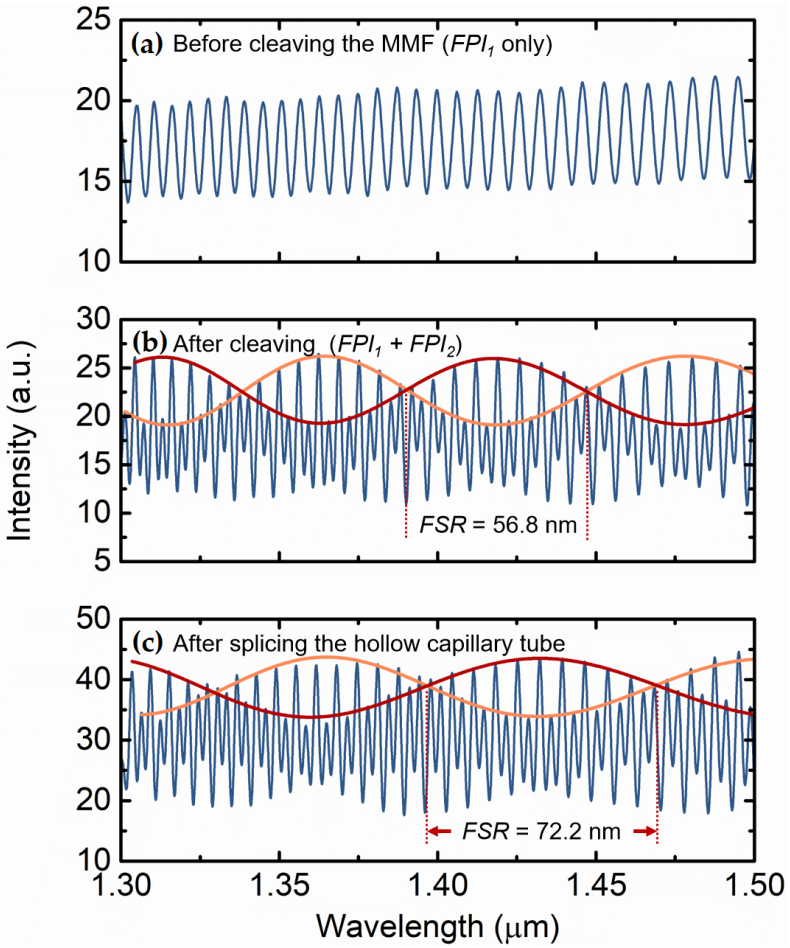

Figure 6.9. – Reflected spectrum at three different fabrication stages. (a) Hollow microsphere (FPI_1), with an FSR of 6.4 nm. (b) Hollow microsphere plus cleaved MMF ($FPI_1 + FPI_2$). The fundamental Vernier effect is introduced with an envelope FSR of 56.8 nm. (c) Hollow capillary tube spliced to the MMF with a small pre-tension. The Vernier envelope FSR increased to 72.2 nm. Internal envelopes indicated by red/orange lines.

As stated before, a fiber extension is required so that the structure can work as a strain sensor. However, the fiber extension must not affect the third interface (M_3). The best case is to add a fiber extension that preserves the silica/air interface. To solve this problem, a hollow capillary tube with an inner diameter of 80 μm (larger than the core of the MMF) and an outer diameter of 125 μm, fabricated at Leibniz IPHT, was used as a fiber extension. The splice between the hollow capillary tube and the MMF was performed with the electric arc centered in the capillary tube to avoid modifications of the MMF edge, corresponding to the third interface (M_3). Such modifications or deformations can cause additional detuning between the two FPIs, reducing the M-factor of the optical Vernier effect and, in extreme cases, leading to the annihilation of the effect. Nevertheless, if the OPL of the second interferometer (FPI_2) is slightly larger than desired, the splice between the MMF and the hollow capillary tube can be used to tune the MMF length. The final length of the MMF can be slightly reduced by compression if a small pre-tension between the fibers is added before the splice. This effect is illustrated in figure 6.9(c), where the reflection spectrum after splicing the hollow capillary tube with a small pre-tension allowed to slightly reduce the OPL of the MMF, and consequently increase the FSR of the internal envelopes compared with the previous case of figure 6.9(b). As a result, the final M-factor of the structure is also increased.

The structure used as an example, whose spectra are presented in figure 6.9, corresponds to the fundamental optical Vernier effect. To obtain a strain sensor with additional enhancement of sensitivity, it is valuable to make use of the optical harmonics of the Vernier effect. In this case, a new hollow microsphere was fabricated using the same method and the OPL of the second interferometer (FPI_2), corresponding to the MMF, was increased by 1-fold the OPL of the hollow microsphere. Such situation generates the first optical harmonic of the Vernier effect. A micrograph of the final sensing structure is shown in figure 6.8(e). The physical length (L_1) of the hollow microsphere is 133.2 µm, while the length of the MMF (L_2) is 178.4 µm. Considering a refractive index (n_2) of around 1.47 for the MMF, the OPL of the second interferometer (FPI_2) is:

$$OPL_2 = 2n_2L_2 = 2 \times 1.47 \times 178.4 = 524.5\,\mu m. \tag{6.4}$$

As for the hollow microsphere, considering a refractive index of air (n_1) equal to 1.0003 (at a temperature of 15 °C and wavelength of 1550 nm [146]), its OPL is given by:

$$OPL_1 = 2n_1L_1 = 2 \times 1.0003 \times 133.2 = 266.5\,\mu m. \tag{6.5}$$

The detuning between the two interferometers can be then estimated using equation 5.3, where the first harmonic corresponds to $i = 1$. Hence, the detuning of the fabricated structure is approximately:

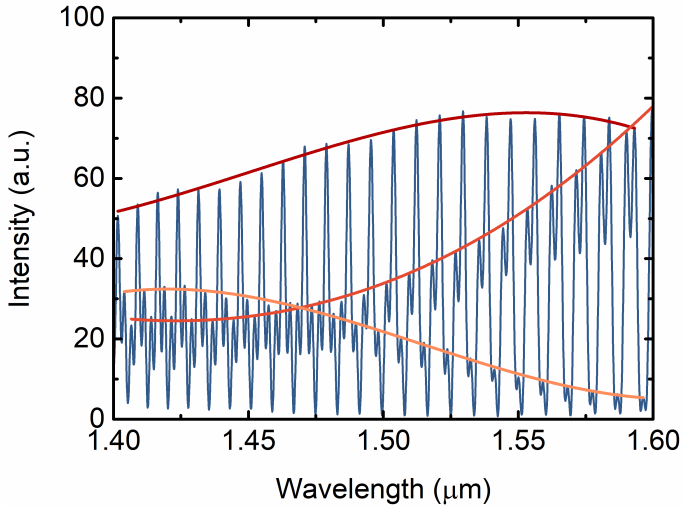

Figure 6.10. – Reflected spectrum of the fabricated structure. The response corresponds to the first harmonic of the Vernier effect in a series configuration.

$$OPL_2 = (i+1)\,OPL_1 - 2\Delta \leftrightarrow \Delta = 4.25\,\mu m. \tag{6.6}$$

Such small detuning value will generate a large Vernier envelope, with high M-factor. The experimental reflected spectrum of this structure is presented in figure 6.10. The presence of large internal envelopes is confirmed, as well as the number of internal envelopes (3) matches expected number of $i+2$ for the first harmonic of the optical Vernier effect in a series configuration, as discussed before in section 5.4. Note that peaks with low visibility are visible in the experimental spectrum. Previously in the simulated reflected spectrum of an equivalent structure, shown in figure 5.12(e), it was already possible to observe the presence of peaks with lower visibility. This effect comes from the light reflected at the third interface (M_3) having much less intensity compared with the light reflected at the other two interfaces. Adding to this, the presence losses and imperfections of the interfaces reduces even more the visibility of the peaks.

6.3.3. Complex Optical Harmonic Vernier Effect

Up to now, all the cases of optical harmonic Vernier effect involved the use of one of the interferometers as a stable reference. As explained in section 4.2.2, under the presence of a stable reference interferometer the M-factor can be defined as the ratio between the sensitivity of the Vernier envelope ($S_{envelope}$) and the sensitivity of the individual sensing interferometer (S_{FPI1}), expressed by equation 4.29.

Although for many sensing structures this description is correct, it is no longer valid for this proposed configuration. Here, both interferometers are affected by the measurands at the same time (strain and/or temperature). Hence, both interferometers are considered as

a combined sensing structure, without employing a specific interferometer as a reference, unlike in a parallel setup. At the end, one expects then that the Vernier envelope sensitivity will depend on the sensitivity of both interferometers.

To further understand the influence and contribution of each interferometer to the sensitivity of the Vernier envelope, let us consider the interferometric component of lower frequency correspondent to the Vernier envelope. The phase of the Vernier envelope is proportional to the difference between the OPLs of the two interferometers and can be expressed as:

$$\varphi_{envelope} = \frac{4\pi}{\lambda}\left(n_1 L_1 - n_2 L_2\right), \tag{6.7}$$

where n_1 and n_2 are the effective refractive indices of the first and second FPIs, respectively, and L_1 and L_2 are the physical lengths of the same interferometers. The strain sensitivity of the Vernier envelope is defined as:

$$S_{envelope} = \frac{d\lambda}{dL} = \frac{4\pi}{\varphi_{envelope}}\left(n_1\frac{\partial}{\partial L}L_1 - n_2\frac{\partial}{\partial L}L_2\right), \tag{6.8}$$

where L is the total length to which strain is applied. In this approach the elasto-optic coefficient $(\partial n/\partial L)$ was assumed as negligible compared with the variations of length. Equation 6.7 can be replaced in equation 6.8 which, for a maximum or minimum wavelength of the Vernier envelope ($\lambda_{max,min}$), results in:

$$S_{envelope} = \frac{\lambda_{max,min}\left(n_1\frac{\partial}{\partial L}L_1 - n_2\frac{\partial}{\partial L}L_2\right)}{\left(n_1 L_1 - n_2 L_2\right)}. \tag{6.9}$$

After some algebraic manipulations, the strain sensitivity of the Vernier envelope can be expressed by the sum of two components, given by:

$$S_{envelope} = \frac{n_1 L_1 \frac{\lambda_{max,min}}{L_1}\frac{\partial L_1}{\partial L}}{n_1 L_1 - n_2 L_2} + \frac{n_2 L_2 \frac{\lambda_{max,min}}{L_2}\frac{\partial L_2}{\partial L}}{n_2 L_2 - n_1 L_1}. \tag{6.10}$$

Equation 6.10 can be rearranged as a function of the strain sensitivities of the interferometers that compose the structure (S_1 and S_2 respectively for FPI_1 and FPI_2). Therefore, equation 6.10 can be rewritten in the form of:

$$S_{envelope} = \frac{n_1 L_1}{n_1 L_1 - n_2 L_2} S_1 + \frac{n_2 L_2}{n_2 L_2 - n_1 L_1} S_2. \tag{6.11}$$

Curiously, the two pre-factors are the M-factors previously described by equation 4.28. Hence, the previous equation can be finally expressed as:

$$S_{envelope} = M_1 S_1 + M_2 S_2, \tag{6.12}$$

where M_1 is the M-factor considering the first interferometer (FPI_1) as the sensing in-

terferometer, while M_2 is the M-factor considering the second interferometer (FPI_2) as the sensing interferometer. The same analysis could also be performed for temperature sensitivity, leading to similar results.

Since the OPLs of the two interferometers have a small detuning between them, one of the quotients of equation 6.11 will be negative. In other words, one of the M-factors in equation 6.12 will be negative. Thus, the sensitivity of the vernier envelope is given by the difference between the sensitivities of the two interferometers that compose the sensing structure, but weighted by their M-factors, respectively.

Under these circumstances, three possible results can be expected. When both interferometers have similar sensitivities, both positive or both negative, the contribution of each interferometer to the sensitivity of the Vernier envelope would cancel each other out. This situation leads to the annihilation of the M-factor provided by the Vernier envelope.

The second scenario, which corresponds to the proposed sensor, consists of having two interferometers with distinct sensitivities, both positive or both negative. Here, the difference between the sensitivities can still be large, and therefore, magnified through the optical Vernier effect. The hollow microsphere interferometric structure has considerably higher strain sensitivity than the FPI given by the MMF. On the other hand, the MMF FPI has higher temperature sensitivity than the hollow microsphere, where light mainly propagates in air. Therefore, the proposed structure can still present higher sensitivities to strain and temperature.

The last scenario, not demonstrated in this dissertation, consists of having two interferometers with opposite sensitivities to the measured parameters. When this happens, the sensitivity of the Vernier envelope would depend on the sum between the sensitivities of the two interferometers, and not on the difference. Such case could achieve even higher M-factors and sensitivities than the previous cases, including the case of having a reference interferometer. An example of the application of such effect is the work of Li *et al.* [202] reported in 2020, which was previously explored in section 4.3.2, and also our recent work (Robalinho *et al.* [18]).

6.3.4. Characterization in Strain and Temperature

The fabricated sensing structure presenting the first harmonic order of the optical Vernier effect was characterized in strain and temperature. To perform strain measurements, the structure was fixed on two translation stages, with a displacement resolution of 0.01 mm, using cyanoacrylate adhesive. The two fixing points are located away from the two FPIs. The first fixing point is at the MMF before the hollow microsphere (FPI_1) and the second fixing point is at the hollow capillary tube after the second MMF (FPI_2). A small pre-tension was added to the system, ensuring that the fiber was not bent. The initial fiber length between the two fixed points was 345 mm. Strain was applied in successive

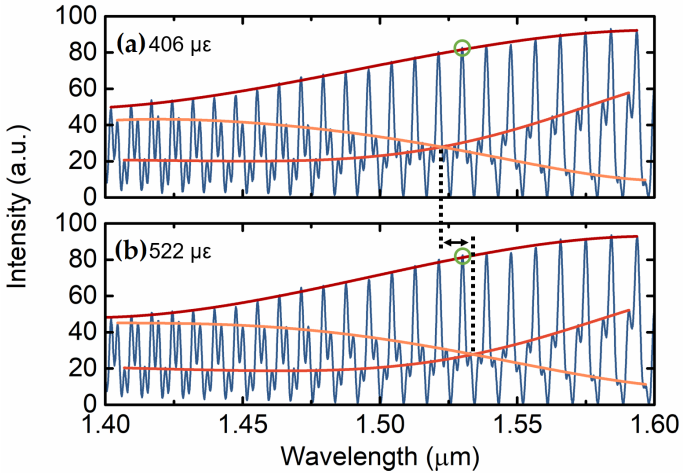

Figure 6.11. – Reflected spectra at two distinct values of applied strain: (a) 406 $\mu\varepsilon$, (b) 522 $\mu\varepsilon$. The Vernier envelope wavelength shift was monitored at the internal envelope intersection. The maximum marked with a green circle was also monitored as a function of the applied strain.

steps of 57.9 $\mu\varepsilon$ (corresponding to 20 μm extension of the translation stage) until a total of approximately 500 $\mu\varepsilon$ was reached, while monitoring simultaneously the reflected spectrum.

Figures 6.11(a) and (b) exhibit the reflected spectrum of the sensing structure under two distinct situations of applied strain (406 $\mu\varepsilon$ and 522 $\mu\varepsilon$). The internal envelope intersection between 1500 nm and 1550 nm was monitored as a function of the applied strain. When strain is applied, the Vernier envelope shifts towards longer wavelengths.

Figure 6.12 presents the wavelength shifts of the Vernier envelope and of an individual

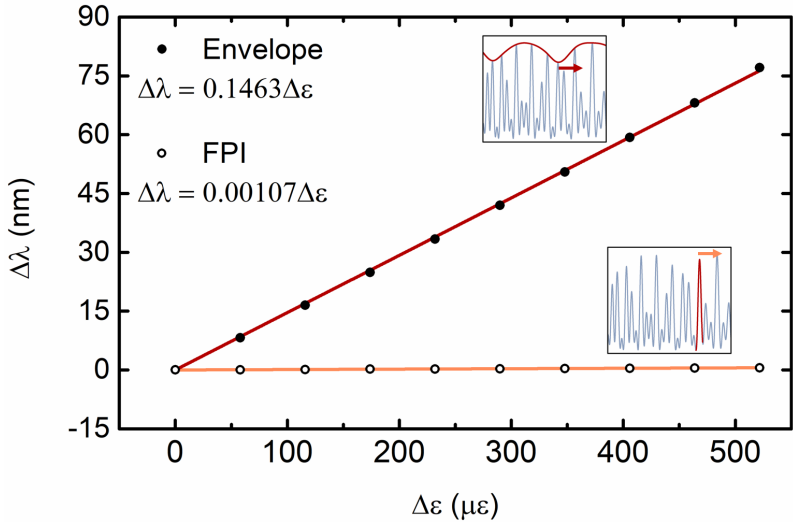

Figure 6.12. – Wavelength shift ($\Delta\lambda$) of the Vernier envelope and individual interference peak as a function of applied strain ($\Delta\varepsilon$).

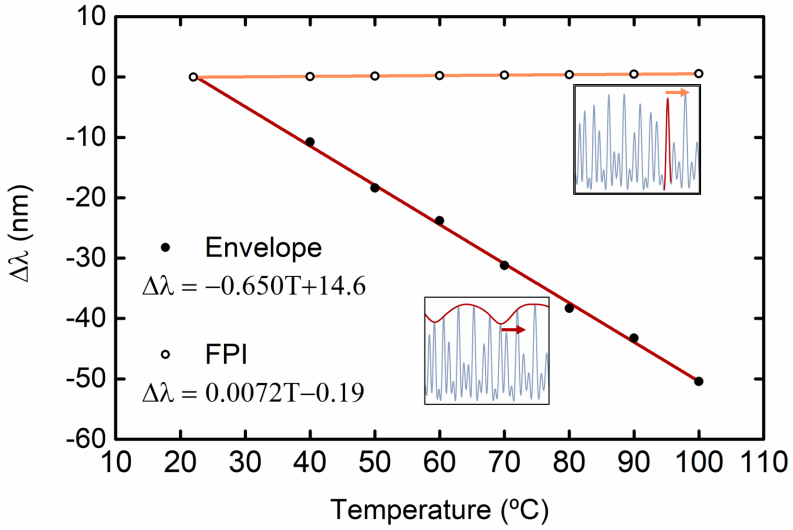

Figure 6.13. – Wavelength shift ($\Delta\lambda$) of the Vernier envelope and individual interference peak as a function of temperature (T).

interference maximum, marked in figure 6.11 with a green circle, as a function of the applied strain. The Vernier envelope achieved a strain sensitivity of $(146.3 \pm 0.4)\,\mathrm{pm}/\mu\varepsilon$, while the individual interference maximum showed a sensitivity of $(1.070 \pm 0.005)\,\mathrm{pm}/\mu\varepsilon$. The high sensitivity to strain achieved by the Vernier envelope is explained by two aspects: first, by a large overall M-factor due to the first harmonic of the optical Vernier effect with small detuning, and second, due the higher strain sensitivity of the hollow microsphere when compared to the sensitivity of the second silica interferometer. The impact of using higher harmonic orders of the optical Vernier effect in this configuration will be analyzed later.

A similar analysis was performed to characterize the response of the sensing structure to temperature. The sensor was placed inside a tubular oven, whose temperature was then increased up to 100 °C. The sensor response was evaluated for a temperature decreasing from 100 °C until room temperature. The wavelength shifts of the Vernier envelope and an individual interference maximum, marked in figure 6.11 with a green circle, are depicted in figure 6.13 as a function of temperature. The Vernier envelope showed a temperature sensitivity of $(-650 \pm 9)\,\mathrm{pm}/°\mathrm{C}$, while the individual interference maximum reached a sensitivity value of $(7.2 \pm 0.2)\,\mathrm{pm}/°\mathrm{C}$.

6.3.5. Simultaneous Measurement of Strain and Temperature

Even though the individual interference maximum does not correspond to the individual response of the hollow microsphere (FPI_1), neither to the individual response of the MMF section (FPI_2), as explored back in section 4.2.2, one can still make use of it.

An additional advantage of having the optical Vernier effect is the possibility of using the sensing structure to perform simultaneous measurement of two parameters, by also making use of the individual interference peaks. In fact, this is possible since the Vernier envelope and the interference peaks have different sensitivities to the measurands.

The relationship matrix, as used in section 3.2, can be derived for this approach using the wavelength shift of Vernier envelope and the individual interference maximum, together with the corresponding variations in strain ($\Delta\varepsilon$) and temperature (ΔT) as:

$$\begin{bmatrix} \Delta T \\ \Delta\varepsilon \end{bmatrix} = \frac{1}{D} \begin{bmatrix} k_{2\varepsilon} & -k_{1\varepsilon} \\ -k_{2T} & k_{1T} \end{bmatrix} \begin{bmatrix} \Delta\lambda_{envelope} \\ \Delta\lambda_{peak} \end{bmatrix}, \tag{6.13}$$

where $\Delta\lambda_{envelope}$ and $\Delta\lambda_{peak}$ are the wavelength shifts of the Vernier envelope and the individual interference peak, respectively. The matrix elements $k_{1\varepsilon}$ and k_{1T} are, respectively, the sensitivities of the Vernier envelope to variations of strain and temperature. As for the matrix elements $k_{2\varepsilon}$ and k_{2T}, they correspond to the sensitivity of the individual interference peaks to strain and temperature, respectively. D is the determinant of the matrix, given by $k_{1T}k_{2\varepsilon} - k_{1\varepsilon}k_{2T}$. Replacing the sensitivity values determined before in equation 6.13, the matrix can be expressed as:

$$\begin{bmatrix} \Delta T \\ \Delta\varepsilon \end{bmatrix} = -571.8 \begin{bmatrix} 0.00107 & -0.1463 \\ -0.0072 & -0.650 \end{bmatrix} \begin{bmatrix} \Delta\lambda_{envelope} \\ \Delta\lambda_{peak} \end{bmatrix}, \tag{6.14}$$

where the wavelength shifts $\Delta\lambda_{envelope}$ and $\Delta\lambda_{peak}$ are given in nanometers, and the output variations ΔT and $\Delta\varepsilon$ are given in °C and $\mu\varepsilon$, respectively. The units of the matrix elements are the same as in the previous subsection.

In real applications, if one measuring parameter is fixed while the other is changing, the output of the matrix will still present small variations for the fixed parameter. The error associated to the matrix method can be estimated by plotting the output of the matrix for variations of strain at constant temperature, and for variations of temperature at constant applied strain. The matrix output is represented in figure 6.14. The standard deviation (σ) of the matrix method is 5.9 $\mu\varepsilon$ and 0.4 °C, respectively in the determination of the resulting strain and temperature.

6.3.6. Considerations about the Optical Harmonic Vernier Effect Enhancement

The enhancement of the M-factor, that scales proportionally to the harmonic order, was already demonstrated for a parallel configuration. However, for a series configuration where both interferometers are physically connected and no reference interferometer is used, as here demonstrated, it is difficult to calculate an overall M-factor for the structure and compare it with other harmonic orders. Nevertheless, it is still possible to visualize

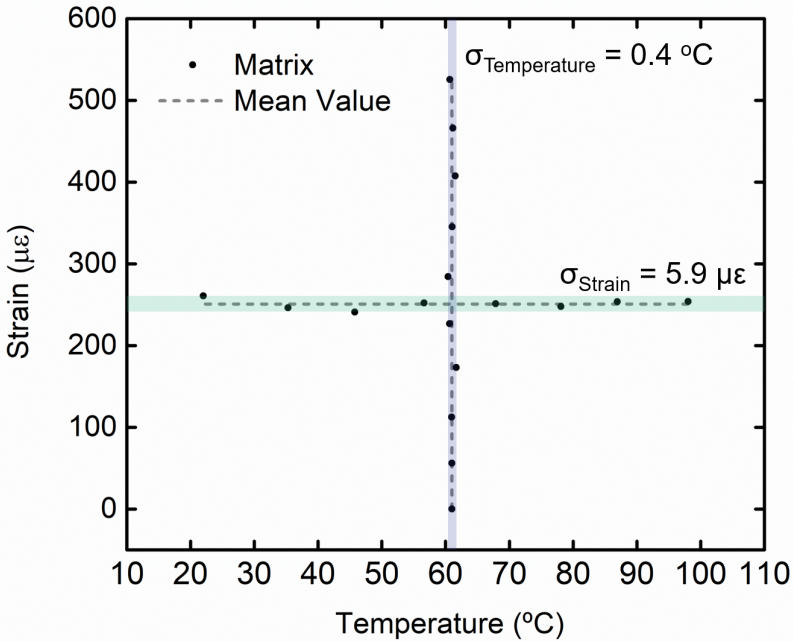

Figure 6.14. – Matrix output as determined by equation 6.14 for an applied strain at constant temperature, and a temperature variation at constant strain.

the enhancement provided by optical harmonic Vernier effect for this case.

To do so, two extra similar sensing structures were fabricated. The dimension of the sensors are such that the fundamental optical Vernier effect is generated. The first sensing structure has a hollow microsphere (FPI_1) with a length of 141 μm in combination with a second MMF FPI, while the second sensing structure has a hollow microsphere (FPI_1) with a length of 114 μm, also in combination with a second MMF FPI. Naturally, due to fabrication constrains, both structures have different detunings between their FPI_1 and FPI_2. Figure 6.15 shows the reflected spectra for the two fabricated structures with the fundamental optical Vernier effect. The FSRs of the Vernier envelope are 116.9 nm and 136.4 nm for the structure with a hollow microsphere of 114 μm and for the structure with a hollow microsphere of 141 μm, respectively.

Both sensors were characterized in strain by the same procedure as described previously. The wavelength shift of the Vernier envelopes is represented in figure 6.16(a) as a function of the applied strain for the two new structures, together with the previously analyzed sensor with the first harmonic of the optical Vernier effect. The first harmonic structure presents a strain sensitivity of (146.3 ± 0.4) pm/$\mu\varepsilon$, much higher than both of the new structure with the fundamental optical Vernier effect, which only present (65.3 ± 0.1) pm/$\mu\varepsilon$ and (28.6 ± 0.5) pm/$\mu\varepsilon$, respectively for an L_1 equal to 141 μm and 114 μm.

Nevertheless, the structures present different detunings, which do not allow a straight-

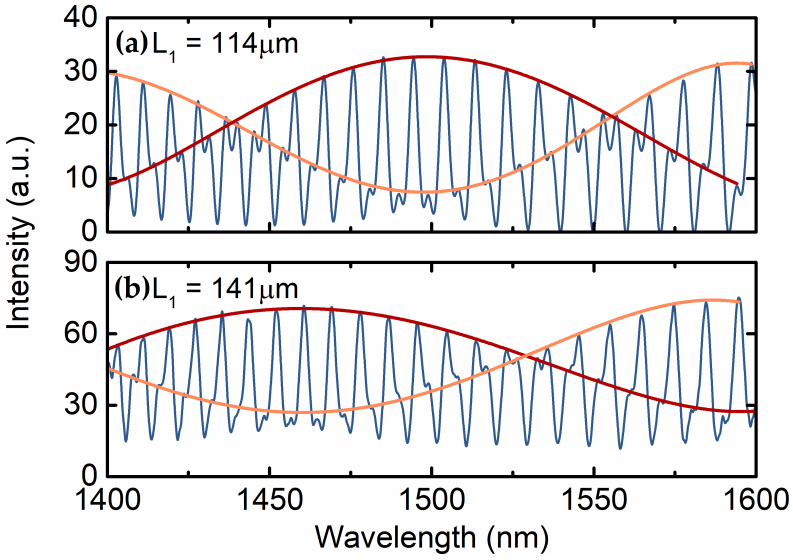

Figure 6.15. – Reflected spectra of the two fabricated structures with the fundamental optical Vernier effect. (a) Hollow microsphere with a length of 114 μm. (b) Hollow microsphere with a length of 141 μm. The detuning (Δ) is different in both cases.

forward comparison between the performance of the first harmonic of the optical Vernier effect and the fundamental case. Therefore, the wavelength shift of each structure was normalized to the corresponding FSR of the Vernier envelope, and represented in the form of envelope phase shift ($\Delta\varphi_{envelope} = 2\pi\Delta\lambda/FSR_{envelope}$), as in section 6.2.4. For the structure with the first harmonic represented in figure 6.10, the FSR of the Vernier envelope was considered as 244.88 nm, corresponding to twice the distance between the two internal envelope intersections (at 1591.70 nm and 1469.26 nm). Figure 6.16(b) shows the Vernier envelope phase shift ($\Delta\varphi_{envelope}$) as a function of the applied strain for the same structures. The Vernier envelope phase sensitivities to strain are now (1.53 ± 0.02) mrad/$\mu\varepsilon$, (3.010 ± 0.006) mrad/$\mu\varepsilon$, and (3.75 ± 0.01) mrad/$\mu\varepsilon$, respectively for the fundamental optical Vernier effect with L_1 equal to 114 μm and 141 μm, and for the 1st harmonic of the Vernier effect with L_1 equal to 133.2 μm.

Note that the sensitivity of the second interferometer (FPI_2) of each structure should not change much with its dimensions, while the sensitivity of a hollow microsphere strongly depends on its dimensions, according to Novais *et al.* [207]. Even though one of the structures with the fundamental optical Vernier effect has a hollow microsphere with a length of 141 μm, the sensitivity of the Vernier envelope is still smaller than that of a structure with the first harmonic of the Vernier effect but with a smaller hollow microsphere size (133.2 μm). This suggests that the overall M-factor for the series configuration should also increase with the order of the harmonic. However, it is not possible to further quantify the improvement provided by the first harmonic for the fabricated structure, due to the complexity of the presented case described by equation 6.12. One would need to have

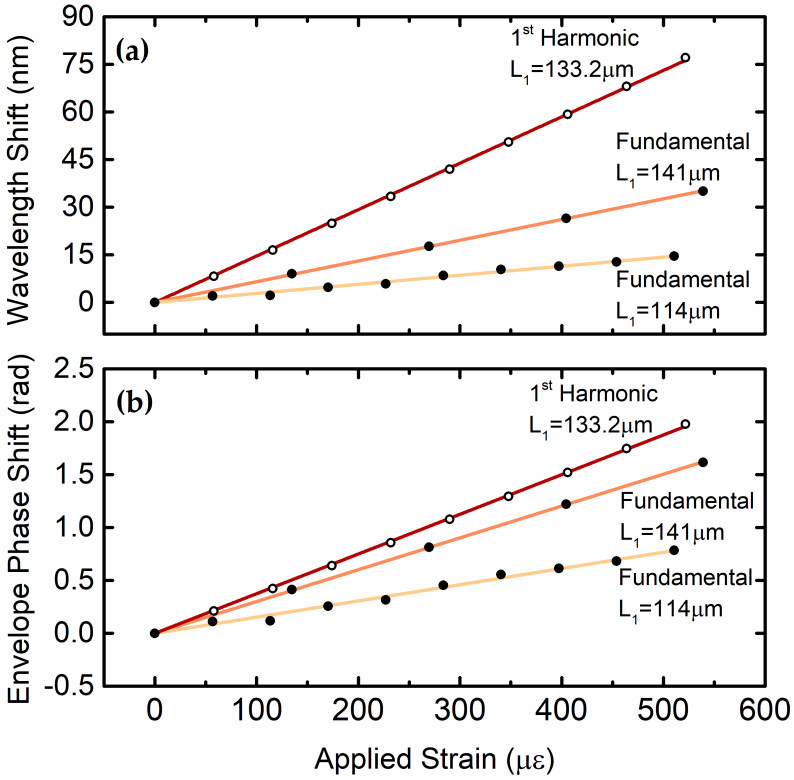

Figure 6.16. – (a) Wavelength shift of the Vernier envelope as a function of the applied strain for the two fabricated sensors with the fundamental optical Vernier effect and for the 1st harmonic analyzed previously. (b) Phase shift of the Vernier envelope as a function of the applied strain for the same structures as in (a).

access to the strain sensitivities of the hollow microspheres for the different dimensions, as well as the strain sensitivity of the FPI_2, which might change due to the OPL scaling needed to introduce the first harmonic when compared to the fundamental case. Moreover, the M_2-factor, corresponding to a situation where the second interferometer (FPI_2) is seen as the sensing interferometer and the first interferometer (FPI_1) is adopted as a reference, might not scale with the harmonic order. As demonstrated in section 5.3, if the sensing interferometer OPL is scaled up to introduce harmonics of the Vernier effect, instead of the reference interferometer, the M-factor might not bring any improvement of sensitivity with the harmonic order. Therefore, the number of variables to be considered is large. Nevertheless, a further quantification of this enhancement would be very valuable to be performed in the near future.

6.4. Conclusion

Optical harmonics of the Vernier effect bring considerable improvements in terms of the sensitivity of interferometric fiber sensors. As experimentally demonstrated in the first

part of this chapter, the use of optical harmonics of the Vernier effect allows to enhance the M-factor by $(i+1)$-times the value obtained for the fundamental optical Vernier effect, considering the same detuning.

Experimentally, it is very difficult to fabricate interferometric structures with exactly the same detuning, due to fabrication constrains. At the same time, one should have control over the detuning, especially if aiming for high M-factors with large envelopes. A small change in the detuning can be enough to reduce quite a lot the M-factor, or to increase the FSR of the Vernier envelope beyond the measurable limits imposed by the detection system. Therefore, it is crucial to explore and develop techniques to adjust the detuning during the fabrication process. In this chapter, the detuning was adjusted by means of adding small compressions, together with an electric arc, to slightly reduce the OPL of a Fabry-Perot interferometer with a larger OPL than expected.

The structure produced to demonstrate the optical harmonic Vernier effect for a parallel configuration simply relies on hollow capillary tubes. Nevertheless, together with a well-tuned second harmonic of the optical Vernier effect, the sensing structure was capable of achieving a strain sensitivity of about 90-fold than that of a fiber Bragg grating (sensitivity of about $1\,\mathrm{pm}/\mu\varepsilon$ [209]).

Regarding the optical harmonic Vernier effect in a series configuration, the approach here adopted was towards the exploration of a complex case of the optical Vernier effect, where no reference interferometer was used. For that, a hollow microsphere was combined with a silica Fabry-Perot interferometer made of a section of multimode fiber, achieving a strain sensitivity for the first harmonic of about 140-fold higher than that of an FBG. Moreover, simultaneous measurement of two parameters (strain and temperature) was achieved by taking advantage of the higher frequency component of the Vernier spectrum, together with the Vernier envelope.

The complex case of optical Vernier effect, without the presence of a reference interferometer, should be further explored. If well designed and dimensioned, especially using two interferometers with opposite sensitivities, this case has potential for the development of sensing structures with even higher sensitivities than the ones reported in the literature using the optical Vernier effect.

Now that the optical harmonic Vernier effect was explored and demonstrated, one can make use of it to create advanced fiber sensing structures for more demanding applications. The next chapter explores advanced optical fiber devices for liquid media sensing. All the structures rely on simple hollow capillary tubes but combine different techniques, such as focused ion beam milling, post-processing with electric arc, and/or optical harmonic Vernier effect, enabling the development of novel and innovative fiber sensing structures. Moreover, a special extreme case of optical harmonic Vernier effect is also presented, allowing giant sensitivities to be achieved.

Chapter 7.

Advanced Fiber Sensors based on Microstructures for Liquid Media

7.1. Introduction

The last two works of this dissertation, discussed in this chapter, are advanced optical fiber sensing configurations for application in liquid media. Knowing the properties of a liquid solution is essential in many important areas, from industry to chemistry, biology, or even pharmacy. For this reason, there is a need for developing measurement techniques adapted to the liquid properties that are relevant for characterization.

Both configurations are still based on microfabricated structures. One of them merges simultaneously different concepts and techniques to obtain a high sensitivity and resolution and the other was designed to measure a liquid property that only a few optical fiber sensors are capable of measuring.

The first configuration combines an extreme case of optical Vernier effect with Fabry-Perot interferometers (FPIs) based on hollow capillary tubes. The structure was developed to create a sensing platform for liquid analytes with giant sensitivity to refractive index. Refractive index measurements are present in medical research, clinical diagnosis, food quality control, contamination of environments, industrial processes, or even to detect chemical and biological analytes. Yet, there is a lack of highly sensitive sensors, capable of providing higher resolution to sense tiny variations of the refractive index in small volumes, important for some state-of-the-art applications, such as tracking molecular binding, application in differential refractometers used for liquid chromatography, or possibly a new way to track molecular photo-switching. Many of these applications require high precision refractometers, in the order of 10^{-5} to 10^{-6} refractive index units (RIU) or lower. Optical microfibers have a sensitivity that could range from around 600 nm/RIU in combination with long period gratings [119], up to around 24000 nm/RIU in combination with a Mach-Zehnder interferometer effect [210]. Alternatively, one can also force light to propagate through the analyte by filling an interferometric cavity. Such approach consists of either

having an open cavity or creating access holes for the analyte. Femtosecond laser-milled cavities have a sensitivity that can go from 1163 nm/RIU (with a resolution of 10^{-6} RIU) for an FPI [211] to about 14297 nm/RIU for a Mach-Zehnder interferometric configuration (with a resolution of 10^{-5} RIU) [212]. The combination of plasmonics and optical fibers enabled the development of new sensing platforms, also for refractive index sensing. Their sensitivity can go up to around 40000 nm/RIU (with a resolution of 10^{-6} [213]). Due to the extreme optical Vernier effect, the configuration proposed in this chapter is able to achieve refractive index sensitivities an order of magnitude higher, close to 500000 nm of wavelength shift per RIU with an experimental resolution of 10^{-7} RIU.

The second configuration uses post-processing with an electric arc to create small hollow probe based on a hollow capillary tube, with a small access hole for liquids. The fiber probe was designed to use interferometric measurements to track the liquid displacement inside the probe, allowing to retrieve the viscosity of the liquid. Viscosity is a challenging property to measure in a fluid, especially if it involves small volumes. This property is directly involved in fluid flow processes, which are relevant and a matter of interest for different research areas. The optical fiber probe viscometer here presented is capable of measuring the viscosity of liquids using only tiny volumes (in the order of picoliters).

7.2. Giant Refractometric Sensivity based on Extreme Optical Vernier Effect

7.2.1. Introduction

All the different cases of optical Vernier effect explored and demonstrated before aimed to achieve high sensitivity values. In all situations, the ultimate parameter that regulates the particular enhancement outcome and the M-factor achieved by the effect is the detuning (Δ) between the two interferometers. However, dimensioning this parameter is quite a tricky problem. To achieve high M-factors (typically in the order of tens, as discussed at the end of chapter 4 and visible in the tables of appendix B), a small detuning value would be desirable. On the other hand, detuning the reference interferometer by a very small amount (as an extreme optical Vernier effect) may result in a beating modulation with a very long period, which may become undetectable for a limited spectral range available, and therefore immeasurable. These contradictory requirements present a considerable challenge for the experimental implementation of such sensors with large M-factors for sensitivity.

This section proposes and demonstrates a method to overcome this dilemma by using few modes instead of a single mode in the sensing interferometer (ideally two modes), preferably with a relatively large effective refractive index between them. The reference interferometer is in tune with the fundamental mode (mode 1) of the sensing interferom-

eter, which would provide a giant M-factor but with an extremely large immeasurable envelope. On the other hand, for a higher order mode (mode 2) it represents a lower M-factor but with a smaller and measurable Vernier envelope, since the effective refractive index of the higher order mode is different, generating a Vernier effect slightly more detuned. However, when both responses superimpose, the Vernier envelope is still measurable, whilst maintaining a giant M-factor typical for large immeasurable envelopes. As will be shown later, the method of combining the two modes in the sensing interferometer provides M-factors an order of magnitude beyond the expected limits for the standard Vernier effect technique.

Such a result with a giant M-factor is here demonstrated by implementing a few-mode FPI refractometer in combination with a single-mode reference FPI. Through the use of the first harmonic of the optical Vernier effect, FPIs made of hollow capillary tubes, FIB milling to open access holes for liquid analytes, and mode interference, the fabricated structure is born from combination of different techniques and knowledge gathered during this PhD. First, the working principle is briefly introduced and the fabrication of the sensing structure is described. Then, simulations are used to further understand the behavior of the sensing structure and to have a first glimpse on the giant enhancement of sensitivity. At last, the sensing FPI is filled with water and characterized for refractive index variations, comparing the result with a single FPI, with the first harmonic of the optical Vernier effect using a single mode sensing FPI, as explored in previous chapter, and also with the simulated results.

7.2.2. Working Principle

The sensor is similar to the structure presented in section 6.2, where two FPIs made from hollow capillary tubes are used to generate the optical Vernier effect in a parallel configuration. In this case, the first harmonic of the optical Vernier effect will be used, since it provides internal envelope intersections to easily monitor the wavelength shift, as previously discussed in this dissertation. A schematic diagram of the working principle is shown in figure 7.1. The sensing FPI is fabricated to present few modes (ideally two). The sensing FPI cavity can be filled with an aqueous solution by opening access holes at the edges of the cavity.

Let us consider the simpler case of two propagating modes in the sensing FPI, as represented in the inset of figure 7.1, while the reference FPI is single mode. The reference FPI is produced to be in tune (detuning: $\Delta \sim 0$) with the fundamental mode (mode 1) of the sensing FPI, while introducing the first harmonic of the Vernier effect. One knows now that this situation produces a Vernier envelope with an infinite period. As a consequence, the sensitivity of the Vernier envelope is theoretically infinite, but there is no way one can measure it.

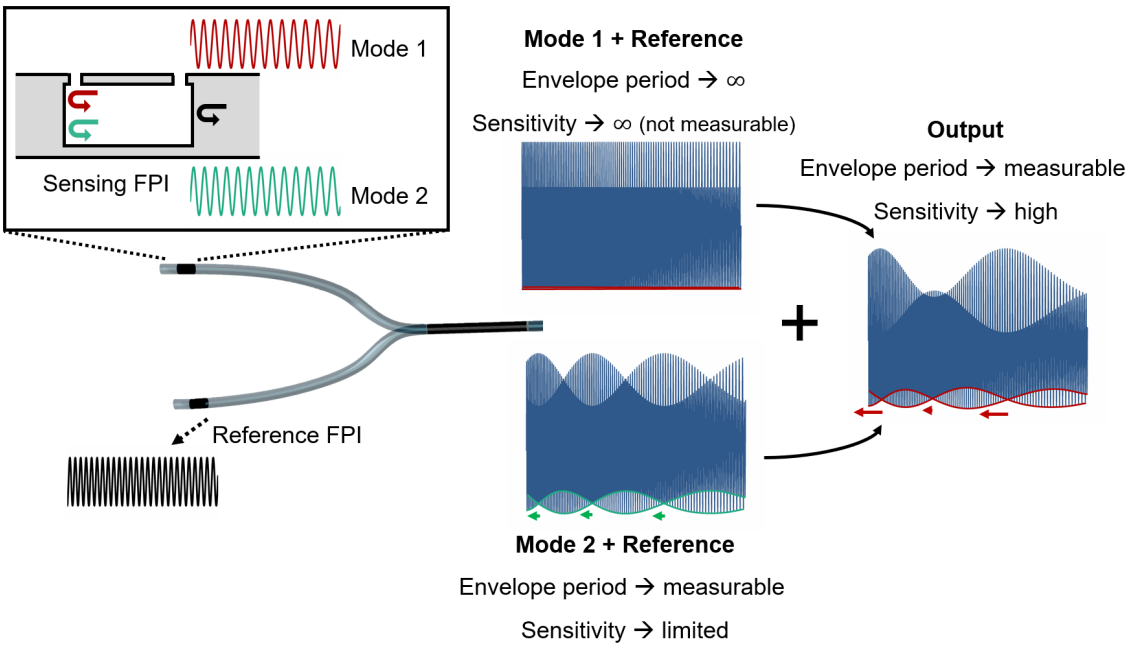

Figure 7.1. – Schematic of the working principle. A complex envelope modulation is produced from the overlap between two Vernier cases (associated with two propagating modes in the sensing FPI. Some envelope intersection points show enhanced sensitivity, expressed qualitatively by the size of the arrow. The Vernier spectra are purely for explanation purposes, their visibilities were adjusted to be visually more perceptive and do not reflect the real case.

As for the higher order mode (mode 2), it is slightly out of tune with the reference FPI, since it has a lower effective refractive index than the fundamental mode (mode 1). The result is a Vernier envelope with a measurable period and with a sensitivity that is limited by the maximum size of the Vernier envelope that one can measure. A qualitative measurement of the envelope intersection shift for a varying measurand is demonstrated in figure 7.1 by the arrows.

The final response of the whole structure is given by the overlap between these two situations, resulting in a more complex Vernier spectrum. This complex Vernier spectrum presents now a Vernier envelope with a measurable period, with internal envelope intersections that one can measure. However, some of these intersections show low sensitivity (short arrow length), while others show enhanced sensitivity (longer arrow length) comparing with the normal Vernier effect case.

Such complex effect results mainly from the relative movement between the internal envelopes, which is quite elaborate to analyze mathematically. Nevertheless, the effect, and especially the enhancement of sensitivity, can still be observed via simulations, as will be presented later. The rest of this section will only focus on the region of interest, given by the envelope intersection that provides an enhanced wavelength shift. Next, the fabrication of the device will be presented.

7.2.3. Fabrication

Sensing Fabry-Perot Interferometer

The hollow capillary tube used for the sensing FPI was fabricated at Leibniz-IPHT and has an internal diameter of 80 μm and an outer diameter of 125 μm. Initially, the cleaved end of an SMF and of the hollow capillary tube were spliced together by means of a splicer (Fitel S177). The electric arc was centered mainly in the SMF using the manual mode of the fusion splicer. This way, one avoids the collapse of the hollow capillary tube. The splice was performed by applying two electric arcs with an arc power of 30 arbitrary units (absolute arc-power was not possible to attain, only relative values) and an arc duration

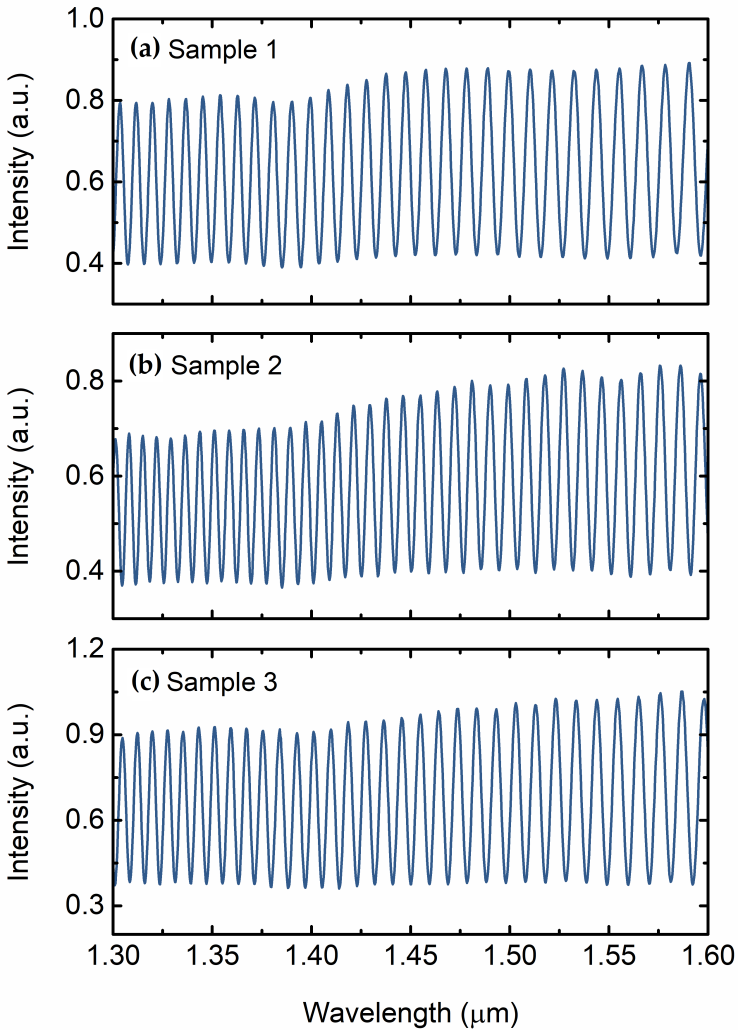

Figure 7.2. – Intensity spectra of three different few-mode sensing FPIs fabricated. (a) Sample 1 corresponds to the FPI used later in the experiment. (b) and (c) are two additional samples fabricated using the same procedures as for sample 1, demonstrating the reproducibility of the fabrication method. The output spectra present a slight low-frequency modulation with visibility increasing towards longer wavelengths.

of 400 ms. Next, the other end of the hollow capillary tube was cleaved with the desired length with the assistance of a magnification lens. In this case, the length of the sensing FPI was approximately 105 μm after cleaving. At last, the cleaved end of the input SMF was spliced to the hollow capillary tube using the same procedures as described before, but applying a slight offset of 5 arbitrary units, followed by two compressions of 15 arbitrary units, each of them accompanied by a cleaning arc. This procedure allows higher order modes to be excited in the hollow capillary tube section, generating a few-mode FPI.

To investigate the reproducibility of the few-mode FPI, three samples were fabricated using the same procedures as described before. The output spectra of the three few-mode sensing FPI samples fabricated are shown in figure 7.2. The three samples show a spectrum that is not purely a two-wave interferometer, as expected from a single-mode FPI. In fact, the spectra are modulated by a small envelope, that indicates the presence of additional modes other than the fundamental one, since it results from the interference between them. The three spectra are very similar, demonstrating the reproducibility of the fabrication method.

For comparison purposes along the fabrication, and later on after characterization of the final structure, a single mode FPI was also fabricated. The single mode FPI was produced with the same procedures as for the few-mode FPI, except the last step involving the application of an offset. The length of the single mode FPI is approximately 101 μm. The spectrum of the few-mode sensing FPI in air, before milling the access holes is shown in figure 7.3(a). Figure 7.3(b) represents the spectrum of the single-mode FPI, also in air. As seen before, there is a slight low-frequency modulation in the few-mode sensing FPI spectrum, which increases with longer wavelengths. However, such low-frequency

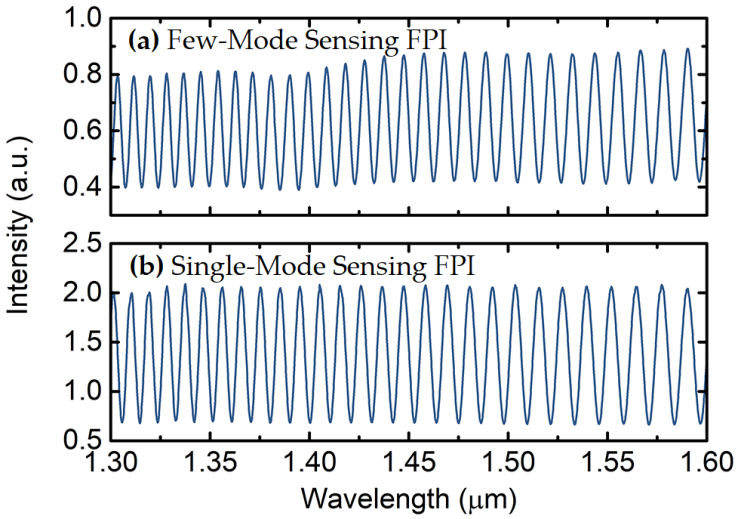

Figure 7.3. – Experimental spectra, in air, before milling. (a) Few-mode sensing FPI. (b) Single-mode sensing FPI.

component is not present in the output spectrum of the single-mode FPI, which resembles only a two-wave interferometer.

Milling of Access Holes

In order to enable the sensing FPI to be filled by liquid analytes, focused ion beam milling was used to open access holes in the cavity. Two access holes for liquid analytes were milled near the splice regions of the few-mode sensing FPI with a Tescan (Lyra XMU) focused ion-beam scanning electron microscope (FIB-SEM). Before milling, the sample was prepared according to the procedures previously described in section 2.4.3. At the end, the sample was coated with a total of 6.4 nm of carbon film.

The first access hole was milled near a splice region, with a sample tilt of -20º in relation to the axis of the FIB (see figure 2.7). A section of 25 μm × 25 μm with a depth of 25 μm was initially milled with an ion current of 7 nA. Then, the access hole was further expanded with the same ion current and using a milling strategy normally applied for polishing. The final dimension of the first access hole was 32 μm × 31 μm. The second access hole was similarly milled at the other splice region. The sample stage was rotated by 180º and tilted by -15º in relation to the axis of the FIB. A section of 20 μm × 10 μm with a depth of 25 μm was initially milled with an ion current of 7.1 nA.

At this point it was necessary to deposit a new carbon coating due to the removal of much of the previous coating during the milling process. This time, the carbon coating was performed in the direction of the milling region, tilting the sample by 10º and applying no

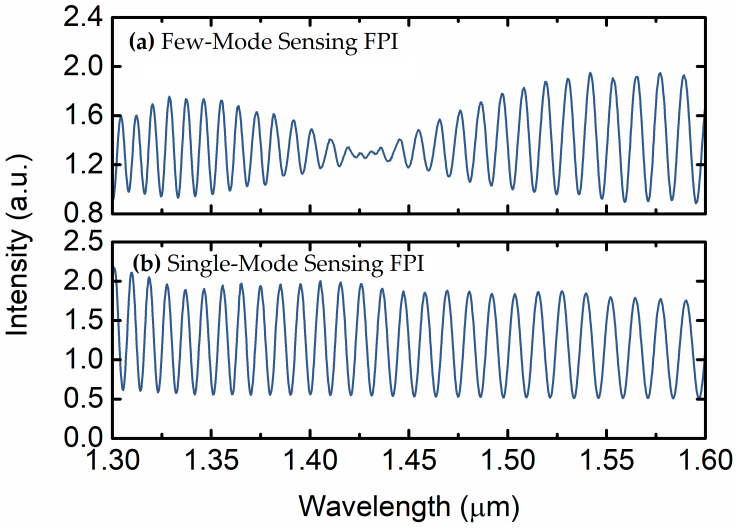

Figure 7.4. – Intensity spectra after milling the access holes. (a) Few-mode sensing FPI. (b) Single-mode sensing FPI. The single-mode sensing FPI does not present a noticeable low-frequency modulation, while the few-mode sensing FPI shows a more predominant low-frequency modulation than before milling, with a node at around 1425 nm.

stage rotation. A thickness of 9.56 nm of carbon was deposited in the sample. Following this, the second access hole was further expanded with an ion current of 6 nA and using again a milling strategy normally applied for polishing. The final dimension of the second access hole was 25 μm × 24 μm. No disturbing effects of volume charging related with drifting effects were observed during the milling processes. An image of the final access holes can be seen later on figure 7.6(b).

Similarly, two access holes were also milled in the single-mode sensing FPI. In this case, the first access hole was milled with an ion current of 6.9 nA and a sample tilt of -15º. The final dimension of the first access hole was 26 μm × 21 μm. The second access hole was milled with an ion current of 5.9 nA, the same tilt and a sample rotation of 180º. The final dimension of the second access hole was 20 μm × 18 μm. In all the cases, the milled interferometers were kept fixed to the sample holder with carbon glue. This helps to maintain the stability of the structures and avoids their movement during later usage, which can induce a fracture at the milled regions.

The output spectra for both, the few-mode sensing FPI and the single-mode sensing FPI, are represented in figure 7.4. After milling the access holes, the visibility of the interference fringes of the output spectrum of the single-mode sensing FPI, represented in figure 7.4(b), is approximately the same. Yet, the output spectrum of the few-mode sensing FPI, presented in figure 7.4(a), shows a more predominant low-frequency modulation than before milling (figure 7.3(a)), with a node at around 1425 nm. Note that all the spectra still correspond to the FPIs in air.

The existence of a node in the few-mode sensing FPI right in the middle of the wavelength range monitored is inconvenient for generating the optical harmonic Vernier effect. This would result in a Vernier spectrum deformed at that wavelength region, which is problematic for tracing the upper Vernier envelope (and/or internal envelopes). Nevertheless, there is a solution to shift the position of this node by using FIB milling, as will be explored next.

Spectral Tuning using FIB Milling

As an advantage, the milling process to open the access holes can be used to shift the low-frequency modulation of the output spectrum. By performing additional milling of the access holes by a few microns, the phase of the low-frequency modulation is slightly changed due to a slight variation of the effective refractive indices of the modes propagating in the FPI. As visible in figure 7.5, the position of the node is shifted towards longer wavelengths if an additional 3 μm are milled. After milling 9 μm from the initial case (A), the node of the low-frequency modulation shifted almost towards the end of the monitored wavelength range, as shown in figure 7.5(c). This last case was taken as the few-mode sensing FPI to form the final structure.

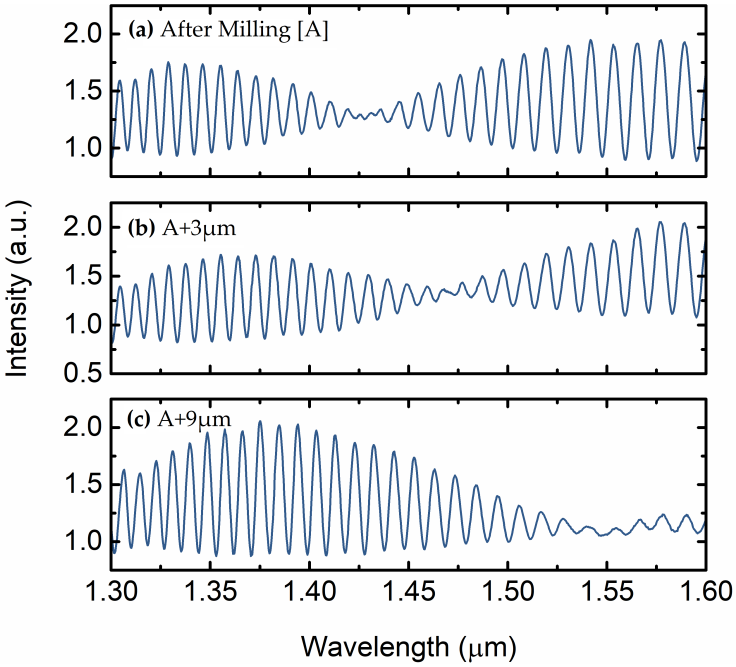

Figure 7.5. – Intensity spectra of the few-mode sensing FPI after additional milling of the access holes. (a) Initial output spectrum [A] as in figure 7.4(a). (b) Output spectrum after additionally milling 3 μm from the initial case [A]. (c) Output spectrum after additionally milling 9 μm from the initial case [A].

Final Structure

As explained before, the first harmonic of the Vernier effect is generated in a parallel configuration, by means of a 3dB fiber coupler, as depicted in figure 7.6. A hollow capillary tube with an internal diameter of 60 μm and an outer diameter of 125 μm, also fabricated at Leibniz-IPHT, was used to form the reference FPI. The reference FPI should be in tune with the fundamental mode of the sensing FPI when filled with water. Due to the necessity of simulating the modes propagating in the water-filled few-mode sensing FPI in order to calculate the length of the reference FPI, the dimensioning of the reference FPI will only be presented in the next section. The structure is illuminated with a supercontinuum source, and the output reflected spectrum is measured with an optical spectrum analyzer (OSA). Figure 7.6(a) shows a micrograph of the two FPIs (sensing and reference). Scanning electron microscope images of the milled sensing FPI and of one of the access holes are also displayed in figure 7.6(b).

This structure will then be used to demonstrate the concept of extreme optical Vernier effect applied to refractive index sensing of liquid analytes.

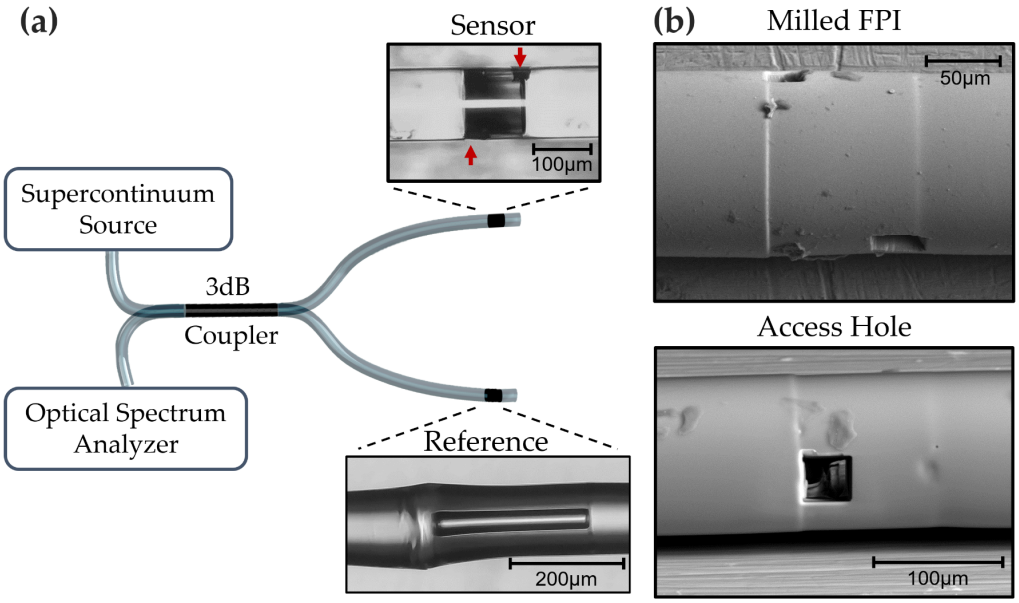

Figure 7.6. – (a) Schematic of the Vernier effect in a parallel configuration. Micrographs of the sensor and reference FPIs are also shown in the inset. (b) Scanning electron microscope image of a milled FPI and of an access hole.

7.2.4. Simulation (Proof-of-Concept)

Next, the simulation of the output spectrum and correspondent enhancement of sensitivity is going to be explored. Before that, it is important to determine the response of the fabricated few-mode sensing FPI when filled with water. Such spectrum will be the starting point to calculate the modes involved in the FPI, to then be used in the simulations.

The spectrum of the few-mode sensing FPI filled with deionized water is shown in figure 7.7. Instead of a clean sinusoidal behavior characteristic of a single-mode FPI with low mirror reflectivities, the measured signal is modulated by a non-uniform envelope. The envelope indicates the presence of other modes in the water-filled cavity, since it results from the interference between them, as explained before. For the few-mode sensing FPI developed, which presents a length of 105 μm, the FSR is estimated to be around 450 nm. As seen in figure 7.7, half a period of the envelope modulation is located between 1375 nm and 1600 nm.

The effective refractive index difference between the fundamental mode (mode 1) and the main higher order mode (mode 2) that produces the envelope modulation in the reflection spectrum can be calculated through:

$$\Delta n = \frac{\lambda_1 \lambda_2}{2L \times FSR}, \tag{7.1}$$

where λ_1 and λ_2 are the wavelength positions of two consecutive maxima (or minima) of the envelope, L is the length of the sensing FPI, and FSR is the free spectral range of

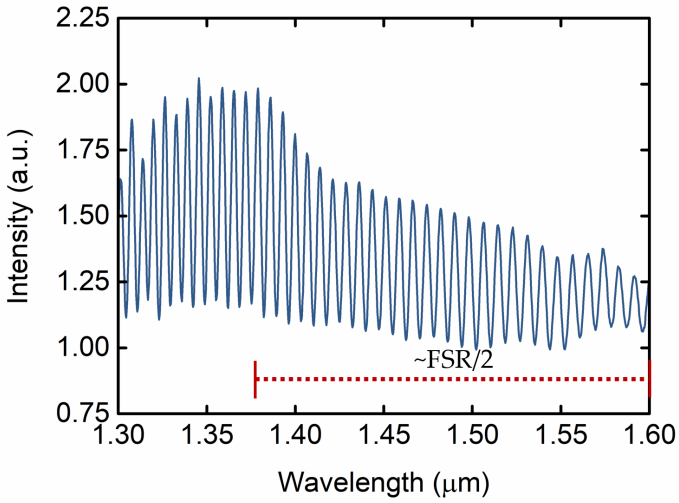

Figure 7.7. – Experimental spectrum of the water-filled few-mode sensing FPI.

the envelope modulation. The wavelength values in equation 7.1, corresponding to the position of two consecutive envelope minima, are assumed as 1150 nm and 1600 nm. With this, a refractive index difference of around 1.94×10^{-2} RIU is obtained.

Although this main higher order mode is expected to carry more energy than other higher order modes, the structure still presents other higher order modes that contribute to the FPI response, which is why the envelope is non-uniform. Such a structure is very challenging to simulate, as it contains multiple variables and degrees of freedom. Therefore, as a first approach, let us consider a sensing FPI with only two modes.

Mode Simulation

Mode analysis using COMSOL Multiphysics was performed to calculate the effective refractive index of modes propagating in the water-filled sensing FPI. The simulated cross-

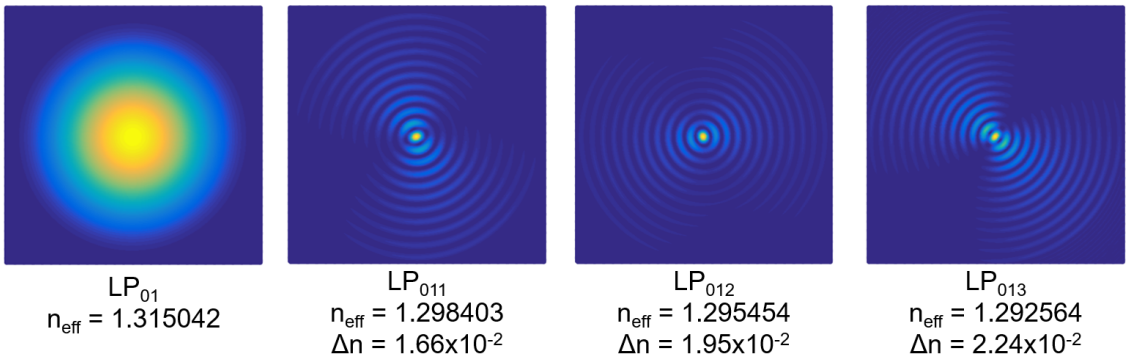

Figure 7.8. – Simulated mode profile of the fundamental mode and the three higher order modes with an effective refractive index difference close to the value calculated through the experimental data (1.94×10^{-2} RIU).

section consists of a capillary tube made of silica (refractive index of 1.444 at 1550 nm [51]) with an inner diameter of 80 μm and an outer diameter of 125 μm. The inner region of the capillary tube and the external environment correspond to water at 22.72 °C, the same as an experimental value (refractive index of 1.315107 at 1550 nm, calculated through equation A.5 in appendix A). The simulated fundamental mode (LP_{01}) has an effective refractive index of 1.315042. Its mode profile is depicted in figure 7.8, together with the simulated higher order modes LP_{011}, LP_{012}, and LP_{013}, for comparison purposes. These higher order modes have an effective refractive index difference, in relation to the fundamental mode, close to the value calculated through the experimental data (1.94×10^{-2} RIU). The mode LP_{012}, which presents the closest effective refractive index difference, was taken as the second mode to simulate the response of a two-mode sensing interferometer.

Simulation of a Two-Mode Sensing FPI

Using the simulated modes, one can calculate the output intensity spectrum for a two-mode FPI. The simulated normalized intensity spectrum for a two-mode FPI is described by equation 4.11, where the output electric field is given by:

$$\begin{aligned} E_{out}(\lambda) = AE_{in}(\lambda) + f_1 BE_{in}(\lambda) \exp\left[-i\left(\frac{4\pi}{\lambda} n_{LP01} L - \pi\right)\right] \\ + f_2 BE_{in}(\lambda) \exp\left[-i\left(\frac{4\pi}{\lambda} n_{LP0m} L - \pi\right)\right], \end{aligned} \tag{7.2}$$

where L is the length of the FPI, n_{LP01} and n_{LP0m} are the effective refractive indices of the fundamental mode (LP_{01}) and the higher order mode m, respectively; λ is the wavelength, and $E_{in}(\lambda)$ is the input electric field. The coefficient A is given by:

$$A = \sqrt{R_1}, \tag{7.3}$$

with R_1 being the intensity reflection coefficient of the first interface of the FPI. The coefficient B is given by:

$$B = (1 - R_1)\sqrt{R_2}, \tag{7.4}$$

where R_2 is the intensity reflection coefficient of the second interface of the FPI. The factors f_1 and f_2 correspond to the percentage of power distributed to the fundamental mode and to the higher order mode, respectively. To approach a real situation, where the fundamental mode carries a lot more power than the higher order mode, in this simulation f_1 was considered as 85% and f_2 as 15%. The length of the FPI was considered as 105 μm, the same as experimentally measured. To also address some losses due to the slight offset of the input fiber and losses due to surface imperfections and mode mismatch, the coefficient

A was reduced by 20%.

Figure 7.9 shows the experimental few-mode sensing FPI spectrum and the simulated spectra for two-mode sensing FPIs consisting of the fundamental mode and one of the three higher order modes determined before. Comparing the intensity spectra of figure 7.9, one can conclude that the two-mode sensing FPI with the higher order mode LP_{012} fits the experimental result best. The modeled spectrum for an FPI composed of these two modes contains a main beating modulation similar to the experimental spectrum. Other higher order modes do not give this high degree of similarity with the experimental result.

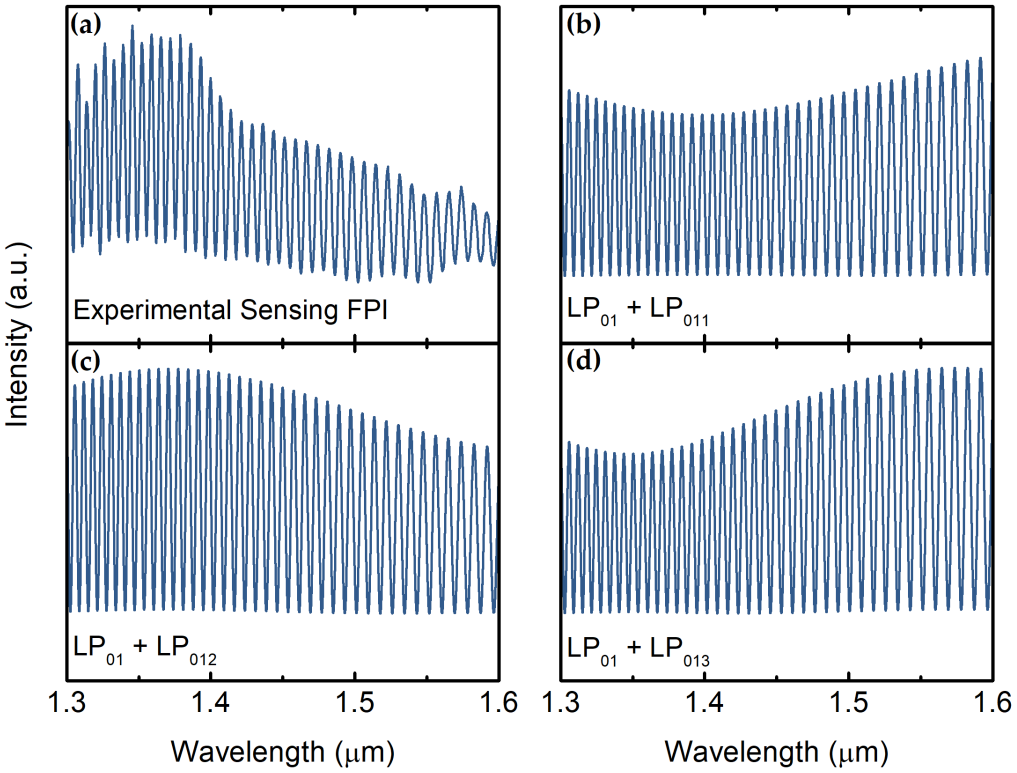

Figure 7.9. – (a) Experimental intensity spectrum of the few-mode sensing FPI. Simulated intensity spectra for a two-mode sensing FPI with: (b) fundamental mode LP_{01} and higher order mode LP_{011}; (c) fundamental mode LP_{01} and higher order mode LP_{012}; (d) fundamental mode LP_{01} and higher order mode LP_{013}.

Simulation of the Extreme Optical Vernier Effect

Now that the effective refractive indices of the main modes propagating in the sensing FPI were calculated, one can use such information to fabricate the reference FPI. The reference FPI was fabricated to be in tune with the fundamental mode of the sensing FPI in water (as discussed before), while generating the first optical harmonic of the Vernier effect.

To generate the first harmonic of the Vernier effect to be in tune with the fundamental mode of the sensing Fabry-Perot interferometer ($n_{LP01} = 1.315042$), the optical path

length (OPL) of the reference interferometer should match closely twice the OPL of the sensing interferometer, as described by:

$$OPL_{reference} \simeq 2OPL_{LP01} \leftrightarrow n_{reference}L_{reference} = 2n_{LP01}L_{sensing} = 276.159\,\mu m. \quad (7.5)$$

In fact, to provide a huge magnification factor, the OPL of the reference interferometer should be slightly detuned from twice the OPL of the sensing interferometer. Therefore, the OPL of the reference interferometer is expressed, according to equation 5.3, as:

$$OPL_{reference} = (i+1)\,OPL_{LP01} - 2\Delta = 2OPL_{LP01} - 2\Delta, \quad (7.6)$$

where Δ is the detuning parameter, as described in the previous chapters, and $i = 1$ for the first harmonic. Twice the detuning parameter (Δ) corresponds to the optical path difference between the actual reference interferometer and the closer situation of a perfect harmonic case (where $OPL_{reference} = (i+1)\,OPL_{sensor}$, being i the order of the harmonic. For the first harmonic, $i = 1$). In other terms, the detuning parameter is in this case defined as $\Delta = 2n_{sensing}L_{sensing} - n_{reference}L_{reference}$.

Since the reference FPI is made of an air-filled cavity, its length is approximately half the optical path length, since the refractive index is about 1. The magnification factor for the first harmonic of the Vernier effect is then approximately given by (equation 4.28 multiplied by $(i+1)$, with $i = 1$):

$$M^{1st\,harmonic} = \frac{2n_{sensing}L_{sensing}}{\Delta}. \quad (7.7)$$

To obtain a negative magnification factor, the optical path length of the reference interferometer should be larger than the optical path length of the sensing interferometer, so that the detuning parameter (Δ) in equation 7.6 becomes negative. Hence, the length of the fabricated reference FPI was 276.2 μm, slightly larger than 276.159 μm. In this situation, the magnification factor (M-factor) for all the modes of the sensing FPI is negative, as seen in figure 7.10. A negative magnification factor simply means a wavelength shift of the Vernier envelope in the opposite direction compared to the normal sensing FPI.

Note that, if the reference FPI was in tune with the fundamental mode of the sensing FPI to provide a huge positive M-factor, the higher order mode would provide an even higher and positive M-factor. If the refractive index difference between the fundamental mode and the higher order mode is quite large, the M-factor for the higher order mode could still be negative, but still high enough to generate an immeasurable envelope. Therefore, choosing a negative M-factor for the fundamental mode allows to have also a negative but lower M-factor for the higher order mode, producing a measurable envelope.

As explained previously in figure 7.1, the structure is in a situation where the funda-

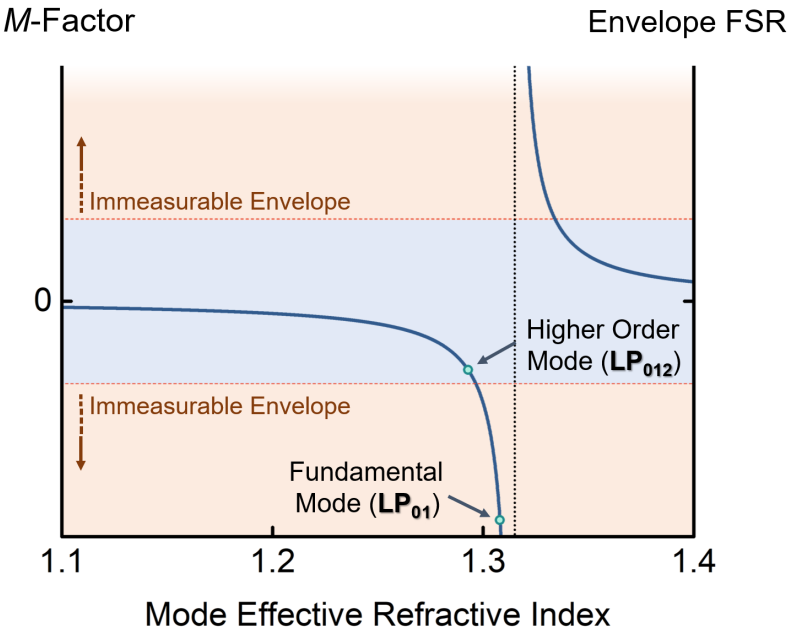

Figure 7.10. – Magnification factor and envelope free spectral range (FSR) for a single mode sensing interferometer as a function of the mode effective refractive index.

mental mode (LP_{01}) of the sensing FPI together with the reference FPI produce a large and immeasurable Vernier envelope, with a huge M-factor and correspondent sensitivity. On the other hand, the higher order mode (LP_{012}) of the sensing FPI together with the reference FPI produce a measurable envelope, but with a lower M-factor value and correspondent sensitivity. One expects then, that the superposition of these two cases generates a complex Vernier envelope, where some of the internal envelope intersections present enhanced sensitivity, as discussed before.

To observe such an effect, let us now simulate the following three situations: (a) sensing FPI with fundamental mode plus reference FPI, (b) sensing FPI with higher order mode plus reference FPI, (c) sensing FPI with fundamental mode and higher order mode plus reference FPI (combined response). The structure is similar to the one previously described in chapter 4, whose output electric field was described by equation 4.9. However, in this case the sensing FPI has two-modes and the length of the reference FPI is longer to introduce the first harmonic of the optical Vernier effect. Therefore, equation 4.9 is now readjusted as:

$$\frac{E_{out}(\lambda)}{E_{in}(\lambda)} = \frac{A}{\sqrt{2}} + \frac{B}{\sqrt{2}}\left\{f_1 \exp\left[-i\left(\frac{4\pi}{\lambda}n_{LP01}L_1 - \pi\right)\right] + f_2 \exp\left[-i\left(\frac{4\pi}{\lambda}n_{LP012}L_1 - \pi\right)\right]\right\} \tag{7.8}$$

$$+ \frac{C}{\sqrt{2}} + \frac{D}{\sqrt{2}} \exp\left[-i\left(\frac{4\pi}{\lambda}n_2 L_2 - \pi\right)\right],$$

where L_1 is the length of the two-mode sensing FPI, n_{LP01} and n_{LP012} are the effective refractive indices of the considered fundamental mode (LP_{01}) and the higher order mode (LP_{012}), respectively, in the two-mode sensing FPI, n_2 and L_2 are the effective refractive index and the length of the reference FPI, λ is the wavelength, and $E_{in}(\lambda)$ is the input electric field. The coefficients A, B, f_1, and f_2, as well as the length of the sensing FPI and the effective refractive indices of the modes LP_{01} and LP_{012} are the same as before. The coefficient C is given by:

$$C = \sqrt{R_1^{ref}}, \tag{7.9}$$

with R_1^{ref} being the intensity reflection coefficient of the first interface of the reference FPI,

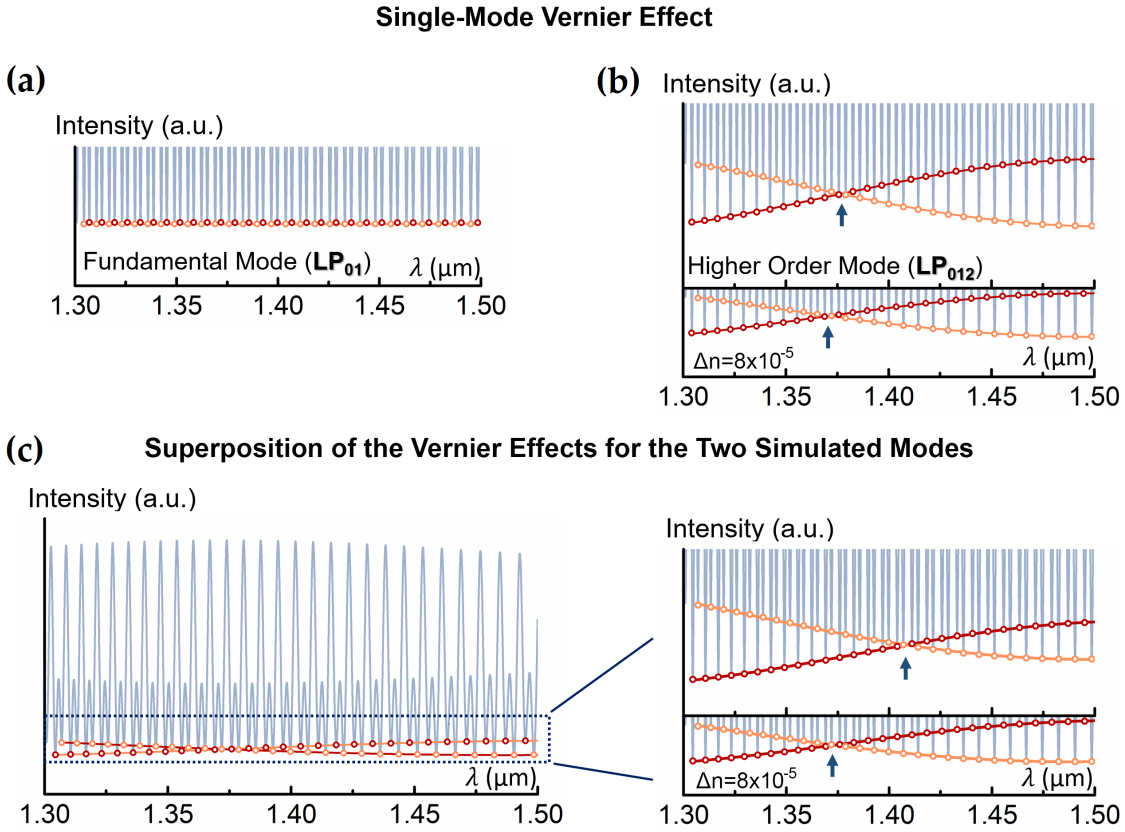

Figure 7.11. – Comparison between the Vernier effect with a single mode and a two-mode sensing FPI. (a) Simulated Vernier spectrum for a sensing FPI with the fundamental mode (LP_{01}). The Vernier spectrum has a high magnification factor, but an envelope too large to be measured. (b) Simulated Vernier spectrum for a sensing FPI with the higher order mode (LP_{012}), before and after applying a refractive index variation of 8×10^{-5} RIU to the sensing FPI mode. The Vernier envelope is measurable but has a lower magnification factor (lower wavelength shift). (c) Simulated Vernier spectrum for a two-mode sensing FPI, before and after applying the same a refractive index variation to the sensing FPI modes. The Vernier envelope is measurable, yet the magnification factor is still high (larger wavelength shift than the single mode case).

which has an air cavity (refractive index considered as 1). The coefficient D is expressed as:

$$D = \left(1 - R_1^{ref}\right)\sqrt{R_2^{ref}}, \tag{7.10}$$

where R_2^{ref} is the intensity reflection coefficient of the second interface of the reference FPI.

The coefficient D was reduced by 70% to adjust the intensity due to losses during the fine-tuning of the reference interferometer by compression. The refractive index of the reference FPI was considered as 1 (air). The length used for the reference FPI was $2\times1.315042\times105\,\mu\text{m} + 0.001\,\mu\text{m}$, making sure that the OPL of the reference interferometer is slightly longer than the perfect harmonic case, inducing a negative M-factor.

The simulated spectra for the three situations (a), (b), and (c) mentioned before are depicted in figure 7.11. If the sensing FPI only presents the fundamental mode (LP_{01}), which is in tune with the reference FPI, the generated Vernier envelope would present an extremely large FSR and a high magnification factor. In practice however, it would be impossible to measure the Vernier envelope shift within the limited spectral range available, as seen in figure 7.11(a). On the other hand, if the sensing FPI only presents the higher order mode (LP_{012}), the Vernier effect is less tuned, resulting in a smaller period Vernier envelope. In this case, the Vernier envelope is now measurable, but it is accompanied by a smaller magnification factor and, therefore, by a smaller wavelength shift, as demonstrated in figure 7.11(b). Hence, in a standard single-mode situation, the maximum magnification factor provided by the Vernier effect is limited by the largest Vernier envelope measurable. However, if the sensing FPI presents both modes simultaneously, the superposition of both responses results in a measurable Vernier envelope but with a higher magnification factor (larger wavelength shift), as observed in figure 7.11(c). The wavelength shift was simulated by changing the effective refractive indices of the sensing FPI modes by 8×10^{-5} RIU, simulating a variation of the analyte. This result was simulated for a two-mode sensing FPI, and it is expected to still be applicable to the fabricated sensing FPI, which may present some additional modes (few mode case).

7.2.5. Characterization

Now that the enhanced wavelength shift provided by the extreme optical Vernier effect was demonstrated via simulations, the fabricated structures were characterized for refractive index variations in a very narrow range around the refractive index of water. This was achieved by slightly changing, in steps, the water temperature, which, through the thermo-optic effect, changes the refractive index of water[1].

[1]Further details can be found in appendix A.

The sensing FPI was immersed in a deionized water bath, where the water was heated up to 23.46 °C and then slowly decreased to 22.72 °C, while simultaneously the sensor spectrum was monitored. The water temperature was monitored by means of a thermocouple (Almemo 1020-2, with a thermoelement Type N) having a resolution of 0.01 °C, placed closely to the sensing FPI. In total, the refractive index of water changed by 7.989×10^{-5} RIU (through equation A.5 in appendix A). In each step, the output spectrum was recorded and the position of the intersection between the internal Vernier envelopes was monitored as a function of the refractive index variation. Note that, if the liquid needs to be changed, the sensing FPI should be cleaned with isopropanol and dried before using it again.

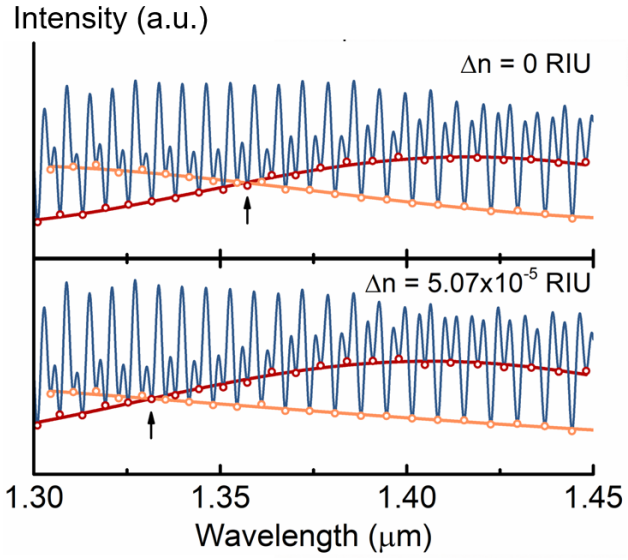

Figure 7.12. – Experimental Vernier spectra for a few-mode water-filled sensing FPI at different values of water refractive index. The internal Vernier envelope intersection, marked with an arrow, is traced and monitored during the characterization.

The experimental Vernier spectra for the fabricated water-filled few-mode sensing FPI, at distinct water refractive index values is depicted in figure 7.12. The internal envelope intersection, marked with an arrow, shifted towards shorter wavelengths for a refractive index variation of 5.07×10^{-5} RIU. This means that the wavelength shift of the Vernier envelope is negative, matching with a negative M-factor (the individual sensing FPI has a positive wavelength shift to refractive index variations, as will be demonstrated later). The full wavelength shift characterization of the experimental Vernier envelope as a function of water refractive index variations is presented in figure 7.13(a), and magnified in (b). A giant refractive index sensitivity of -500699 nm/RIU was achieved using the fabricated structure for a variation of 7.989×10^{-5} RIU around the refractive index of water.

The simulated wavelength shift for a simplified Vernier structure with only a two-mode sensing FPI is also shown in figure 7.13(a), and magnified in (b) for a better comparison with the experimental case. For the simulated case, the refractive index sensitivity achieved

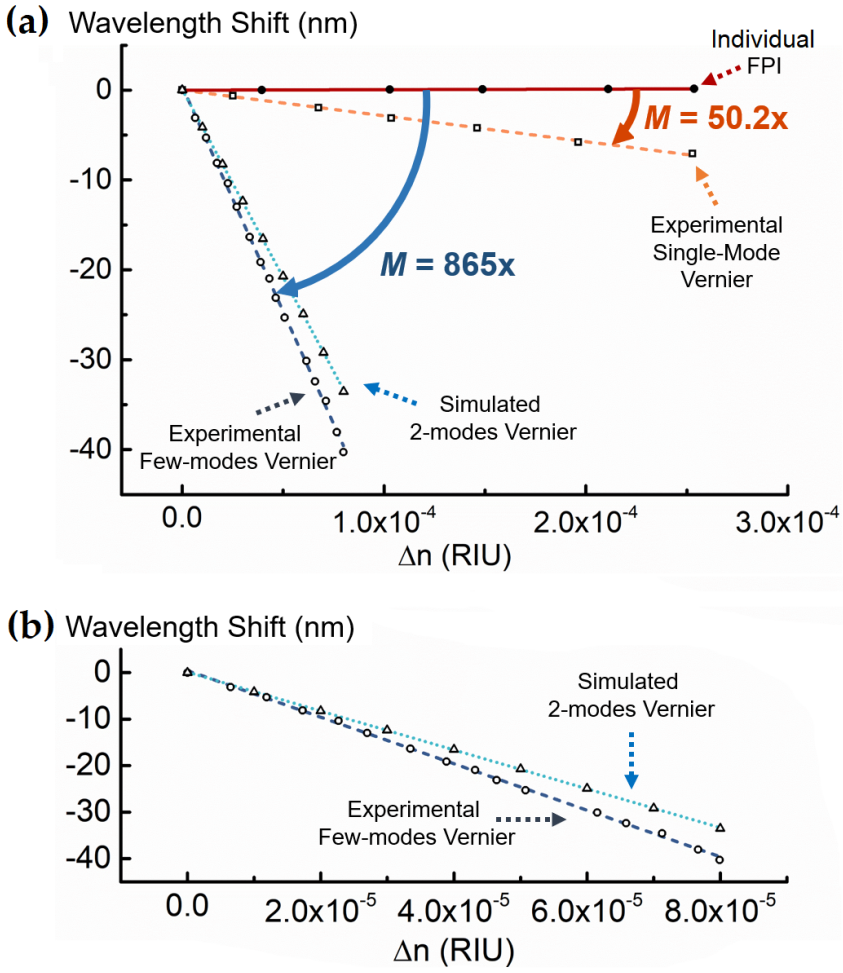

Figure 7.13. – (a) Wavelength shift as a function of water refractive index variations for different configurations: individual sensing FPI, experimental Vernier effect for a single mode sensing FPI, simulated Vernier effect for a two-mode sensing FPI, and experimental Vernier effect for a few-mode sensing FPI. The M-factor achieved by the Vernier effect with a few-mode sensing FPI is an order of magnitude higher than the Vernier effect with a single mode sensing FPI. (b) Zoom in of the experimental few-mode case and of the simulated two-mode case.

was -418387 nm/RIU. The result is in the same order of magnitude as the experimental structure with a few-mode sensing FPI. It is important to note that the few-mode sensing FPI still presents modes other than the two considered for simulations, which contribute to a slight further increase of the magnification factor.

For comparison purposes, the single mode sensing FPI was used to introduce the first harmonic of the optical Vernier effect, with properties as described in chapter 5. Taking into consideration the length of the single mode sensing FPI (101 μm), using equation 7.5 the length of the reference FPI should closely match 265.6 μm, but still be slightly larger. Hence, the fabricated reference FPI has a length of around 269.5 μm, corresponding to a

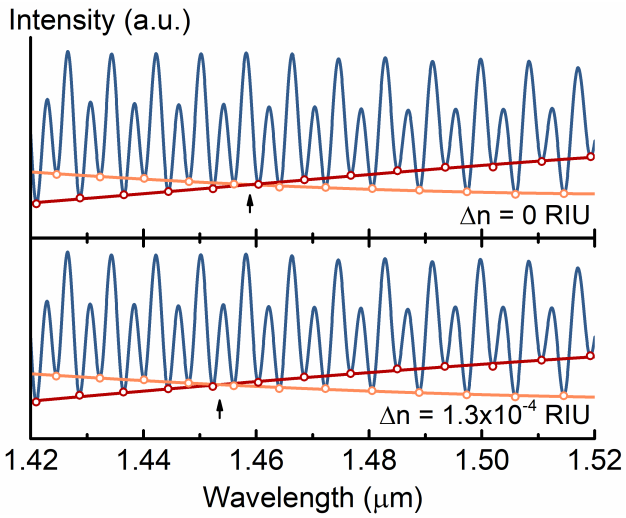

Figure 7.14. – Experimental Vernier spectra for the single mode water-filled sensing FPI at different values of water refractive index. The internal Vernier envelope intersection, marked with an arrow, is traced and monitored during the characterization.

detuning (Δ) of $-3.9\,\mu$m, which still produces a measurable Vernier envelope.

Figure 7.14 shows the experimental Vernier spectra using the single mode sensing FPI, at distinct water refractive index values. The internal envelope intersection, marked with an arrow, shifted towards shorter wavelengths for a refractive index variation of 1.3×10^{-4} RIU. The wavelength shift of the Vernier envelope as a function of water refractive index variations for the experimental first harmonic of the Vernier effect using a single mode sensing FPI is also depicted in figure 7.13(a). The sensitivity obtained was -28496 nm/RIU for a variation of 2.528×10^{-4} RIU around the refractive index of water.

To finally calculate the M-factor value for each case, the response of the single mode sensing FPI alone should also be determined. The experimental intensity spectra for the single mode sensing FPI alone, at distinct water refractive index values is represented in figure 7.15. The FPI spectrum shifted towards longer wavelength, as indicated by the arrow, for a refractive index variation of 7.6×10^{-4} RIU. The complete wavelength shift characterization as a function of water refractive index variations is also depicted in figure 7.13(a). The sensitivity of the individual single mode sensing FPI to water refractive index variations is 568 nm/RIU for a variation of 2.536×10^{-4} RIU around the refractive index of water.

The M-factor can now be calculated by means of the determined sensitivities, through equation 4.29. For the first harmonic of the optical Vernier effect with a single mode sensing FPI, the M-factor achieved was around 50.2. On the other hand, the M-factor of the proposed Vernier structure with a few-mode sensing FPI is higher than 850, which is an order of magnitude higher than the M-factor obtained in the single mode case.

The response of the structure is limited by the resolution of the detection system, cor-

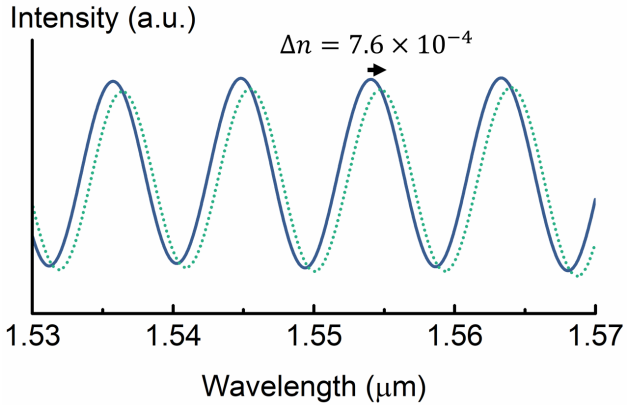

Figure 7.15. – Experimental intensity spectra for single mode water-filled sensing FPI, before and after a water refractive index variation of 7.6×10^{-4} RIU.

responding to a refractive index resolution of 5×10^{-7} RIU. In theory, a resolution of 2×10^{-9} RIU could be achieved by using a detection system with a resolution of 1 pm, which nowadays is commercially available.

Note that, until now the refractive index of water was changed via variations of temperature, through the thermo-optic effect. However, the thermal expansion of the FPI structure was neglected during the whole experiment. Nevertheless, it is worth doing some estimations of the error associated of ignoring the thermal expansion of the cavity. The typical temperature sensitivity of an FPI made of a hollow capillary tube, due to thermal expansion of the structure, is in the order of 0.83 pm/°C [214, 215]. This sensitivity value is also magnified by the optical Vernier effect (M-factor around 865), which means that the sensitivity of the Vernier envelope due to thermal expansion should be around -718 pm/°C (note that the magnification factor is negative, which results in a negative response of the Vernier envelope).

Converting the experimental sensitivity to refractive index ($S_{RI} = -500699$ nm/RIU) back into the corresponding temperature sensitivity (S_T), one obtains that:

$$S_T = S_{RI}\frac{\Delta RI}{\Delta T} = -500699 \times \frac{7.989 \times 10^{-5}}{0.74} = -54.055\, nm/°C, \tag{7.11}$$

where ΔT is the temperature variation used in the experiment (from 23.46 °C to 22.72 °C) and ΔRI is the correspondent refractive index variation due to the thermo-optic effect, as previously discussed.

The value of temperature sensitivity ($S_T = -54055$ pm/°C) corresponds actually to the sum between the thermo-optic effect and the thermal expansion. By subtracting the thermal expansion estimated before (-718 pm/°C), the temperature sensitivity due only to the thermo-optic effect is -53377 pm/°C. Hence, the thermal expansion was negligible during the experiments, as it is only about 1.3% of the final value.

7.3. Viscometer based on Hollow Capillary Tube

7.3.1. Introduction

An alternative way to post-process a hollow capillary tube is proposed in this section, to form a small-size optical fiber probe for measuring the viscosity of liquids. The traditional way to measure the viscosity of liquids is the well-known falling sphere technique, used to measure blood viscosity [216]. Currently, vibration methods are being used to measure viscosity by tracking the change in the resonant frequency of vibration [217, 218]. These kind of methods involve mainly cantilevers and piezoelectric resonators [218, 219].

The use of optical fiber sensors to measure viscosity is not quite explored. Most of the reported sensors involve complex structures [217], indirect measurements through bending loss mechanisms [220], or the use of viscosity-sensitive fluorescent probes [221]. Fiber gratings were also explored for this purpose. For example, a compact viscosity sensing probe was developed based on the acoustic excitation of a long period fiber grating (LPFG) [222], providing full optical interrogation. An optical fiber viscometer was also produced using an LPFG with a capillary tube [223].

The optical fiber probe viscometer presented in this section is low-cost and easy to fabricate, since it only requires a single mode fiber, a hollow silica capillary tube, and a splicing machine. The viscosity of a fluid is obtained through the interferometric measurement of the velocity of the fluid inside the probe and employing again the properties of a microstructured FPI. A discussion regarding reproducibility and the influence of temperature in the measurements is also included.

7.3.2. Fabrication

The viscometer fiber sensing probe is composed of a hollow silica capillary tube, with an inner diameter of 57 μm and a standard outer diameter (125 μm), spliced to a single mode fiber (SMF), and post-processed with electric arc. The fabrication process consists of three simple steps represented in figures 7.16(a-c).

Initially, the hollow capillary tube was spliced to the input SMF using a Sumitomo Electronics splicer (TYPE-71C). The splice was performed in the manual mode of the splicing machine, with the electric arc centered on the SMF to avoid the collapse of the hollow capillary tube, as depicted in figure 7.16(a). The following parameters were used in the splicing process: 0 ms pre-fusion time, 300 ms fusion time, standard arc power -100 arbitrary units (absolute arc-power was not possible to attain, only relative values).

After the splice, the hollow capillary tube was cleaved near the splicing region, leaving just a small section of hollow capillary tube with a few hundred microns, as shown in figure 7.16(b). This section will later form the sensing head. The length of this capillary tube will define approximately the final length of the sensing head. Similarly to the fabrication

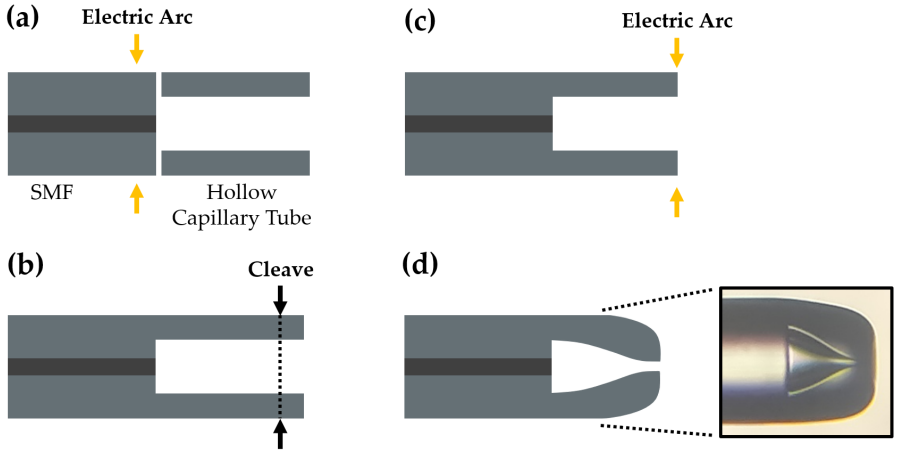

Figure 7.16. – Schematic of the fabrication process. The probe is fabricated using three simple steps: (a) splice between the hollow capillary tube and the input SMF; (b) hollow capillary tube cleavage; (c) electric discharges on the tube edge. (d) Final structure, together with a micrograph of the sensing head.

of the Fabry-Perot interferometers for the optical Vernier effect in the previous section, a magnification lens can also be used here to provide a better control of the cleaving process. With this, the desired length of hollow capillary tube is obtained with more precision.

In the last step, four electric arcs were applied at the end of the cleaved hollow capillary tube, as indicated in figure 7.16(c), in order to create a small access hole. The size of the access hole can be controlled by changing the number of electric arcs applied and/or the power/fusing time used in each electric discharge. In this step, the electric arc parameters used were the same as in the splicing step. The final result is a compact fiber probe composed of an air reservoir and a small access hole, as visible in the micrograph of figure 7.16(d).

7.3.3. Principle and Experimental Setup

The fiber probe viscometer works by dipping and removing it vertically from the liquid solution to be measured. The process is schematized in figure 7.17. During the dipping process, liquid enters the air cavity through the access hole, as represented in figure 7.17(a). Since the cavity has only one access hole, the fluid does not fill it completely due to the presence of air that increases in the inner pressure. Therefore, the cavity is only partially filled with a small amount of fluid. Afterwards, the fiber probe is removed from the liquid solution, as shown in figure 7.17(b), causing the liquid inside the cavity to evacuate. This process contributes to a variation, in time, of the air cavity length, as pointed in figure 7.17(c).

Figure 7.18 presents a micrograph of a fiber probe viscometer immersed in liquid. After entering through the access hole, the liquid partially filled the air cavity. Optically, the

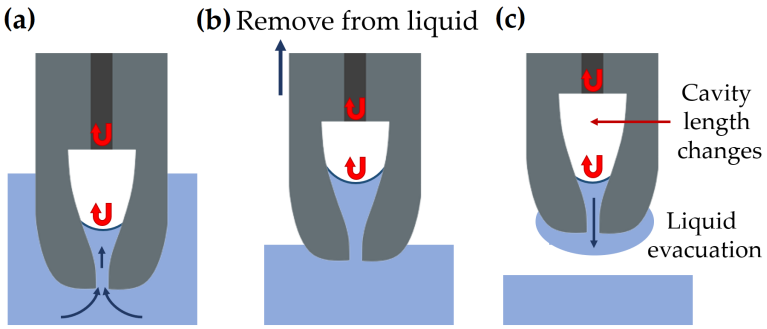

Figure 7.17. – Schematic diagram of the sensor operation. (a) Immersion in the liquid to be measured. The liquid enters the air cavity (b) Removal from the liquid. This step is performed when no more liquid is entering the cavity. (c) Liquid evacuation. The air cavity length increases due to the liquid evacuation.

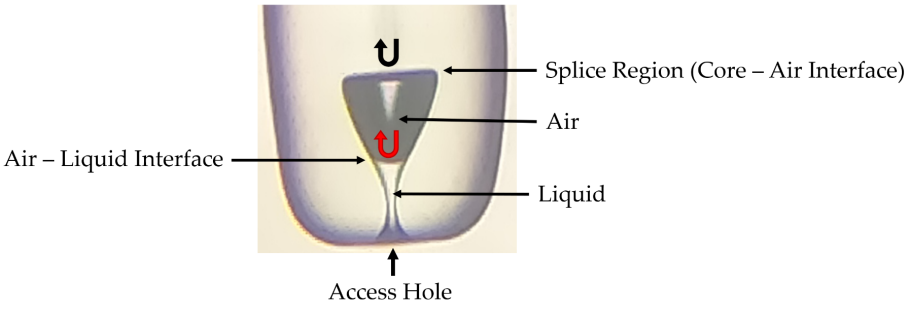

Figure 7.18. – Micrograph of the sensing head immersed in liquid. The fluid fills partially the air cavity, creating a reflective interface.

fiber probe behaves as a two-wave interferometer in a reflection configuration. The first reflection occurs at the interface between the input fiber and the air cavity, namely at the splice region. This reflection corresponds to a silica/air Fresnel reflection. Part of the input light still propagates through the air cavity and is reflected at the liquid interface, namely at the meniscus of the fluid. Hence, this second reflection corresponds to an air/liquid Fresnel reflection. These two reflective interfaces are marked in figure 7.18 with a black and a red arrow, respectively.

The two interfaces have low reflectivity (the reflection coefficients are small), and therefore only one reflection at each interface can be considered as a two-wave interferometer approximation. The position of the liquid interface, corresponding to the second mirror, changes in time due to the motion of the liquid (filling and evacuation). Hence, the intensity of the measured signal is also time dependent. The reflected signal intensity, $I(t)$, is described by the two-wave interference equation, assuming a flat liquid meniscus surface for simplification, given by [224]:

$$I(t) = |E_1|^2 + |E_2|^2 + 2|E_1||E_2| \cos\left[\frac{4\pi}{\lambda} nL(t) + \varphi_0\right], \tag{7.12}$$

where E_1 and E_2 are the electric fields of the reflected light at the first and second interfaces, respectively, λ is wavelength of the input light, n is the refractive index of the cavity (the cavity is always in air, so n can be simplified as 1), $L(t)$ corresponds to the length of the cavity, which changes in time, and φ_0 is the initial phase. By monitoring a single wavelength over time, the reflected signal intensity will change in time with an oscillatory behavior, according to equation 7.12, due to the variations of the cavity length.

Figure 7.19 displays an example of the reflected signal as a function of time when dipping and removing the fiber probe from a sucrose solution with a refractive index of 1.415 and a viscosity of 12.102 mPas. Initially, the intensity is stable and corresponds to a single reflection coming from the first interface (silica/air reflection). When the fiber probe viscometer is immersed in the solution, the liquid enters the cavity and the meniscus starts reflecting light, originating the two-wave interferometer. The quick displacement of the meniscus due to the quick filling of the cavity causes the intensity of the reflected signal to oscillate very fast. As the inner pressure raises, the liquid stops filling the cavity, and consequently the intensity of the reflected signal stabilizes and stops oscillating. When the fiber probe is removed vertically from the solution, the liquid flows out of the cavity, producing once more an oscillatory reflected signal. The oscillation frequency decreases until the intensity signal is again stable after all the liquid is removed from the cavity.

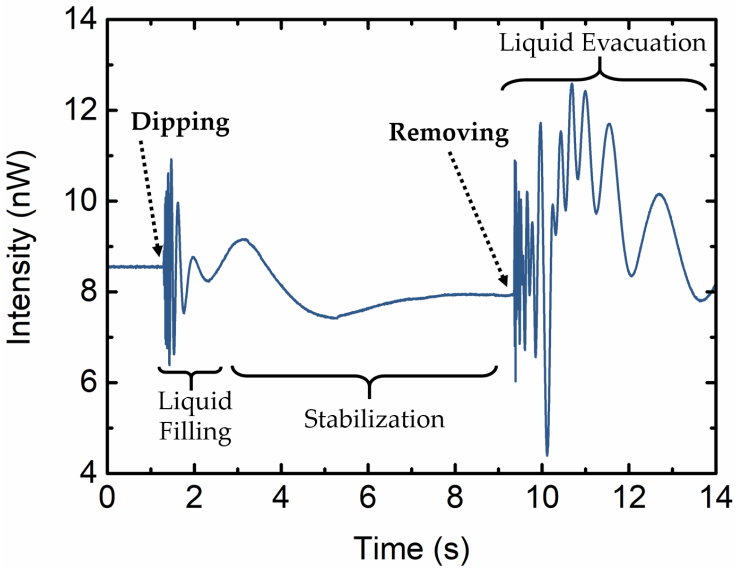

Figure 7.19. – Reflected intensity as a function of time, at 1550 nm, for a sucrose solution with a refractive index of 1.415 and a viscosity of 12.102 mPas. The fluid displacement inside the cavity causes fast oscillations in the intensity signal, happening especially during the dipping and removing processes.

The period of oscillation of the intensity signal depends on the variation of the cosine phase $\left(\Delta\varphi = \frac{4\pi}{\lambda} n \Delta L\right)$ in equation 7.12. Each period of oscillation (P) of the intensity signal corresponds to a phase change of 2π. Such phase change depends on the liquid

displacement, which produces a variation of the cavity length (ΔL) with time. With this, one can correlate the period of oscillation (P) of the intensity signal with temporal frequency (ν_t) with the correspondent variation of the cavity length (ΔL) as follows:

$$\upsilon_t P = 2\pi = \Delta\varphi \longleftrightarrow \frac{4\pi}{\lambda} n\Delta L = 2\pi \longleftrightarrow \Delta L = \frac{\lambda}{2n}. \tag{7.13}$$

The measurement was performed at a wavelength of 1550 nm which, for a refractive index of the air cavity assumed as 1, makes a period of oscillation (P) correspond to a change in the cavity length (ΔL) of 775 nm.

If the period of oscillation (P) is constant at different times, the fluid displacement shows a linear relation with respect to time. If the period of oscillation (P) is changing with time, also the fluid displacement correspondent to the change in the cavity length (ΔL) will vary with time, resulting in a non-linear behavior of the fluid displacement with respect to time.

The key point of this sensing structure is that the fluid displacement (d) is the sum over time of the changes in the cavity length (ΔL):

$$d = \sum_t \Delta L, \tag{7.14}$$

where ΔL is the change in the cavity length during a period of oscillation. Note that the integration time step (t) is, in general, not constant. Since the liquid movement is slowing down, the frequency of the oscillatory signal is also reducing in time (the period of oscillation is increasing), and therefore the time step of the integration is increasing.

By using the previous relationship one can track the fluid movement inside of the sensing probe during its evacuation by simply monitoring the variations of the intensity signal over time and converting it to fluid displacement. In the following analysis, a simple conversion was performed by considering half the periods ($P/2$) of the intensity signal and sum the corresponding cavity length changes ($\Delta L/2 = 775/2 = 387.5\,nm$) over time. This can be done by taking the maxima and minima of the oscillatory intensity signal. The time between a minimum (maximum) and the following maximum (minimum) corresponds to half a period.

Figure 7.20 shows the fluid displacement as a function of time converted from the intensity signal of figure 7.19. The fluid displacement follows the dynamics described before: displacement of the fluid during the filling process, stabilization, and evacuation of the fluid after removing the fiber probe from the solution.

The fluid viscosity (η) is a function of the fluid velocity (v): $\eta = func(v)$. This dependency can be experimentally derived by a calibration measurement with a fluid of known viscosity. Naturally, the fluid velocity depends on the cavity access hole size, as will be discussed later, which can be different from structure to structure. Therefore, each

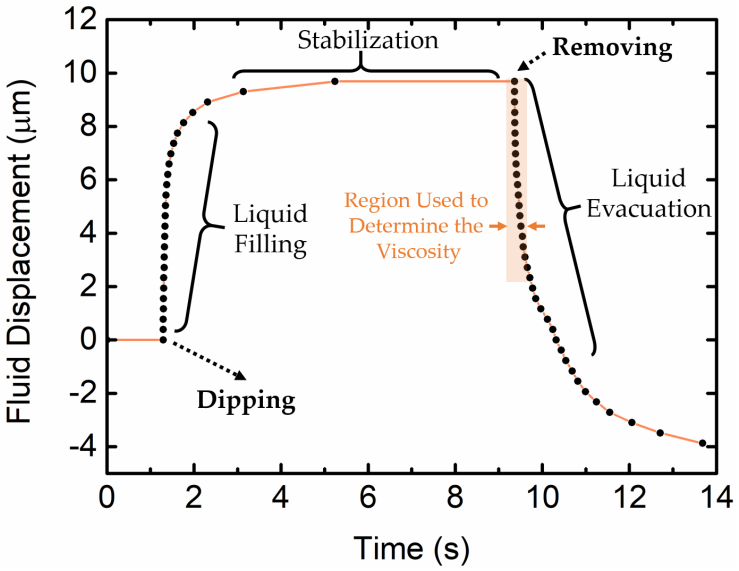

Figure 7.20. – Fluid displacement as a function of time converted from the intensity signal of figure 7.19. The region marked with the orang arrow is used to determine the viscosity.

new structure should be calibrated independently from the others. The fluid velocity (v) is obtained, for a liquid with unknown viscosity, through the slope of the fluid displacement as a function of time from the interferometric measurement:

$$v = \frac{fluid\,displacement}{time} \sim \frac{cavity\,length\,change\ (\Delta L)}{1/signal\,frequency\ (\nu_t)} = \frac{\lambda}{2}\nu_t. \tag{7.15}$$

Since the wavelength is known, the fluid velocity can be obtained from the measurement of the period of the intensity oscillations. As explained before, the dependency of the viscosity on the fluid velocity, $\eta = func\,(v)$, is obtained from the sensor characterization. Therefore, given an unknown fluid, the fluid velocity in the first moments of the evacuation process (where a linear regime of fluid displacement can be observed) is determined through the interferometric measurement, and then the viscosity is obtained through the relationship $\eta\,(v)$ derived from the calibration measurement.

Note that the important parameter to obtain the viscosity of different fluids is the variation of the cavity length (ΔL), responsible for the oscillatory behavior of the intensity signal over time. The cavity length itself (L) only contributes to the initial phase (φ_0) and, therefore, it is not relevant for the measurement. A Newtonian viscosity behavior of the fluids was assumed in the whole experiment.

The interrogation of the fiber probe is done in a reflection configuration, using an optical circulator. The input light source was an erbium-doped broadband optical fiber source with a central wavelength of 1550 nm and a bandwidth of 100 nm. The reflected intensity signal as a function of time was monitored at a single wavelength (1550 nm) with an optical spectrum analyzer (OSA). Such time measurement is achieved by selecting, in the OSA, a

central wavelength of 1550 nm and a measurement span of 0 nm. These settings allow the OSA to measure the intensity at 1550 nm as a function of time, with a time step of 3 ms (the time step might vary depending on the OSA model and settings).

Ideally, a fast photodetector should be used to monitor the intensity signal as a function of time with high temporal resolution. The time resolution achieved by the OSA might be problematic to resolve fast oscillations at the beginning of the dipping process. In this situation, the liquid enters so fast in the cavity that the time resolution of the OSA cannot measure correctly the oscillations produced in the intensity signal. Therefore in figure 7.20, the displacement obtained after the evacuation process appears to be lower than the displacement obtained at the start of the dipping process (difference of around 4 μm). In fact, it does not mean that the amount of liquid entering the cavity is less than the amount of liquid evacuating the cavity. The problem simply arises from the lack of time resolution to observe correctly the initial condition. Apart from using a fast photodetector, another solution to overcome such issue is to use longer wavelengths. From equation 7.13, increasing the wavelength used in the experiment makes a period of oscillation correspond to a larger cavity length change (ΔL). Hence, this reduces the signal frequency, being easier to measure fast displacements of liquid inside the cavity. Nevertheless, this problem is not relevant for the final application of the fiber probe, since the initial region corresponding to the dipping process is not used for viscosity measurements. To perform viscosity measurements, only the variations of the intensity signal after removing the sensor from the sucrose solution are considered, as indicated in figure 7.20.

Taking as a reference the reflected signal from a cleaved single mode fiber in air (3.3% Fresnel reflection at 1550 nm), the splice losses have been measured to be about 0.5 dB, assuring a good optical signal quality.

7.3.4. Characterization

Mixtures of sugar in water with different viscosities were used as calibrated solutions to characterize the viscometer fiber probe. The relation between sugar concentration, refractive index, viscosity, and temperature is well studied and can be found in different books [9, 10]. The viscosity (η) of the different sucrose solutions, at 20 °C, was determined using the following relationship[2]:

$$\eta\,(n) = 0.59269 + 0.00758e^{[(n-1.35348)/0.01054]} + 0.89366e^{[(n-1.35348)/0.02675]}, \qquad (7.16)$$

where η is the viscosity given in millipascal-second (mPa.s), and n is the refractive index of the sucrose solution. It is important to mention that the coefficients in equation 7.16

[2]Further details can be found in appendix D.

are material dependent. Therefore, this equation is only valid for sucrose solutions. These solutions of known viscosity were then used to characterize and calibrate the viscometer fiber probe. The objective is to obtain the relationship between the viscosity and the fluid velocity during the evacuation: $\eta = func\,(v)$.

The intensity signal as a function of time for two sucrose solutions with distinct viscosities (1.887 mPa.s and 12.102 mPa.s), after removing the fiber probe from the solutions, is shown in figure 7.21. As expected, the solution of lower viscosity moves faster and produced a higher frequency signal, while the higher viscosity solution is slower and originates a low frequency signal. Another interesting property is also visible in figure 7.21. The visibility of the interference signal is higher for the solution of higher viscosity, due to its higher refractive index. The reflection coefficient at the interface of the higher viscosity solution (second interface) is closer to the reflection coefficient of the first interface. Therefore, the two interfering waves have closer intensities in the case of a higher viscosity solution than in the case of a lower viscosity solution.

The viscometer fiber probe was then characterized using sucrose solutions with different viscosities ranging from 1.887 mPa.s (19.5 %wt/wt of sucrose) to 19.170 mPa.s (51.8 %wt/wt of sucrose). The liquid displacement at the evacuation process as a function of time was obtained for each solution. The results can be found in figure 7.22.

As expected, lower viscosity solutions evacuate faster from the cavity than the ones of higher viscosity, showing a larger fluid displacement in a smaller time frame. Between every measurement, the probe was always cleaned by dipping it several times in deionized

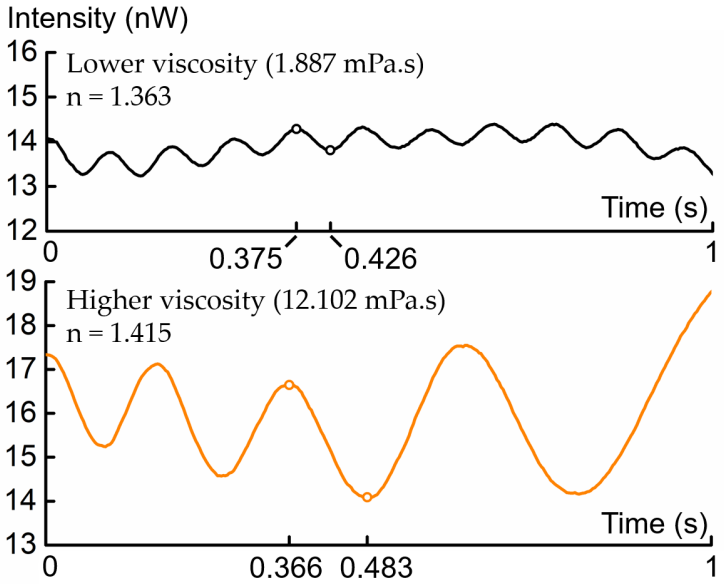

Figure 7.21. – Reflected intensity as a function of time, at 1550 nm, for two sucrose solutions of distinct viscosities: 1.887 mPa.s and 12.102 mPa.s. Higher viscosity solutions produce slower intensity oscillations.

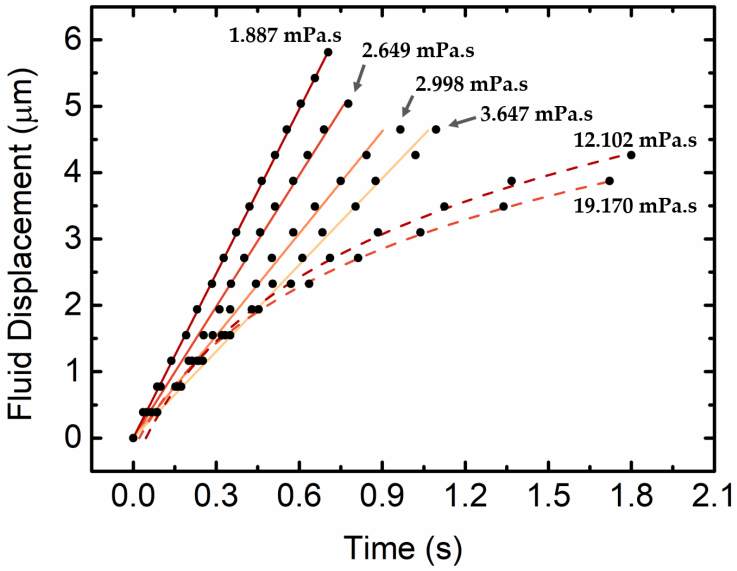

Figure 7.22. – Fluid displacement as a function of time for sucrose solutions with different viscosities. Solutions of higher viscosity tend to have a more non-linear displacement inside the cavity.

water, followed by ethanol, in order to avoid contamination from previous solutions. Then, the probe was dried until a stable reflected signal from an empty cavity is obtained.

A linear fit was applied to the data presented in figure 7.22 to retrieve the fluid evacuation velocity. In this step only the first 300 ms of resolved oscillations were considered, where the liquid displacement follows approximately a linear regime. The slope corresponds to the fluid evacuation velocity, which is different according to the viscosity of the fluid. Therefore, analyzing the fluid evacuation velocity, the liquid viscosity can be obtained. The fluid viscosity as a function of the obtained fluid evacuation velocity is shown in figure 7.23. The dependence of the fluid viscosity on the evacuation velocity can be separated into two linear regimes. The first corresponds to a low viscosity regime, for fluid viscosities up to around 4.34 mPa.s. In that regime, the fluid viscosity as a function of the evacuation velocity follows approximately a linear dependency expressed by:

$$\eta\,(v) = 15.85777 - 0.45284v,\ \eta \leq 4.34\,mPa.s. \tag{7.17}$$

The second regime occurs for higher viscosities, starting from around 4 mPa.s, where the fluid viscosity as a function of the evacuation velocity can be described as:

$$\eta\,(v) = 84.43479 - 18.61649v,\ \eta > 4\,mPa.s. \tag{7.18}$$

To study the reproducibility of the fluid displacement behavior, three measurements in a row were performed in two solutions with distinct viscosities: 2.10 mPa.s and 9.95 mPa.s.

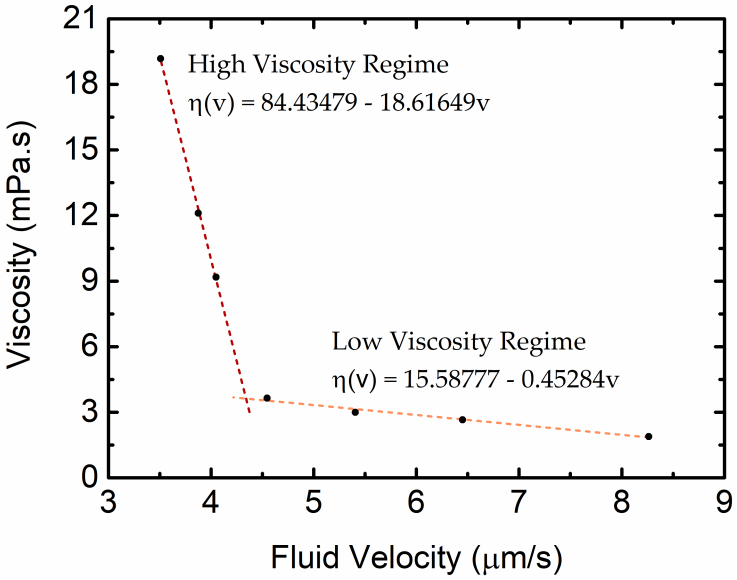

Figure 7.23. – Fluid viscosity as a function of the fluid evacuation velocity. The result can be divided into two regimes: low viscosity (up to around 4 mPa.s) and high viscosity (starting from around 4 mPa.s.

The resultant intensity signal was then converted into fluid displacement as a function of time. The reproducibility results are presented in figure 7.24. The three measurements for each solution show the same fluid displacement behavior as a function of time. The fluid displacement has a standard deviation of 42 nm and maximum deviation of 83 nm for the lower viscosity solution (2.10 mPa.s), and a standard deviation of 105 nm and the maximum deviation of 312 nm for the higher viscosity solution (9.95 mPa.s). In this last case, the deviation is larger for the last value of fluid displacement, which is mainly caused by the fact that the cavity is almost in an empty state.

When performing viscosity measurements, one must be aware that the value of viscosity is highly influenced by temperature variations. From the fiber probe point of view, the sensing region consists mainly of air, presenting an outer part made of silica. Therefore, the effect of thermal expansion in the structure does not have a great impact on the measurements. The thermal expansion affects the length of the cavity, $L\,(t)$, in equation 7.12, adding a phase delay (or advance) proportional to the physical expansion of the cavity. Such additional phase is seen as a D.C. component in the fluid displacement as a function of time. To estimate the cavity length change due to thermal expansion, the thermal expansion coefficient of silica was considered as $0.55\times10^{-6}\,°C^{-1}$ [104]. Considering an hypothetical worst case scenario, where the temperature changes by 50 °C (in reality, during a measurement the temperature should not fluctuate more than a few degrees at most), the modulus of the relative expansion of the cavity is $\delta L = 2.75\times10^{-5}$. For a cavity length of 200 μm, the change in length due to thermal expansion is $\Delta L_T = L\times\delta L = 5.5$ nm,

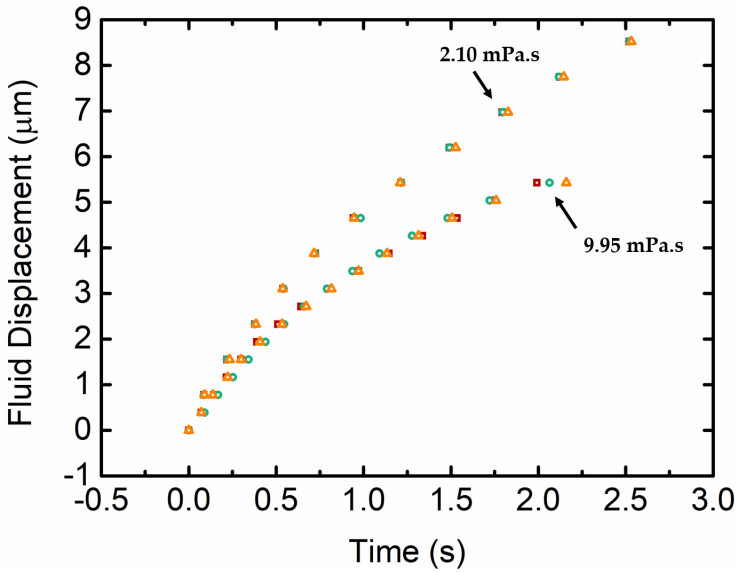

Figure 7.24. – Three different measurements for two solutions with distinct viscosities: 2.10 mPa.s and 9.95 mPa.s. The measurements show a good reproducibility with a standard deviation of 42 nm and 105 nm for the two cases, respectively.

which is much smaller than the fluid displacement values (within the order of microns). Consequently, the effect of thermal expansion of the cavity can be neglected.

The sensor is then able to measure the changes in the fluid viscosity due to temperature variations. To demonstrate this, different measurements were performed using the same solution at distinct temperatures. The solution used was a 47 %wt/wt sucrose solution. The viscosity of the prepared sucrose solutions at different temperatures[3] was determined using tabulated values [11]. The solution was poured inside a glass contained and placed on top of a heating plate. To ensure a good homogeneity, a magnetic stirrer was used to constantly mix the solution while heating. Figure 7.25 represents the fluid displacement inside the cavity as a function of time for the the sucrose solution at different temperatures. As the temperature increases, the velocity of the fluid displacement (given by the slope of the data) increases due to a decrease in the viscosity of the sucrose solution.

The fluid dynamics is different for every fabricated fiber probe. It depends on the size of the cavity and, more important, on the size of the access hole. Hence, one needs to fully characterize every fabricated probe independently. On one hand, for target solutions with low viscosities, a small access hole is desirable to provide a slower evacuation of the cavity. On the other hand, high viscosity solutions cannot enter small access holes, and therefore a larger access hole is desirable.

To investigate the influence of the access hole dimension, three probes were fabricated with different access hole diameters. The larger access hole, with a diameter of around

[3]Further details can be found in appendix D.

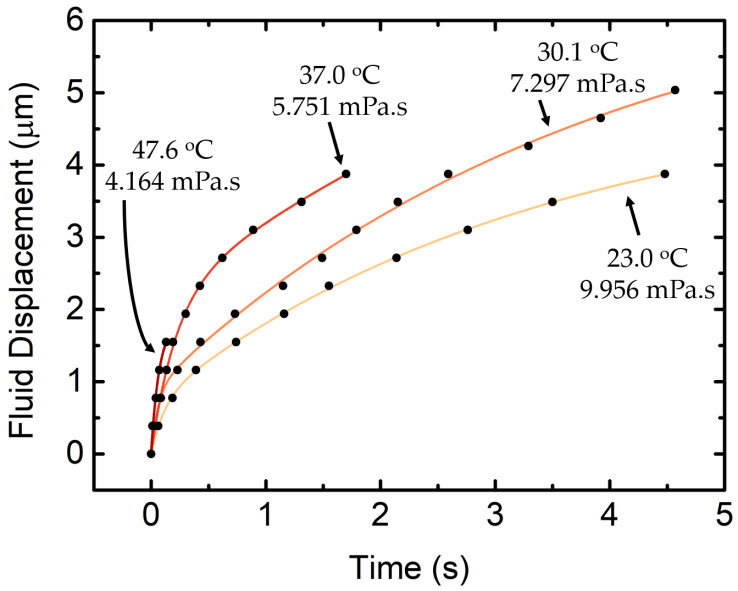

Figure 7.25. – Fluid displacement as a function of time for 47%wt/wt sucrose solution at different temperatures. The viscosity changes due to temperature variations are also detected by the sensing structure, producing distinct responses.

31 μm, was fabricated using three electric arcs with an arc power of -100 arbitrary units and a fusion time of 200 ms. The medium size access hole, with a diameter of around 19 μm, was produced using three electric arcs with the same arc power and a fusion time of 300 ms. As for the smaller access hole, with a diameter of around 6 μm, five electric

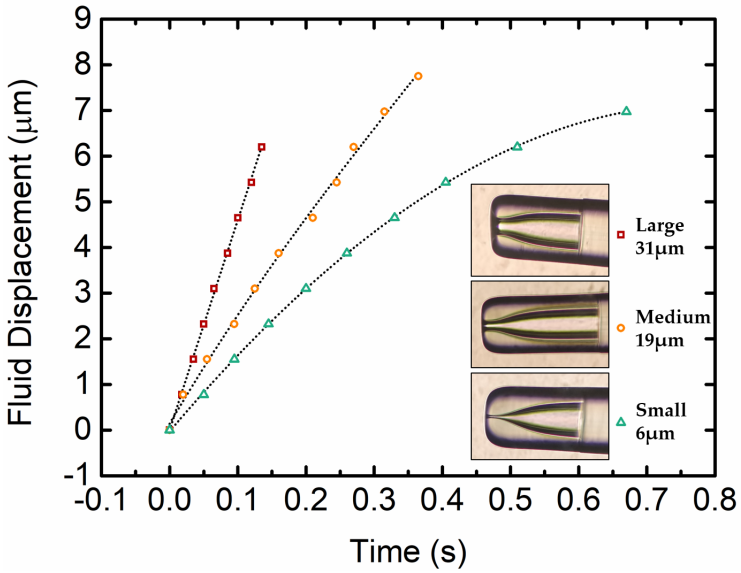

Figure 7.26. – Fluid displacement as a function of time for different access hole diameters. The same sucrose solution with a viscosity of 3.0 mPa.s was used in all cases. The fluid displacement tends to be slower and non-linear for smaller access holes.

arcs were applied with the same arc power and a fusion time of 300 ms. All three samples were used to measure a sucrose solution with a viscosity of 3.0 mPa.s (at 20 °C). The fluid displacement as a function of time for the three samples is depicted in figure 7.26, together with microscope images of the samples. The probe with a small access hole presents a non-linear behavior of the fluid displacement over time. For high viscosity solutions, the fluid displacement is very slow or the fluid might not even be able to enter the cavity through the access hole. Therefore, small access holes are more suitable to measure low viscosity solutions. On the other hand, larger access holes result in faster fluid displacements, which can be problematic for low viscosity fluids. The produced intensity signal oscillations are very fast, making them hard to be resolved in time. In sum, the best option is to dimension the access hole of the viscometer fiber probe depending on the range of viscosities to be measured. Nevertheless, one should not forget that a measurement system with a fast photodetector (instead of an OSA) is enough to track the fast oscillations originated by a low viscosity fluid measured with a large access hole probe.

7.4. Conclusion

Two advanced sensing structures for application in liquid media were explored in this chapter. The first structure was based on a new method that combines an extreme optical Vernier effect with a few-mode sensing interferometer. The demonstrated method proved to be capable of overcoming the limitations of the standard optical Vernier effect techniques. The implementation of a few-mode fiber refractometer with such method registered a record M-factor of 865, also reaching a record value in terms of refractive index sensitivity for this kind of interferometric fiber structure. In fact, for a single-mode Vernier structure to achieve an extreme M-factor of 865, it would correspond to an immeasurable Vernier envelope FSR longer than 6400 nm. Therefore, the proposed method allows us to achieve such giant M-factors whilst maintaining a measurable envelope. From the obtained results for refractive index sensing, it would be very attractive to apply a similar structure for high resolution gas sensing and biosensing, namely in extreme environments, where it is necessary to detect very small concentrations.

Although the concept was demonstrated experimentally and also via simulations, it is still open the possibility of further exploration of the enhanced sensitivity observed at some internal envelope intersections mathematically. The relative movement between the internal envelopes was not fully explored, and it is the key for the behavior of this extreme case of optical Vernier effect.

The proposed concept of extreme optical Vernier effect can also be adapted to other sensing interferometers (Mach-Zehnder interferometers, Michelson interferometers, hybrid interferometric structures, among others), to obtain giant sensitivities to other physical and chemical parameters. Therefore, the proposed method opens new horizons for the

development of a new generation of sensors with extreme sensitivities and resolutions for demanding state-of-the-art applications.

Regarding the second structure proposed in this chapter, the optical fiber probe viscometer was capable of performing an all-optical interferometric measurement of the viscosity of a liquid. Besides, the total volume of the cavity is approximately 50 pL, which makes the volume of liquid required to perform the measurement negligible. In other words, practically only a very small sample volume is required to realize the measurement.

For specific applications, a different configuration involving a temperature sensor in parallel should be studied in the future, for instance incorporating a fiber Bragg grating next to the cavity to read the temperature while the probe is immersed in the liquid. The aim is to provide simultaneous temperature measurements and/or to compensate the change of a fluid viscosity due to temperature. Another point worth of further investigation is the influence of the size of the access hole in the maximum viscosity value measurable. Moreover, the next step for future studies is also to determine the feasibility of applying this sensing structure to the measurement of biological fluids.

Chapter 8.

Conclusions and Final Remarks

The works presented along this dissertation were focused on two main points of study. The first was the study, design, and realization of advanced interferometric fiber sensors based on microstructures. This included the combination of optical microfibers, which allow the propagating light to interact better with the environment, together with microstructured interferometers such as microfiber knot resonators, Mach-Zehnder interferometers, and Fabry-Perot interferometers. Focused ion beam milling was also explored as a technology to create not only microstructured interferometers in optical microfibers, but also to open access holes in specialty fibers for liquid sensing. The second main point was the interest of increasing the performance of the interferometric fiber sensors (i.e. enhance the sensitivity). In this context, an in-depth study, further development, and application of the optical Vernier effect to optical fiber interferometers as a tool to surpass the sensitivity limits of conventional fiber interferometers were performed. Some of the enormous potentials of this effect applied to optical fiber sensing were discussed and demonstrated in this dissertation. However there are still other variants that have not been here explored and that could still lead to very interesting results. This dissertation was meant to guide the reader across the different topics and works, providing also the basic background and the state-of-the-art of these topics for a better contextualization and understanding of the concepts presented.

Chapter 2 introduced the reader to optical microfibers and their fabrication methods, as well as to the different interferometric sensing structures that were later on being used. The basic concepts and properties of the different interferometric sensing structures were presented, together with a small state-of-the-art review on different applications, especially when combined with optical microfibers. Since focused ion beam milling was used along the dissertation, chapter 2 also included a brief overview on the focused ion beam technology, with special focus on the application to optical fibers and respective sample preparation.

Chapter 3 explored microstructured sensing devices with optical microfibers, where the different interferometric structures previously introduced (microfiber knot resonator, Mach-Zehnder interferometer, and Fabry-Perot interferometer) were microfabricated in

optical microfibers and microfiber probes. The two devices proposed in this chapter targeted two different issues related with optical fiber sensing. The first structure tackled the problem of cross-sensitivity. By combining a microfiber knot resonator and a Mach-Zehnder interferometer embedded in the same optical microfiber, the final response could be used for simultaneous measurement of refractive index of liquids and temperature. The use of a single optical microfiber and two co-propagating modes to form the Mach-Zehnder interferometer is a novel alternative that makes the final structure more compact. The use of microfiber knot resonators to sense liquids might lead to some problems: the microfiber knot resonator can be very fragile and the surface tension of water is, in some cases, enough to change the size of the knot or to break the microfiber. Therefore, it would be useful to explored some protection techniques, like coating the structure with a low refractive index polymer to ensure a good stability and protection of the microfiber knot resonator. The second proposed device was meant to be a miniaturized sensing probe, with potential to perform point measurements, but simultaneously with the possibility to achieve higher sensitivities than what has been previously reported in the literature for these kind of structures. A Fabry-Perot interferometer microfabricated with focused ion beam milling in an optical microfiber probe (similar to what has already been published [3]) was taken as the main structure. However, the Fabry-Perot interferometer was designed to be multimode, which was different from the other works. The beating generated in the output spectrum showed a higher wavelength shift in comparison to the normal sensing Fabry-Perot interferometer signal. This phenomenon was actually the result of the optical Vernier effect, however in an uncontrolled way, as one could not control the modes propagating in the structure. This last work allowed to only have a small glimpse of the capabilities of using the optical Vernier effect combined with fiber sensing. For this reason, the following works headed in this new direction, trying to understand the essence of such an effect. To fully understand and control the optical Vernier effect, it was first necessary to look deep into its origins.

Chapter 4 presented the full mathematical description of the optical Vernier effect and its properties. Important comments and small details were included along this chapter for a deeper understanding and to avoid misuse and misinterpretation of the effect in the future. Before starting to apply the effect, it was essential to have an overview of what was published in this field until now. Therefore, the state-of-the-art, presented also in chapter 4, focused on the different configurations explored over the last few years to introduce the optical Vernier effect, as well as the distinct applications that it can be used for.

Upon exploring the fundamentals of the optical Vernier effect, the following questions were asked: “what is the limit? What is the maximum magnification that one can obtain from such an effect?”. The answer led to a contradictory requirement: the smaller the detuning between the two interferometers, the higher was the magnification factor obtained, but also the larger was the Vernier envelope. The detection system imposes then

a limitation on how large the Vernier envelope could be to still be measurable, which in return dictates the maximum magnification factor achievable.

Chapter 5 explored a new extended concept of the optical Vernier effect was found during the investigations: the existence of optical harmonics of the Vernier effect, which enable greater magnification factors to be achieved, beyond the limitations previously described. This novel concept required the development of a new mathematical description, presented in this chapter, that could describe correctly the effect and all its new properties. By up-scaling the optical path length of the reference interferometer by multiples of the optical path length of the sensing interferometer, different output spectra with harmonic properties were generated. The important message here is that the magnification factor can increase proportionally to the harmonic order (it increases by $(i+1)$, being i the order of the harmonic), for the same detuning, while maintaining the size of the Vernier envelope.

Naturally, under certain conditions the effect does not work as desired and does not provide the enhancements discussed before. One of these situations, also discussed in chapter 5, is when the up-scaling of the optical path length is done in the sensing interferometer, rather than in the reference interferometer. The result of such case was actually no improvement of the sensitivity with the harmonic order. Apart from this special situation, there are also differences between the parallel and series configurations, reason why it was important to present them in chapter 5, before experimentally applying the effect.

Once more, the same question as before can be asked: "what is now the limit? What is the maximum harmonic order achievable?". These questions were also examined at the end of chapter 5. To my view, one of the most limiting factors here is the complexity of the obtained spectrum. The higher the harmonic order, the more complex the spectrum is. This requires a lot of signal processing and effort to be able to extract the wavelength shift of the Vernier envelope. Hence, the limits depend on the processing capabilities and, not less important, on the resolution of the interrogation system.

Now that the fundamentals of the optical harmonic Vernier effect were studied, the next step was to experimentally demonstrate the effect and validate its properties. At the same time, the sensing structures were applied to measure strain.

Chapter 6 presented the experimental demonstration of the optical harmonic Vernier effect for two configurations, parallel and series, using Fabry-Perot interferometers. The parallel configuration relied on Fabry-Perot interferometers made from hollow capillary tubes. The structures were characterized in terms of applied strain for the first three harmonic orders of the optical Vernier effect. It has been experimentally proven that the enhancement of the magnification factor, and respective sensitivity, increased with the order of the harmonic. An important message from this work is the importance of the detuning between the optical path lengths of the two interferometers. The magnification factor depends on this detuning, which is highly dependent on the fabrication methods. It

is very difficult to create multiple interferometric structures with exactly the same optical path length, due to fabrication constrains. Hence, the envelope phase sensitivity was determined in each case, in order to make a fair comparison between the different structures used to introduce the three harmonic orders of the optical Vernier effect. The envelope phase sensitivity takes into account the free spectral range of the Vernier envelope, and therefore it is independent of the detuning. The series configuration, also demonstrated in chapter 6, combined a hollow microsphere and a section of a multimode fiber to form two Fabry-Perot interferometers physically connected. A special case of optical Vernier effect was here explored, where none of the two interferometers was used as a reference. In this specific case, the sensitivity of the Vernier envelope depends on the difference between the sensitivities of the two interferometers, weighted by their magnification factors. One saw that, if both interferometers have similar sensitivities, there would be no improvement of sensitivity when using the optical Vernier effect. Yet, a high sensitivity to strain was still observed for the proposed structure (about 140-fold larger than a fiber Bragg grating), since the hollow microsphere alone had more strain sensitivity than the section of multimode fiber used. Simultaneous measurement of strain and temperature was also demonstrated with this structure, by using the Vernier envelope response together with the high frequency response of the spectrum.

Chapter 7 demonstrates two last works dedicated to the measurement of liquid properties, in this case refractive index and viscosity. The first work results from the combination of different concepts and techniques developed during the PhD: Fabry-Perot interferometers using hollow capillary tubes, focused ion beam milling to open access holes in one of the interferometers, and an extreme case of optical Vernier effect. The extreme optical Vernier effect was discovered and proposed as a way to surpass once more the limitations of the conventional optical Vernier effect. The use of a few-mode Fabry-Perot interferometer, together with the optical Vernier effect in tune with the fundamental propagating mode, allowed to achieve a magnification factor an order of magnitude higher than the expected limit for the conventional optical Vernier effect, whilst maintaining a measurable Vernier envelope. When applied to liquid sensing, the proposed arrangement is capable of achieving a giant sensitivity to refractive index, allowing to measure fine variations of this quantity. To the best of the author's knowledge, the obtained sensitivity value (about 500000 nm/RIU) is a record value for a Fabry-Perot interferometer structure of this kind. The second work explored in chapter 7 makes use of a similar hollow capillary tube, but now post-processed with an electric arc to form a small-size optical fiber probe with an access hole for viscosity sensing of liquids. The developed sensor works as a two-wave interferometer once the liquid enters the probe, being the air-liquid interface inside the microstructured hollow capillary tube one of the mirrors of the interferometer. Through interferometric measurement of the liquid displacement inside the probe, the viscosity of the liquid was retrieved. The fact that there are not many options for optical fiber sen-

sors to measure viscosity makes this novel approach very attractive. Additionally, the probe volume is so small (about 50 pL) that practically no liquid is consumed during the measurement.

The works developed during this PhD were very diverse, not just in terms of sensing configurations, but also in the different possible options for the application of the optical Vernier effect. Nevertheless, there is still space for improvement and for new ideas to be explored in the future. The introduction of the optical Vernier effect, now in a controlled way, to the focused ion beam-milled Fabry-Perot interferometer in a microfiber probe could still be further explored. The concept of optical harmonic Vernier effect here proposed can, from now on, be applied to other types of optical fiber interferometers, creating a new generation of highly sensitive fiber sensors for different applications. By taking a closer look into the state-of-the-art configurations for the optical Vernier effect, the future trend will involve the use of hybrid configurations. The combination of different types of interferometers in a hybrid configuration to introduce the optical Vernier effect is still very attractive and can provide innovative results. One of these cases is the use of two interferometer with opposite responses to the measured parameter, in a configuration without a reference interferometer, which could lead to even further improvements in the magnification factors obtained. Moreover, the viability of such a structure for simultaneous measurement of parameters is higher, since each of the two interferometer can be especially optimized to sense a specific different measurand. Regarding the sensing structure with giant refractometric sensitivity, further studies should be performed to improve its applicability, namely by exploring the possibility of functionalization of the Fabry-Perot cavity to different substances. If viable, this approach could lead to a highly sensitive platform for biological fluid analysis or chemical compound detection.

At last, a huge downside of the optical Vernier effect, that still requires a lot of investigation, is the interrogation system. There is a urgent need for the development of a simpler interrogation system to analyze the response of the effect. The need of a broadband source and an optical spectrum analyzer to measure a broad range of wavelengths, plus the additional signal processing required to extract the Vernier envelope wavelength shift from the spectrum, makes the use of this effect less attractive. If there was an interrogation system relying only on photodetectors and two, or a few more, laser lines to measure and characterize in a simpler, faster, and cheaper way the response of the optical Vernier effect, it would represent a huge step towards the acceptance and quick adoption of the optical Vernier effect as a viable sensing solution in different areas.

Bibliography

[1] Byeong Ha Lee, Young Ho Kim, Kwan Seob Park, Joo Beom Eom, Myoung Jin Kim, Byung Sup Rho, and Hae Young Choi. Interferometric fiber optic sensors. *Sensors*, 12(3):2467–2486, 2012.

[2] Masaru Muranishi, Kazutaka Sato, Sumio Hosaka, Atsushi Kikukawa, Toshimichi Shintani, and Kenchi Ito. Control of aperture size of optical probes for scanning near-Field Optical microscopy using focused ion beam technology. *Japanese Journal of Applied Physics*, 36(Part 2, No. 7B):L942–L944, jul 1997.

[3] Ricardo M André, Stephen C. Warren-Smith, Martin Becker, Jan Dellith, Manfred Rothhardt, M I Zibaii, H Latifi, Manuel B Marques, Hartmut Bartelt, and Orlando Frazão. Simultaneous measurement of temperature and refractive index using focused ion beam milled Fabry-Perot cavities in optical fiber micro-tips. *Optics Express*, 24(13):14053–14065, jun 2016.

[4] Stephen C. Warren-Smith, Ricardo M. André, Jan Dellith, Tina Eschrich, Martin Becker, and Hartmut Bartelt. Sensing with ultra-short Fabry-Perot cavities written into optical micro-fibers. *Sensors and Actuators B: Chemical*, 244:1016–1021, jun 2017.

[5] Shaoxian Zhang, Yin Liu, Huiyong Guo, Ai Zhou, and Libo Yuan. Highly sensitive vector curvature sensor based on two juxtaposed fiber Michelson interferometers with Vernier-like effect. *IEEE Sensors Journal*, 19(6):2148–2154, mar 2019.

[6] Zhilin Xu, Qizhen Sun, Borui Li, Yiyang Luo, Wengao Lu, Deming Liu, Perry Ping Shum, and Lin Zhang. Highly sensitive refractive index sensor based on cascaded microfiber knots with Vernier effect. *Optics Express*, 23(5):6662, mar 2015.

[7] Zhilin Xu, Yiyang Luo, Deming Liu, Perry Ping Shum, and Qizhen Sun. Sensitivity-controllable refractive index sensor based on reflective θ-shaped microfiber resonator cooperated with Vernier effect. *Scientific Reports*, 7(1):1–8, 2017.

[8] Ling Liu, Tigang Ning, Jingjing Zheng, Li Pei, Jing Li, Jihong Cao, Xuekai Gao, and Chuanbiao Zhang. High-sensitivity strain sensor implemented by hybrid cascaded

interferometers and the Vernier-effect. *Optics & Laser Technology*, 119:105591, nov 2019.

[9] Mosen Asadi. Tables. In *Beet-Sugar Handbook*, pages 779–801. John Wiley & Sons, Inc., 2005.

[10] United States Department of Agriculture. Technical Procedures Manual. In *SCI Division Inspection Series*, pages 1–169. 2013.

[11] J.F. Swindells, C.F. Snyder, R.C. Hardy, and P.E. Golden. *Viscosities of Sucrose Solutions at Various Temperatures: Tables of Recalculated Values*. U.S. Department of commerce, National Bureau of standards, united sta edition, 1958.

[12] Alexey N Bashkatov and Elina A Genina. Water refractive index in dependence on temperature and wavelength: a simple approximation. In Valery V Tuchin, editor, *Saratov Fall Meeting 2002: Optical Technologies in Biophysics and Medicine IV*, volume 5068, pages 393–395. International Society for Optics and Photonics, SPIE, oct 2003.

[13] Bernard S. Finn. *City of Light: The Story of Fiber Optics (review)*, volume 43. 2002.

[14] K.C. Kao and G.A. Hockham. Dielectric-fibre surface waveguides for optical frequencies. *Proceedings of the Institution of Electrical Engineers*, 113(7):1151–1158, jul 1966.

[15] André D. Gomes, Jiangbo Tim Zhao, Alessandro Tuniz, and Markus A. Schmidt. Direct observation of modal hybridization in nanofluidic fiber [Invited]. *Optical Materials Express*, 11(2):559, feb 2021.

[16] André D. Gomes, Jens Kobelke, Jörg Bierlich, Jan Dellith, Manfred Rothhardt, Hartmut Bartelt, and Orlando Frazão. Giant refractometric sensitivity by combining extreme optical Vernier effect and modal interference. *Scientific Reports*, 10(1):19313, dec 2020.

[17] Paulo Robalinho, Andre Gomes, and Orlando Frazao. Colossal Enhancement of Strain Sensitivity Using the Push-Pull Deformation Method. *IEEE Sensors Journal*, 21(4):4623–4627, feb 2021.

[18] Paulo Manuel Ribeiro Robalinho, Andre D. Gomes, and Orlando Frazao. High Enhancement Strain Sensor Based on Vernier Effect Using 2-Fiber Loop Mirrors. *IEEE Photonics Technology Letters*, 32(18):1139–1142, sep 2020.

[19] André D Gomes, Marta S Ferreira, Jörg Bierlich, Jens Kobelke, Manfred Rothhardt, Hartmut Bartelt, and Orlando Frazão. Hollow microsphere combined with optical

harmonic Vernier effect for strain and temperature discrimination. *Optics and Laser Technology*, 127(February):106198, 2020.

[20] André D. Gomes, Marta S. Ferreira, Jörg Bierlich, Jens Kobelke, Manfred Rothhardt, Hartmut Bartelt, and Orlando Frazão. Optical harmonic Vernier effect: a new tool for high performance interferometric fibre sensors. *Sensors*, 19(24):5431, 2019.

[21] André D. Gomes, Martin Becker, Jan Dellith, Mohammad I. Zibaii, Hamid Latifi, Manfred Rothhardt, Hartmut Bartelt, and Orlando Frazão. Multimode Fabry-Perot Interferometer Probe Based on Vernier Effect for Enhanced Temperature Sensing. *Sensors*, 19(3):453, jan 2019.

[22] Andre D. Gomes, Jens Kobelke, Jorg Bierlich, Kay Schuster, Hartmut Bartelt, and Orlando Frazao. Optical fiber probe viscometer based on hollow capillary tube. *Journal of Lightwave Technology*, 37(18):4456–4461, sep 2019.

[23] Beatriz Silveira, André Gomes, Martin Becker, Henrik Schneidewind, and Orlando Frazão. Bunimovich stadium-like resonator for randomized fiber laser operation. *Photonics*, 5(3):17, jul 2018.

[24] André Gomes, Catarina Monteiro, Beatriz Silveira, and Orlando Frazão. A brief review of new fiber microsphere geometries. *Fibers*, 6(3):48, jul 2018.

[25] Andre D Gomes, Fatemeh Karami, Mohammad I Zibaii, Hamid Latifi, Orlando Frazao, Orlando Frazão, and O Frazo. Multipath interferometer polished microsphere for enhanced temperature sensing. *IEEE Sensors Letters*, 2(2):1–4, jun 2018.

[26] A. D. Gomes, B. Silveira, J. Dellith, M. Becker, M. Rothhard, H. Bartelt, and O. Frazao. Cleaved Silica Microsphere for Temperature Measurement. *IEEE Photonics Technology Letters*, 30(9):797–800, may 2018.

[27] Andre D. Gomes and Orlando Frazao. Microfiber knot with taper interferometer for temperature and refractive index discrimination. *IEEE Photonics Technology Letters*, 29(18):1517–1520, 2017.

[28] André D. Gomes, Martin Becker, Jan Dellith, Mohammad I. Zibaii, Hamid Latifi, Manfred Rothhardt, Hartmut Bartelt, and Orlando Frazão. Enhanced temperature sensing with Vernier effect on fiber probe based on multimode Fabry-Perot interferometer. In Manuel Filipe P. Martins Costa, editor, *Fourth International Conference on Applications of Optics and Photonics*, page 117. SPIE, oct 2019.

[29] André D. Gomes, Jens Kobelke, Jörg Bierlich, Kay Schuster, Hartmut Bartelt, and Orlando Frazão. Optical fiber probe for viscosity measurements. In *26th International Conference on Optical Fiber Sensors*, volume 100, page TuE8, Washington, D.C., 2018. OSA.

[30] André D Gomes, Beatriz Silveira, Fatemeh Karami, Mohammad I Zibaii, Hamid Latifi, Jan Dellith, Martin Becker, Manfred Rothhardt, Hartmut Bartelt, and Orlando Frazão. Multi-path interferometer structures with cleaved silica microspheres . In Katherine Creath, Jan Burke, Michael B North Morris, and Angela D Davies, editors, *Interferometry XIX*, volume 10749, pages 195–200. International Society for Optics and Photonics, SPIE, aug 2018.

[31] Orlando Frazão and André Delgado Gomes. Simultaneous measurement of temperature and refractive index based on microfiber knot resonator integrated in an abrupt taper Mach-Zehnder interferometer. In Manuel Filipe P. Martins Costa, editor, *Third International Conference on Applications of Optics and Photonics*, volume 10453, page 141. SPIE, aug 2017.

[32] André Gomes and Orlando Frazão. Microfiber knot resonators as sensors - a review. In *Proceedings of the 5th International Conference on Photonics, Optics and Laser Technology*, number Photoptics, pages 356–364. SCITEPRESS - Science and Technology Publications, mar 2017.

[33] A. D. Gomes and O. Frazão. Microfiber knot resonators for sensing applications. In *Springer Series in Optical Sciences*, pages 145–163. 2019.

[34] Takeshi Ozeki and B. S. Kawasaki. Optical directional coupler using tapered sections in multimode fibers. *Applied Physics Letters*, 28(9):528–529, 1976.

[35] B S Kawasaki and K O Hill. Low-loss access coupler for multimode optical fiber distribution networks. *Applied optics*, 16(7):1794–1795, 1977.

[36] B S Kawasaki, K O Hill, and R G Lamont. Biconical-taper single-mode fiber coupler. *Optics letters*, 6(7):327–328, 1981.

[37] Khanh Quoc Kieu and Masud Mansuripur. Biconical fiber taper sensors. *IEEE Photonics Technology Letters*, 18(21):2239–2241, 2006.

[38] Xu Zeng, Yu Wu, Changlun Hou, Jian Bai, and Guoguang Yang. A temperature sensor based on optical microfiber knot resonator. *Optics Communications*, 282(18):3817–3819, 2009.

[39] J Yang, L Jiang, S Wang, B Li, M Wang, H Xiao, Y Lu, and H Tsai. High sensitivity of taper-based Mach-Zehnder interferometer embedded in a thinned optical fiber for refractive index sensing. *Applied optics*, 50(28):5503–5507, 2011.

[40] X Fang, C R Liao, and D N Wang. Femtosecond laser fabricated fiber Bragg grating in microfiber for refractive index sensing. *Optics letters*, 35(7):1007–1009, 2010.

[41] Ping Zhao, Yuhua Li, Jihua Zhang, Lei Shi, and Xinliang Zhang. Nanohole induced microfiber Bragg gratings. *Optics Express*, 20(27):28625–28630, dec 2012.

[42] Jing Feng, Ming Ding, Jun Long Kou, Fei Xu, and Yan Qing Lu. An optical fiber tip micrograting thermometer. *IEEE Photonics Journal*, 3(5):810–814, 2011.

[43] Timothy a. Birks and Youwei W. Li. The shape of fiber tapers. *Journal of Lightwave Technology*, 10(4):432–438, 1992.

[44] Limin Tong, Rafael R. Gattass, Jonathan B. Ashcom, Sailing He, Jingyi Lou, Mengyan Shen, Iva Maxwell, and Eric Mazur. Subwavelength-diameter silica wires for low-loss optical wave guiding. *Nature*, 426(6968):816–819, 2003.

[45] Fei Xu, Valerio Pruneri, Vittoria Finazzi, and Gilberto Brambilla. An embedded optical nanowire loop resonator refractometric sensor. *Optics express*, 16(2):1062–1067, 2008.

[46] Limin Xiao and T a Birks. High finesse microfiber knot resonators made from double-ended tapered fibers. *Optics letters*, 36(7):1098–1100, 2011.

[47] Xiaoqin Wu and Limin Tong. Optical microfibers and nanofibers. *Nanophotonics*, 2(5-6):407–428, 2013.

[48] Limin Tong, Jingyi Lou, and Eric Mazur. Single-mode guiding properties of subwavelength-diameter silica and silicon wire waveguides. *Optics Express*, 12(6):1025, 2004.

[49] Gilberto Brambilla, Fei Xu, Peter Horak, Yongmin Jung, Fumihito Koizumi, Neil P. Sessions, Elena Koukharenko, Xian Feng, Ganapathy S. Murugan, James S. Wilkinson, and David J. Richardson. Optical fiber nanowires and microwires: fabrication and applications. *Advances in Optics and Photonics*, 1(1):107–161, jan 2009.

[50] M. Sumetsky. Basic elements for microfiber photonics: micro/nanofibers and microfiber coil resonators. *Journal of Lightwave Technology*, 26(1):21–27, 2008.

[51] I. H. Malitson. Interspecimen comparison of the refractive index of fused silica. *Journal of the Optical Society of America*, 55(10):1205–1209, oct 1965.

[52] S. W. Harun, K. S. Lim, C. K. Tio, K. Dimyati, and H. Ahmad. Theoretical analysis and fabrication of tapered fiber. *Optik*, 124(6):538–543, 2013.

[53] J. M. Ward, A. Maimaiti, Vu H. Le, and S. Nic Chormaic. Contributed Review: Optical micro- and nanofiber pulling rig. *Review of Scientific Instruments*, 85(11):111501–10, nov 2014.

[54] Zhaobing Tian, S. S H Yam, Jack Barnes, Wojtek Bock, Patricia Greig, James M. Fraser, Hans Peter Loock, and Richard D. Oleschuk. Refractive index sensing with Mach-Zehnder interferometer based on concatenating two single-mode fiber tapers. *IEEE Photonics Technology Letters*, 20(8):626–628, 2008.

[55] Jie Shi, Shilin Xiao, Lilin Yi, and Meihua Bi. A sensitivity-enhanced refractive index sensor using a single-mode thin-core fiber incorporating an abrupt taper. *Sensors*, 12:4697–4705, 2012.

[56] Robert Wiley and Brett Clark. High-power fused assemblies enabled by advances in fiber-processing technologies. In Jay W. Dawson, editor, *Fiber Lasers VIII: Technology, Systems, and Applications*, volume 7914, page 79140F, feb 2011.

[57] Timothy E. Dimmick, George Kakarantzas, Timothy A. Birks, and Philip St. J. Russell. Carbon dioxide laser fabrication of fused-fiber couplers and tapers. *Applied Optics*, 38(33):6845–6848, nov 1999.

[58] Jonathan M. Ward, Danny G. O'Shea, Brian J. Shortt, Michael J. Morrissey, Kieran Deasy, and Síle G. Nic Chormaic. Heat-and-pull rig for fiber taper fabrication. *Review of Scientific Instruments*, 77(8):083105, aug 2006.

[59] G. Brambilla, F. Koizumi, X. Feng, and D.J. Richardson. Compound-glass optical nanowires. *Electronics Letters*, 41(7):400, 2005.

[60] Lu Ding, Cherif Belacel, Sara Ducci, Giuseppe Leo, and Ivan Favero. Ultralow loss single-mode silica tapers manufactured by a microheater. *Applied Optics*, 49(13):2441–2445, 2010.

[61] B. Musa, A. A. Rozi, A. S. M. Noor, A. Ismail, and M. A. Mahdi. Effect of fiber profile parameters on the transmission properties of the tapered optical fibers. In *2011 2nd International Conference on Photonics*, pages 1–4. IEEE, oct 2011.

[62] R. Wonko, P. Marć, and L. R. Jaroszewicz. Fabrication of tapered long period fiber gratings for sensors application by filament heating. In Jan Dorosz and Ryszard S. Romaniuk, editors, *Optical Fibers and Their Applications 2017*, volume 10325, page 1032507, feb 2017.

[63] Gilberto Brambilla, Vittoria Finazzi, and David Richardson. Ultra-low-loss optical fiber nanotapers. *Optics express*, 12(10):2258–2263, 2004.

[64] G Brambilla, F Xu, and X Feng. Fabrication of optical fibre nanowires and their optical and mechanical characterisation. *Electronics Letters*, 42(9):517–519, 2006.

[65] Ryutaro Nagai and Takao Aoki. Ultra-low-loss tapered optical fibers with minimal lengths. *Optics Express*, 22(23):28427–28436, 2014.

[66] Alexander Hartung, Sven Brueckner, and Hartmut Bartelt. Limits of light guidance in optical nanofibers. *Opt. Express*, 18(4):3754–3761, 2010.

[67] A.J.C. J C Grellier, N.K. K Zayer, and C.N. N Pannell. Heat transfer modelling in CO2 laser processing of optical fibres. *Optics Communications*, 152(4-6):324–328, 1998.

[68] M Sumetsky, Y Dulashko, and A Hale. Fabrication and study of bent and coiled free silica nanowires: Self-coupling microloop optical interferometer. *Optics express*, 12(15):3521–31, 2004.

[69] Cheng-Ju Ju Ma, Li-Yong Yong Ren, Yi-Ping Ping Xu, Ying-Li Li Wang, Jian Liang, and En-Shi Shi Qu. Design and fabrication of tapered microfiber waveguide with good optical and mechanical performance. *Journal of Modern Optics*, 61(8):683–687, 2014.

[70] Bishnu P. Pal. *Guided Wave Optical Components and Devices*. 2006.

[71] John F Ready. Fiber Optics. In John F B T Industrial Applications of Lasers (Second Edition) Ready, editor, *Industrial Applications of Lasers*, pages 530–545. Elsevier, San Diego, 1997.

[72] Hongjuan Yang, Shanshan Wang, Xin Wang, Jing Wang, Yipeng Liao, Xin Liao, and Jing Wang. Temperature sensing in seawater based on microfiber knot resonator. *Sensors*, 14(10):18515–18525, oct 2014.

[73] Yu Wu, Yun-Jiang Rao, Yi-huai Chen, and Yuan Gong. Miniature fiber-optic temperature sensors based on silica/polymer microfiber knot resonators. *Optics Express*, 17(20):18142–18147, sep 2009.

[74] Xianli Li and Hui Ding. A stable evanescent field-based microfiber knot resonator refractive index sensor. *IEEE Photonics Technology Letters*, 26(16):1625–1628, 2014.

[75] Kok-Sing Sing Lim, Iman Aryanfar, Wu-Yi Yi Chong, Yew-Ken Ken Cheong, Sulaiman W. Harun, and Harith Ahmad. Integrated microfibre device for refractive index and temperature sensing. *Sensors*, 12(9):11782–11789, aug 2012.

[76] Lecheng Li, Li Xia, Zhenhai Xie, and Deming Liu. All-fiber Mach-Zehnder interferometers for sensing applications. *Optics Express*, 20(10):11109, 2012.

[77] Th Schubert, N Haase, and H Kück. Refractive-index measurements using an integrated Mach-Zehnder interferometer. *Sensors and Actuators A*, 60(100):108–112, 1997.

[78] Shiuh-Chuan Her and Chih-Min Yang. Dynamic strain measured by Mach-Zehnder interferometric optical fiber sensors. *Sensors*, 12(3):3314–3326, mar 2012.

[79] Jianmin Gong, J. M. K. MacAlpine, Wei Jin, and Yanbiao Liao. Locating acoustic emission with an amplitude-multiplexed acoustic sensor array based on a modified Mach-Zehnder interferometer. *Applied Optics*, 40(34):6199, dec 2001.

[80] André D Gomes and Orlando Frazão. Mach-Zehnder based on large knot fiber resonator for refractive index measurement. *IEEE Photonics Technology Letters*, 28(12):1279–1281, jun 2016.

[81] Ping Lu, Liqiu Men, Kevin Sooley, and Qiying Chen. Tapered fiber Mach-Zehnder interferometer for simultaneous measurement of refractive index and temperature. *Applied Physics Letters*, 94(13):3–5, 2009.

[82] Haipeng Luo, Qizhen Sun, Zhilin Xu, Deming Liu, and Lin Zhang. Simultaneous measurement of refractive index and temperature using multimode microfiber-based dual Mach-Zehnder interferometer. *Optics Letters*, 39(13):4049, 2014.

[83] Haipeng Luo, Qizhen Sun, Zhilin Xu, Weihua Jia, Deming Liu, and Lin Zhang. Microfiber-based inline Mach-Zehnder interferometer for dual-parameter measurement. *IEEE Photonics Journal*, 7(2):1–8, apr 2015.

[84] Yipeng Liao, Jing Wang, Shanshan Wang, Hongjuan Yang, and Xin Wang. Simultaneous measurement of seawater temperature and salinity based on microfiber MZ interferometer with a knot resonator. *Journal of Lightwave Technology*, 34(01):5378–5384, 2016.

[85] Yipeng Liao, Jing Wang, Shanshan Wang, Hongjuan Yang, and Xin Wang. Spectral characteristics of the microfiber MZ interferometer with a knot resonator. *Optics Communications*, 389(October 2016):253–257, apr 2017.

[86] A. D. Kersey, D. A. Jackson, and M. Corke. A simple fibre Fabry-Pérot sensor. *Optics and Lasers in Engineering*, 5(3):141–154, 1984.

[87] M Born and E Wolf. *Principles of Optics: Electromagnetic Theory of Propagation, Interference and Diffraction of Light*. Cambridge University Press, 1999.

[88] Yan Zhang, Helen Shibru, Kristie L. Cooper, and Anbo Wang. Miniature fiber-optic multicavity Fabry-Perot interferometric biosensor. *Optics Letters*, 30(9):1021–1023, may 2005.

[89] Yan Zhang, K.L. Cooper, and Anbo Wang. Multicavity Fabry-Pérot interferometric thin-film sensor with built-in temperature compensation. *IEEE Photonics Technology Letters*, 17(12):2712–2714, dec 2005.

[90] Marta S Ferreira, Luís Coelho, Kay Schuster, Jens Kobelke, José L Santos, and Orlando Frazão. Fabry-Perot cavity based on a diaphragm-free hollow-core silica tube. *Optics Letters*, 36(20):4029–4031, 2011.

[91] Ruohui Wang and Xueguang Qiao. Hybrid optical fiber Fabry-Perot interferometer for simultaneous measurement of gas refractive index and temperature. *Applied Optics*, 53(32):7724, 2014.

[92] Shaolin Zhang, Ziwen Zhao, Na Chen, Fufei Pang, Zhenyi Chen, Yunqi Liu, and Tingyun Wang. Temperature characteristics of silicon core optical fiber Fabry-Perot interferometer. *Optics Letters*, 40(7):1362–1365, apr 2015.

[93] Joel Villatoro, Vittoria Finazzi, Gianluca Coviello, and Valerio Pruneri. Photonic-crystal-fiber-enabled micro-Fabry-Perot interferometer. *Optics letters*, 34(16):2441–2443, 2009.

[94] Ming Deng, Chang-Ping Tang, Tao Zhu, Yun-Jiang Rao, Lai-Cai Xu, and Meng Han. Refractive index measurement using photonic crystal fiber-based Fabry-Perot interferometer. *Applied optics*, 49(9):1593–1598, 2010.

[95] Fernando. C. Favero, Geraud Bouwmans, Vittoria Finazzi, Joel Villatoro, and Valerio Pruneri. Fabry-Perot interferometers built by photonic crystal fiber pressurization during fusion splicing. *Optics letters*, 36(21):4191–4193, nov 2011.

[96] F. C. Favero, L. Araujo, G. Bouwmans, V. Finazzi, J. Villatoro, and V. Pruneri. Spheroidal Fabry-Perot microcavities in optical fibers for high-sensitivity sensing. *Optics Express*, 20(7):7112, 2012.

[97] Hao Sun, Xiaolei Zhang, Liutong Yuan, Libin Zhou, Xueguang Qiao, and Manli Hu. An optical fiber Fabry-Perot interferometer sensor for simultaneous measurement of relative humidity and temperature. *IEEE Sensors Journal*, 15(5):2891–2897, 2015.

[98] Jun Ma, Jian Ju, Long Jin, Wei Jin, and Dongning Wang. Fiber-tip micro-cavity for temperature and transverse load sensing. *Optics Express*, 19(13):12418–12426, 2011.

[99] Lu Yan, Zhiguo Gui, Gao Guanjun Gao Guanjun Wang, Yongquan An, Jinyu Gu, Meiqin Zhang, Xinglin Liu, Zhibin Wang, Gao Guanjun Gao Guanjun Wang, and Pinggang Jia. A micro bubble structure based Fabry-Perot optical fiber strain sensor with high sensitivity and low-cost characteristics. *Sensors*, 17(3):555, 2017.

[100] Catarina Monteiro, Susana Silva, and Orlando Frazao. Hollow microsphere Fabry-Perot cavity for sensing applications. *IEEE Photonics Technology Letters*, 29(15):1229–1232, aug 2017.

[101] Yong Zhao, Feng Xia, Mao-qing Chen, Rui-jie Tong, and Yun Peng. Optical fiber axial contact force sensor based on bubble-expanded Fabry-Pérot interferometer. *Sensors and Actuators A: Physical*, 272:318–324, 2018.

[102] Yun-Jiang Rao, Ming Deng, De-Wen Duan, Xiao-Chen Yang, Tao Zhu, and Guang-Hua Cheng. Micro Fabry-Perot interferometers in silica fibers machined by femtosecond laser. *Optics Express*, 15(21):14123–14128, 2007.

[103] Tao Wei, Yukun Han, Hai-Lung Tsai, and Hai Xiao. Miniaturized fiber inline Fabry-Perot interferometer fabricated with a femtosecond laser. *Optics letters*, 33(6):536–538, 2008.

[104] C. R. Liao, T Y Hu, and D. N. Wang. Optical fiber Fabry-Perot interferometer cavity fabricated by femtosecond laser micromachining and fusion splicing for refractive index sensing. *Optics express*, 20(20):22813–22818, sep 2012.

[105] C. A. Volkert and A. M. Minor. Focused ion beam microscopy and micromachining. *MRS Bulletin*, 32(05):389–399, 2007.

[106] AA Ampere A Tseng. Recent developments in micromilling using focused ion beam technology. *Journal of Micromechanics and Microengineering*, 14(4):R15–R34, 2004.

[107] Steve Reyntjens and Robert Puers. A review of focused ion beam applications in microsystem technology. *Journal of Micromechanics and Microengineering*, 11(4):287–300, 2001.

[108] Nan Yao. Introduction to the focused ion beam system. *Focused Ion Beam Systems: Basics and Applications*, pages 1–10, 2007.

[109] S.A. Boden, Z. Moktadir, D.M. Bagnall, H. Mizuta, and H.N. Rutt. Focused helium ion beam milling and deposition. *Microelectronic Engineering*, 88(8):2452–2455, aug 2011.

[110] Cicero Martelli, Paolo Olivero, John Canning, Nathaniel Groothoff, Brant Gibson, and Shane Huntington. Micromachining structured optical fibers using focused ion beam milling. *Optics letters*, 32(11):1575–1577, 2007.

[111] Peter Sigmund. Theory of Sputtering. I. Sputtering Yield of Amorphous and Polycrystalline Targets. *Physical Review*, 184(2):383–416, aug 1969.

[112] Th Lacoste, Th Huser, R. Prioli, and H. Heinzelmann. Contrast enhancement using polarization-modulation scanning near-field optical microscopy (PM-SNOM). *Ultramicroscopy*, 71(1-4):333–340, mar 1998.

[113] Saeed Pilevar, Klaus Edinger, Walid Atia, Igor Smolyaninov, and Christopher Davis. Focused ion-beam fabrication of fiber probes with well-defined apertures for use in near-field scanning optical microscopy. *Applied Physics Letters*, 72(24):3133–3135, jun 1998.

[114] A. Micco, A. Ricciardi, M. Pisco, V. La Ferrara, and A. Cusano. Optical fiber tip templating using direct focused ion beam milling. *Scientific Reports*, 5:15935, 2015.

[115] S. Cabrini, C. Liberale, D. Cojoc, A. Carpentiero, M. Prasciolu, S. Mora, V. Degiorgio, F. De Angelis, and E. Di Fabrizio. Axicon lens on optical fiber forming optical tweezers, made by focused ion beam milling. *Microelectronic Engineering*, 83(4-9 SPEC. ISS.):804–807, 2006.

[116] Rita S. Rodrigues Ribeiro, Pabitra Dahal, Ariel Guerreiro, Pedro A. S. Jorge, and Jaime Viegas. Fabrication of Fresnel plates on optical fibres by FIB milling for optical trapping, manipulation and detection of single cells. *Scientific Reports*, 7(1):4485, dec 2017.

[117] M L von Bibra, A Roberts, and J Canning. Fabrication of long-period fiber gratings by use of focused ion-beam irradiation. *Optics letters*, 26(11):765–7, 2001.

[118] Jun-long Kou, Sun-jie Qiu, Fei Xu, and Yan-qing Lu. Demonstration of a compact temperature sensor based on first-order Bragg grating in a tapered fiber probe. *Optics express*, 19(19):18452–18457, 2011.

[119] Yanxin Liu, Chao Meng, a Ping Zhang, Yao Xiao, Huakang Yu, and Limin Tong. Compact microfiber Bragg gratings with high-index contrast. *Optics letters*, 36(16):3115–3117, 2011.

[120] K. P. Nayak, Fam Le Kien, Y. Kawai, K. Hakuta, K. Nakajima, H. T. Miyazaki, and Y. Sugimoto. Cavity formation on an optical nanofiber using focused ion beam milling technique. *Opt. Express Opt. Express*, 19(15):14040–14050, 2011.

[121] Jun-long Kou, Jing Feng, Qian-jin Wang, Fei Xu, and Yan-qing Lu. Microfiber-probe-based ultrasmall interferometric sensor. *Optics letters*, 35(13):2308–10, 2010.

[122] T. Wieduwilt, J. Dellith, F. Talkenberg, H. Bartelt, and M. a. Schmidt. Reflectivity enhanced refractive index sensor based on a fiber-integrated Fabry-Perot microresonator. *Optics Express*, 22(21):25333–25346, 2014.

[123] Ricardo M André, Simon Pevec, Martin Becker, Jan Dellith, Manfred Rothhardt, Manuel B Marques, Denis Donlagic, Hartmut Bartelt, and Orlando Frazão. Focused ion beam post-processing of optical fiber Fabry-Perot cavities for sensing applications. *Optics express*, 22(11):13102–13108, jun 2014.

[124] André D. Gomes, Ricardo M. André, Stephen C. Warren-Smith, Jan Dellith, Martin Becker, Manfred Rothhardt, and Orlando Frazão. Combined microfiber knot resonator and focused ion beam-milled Mach-Zehnder interferometer for refractive index measurement. In Youngjoo Chung, Wei Jin, Byoungho Lee, John Canning, Kentaro Nakamura, and Libo Yuan, editors, *Proceedings of SPIE - The International Society for Optical Engineering*, volume 10323, page 1032340, apr 2017.

[125] Stephen C. Warren-Smith, Ricardo M. André, Christopher Perrella, Jan Dellith, Manfred Rothhardt, and Hartmut Bartelt. Direct core structuring of microstructured optical fibers using focused ion beam milling. *Optics Express*, 24(1):378–387, 2016.

[126] A.D. D. Gomes, M.F.S. F. S. Ferreira, J.P. P. Moura, R.M. M. André, J. Kobelke, J. Bierlich, K. Wondraczek, K. Schuster, and O. Frazão. Acetone evaporation and water vapor detection using a caterpillar-like microstructured fiber. *Microwave and Optical Technology Letters*, 58(3):679–683, 2016.

[127] A. Ping Zhang, Li Yang Shao, Jin Fei Ding, and Sailing He. Sandwiched long-period gratings for simultaneous measurement of refractive index and temperature. *IEEE Photonics Technology Letters*, 17(11):2397–2399, 2005.

[128] Orlando Frazão, Diogo Egypto, Lucas Aragao-Bittencourt, Maria T M R Giraldi, and Manuel B Marques. Strain and Temperature Discrimination Using High-Birefringence Erbium-Doped Fiber Loop Mirror With High Pump Power Laser. *IEEE Photonics Technology Letters*, 20(12):1033–1035, jun 2008.

[129] Orlando Frazão, S. H. Aref, José M. Baptista, José L. Santos, H. Latifi, F. Farahi, Jens Kobelke, and Kay Schuster. Fabry-pérot cavity based on a suspended-core fiber for strain and temperature measurement. *IEEE Photonics Technology Letters*, 21(17):1229–1231, 2009.

[130] Yang Ran, Long Jin, Li-peng Sun, Jie Li, and Bai-ou Guan. Temperature-Compensated Refractive-Index Sensing Using a Single Bragg Grating in an Abrupt Fiber Taper. *IEEE Photonics Journal*, 5(2):7100208–7100208, 2013.

[131] André D. Gomes, Beatriz Silveira, Stephen C. Warren-Smith, Martin Becker, Manfred Rothhardt, and Orlando Frazão. Temperature independent refractive index measurement using a fiber Bragg grating on abrupt tapered tip. *Optics and Laser Technology*, 101:227–231, 2018.

[132] Qiqi Yao, Hongyun Meng, Wei Wang, Hongchao Xue, Rui Xiong, Ben Huang, Chunhua Tan, and Xuguang Huang. Simultaneous measurement of refractive index and temperature based on a core-offset Mach-Zehnder interferometer combined with a fiber Bragg grating. *Sensors and Actuators, A: Physical*, 209:73–77, 2014.

[133] Jinjie Chen, Bo Liu, and Hao Zhang. Review of fiber Bragg grating sensor technology. *Frontiers of Optoelectronics in China*, 4(2):204–212, 2011.

[134] A. Ping Zhang, Shaorui Gao, Guofeng Yan, and Yinbing Bai. Advances in optical fiber Bragg grating sensor technologies. *Photonic Sensors*, 2(1):1–13, mar 2012.

[135] F Farahi, D J Webb, J D C Jones, David A Jackson, F Farahi, D J Webb, J D C Jones, and David A Jackson. Simultaneous measurement of temperature and strain: cross-sensitivity considerations. *Journal of Lightwave Technology*, 8(2):138–142, 1990.

[136] A.W. Snyder. Coupling of modes on a tapered dielectric cylinder. *IEEE Transactions on Microwave Theory and Techniques*, 18(7):383–392, jul 1970.

[137] Daniel T. Cassidy, Derwyn C. Johnson, and Kenneth O. Hill. Wavelength-dependent transmission of monomode optical fiber tapers. *Applied Optics*, 25(3):328, feb 1986.

[138] Anh Duy Duong Le and Young-Geun Geun Han. Relative Humidity Sensor Based on a Few-Mode Microfiber Knot Resonator by Mitigating the Group Index Difference of a Few-Mode Microfiber. *Journal of Lightwave Technology*, 36(4):904–909, feb 2018.

[139] Susana Novais, Marta S. Ferreira, and João L. Pinto. Determination of thermo-optic coefficient of ethanol-water mixtures with optical fiber tip sensor. *Optical Fiber Technology*, 45(August):276–279, 2018.

[140] S Kedenburg, M Vieweg, T Gissibl, and H Giessen. Linear refractive index and absorption measurements of nonlinear optical liquids in the visible and near-infrared spectral region. *Opt. Mater. Express*, 2(11):1588–1611, nov 2012.

[141] Md. Islam, Muhammad Ali, Man-Hong Lai, Kok-Sing Lim, and Harith Ahmad. Chronology of Fabry-Perot Interferometer Fiber-Optic Sensors and Their Applications: A Review. *Sensors*, 14(4):7451–7488, apr 2014.

[142] Jun-long Kou, Jing Feng, Liang Ye, Fei Xu, and Yan-qing Lu. Miniaturized fiber taper reflective interferometer for high temperature measurement. *Optics express*, 18(13):14245–14250, jun 2010.

[143] Qiangzhou Rong, Hao Sun, Xueguang Qiao, Jing Zhang, Manli Hu, and Zhongyao Feng. A miniature fiber-optic temperature sensor based on a Fabry-Perot interferometer. *Journal of Optics*, 14(4):045002, apr 2012.

[144] Meng Ge, Yan Li, Yanhua Han, Zehua Xia, Zhongyi Guo, Jianmin Gao, and Shiliang Qu. High-sensitivity double-parameter sensor based on the fibre-tip Fabry-Pérot interferometer. *Journal of Modern Optics*, 64(6):596–600, mar 2017.

[145] W. P. Chen, D. N. Wang, Ben Xu, C. L. Zhao, and H. F. Chen. Multimode fiber tip Fabry-Perot cavity for highly sensitive pressure measurement. *Scientific Reports*, 7(1):368, dec 2017.

[146] Philip E. Ciddor. Refractive index of air: new equations for the visible and near infrared. *Applied Optics*, 35(9):1566, 1996.

[147] Guigen Liu, Ming Han, and Weilin Hou. High-resolution and fast-response fiber-optic temperature sensor using silicon Fabry-Pérot cavity. *Optics express*, 23(6):7237–7247, mar 2015.

[148] Peng Zhang, Ming Tang, Feng Gao, Benpeng Zhu, Zhiyong Zhao, Li Duan, Songnian Fu, Jun Ouyang, Huifeng Wei, Perry Ping Shum, and Deming Liu. Simplified hollow-core fiber-based Fabry-Perot interferometer with modified Vernier effect for highly sensitive high-temperature measurement. *IEEE Photonics Journal*, 7(1):1–10, 2015.

[149] Yina Li, Chunliu Zhao, Ben Xu, Dongning Wang, and Minghong Yang. Optical cascaded Fabry-Perot interferometer hydrogen sensor based on Vernier effect. *Optics Communications*, 414(2017):166–171, 2018.

[150] Jin Jiangshan Jin Zhang, Hao Liao, Ping Lu, Xinyue Jiang, Xin Fu, Wenjun Ni, Deming Liu, Jin Jiangshan Jin Zhang, Hao Liao, Ping Lu, Xinyue Jiang, Xin Fu, Wenjun Ni, Deming Liu, and Jin Jiangshan Jin Zhang. Ultrasensitive temperature sensor with cascaded fiber optic Fabry-Perot interferometers based on Vernier effect. *IEEE Photonics Journal*, 10(5):1–11, oct 2018.

[151] J Barrow. *Navigatio britannica: or, A complete system of navigation in all its branches, both with regard to theory and practice ...* W. and J. Mount and T. Page, 1750.

[152] Maurice Daumas. *Scientific instruments of the seventeenth and eighteenth centuries and their makers*. Portman Books, London, 1989.

[153] Paul Urquhart. Compound optical-fiber-based resonators. *Journal of the Optical Society of America A*, 5(6):803, 1988.

[154] John L. Hall. Defining and measuring optical frequencies: The optical clock opportunity - and more (Nobel lecture), 2006.

[155] Theodor W. Hänsch. Nobel lecture: Passion for precision. *Reviews of Modern Physics*, 2006.

[156] Nathalie Picqué and Theodor W. Hänsch. Frequency comb spectroscopy. *Nature Photonics*, 13(3):146–157, 2019.

[157] Rongrong Xu, Shuang Liu, Qizhen Sun, Ping Lu, and Deming Liu. Experimental Characterization of a Vernier Strain Sensor Using Cascaded Fiber Rings. *IEEE Photonics Technology Letters*, 24(23):2125–2128, dec 2012.

[158] Peng Zhang, Ming Tang, Feng Gao, Benpeng Zhu, Songnian Fu, Jun Ouyang, Perry Ping Shum, and Deming Liu. Cascaded fiber-optic Fabry-Perot interferometers with Vernier effect for highly sensitive measurement of axial strain and magnetic field. *Optics Express*, 22(16):19581–19588, aug 2014.

[159] Dora Juan Juan Hu, Yixin Wang, Jun Long Lim, Taishi Zhang, Karolina Barbara Milenko, Zhihao Chen, Meng Jiang, Guanghui Wang, Feng Luan, Ping P. Shum, Qizhen Sun, Huifeng Wei, Weijun Tong, and Tomasz R. Wolinski. Novel miniaturized Fabry-Perot refractometer based on a simplified hollow-core fiber with a hollow silica sphere tip. *IEEE Sensors Journal*, 12(5):1239–1245, may 2012.

[160] Tianjun Yao, Shengli Pu, Yongliang Zhao, and Yuqi Li. Ultrasensitive refractive index sensor based on parallel-connected dual Fabry-Perot interferometers with Vernier effect. *Sensors and Actuators A: Physical*, 290:14–19, 2019.

[161] Tong Nan, Bo Liu, Yongfeng Wu, Junfeng Wang, Yaya Mao, Lilong Zhao, Tingting Sun, and Jin Wang. Ultrasensitive strain sensor based on Vernier-effect improved parallel structured fiber-optic Fabry-Perot interferometer. *Optics Express*, 27(12):17239, jun 2019.

[162] Zhe Li, Yan-Xin Zhang, Wei-Gang Zhang, Ling-Xin Kong, Tie-Yi Yan, Peng-Cheng Geng, and Biao Wang. High-sensitivity gas pressure Fabry-Perot fiber probe with micro-channel based on Vernier effect. *Journal of Lightwave Technology*, 37(14):3444–3451, 2019.

[163] Jiajun Tian, Zhigang Li, Yunxu Sun, and Yong Yao. High-sensitivity fiber-optic strain sensor based on the Vernier effect and separated Fabry-Perot interferometers. *Journal of Lightwave Technology*, page 1, 2019.

[164] Jun Deng and D N Wang. Ultra-sensitive strain sensor based on femtosecond laser inscribed in-fiber reflection mirrors and Vernier effect. *Journal of Lightwave Technology*, 37(19):4935–4939, oct 2019.

[165] Tiago Paixão, Francisco Araújo, and Paulo Antunes. Highly sensitive fiber optic temperature and strain sensor based on an intrinsic Fabry-Perot interferometer fabricated by a femtosecond laser. *Optics Letters*, 44(19):4833, oct 2019.

[166] Mingran Quan, Jiajun Tian, and Yong Yao. Ultra-high sensitivity Fabry-Perot interferometer gas refractive index fiber sensor based on photonic crystal fiber and Vernier effect. *Optics Letters*, 40(21):4891–4894, nov 2015.

[167] Yong Zhao, Peng Wang, Riqing Lv, and Xu Liu. Highly sensitive airflow sensor based on Fabry-Perot interferometer and Vernier effect. *Journal of Lightwave Technology*, 34(23):5351–5356, 2016.

[168] Lingxin Kong, Yanxin Zhang, Weigang Zhang, Yunshan Zhang, Lin Yu, Tieyi Yan, and Pengcheng Geng. Cylinder-type fiber-optic Vernier probe based on cascaded Fabry-Perot interferometers with a controlled FSR ratio. *Applied Optics*, 57(18):5043–5047, 2018.

[169] Peng Chen, Yutang Dai, Dongsheng Zhang, Xiaoyan Wen, and Minghong Yang. Cascaded-cavity Fabry-Perot interferometric gas pressure sensor based on Vernier effect. *Sensors*, 18(11):3677, oct 2018.

[170] Feiru Wang, Yongjun Liu, Yuelan Lu, Lingli Zhang, Ji Ma, Lei Wang, and Weimin Sun. High-sensitivity Fabry-Perot interferometer temperature sensor probe based on liquid crystal and the Vernier effect. *Optics Letters*, 43(21):5355, nov 2018.

[171] Yuqiang Yang, Yongguang Wang, Jiuxing Jiang, Yuxin Zhao, Xunjun He, and Linjun Li. High-sensitive all-fiber Fabry-Perot interferometer gas refractive index sensor based on lateral offset splicing and Vernier effect. *Optik*, 196(June):163181, nov 2019.

[172] Wei Zhang, Yinggang Liu, Ting Zhang, Danqing Yang, Yuxi Wang, and Dakuan Yu. Integrated fiber-optic Fabry-Pérot interferometer sensor for simultaneous measurement of liquid refractive index and temperature. *IEEE Sensors Journal*, 19(13):5007–5013, jul 2019.

[173] Chunliu Zhao, Fei Han, Yina Li, Bangning Mao, Juan Kang, Changyu Shen, and Xinyong Dong. Volatile organic compound sensor based on PDMS coated Fabry-Perot interferometer with Vernier effect. *IEEE Sensors Journal*, 19(12):4443–4450, 2019.

[174] Gang Zhang, Xuqiang Wu, Wujun Zhang, Shili Li, Jinhui Shi, Cheng Zuo, Shasha Fang, and Benli Yu. High temperature Vernier probe utilizing photonic crystal fiber-based Fabry-Perot interferometers. *Optics Express*, 27(26):37308, dec 2019.

[175] Yong Zhao, Rui-jie Tong, Mao-qing Chen, and Yun Peng. Relative humidity sensor based on Vernier effect with GQDs-PVA un-fully filled in hollow core fiber. *Sensors and Actuators A: Physical*, 285:329–337, 2019.

[176] Changpeng Lang, Yi Liu, Yingying Liao, Jinjian Li, and Shiliang Qu. Ultra-sensitive fiber-optic temperature sensor consisting of cascaded liquid-air cavities based on Vernier effect. *IEEE Sensors Journal*, pages 1–1, 2020.

[177] Huaiyin Su, Yundong Zhang, Yongpeng Zhao, Kai Ma, Kaiyue Qi, Ying Guo, and Fuxing Zhu. Parallel double-FPIs temperature sensor based on suspended-core microstructured optical fiber. *IEEE Photonics Technology Letters*, 31(24):1905–1908, dec 2019.

[178] Raquel Flores, Ricardo Janeiro, and Jaime Viegas. Optical fibre Fabry-Pérot interferometer based on inline microcavities for salinity and temperature sensing. *Scientific Reports*, 9(1):9556, 2019.

[179] Leyi Hou, Chunliu Zhao, Ben Xu, Bangning Mao, Changyu Shen, and D N Wang. Highly sensitive PDMS-filled Fabry-Perot interferometer temperature sensor based on the Vernier effect. *Applied Optics*, 58(18):4858–4865, 2019.

[180] Yongfeng Wu, Bo Liu, Jing Wu, Lilong Zhao, Tingting Sun, Yaya Mao, Tong Nan, and Jin Wang. A transverse load sensor with ultra-sensitivity employing Vernier-effect improved parallel-structured fiber-optic Fabry-Perot interferometer. *IEEE Access*, 7:120297–120303, 2019.

[181] Tong Nan, Bo Liu, Yongfeng Wu, Junfeng Wang, Yaya Mao, Lilong Zhao, Tingting Sun, Jin Wang, and Delin Zhao. High-temperature fiber sensor based on two paralleled fiber-optic Fabry-Perot interferometers with ultrahigh sensitivity. *Optical Engineering*, 59(02):1, feb 2020.

[182] Hao Liao, Ping Lu, Xin Fu, Xinyue Jiang, Wenjun Ni, Deming Liu, and Jiangshan Zhang. Sensitivity amplification of fiber-optic in-line Mach-Zehnder interferometer sensors with modified Vernier-effect. *Optics Express*, 25(22):26898–26909, oct 2017.

[183] Mingyang Xie, Huaping Gong, Jun Zhang, Chun-Liu Zhao, and Xinyong Dong. Vernier effect of two cascaded in-fiber Mach-Zehnder interferometers based on a spherical-shaped structure. *Appl. Opt.*, 58(23):6204–6210, 2019.

[184] Chenxu Lu, Xiaopeng Dong, Lihua Lu, Yunqing Guan, and Shiqi Ding. Label free all-fiber static pressure sensor based on Vernier effect with temperature compensation. *IEEE Sensors Journal*, 20(9):4726–4731, may 2020.

[185] Hongfeng Lin, Fufei Liu, Yutang Dai, and Ai Zhou. Cascaded fiber Mach-Zehnder interferometers for sensitivity-enhanced gas pressure measurement. *IEEE Sensors Journal*, 19(7):2581–2586, apr 2019.

[186] Yujia Zhao, Hongfeng Lin, Ciming Zhou, Hongchang Deng, Ai Zhou, and Libo Yuan. Cascaded Mach-Zehnder interferometers with Vernier effect for gas pressure sensing. *IEEE Photonics Technology Letters*, 31(8):591–594, apr 2019.

[187] Hongfeng Lin, Fufei Liu, Huiyong Guo, Ai Zhou, and Yutang Dai. Ultra-highly sensitive gas pressure sensor based on dual side-hole fiber interferometers with Vernier effect. *Optics Express*, 26(22):28763–28772, 2018.

[188] Wenjun Ni, Ping Lu, Xin Fu, Handong Sun, Perry Ping Shum, Hao Liao, Xinyue Jiang, Deming Liu, Chunyong Yang, Jiangshan Zhang, and Zhengang Lian. Simultaneous implementation of enhanced resolution and large dynamic range for fiber temperature sensing based on different optical transmission mechanisms. *Optics Express*, 26(14):18341, 2018.

[189] Jie Hu, Mateusz Smietana, Taihong Wang, Tingting Lang, Liyang Shao, Guoqiang Gu, Xuming Zhang, Yanjun Liu, Xuefeng Song, Zhangqi Song, Jiansong Feng, and Ryszard Buczynski. Dual Mach-Zehnder interferometer based on side-hole fiber for high-sensitivity refractive index sensing. *IEEE Photonics Journal*, 11(6):1–13, dec 2019.

[190] Zhenru Wang, Lin Huang, Chi Liu, Haiyong Wang, Shanshan Sun, and Dexing Yang. Sensitivity-enhanced fiber temperature sensor based on Vernier effect and dual in-line Mach-Zehnder interferometers. *IEEE Sensors Journal*, 19(18):7983–7987, sep 2019.

[191] Li-Yang Shao, Yuan Luo, Zhiyong Zhang, Xihua Zou, Bin Luo, Wei Pan, and Lianshan Yan. Sensitivity-enhanced temperature sensor with cascaded fiber optic Sagnac interferometers based on Vernier-effect. *Optics Communications*, 336:73–76, feb 2015.

[192] Xue-Zhou Wang and Qi Wang. A high-birefringence microfiber sagnac-interferometer biosensor based on the Vernier effect. *Sensors*, 18(12):4114, nov 2018.

[193] Zuowei Xu, Xuewen Shu, and Hongyan Fu. Sensitivity enhanced fiber sensor based on a fiber ring microwave photonic filter with the Vernier effect. *Optics Express*, 25(18):21559, 2017.

[194] Yixin Zhang, Ben Xu, D. N. Wang, Huaping Gong, Yi Li, and Chun Liu Zhao. Sensitivity-enhanced fiber strain sensing system based on microwave frequency scanning with the Vernier effect. *Optical Fiber Technology*, 43(April):175–179, 2018.

[195] Binqing Wu, Chunliu Zhao, Ben Xu, and Yina Li. Optical fiber hydrogen sensor with single Sagnac interferometer loop based on vernier effect. *Sensors and Actuators B: Chemical*, 255:3011–3016, feb 2018.

[196] Shun Liu, Ping Lu, Enci Chen, Wenjun Ni, Deming Liu, Jiangshan Zhang, and Zhenggang Lian. Vernier effect of fiber interferometer based on cascaded PANDA polarization maintaining fiber. *Chinese Optics Letters*, 17(8):080601, 2019.

[197] Binqing Wu, Lihan Chen, Chunliu Zhao, and Chi Chiu Chan. Polypyrrole-coated polarization maintaining fiber-based Vernier effect for isopropanol measurement. *Journal of Lightwave Technology*, 37(11):2768–2772, jun 2019.

[198] Shaoxian Zhang, Liu Yin, Yujia Zhao, Ai Zhou, and Libo Yuan. Bending sensor with parallel fiber Michelson interferometers based on Vernier-like effect. *Optics & Laser Technology*, 120(May):105679, dec 2019.

[199] Kaiwei Li, Nan Zhang, Nancy Meng Ying Zhang, Wenchao Zhou, Ting Zhang, Ming Chen, and Lei Wei. Birefringence induced Vernier effect in optical fiber modal interferometers for enhanced sensing. *Sensors and Actuators, B: Chemical*, 275(August):16–24, 2018.

[200] Guan-Tao Chen, Yan-Xin Zhang, Wei-Gang Zhang, Ling-Xin Kong, Xinlei Zhao, Yunshan Zhang, Zhe Li, and Tie-Yi Yan. Double helix microfiber coupler enhances refractive index sensing based on Vernier effect. *Optical Fiber Technology*, 54:102112, jan 2020.

[201] Yunbin Ying, Chunliu Zhao, Huaping Gong, Shiyan Shang, and Leyi Hou. Demodulation method of Fabry-Perot sensor by cascading a traditional Mach-Zehnder interferometer. *Optics & Laser Technology*, 118:126–131, oct 2019.

[202] Jiewen Li, Meng Zhang, Minggui Wan, Chunli Lin, Shihong Huang, Cuihong Liu, Qingping He, Xiaozhong Qiu, and Xiaohui Fang. Ultrasensitive refractive index sensor based on enhanced Vernier effect through cascaded fiber core-offset pairs. *Optics Express*, 28(3):4145, feb 2020.

[203] Xuefang Zhou, Yu Zhou, Zengyang Li, Meihua Bi, and Guowei Yang. Research on temperature sensing characteristics with cascaded fiber Sagnac interferometer and fiber Fabry-Perot interferometer-based fiber laser. *Optical Engineering*, 58(05):1, may 2019.

[204] Yuqiang Yang, Yongguang Wang, Yuxin Zhao, Jiuxing Jiang, Xunjun He, Wenlong Yang, Zhihan Zhu, Wei Gao, and Linjun Li. Sensitivity-enhanced temperature sensor by hybrid cascaded configuration of a Sagnac loop and a F-P cavity. *Optics Express*, 25(26):33290–33296, dec 2017.

[205] Shuai Wang, Shun Wang, Rui-bo Jin, Mingzhe Feng, Shun Wu, Liang Zhang, and Peixiang Lu. All-optical demodulation fiber acoustic sensor with real-time controllable sensitivity based on optical Vernier effect. *IEEE Photonics Journal*, 11(4):1–11, aug 2019.

[206] Pengfei Wang, Yuxuan Jiang, yating Yi, and Gilberto Brambilla. Ultra-high-sensitivity refractive index sensor based on dual-microfiber coupler structure with Vernier effect. *Optics Letters*, 45(5):1268–1271, 2020.

[207] Susana Novais, Marta S. Ferreira, and João L. Pinto. Fabry-Perot cavity based on air bubble for high sensitivity lateral load and strain measurements. In Manuel Filipe P. Martins Costa, editor, *Third International Conference on Applications of Optics and Photonics*, number August 2017, page 204. SPIE, aug 2017.

[208] Susana Novais, Marta S Ferreira, and Joao L Pinto. Lateral load sensing with an optical fiber inline microcavity. *IEEE Photonics Technology Letters*, 29(17):1502–1505, 2017.

[209] Orlando Frazão, Susana F O Silva, Ariel Guerreiro, José L Santos, Luis A Ferreira, and Francisco M Araújo. Strain sensitivity control of fiber Bragg grating structures with fused tapers. *Applied Optics*, 46(36):8578–8582, 2007.

[210] Feng Xia, Yong Zhao, and Yun Peng. In-line microfiber MZI operating at two sides of the dispersion turning point for ultrasensitive RI and temperature measurement. *Sensors and Actuators A: Physical*, 301:111754, jan 2020.

[211] Tao Wei, Yukun Han, Yanjun Li, Hai-Lung Tsai, and Hai Xiao. Temperature-insensitive miniaturized fiber inline Fabry-Perot interferometer for highly sensitive refractive index measurement. *Optics express*, 16(8):5764–5769, 2008.

[212] Yi Liu, Min Li, Huihui Sun, Yan Li, and Shiliang Qu. Ultrasensitive liquid refractometer based on a Mach-Zehnder micro-cavity in optical fibre fabricated by femtosecond laser-induced water breakdown. *Journal of Modern Optics*, 63(21):2285–2290, nov 2016.

[213] Xinyu Wang, Shuguang Li, Junjun Wu, Shuhuan Zhang, Ying Guo, and Yundong Liu. Ultrahigh-sensitivity refractive-index sensor based on gold-coated side-polished photonic crystal fiber. *Applied Physics Express*, 11(10):102202, oct 2018.

[214] Catarina S. Monteiro, Marta S. Ferreira, Susana O. Silva, Jens Kobelke, Kay Schuster, Jörg Bierlich, and Orlando Frazão. Fiber Fabry-Perot interferometer for curvature sensing. *Photonic Sensors*, 6(4):339–344, 2016.

[215] Marta S. Ferreira, Paulo Roriz, Jörg Bierlich, Jens Kobelke, Katrin Wondraczek, Claudia Aichele, Kay Schuster, José L. Santos, and Orlando Frazão. Fabry-Perot cavity based on silica tube for strain sensing at high temperatures. *Optics Express*, 23(12):16063–16070, jun 2015.

[216] Yoko Eguchi and Takeshi Karino. Measurement of rheologic property of blood by a falling-ball blood viscometer. *Annals of Biomedical Engineering*, 36(4):545–553, 2008.

[217] Jinyu Ma, Xinjing Huang, Hyungdae Bae, Yelong Zheng, Cong Liu, Meirong Zhao, and Miao Yu. Liquid Viscosity Measurement Using a Vibrating Flexure Hinged Structure and a Fiber-Optic Sensor. *IEEE Sensors Journal*, 16(13):5249–5258, 2016.

[218] H. Muramatsu, M. Suda, T. Ataka, A. Seki, E. Tamiya, and I. Karube. Piezoelectric resonator as a chemical and biochemical sensing device. *Sensors and Actuators: A. Physical*, 21(1-3):362–368, 1990.

[219] Frieder Lucklum, Erwin K. Reichel, and Bernhard Jakoby. Miniature density-viscosity measurement cell utilizing electrodynamic- acoustic resonator sensors. *Sensors and Actuators, A: Physical*, 172(1):75–81, 2011.

[220] Alexander I. Fedorchenko, Zdenek Travnicek, Cheng Ling Chang, and Wei Chih Wang. Viscosity measurement using fiber bend loss sensor. *2012 International Symposium on Optomechatronic Technologies, ISOT 2012*, pages 0–4, 2012.

[221] Mark a Haidekker, Walter J Akers, Derek Fischer, and Emmanuel a Theodorakis. Optical fiber-based fluorescent viscosity sensor. *Optics letters*, 31(17):2529–2531, 2006.

[222] R. A. Oliveira, J. Canning, K. Cook, M. Nashqbandi, and A. A.P. Pohl. Compact dip-style viscometer based on the acousto-optic effect in a long period fiber grating. *Sensors and Actuators, B: Chemical*, 157(2):621–626, 2011.

[223] Jian Neng Wang and Jaw Luen Tang. An optical fiber viscometer based on long-period fiber grating technology and capillary tube mechanism. *Sensors*, 10(12):11174–11188, 2010.

[224] Min-Hwan Lee, Sung-Hyun Kim, Eun-Sun Kim, and In-Kag Hwang. Interference-based optical measurement of fluidic flow in a hollow-core fiber. *Photonic Sensors*, 8(1):7–12, mar 2018.

[225] Xinlei Zhou, Qingxu Yu, and Wei Peng. Fiber-optic Fabry-Perot pressure sensor for down-hole application. *Optics and Lasers in Engineering*, 121(May):289–299, 2019.

[226] Ying Wu, Li Xia, Wei Li, and Jianchun Xia. Highly sensitive Fabry-Perot demodulation based on coarse wavelength sampling and Vernier effect. *IEEE Photonics Technology Letters*, 31(6):487–490, 2019.

[227] Tom Claes, Wim Bogaerts, and Peter Bienstman. Experimental characterization of a silicon photonic biosensor consisting of two cascaded ring resonators based on the Vernier-effect and introduction of a curve fitting method for an improved detection limit. *Optics Express*, 18(22):22747, 2010.

Appendix A.

Water Refractive Index

The refractive index of water as a function of temperature, at a wavelength of 632.8 nm, found in [12] is presented in table A.1. The values are represented in figure A.1. A polynomial fit was performed to the values, obtaining an expression for the refractive index of water as a function of temperature:

$$\begin{aligned} n(T) = {} & 1.3331036 - 1.4868298 \times 10^{-5} T \\ & - 1.9328089 \times 10^{-6} T^2 + 5.1806927 \times 10^{-9} T^3, \end{aligned} \tag{A.1}$$

where n is given in refractive index units (RIU) and T is given in degrees Celsius.

Table A.1. – Refractive index of water as a function of temperature, at a wavelength of 632.8 nm [12].

Temperature (°C)	**Refractive Index** (RIU)
0	1.33306
10	1.33282
20	1.33211
30	1.33105
40	1.32972
50	1.32814
60	1.32636
70	1.32438
80	1.32223
90	1.31991
100	1.31744

Equation A.1 was used in chapter 3, section 3.2, to calculate the refractive index of water at 44 °C, obtaining 1.32915.

A different approach was considered in order to obtain the refractive index as a function of temperature at a wavelength of 1550 nm. Initially, the Sellmeier equation for water at 20 °C was used to calculate the refractive index of water at 1550 nm. The Sellmeier

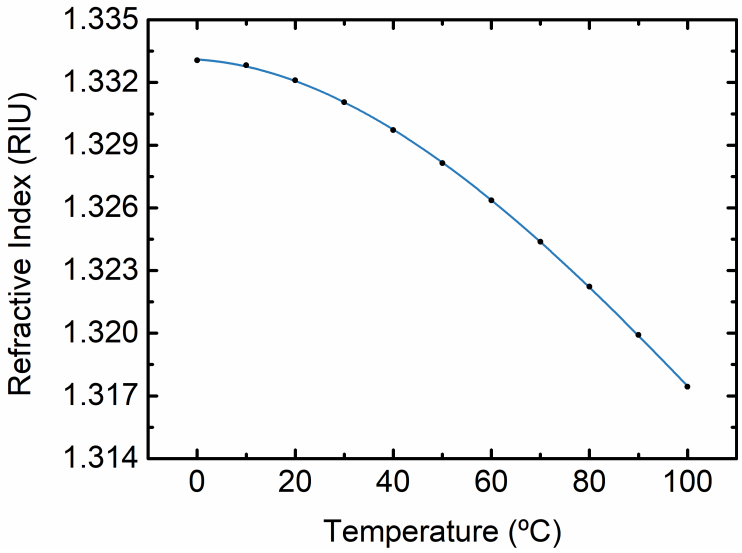

Figure A.1. – Refractive index of water as a function of temperature, at a wavelength of 632.8 nm. The data points correspond to the values of table A.1.

equation for water at 20 °C can be found in [140], and is given by:

$$n^2(\lambda) = 1 + \frac{0.75831\lambda^2}{\lambda^2 - 0.01007} + \frac{0.08495\lambda^2}{\lambda^2 - 8.91377}, \tag{A.2}$$

where n is the refractive index and λ is the wavelength given in micrometers (μm). Using equation A.2, the refractive index of water at 20 °C, at a wavelength of 1550 nm is 1.3154.

To obtain the value of refractive index at a wavelength of 1550 nm, but at a temperature of 44 °C, the thermo-optic coefficient of water was now considered. As mentioned later in section 3.2, the thermo-optic coefficient of water, $\frac{dn}{dT}$, at a wavelength of 1550 nm, is given by equation 3.3 [139]. For the sake of clarity, equation 3.3 will now be described again:

$$\frac{dn}{dT} = -1.044 \times 10^{-4} - 1.543 \times 10^{-7} T, \tag{A.3}$$

where T is the water temperature, given in degrees Celsius, and n is the refractive index of water, given in RIU. Integrating the previous equation, one obtains:

$$\Delta n(T) = -1.044 \times 10^{-4} T - 7.715 \times 10^{-8} T^2 + C, \tag{A.4}$$

where Δn is the refractive index variation, T is the temperature, given in degrees Celsius, and C is an integration constant. Taking into consideration that the previously calculated value of refractive index at 1550 nm, using the Sellmeier equation, corresponds to a temperature of 20 °C, the refractive index variation (Δn) should be considered zero at 20 °C. Hence, the constant C is 2.11886×10^{-3}. Together with the determined refractive index through equation A.2 (1.3154), one obtains the refractive index of water as a function of

temperature, at a wavelength of 1550 nm, given by equation 3.4. Once again, for the sake of clarity, equation 3.4 will now be described again:

$$n(T) = 1.3154 + 2.11886 \times 10^{-3} - 1.044 \times 10^{-4} T - 7.715 \times 10^{-8} T^2, \tag{A.5}$$

with T given in degrees Celsius and n given in RIU.

Appendix B.

Summary of Optical Vernier Effect Configurations

Table B.1. – Summary of the optical Vernier effect configurations using single-type FPI.

Year	Configuration	Sensitivity	Range	M	Ref
2012	SHCF+hollow silica μsphere	Temperature: 17.604 pm/°C	100-1000 °C	N/A	[159]
2014	HC-PCF in series	Strain: 47.14 pm/$\mu\varepsilon$	0-200 $\mu\varepsilon$	29.5	[158]
2014	HC-PCF in series	Magnetic Field: 71.57 pm/Oe	20-35 Oe	28.6	[158]
2015	Simplified HCF+SMF	Temperature: 1.019 nm/°C	250-300 °C	N/A	[148]
2015	HCF+PCF	Gas RI: 30899 nm/RIU	1.00277-1.00372 RIU	N/A	[166]
2016	HCF+SMF	Airflow: 1.541 nm/(m/s)	3-7 m/s	N/A	[167]
2018	HC+ferrule	Temperature: 67.35 pm/°C	20-24 °C	23.4	[150]
2018	HCF+SMF+HCF+μsphere	Temperature: -1.081 nm/°C	30-42 °C	N/A	[168]
2018	SMFs in HCF+fusion hole	Gas Pressure: 86.64 nm/MPa	0-0.6 MPa	32.8	[169]
2018	SMFs in HCF+fusion hole	Temperature: 449 pm/°C	40-100 °C	N/A	[169]
2018	HCF+coated LMAF	Hydrogen: -1.04 nm/%	0-2.4%	N/A	[149]
2018	SMF in HCF with LC	Temperature: 19.55 nm/°C	N/A	N/A	[170]

Table B.2. – Summary of the optical Vernier effect configurations using single-type FPI (continuation).

Year	Configuration	Sensitivity	Range	M	Ref
2019	SCF in parallel	Temperature: 153.8 pm/°C	40-220 °C	14.6	[177]
2019	SMFs in HCF	Temperature: 10.28 nm/°C	23-25 °C	6.0	[225]
2019	HCF between SMFs	Strain: 18.36 pm/$\mu\varepsilon$	0-320 $\mu\varepsilon$	14.0	[226]
2019	Milled HCF+SMF	Gas Pressure: 80.3 pm/kPa	180-220 kPa	N/A	[162]
2019	Milled HCF+SMF	Temperature: -107.0 pm/°C	25-65 °C	N/A	[162]
2019	Offset SMF+SMF	Gas RI: -11368.5 nm/RIU	1.00003-1.00026 RIU	N/A	[171]
2019	Offset SMF+SMF	Temperature: 98 pm/°C	35-65 °C	N/A	[171]
2019	HCF+SMF+Airgap+SMF	Strain: 1.15 nm/$\mu\varepsilon$	0-160 $\mu\varepsilon$	N/A	[163]
2019	HCF+SMF+Airgap+SMF	Temperature: 3.6 pm/°C	50-160 °C	N/A	[163]
2019	Microhole+SMF	RI: 1143.0 nm/RIU	1.3352-1.3469 RIU	N/A	[172]
2019	Microhole+SMF	Temperature: -180.5 pm/°C	30-90 °C	N/A	[172]
2019	Milled μsphere in parallel	Salinity: 82.61 nm/M	0-0.297 M	6.8	[178]
2019	Milled μsphere in parallel	RI: 6830.0 nm/RIU	1.3176-1.3212 RIU	6.8	[178]
2019	Milled μsphere in parallel	Temperature -587.37 pm/°C	21.7-30 °C	5.1	[178]
2019	HCF partially with PDMS	Temperature: 17.758 nm/°C	N/A	27.2	[179]
2019	Fs-laser mirrors in SMF	Strain: 28.11 pm/$\mu\varepsilon$	0-1500 $\mu\varepsilon$	23.8	[164]
2019	Fs-laser mirrors in SMF	Temperature: 278.48 pm/°C	30-100 °C	24.6	[164]
2019	Fs-laser mirrors in SMF	Strain: 145 pm/$\mu\varepsilon$	0-200 $\mu\varepsilon$	N/A	[165]
2019	Fs-laser mirrors in SMF	Temperature: 927 pm/°C	30-60 °C	N/A	[165]
2019	HCF+LMAF	Isopropanol: 20 pm/ppm	0-500 ppm	N/A	[173]
2019	HCF+Offset SMF in parallel	Strain: -43.2 pm/$\mu\varepsilon$	0-1750 $\mu\varepsilon$	4.6	[161]
2019	HCF+Offset SMF in parallel	Temperature: -27 pm/°C	30-100 °C	4.2	[161]
2019	PM-PCF+HC-PCF	Temperature: 535.16 pm/°C	24-1000 °C	45	[174]
2019	μsphere+HCF in parallel	Transverse Load: -3.75 nm/N	0-1 N	3.4	[180]
2019	μsphere+HCF in parallel	Temperature: -3.33 pm/°C	50-200 °C	4.2	[180]
2019	HCF in parallel	RI: 30801.53 nm/RIU	1.3347-1.33733 RIU	33	[160]
2019	HCF in parallel	Temperature: 250 pm/°C	20-30 °C	N/A	[160]
2019	PCF+HCF partially filled	Humidity: 456 pm/%RH	19.63-78.63 %RH	N/A	[175]
2019	**FIB-structured MMF TIP**	**Temperature: -654 pm/°C**	**30-120 °C**	**>60**	**[21]**
2019	**HCF in parallel + Harmonics**	**Strain: 93.4 pm/$\mu\varepsilon$**	**0-600 $\mu\varepsilon$**	**27.7**	**[20]**
2020	HCF filled with DSO	Temperature: 39.21 nm/°C	around 35 °C	N/A	[176]
2020	HCF+PM-PCF in parallel	Temperature: -45 pm/°C	100-300 °C	3.9	[181]
2020	HCF+PM-PCF in parallel	Temperature: -92 pm/°C	300-800 °C	5.3	[181]
2020	**H-μsphere+MMF+Harmonics**	**Strain: 146.3 pm/$\mu\varepsilon$**	**0-500 $\mu\varepsilon$**	**N/A**	**[19]**
2020	**H-μsphere+MMF+Harmonics**	**Temperature: 650 pm/°C**	**22-100 °C**	**N/A**	**[19]**

Table B.3. – Summary of the optical Vernier effect configurations using other single-type interferometers, as well as hybrid configurations.

Year	Configuration	Sensitivity	Range	M	Ref
2017	**MZI:** offset spliced SMF	Curvature: -36.26 nm/m^{-1}	0.3-0.5 m^{-1}	8.0	[182]
2017	**MZI:** offset spliced SMF	Temperature: 397.36 pm/°C	10-75 °C	8.8	[182]
2018	**MZI:** MMF+DSHF+MMF	Gas P.: -63.584 nm/MPa	0-0.8 MPa	7	[187]
2018	**MZI:** MMF+DSHF+MMF	Temperature: 34.7 pm/°C	35-60 °C	N/A	[187]
2018	**MZI:** SHTECF	Temperature: 2.057 nm/°C	25-30 °C	48.8	[188]
2018	**MZI:** MMF with milled air slit	Gas P.: -82.131 nm/MPa	0-0.7 MPa	9.4	[185]
2018	**MZI:** MMF with milled air slit	Temperature: 355.2 pm/°C	25-100 °C	10.1	[185]
2019	**MZI:** spherical-shaped structure	Strain: -8.47 pm/$\mu\varepsilon$	N/A	5.4	[183]
2019	**MZI:** spherical-shaped structure	Curvature: -33.70 nm/m^{-1}	N/A	5.4	[183]
2019	**MZI:** (MMF+HCF+MMF)×2	Gas P.: -73.32 nm/MPa	0-0.8 MPa	8.5	[186]
2019	**MZI:** (MMF+HCF+MMF)×2	Temperature: 52.60 pm/°C	30-100 °C	8.5	[186]
2019	**MZI:** Coreless+SHF+Coreless	RI: 44084 nm/RIU	1.33288-1.33311 RIU	3.1	[189]
2019	**MZI:** MMF+HCF+MMF	Temperature: 528.5 pm/°C	0-100 °C	17.5	[190]
2020	**MZI:** SMF+FMF+SMF	Static P.: 4.072 nm/MPa	N/A	N/A	[184]
2020	**MZI:** SMF+FMF+SMF	Temperature: 1.753 nm/°C	N/A	N/A	[184]
2015	**Sagnac:** PANDA+PANDA	Temperature: -13.36 nm/°C	30-40 °C	9.2	[191]
2018	**Sagnac:** PANDA+Hi-Bi μ-fiber	RI: 2429 nm/RIU	1.3320-1.3369 RIU	5.4	[192]
2018	**Sagnac:** Coated PMF w/ º Shift	Hydrogen: -14.61 nm/%	0-0.8 %	1.9	[195]
2018	**Sagnac:** Coated PMF w/ º Shift	Temperature: -2.44 nm/°C	30-60 °C	15.0	[195]
2019	**Sagnac:** PANDA w/ º Shift	Strain: 58 pm/$\mu\varepsilon$	0-1440 $\mu\varepsilon$	9.8	[196]
2019	**Sagnac:** PANDA w/ º Shift	Temperature: -1.05 nm/°C	20-80 °C	0.8	[196]
2019	**Sagnac:** Coated PMF w/ º Shift	Isopropanol: 239 pm/ppm	0-42 ppm	4.2	[197]
2019	**Sagnac:** Coated PMF w/ º Shift	Strain: 53.8 pm/$\mu\varepsilon$	0-365.82 $\mu\varepsilon$	N/A	[197]
2019	**Michelson:** DCF+DSHF	Bending: 38.53 nm/m^{-1}	0-1.24 m^{-1}	N/A	[198]
2019	**Michelson:** DCF+DSHF	Temperature: 67.2 pm/°C	50-130 °C	N/A	[198]
2019	**Michelson:** TCF+DSHF	Curvature: 57 nm/m^{-1}	0-1.14 m^{-1}	N/A	[5]
2019	**Michelson:** TCF+DSHF	Temperature: 143 pm/°C	30-100 °C	N/A	[5]
2018	**Coupler:** Hi-Bi Coupler	RI: 35823.3 nm/RIU	1.3330-1.3347 RIU	N/A	[199]
2020	**Coupler:** Parallel Couplers	RI: 114620 nm/RIU	1.3350-1.3355 RIU	19.7	[206]
2020	**Coupler:** Parallel Couplers	RI: 126540 nm/RIU	1.3450-1.3455 RIU	21.7	[206]
2020	**Coupler:** Double Helix Coupler	RI: 27326.59 nm/RIU	1.3333-1.3394 RIU	5.3	[200]
2015	**MKR:** Cascaded MKR	RI: 6523 nm/RIU	1.3320-1.3350 RIU	N/A	[6]
2019	**Hybrid:** HCF FPI+MZI	Temperature: -107.2 pm/°C	30-80 °C	89.3	[201]
2020	**Hybrid:** FPI+MZI	RI: -87261.06 nm/RIU	1.332-1.334	N/A	[202]
2020	**Hybrid:** FPI+MZI	Temperature: 204.7 pm/°C	30-130 °C	N/A	[202]
2017	**Hybrid:** Sagnac+FPI	Temperature: -29 nm/°C	42-44 °C	20.7	[204]
2019	**Hybrid:** Sagnac+FPI	Sound P.: 37.1 nm/MPa	62.2-92.4 dB	N/A	[205]
2019	**Hybrid:** Sagnac+FPI	Temperature: 10.28 nm/°C	23-25 °C	6.0	[203]
2019	**Hybrid:** Sagnac+MZI	Strain: 65.71 pm/$\mu\varepsilon$	0-300 $\mu\varepsilon$	20.8	[8]
2017	**Hybrid:** MKR+FPI	RI: 311.77-2460.07 nm/RIU	1.3319-1.3550 RIU	12-73	[7]

Appendix C.

Vernier Envelope Extraction Methods

There are multiple ways to fit and extract the internal Vernier envelopes and they mainly depend on the appearance of the spectrum. They all start by detecting the maxima of the Vernier spectrum and then group them according to each internal envelope, as already discussed in chapter 5. The internal envelopes should follow a cosine behavior that depends on the inverse of the wavelength. In fact, it results in an internal envelope with a period that increases for longer wavelengths. Under these circumstances it is still possible to fit the internal envelopes. However, it is easier to perform the fitting in a situation where no wavelength dependency exists.

Therefore, it is useful to convert the Vernier spectrum from the wavelength domain into the frequency domain, similarly to what was performed in section 3.3.2. The X-axis of the spectrum will then represent the optical frequency, given by:

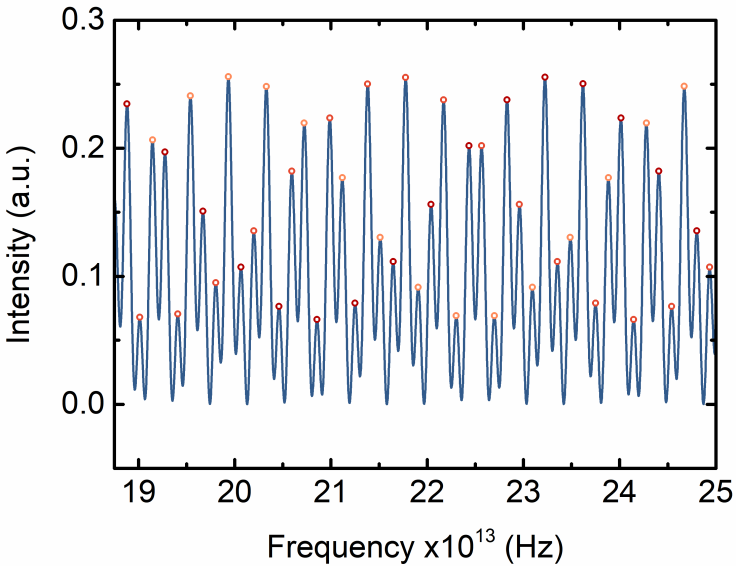

Figure C.1. – Spectrum from figure 5.5 represented in the frequency domain. The maxima are marked with a dot and colored according to the respective internal envelope.

$$\nu = \frac{c}{\lambda},$$

where c is the speed of light in vacuum and λ is the wavelength. Taking figure 5.5 as an example, the corresponding spectrum in the frequency domain is depicted in figure C.1.

Now that the period of the internal envelopes do not depend on the wavelength, one can fit the groups of maxima with a sinusoidal function such as:

$$I(\nu) = I_0 + A \sin\left(\frac{\nu - \nu_0}{w}\right), \tag{C.1}$$

where the fitting parameters are I_0, A, ν_0, and w. I_0 corresponds to the offset component (D.C. component), A is the amplitude of the envelope oscillation, ν_0 is related with the initial phase, and w is related with the inverse frequency of oscillation. Due to the previously mentioned conditions, and also to the fact that the spectrum is "perfect" (simulated), this function fits very well the maxima, as shown in figure C.2.

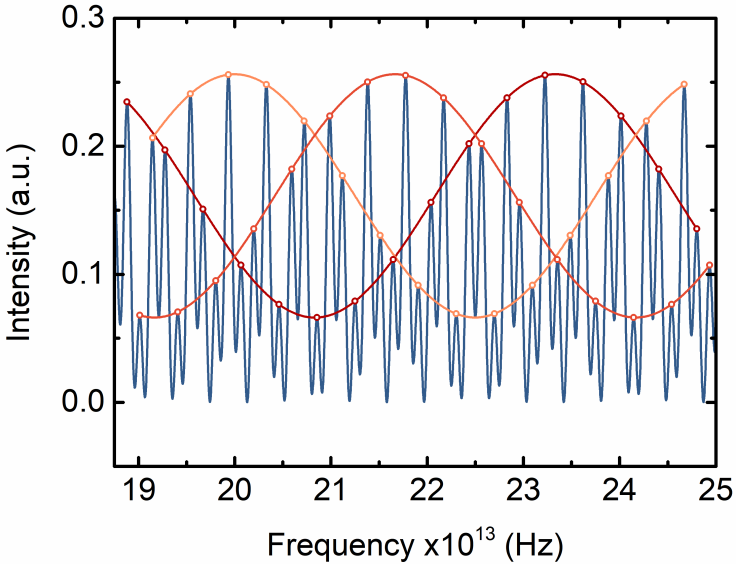

Figure C.2. – Spectrum from figure 5.5 represented in the frequency domain after fitting the internal envelopes according to equation C.1.

The problem of fitting internal Vernier envelopes starts when the experimental data presents some imperfections due to experimental conditions and to the sensing structure itself. One of the interferometers used to introduce the Vernier effect might have more losses, or have more modes other than the fundamental mode, which might generate an asymmetric spectrum. In such case the internal envelopes might no longer be fitted by equation C.1. Figures 6.3(b) or (d) are interesting examples, where the D.C. component and the amplitude of the internal envelopes increase for longer wavelengths. For this case, a different fitting approach must be considered. Given the features of these spectra, the

following fit was used for those cases:

$$I(\nu) = I_0 \exp\left(\frac{bc}{\nu}\right) + A\frac{c}{\nu}\sin\left(\frac{\nu-\nu_0}{w}\right), \tag{C.2}$$

where $I_0 \exp(bc/\nu)$ represents the D.C. component that increases with the wavelength (decreases with the frequency), where b is a fitting parameter and c is the speed of light, A is again a fitting parameter that corresponds to the amplitude of the envelope oscillation, which is now multiplied by c/ν to include the increasing amplitude with the wavelength (decrease with the frequency). Nevertheless, the previous fitting can be hard to converge.

In many cases, such as in figure 6.10 or 6.11, the internal envelopes are so large that a period of oscillation does not fit within the wavelength range available. Yet, the main interest still relies on the intersection between these internal envelopes. Adding to this, the maxima suffer from intensity fluctuations. Given the circumstances, a sinusoidal fit might be complex to achieve. An alternative way to fit these kind of internal envelopes is to use a polynomial fitting as an approximation. In this case, it might not be necessary to convert the spectrum into the frequency domain. For these two figures (6.10 and 6.11), the polynomial fit used was of 5^{th} order:

$$I(\lambda) = I_0 + A\lambda + B\lambda^2 + C\lambda^3 + D^4 + E\lambda^5, \tag{C.3}$$

where I_0 is the offset components, and A, B, C, D, and E are the other fitting parameters.

Some fittings introduce more errors than other, however the important message here is that, when performing measurements, the same fitting must be applied to all the measured spectra. The errors associated with using the same fitting method will approximately be systematic, which upon calibration can be slightly corrected. If different fitting methods are used along the measurement, the errors between the different measurements start to be random, which are more problematic for the experiment, since one cannot estimate them.

Regarding the upper Vernier envelope, it can be traced using conventional envelope extraction methods (signal processing) available in software like Origin or Matlab. Nevertheless, the visual aspect of the upper envelope and the position of the maxima using those methods highly depends on the number of points considered (smooth points). As an alternative, some works use Lorentzian [6, 227] or Gaussian [82, 196] fitting curves to find the position of the upper envelope maxima.

Appendix D.

Calibration Curves for Sucrose Solutions

This appendix contains the calibration curves used in the characterization of the optical fiber probe viscometer in chapter 7. The calibration curves are based on tabulated values for the viscosity as a function of three parameters: sucrose concentration, refractive index of the sucrose solution, and temperature (for a specific concentration).

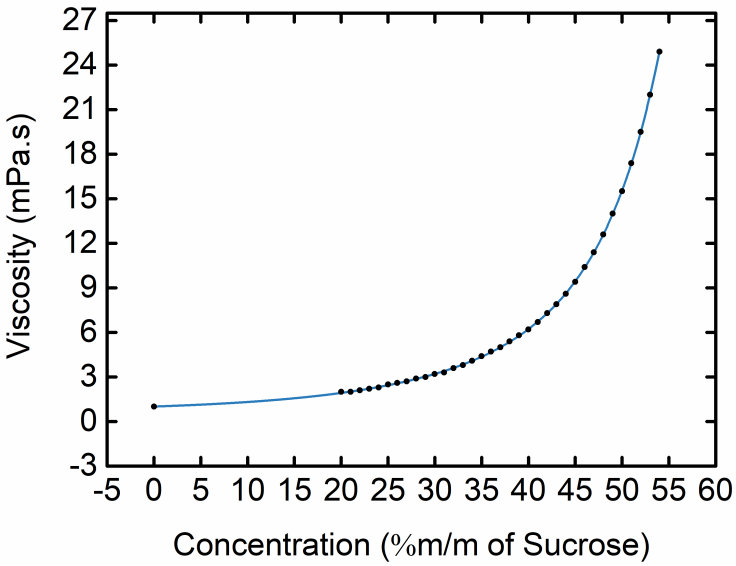

Figure D.1. – Viscosity as a function of the sucrose concentration. The data points can be found at [9].

The viscosity of a sucrose solution as a function of the sucrose concentration in mass percent (%m/m) [9] is depicted in figure D.1. The tabulated values were fitted to obtain an expression for the viscosity as a function of the sucrose concentration:

$$\eta(c) = 0.7022 + 0.00214\exp\left[(c - 9.07787)/5.20275\right] + 0.57656\exp\left[(c - 9.07787)/14.73627\right], \quad \text{(D.1)}$$

where η is the viscosity in millipascal-second (mPa.s) and c is the concentration in %m/m of sucrose.

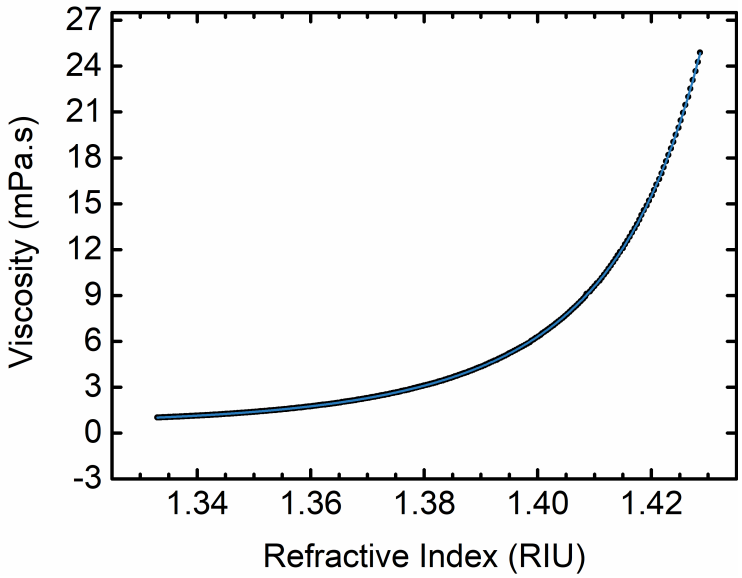

Figure D.2. – Viscosity as a function of the refractive index of the sucrose solution. The data points can be found at [10].

The viscosity of a sucrose solution as a function of its refractive index [10] is shown in figure D.2. The tabulated values were fitted to obtain an expression for the viscosity as a function of the refractive index of the sucrose solution:

$$\eta(n) = 0.59269 + 0.00758\exp\left[(n - 1.35348)/0.01054\right] + 0.89366\exp\left[(n - 1.35348)/0.02675\right], \quad \text{(D.2)}$$

where the viscosity (η) is given in mPa.s and n is the refractive index of the sucrose solution given in refractive index units (RIU).

The temperature dependence of the viscosity of sucrose solutions is also tabulated for distinct concentration values [11]. Figure D.3 presents the viscosity of a 47 %m/m sucrose solution as a function of temperature. Similarly, the tabulated values were fitted to obtain an expression for the viscosity of a 47 %m/m sucrose solution as a function of temperature:

$$\eta\,(T)_{47\%m/m} = 0.53596 + 12.03746\exp\left(-T/36.57479\right) + 17.325\exp\left(-T/13.21445\right) + 0.70162\exp\left(-T/4.79466\right), \quad \text{(D.3)}$$

where the viscosity (η) is given in mPa.s and T is the temperature expressed in degree Celsius (°C).

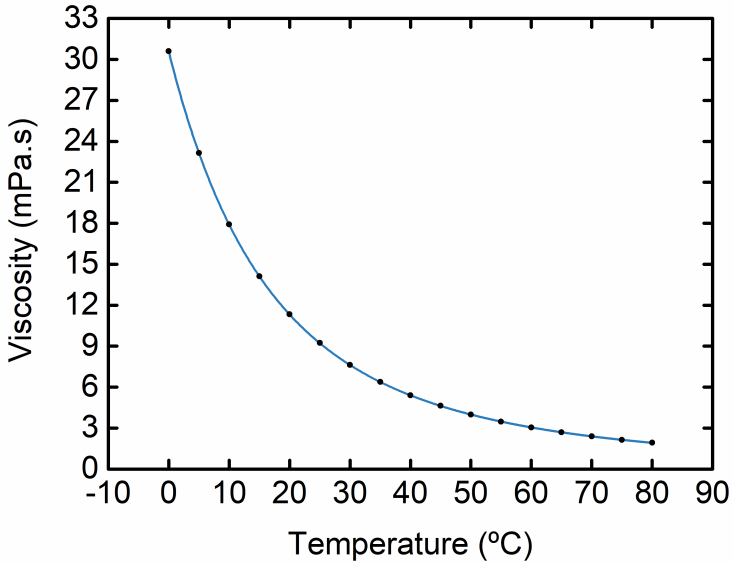

Figure D.3. – Viscosity as a function of the temperature for a sucrose solution with a concentration of 47 %m/m. The data points can be found at [11].